The Dynamics of an Excited Hydrogen Atom in a Parallel Low Frequency Microwave and Static Field

Thesis

UNRESTRICTED

The Dynamics of an Excited Hydrogen Atom in a Parallel Low Frequency Microwave and Static Field

Nicholas Christopher Kelly, B.Sc. (Hons.)

Thesis submitted to The Open University

for the degree of Doctor of Philosophy

30th January 2011

Department of Mathematics and Statistics

Date of Submission: 4 October 2010
Date of Award: 10 February 2011

Abstract

This thesis examines the effect of parallel static and low frequency microwave fields on excited hydrogen atoms. By low frequency we mean, $\Omega_0 = \Omega/\omega_K \ll 1$, where Ω is the field frequency and ω_K is the Kepler frequency of the unperturbed excited electron. Experiments and calculations have shown that for certain field strengths, resonances arise, sometimes leading to enhanced ionisation.

Approximate time-dependent one-dimensional Hamiltonians describing the classical dynamics were derived previously by Richards [51]. Here we derive a number of properties from these Hamiltonians and use these to predict and explain ionisation behaviour.

Because the separatrix is a construct of classical dynamics affecting a relatively small area of phase space, it is unclear how it will affect the quantum mechanics of the system or how large the quantum numbers must be for measurable effects. For this reason, we derive a new quantal method to compute the ionisation probability for the system. The method is tested where possible and shown to accurately describe the general behaviour of the system. The method is applied to slowly switched fields and is computationally efficient, allowing calculations for high principal quantum numbers, $n \geq 800$.

We compare classical and quantum ionisation behaviour. Significant qualitative differences exist for low quantum numbers, $n \approx 10$, but quantitative differences exist, for higher quantum numbers, even for $n \geq 100$.

For slowly switched fields, the separatrix can considerably affect the ionisation structure. These effects are also manifest in the quantum mechanics for sufficiently high n, but even for $n = 39$, the influence of the separatrix is seen.

Ionisation times are calculated for systems prepared in a single initial state and for mi-

crocanonical distributions of initial states. Classically, motion near the separatrix is shown to lead to longer ionisation times at resonance. This is also seen in quantal calculations, even for quantum numbers as low as $n = 39$, that is, those accessible by experiment.

Acknowledgements

I would like to thank my supervisor, Professor Derek Richards, for his support and guidance. I am hugely grateful to him for providing me with the opportunity to carry out this research and for his continual support and encouragement throughout. I wish him the very best in his retirement.

My thanks go to my parents, and my mum in particular for giving me the initial kick to start this and whose support has always been there.

Mostly I would like to thank Sandra, Jake, Rosie and Megs for their love and support and, of course, for putting up with me over the many years that this has taken to complete.

Contents

Chapter 1

Introduction

1.1 Background

Experiments on the ionisation of excited hydrogen atoms subjected to microwave fields began in 1974 with the experiments of Bayfield and Koch [5, 6]. In the experiments, hydrogen atoms are excited to a particular, known principal quantum number, $n \gg 1$, and then subjected to a microwave field before measuring the fraction of atoms for which ionisation occurs.

A key characteristic of the microwave experiments is that the photon energy for the microwave field is small relative to the energy required for ionisation. For example, for an initial principal quantum number, $n = 66$, in a microwave field of frequency $\Omega/2\pi = 9.92\text{GHz}$, the energy difference between the initial state and the continuum is more than $70\Omega\hbar$. For ionisation to occur at all was surprising and not amenable to the quantum techniques available at the time. Previous work on *multi-photon ionisation* (MPI) had focused on the effects of pulsed lasers on ground state atoms where the ionisation energies are typically 1-5 photons. However, an application of quantal perturbation theory using a basis of zero-field states would require 70 orders of perturbation to reach the continuum. The field intensity required for ionisation, according to this theory, is far larger than observed experimentally; however, this theory is invalid because the radius of convergence of the perturbation expansion is much smaller than the field sizes used, although estimates for the radius of convergence are difficult to calculate. We denote the energy for an unperturbed state of principal quantum number, n,

by E_n. For the microwave experiments, $E_{n+1} - E_n \simeq \hbar\Omega$, and so the coupling between unperturbed quantum states is strong. The number of unperturbed states that must be included and the necessary inclusion of the continuum makes the quantum mechanical treatment of this problem numerically intractable without further approximation.

Briefly, the experiments typically comprise the following arrangement. A beam of initially excited hydrogen atoms in a low n substate is passed through a pair of CO_2 lasers in a static field to cause a double excitation of the hydrogen atoms firstly to a substate, n' where $n' \approx 10$, and then by tuning the frequency of the second laser, a second excitation is made to a selected high n state, with n in the range 23–90.

The atomic beam is passed axially through a TM mode microwave cylindrical cavity where the microwave field is applied; the microwave frequency is typically of the order, $\Omega/2\pi =$ 10GHz. On their travel to the microwave cavity the atoms pass through a nominally zero field region, where stray fields cause a mixing between substates.

In the cavity the hydrogen atoms are subjected to a field whose amplitude is modified by the geometry of the wave cavity. From the perspective of a hydrogen atom transiting the cavity the field is seen to rise gradually over a number of field cycles (about 16) as the atom passes through a hole machined in the entry wall of the cavity. The atom then sees an approximately constant amplitude field over a number of cycles (about 100) before seeing the field gradually reduce to zero again as it passes through a hole in the exit wall of the cavity. The particle beam density is small, typically with only one excited hydrogen atom in the cavity at any one time.

The effect of the applied field on the hydrogen atoms depends on $\Omega_0 = n^3\Omega \times (\hbar^3/\mu e^4)$, where μ is the reduced electron mass, e is the electron charge and n is the principal quantum number of the excited state. If $\Omega_0 \ll 1$, then the hydrogen atoms leaving the cavity are either ionised or remain in approximately the same initial excited state, n. If $\Omega_0 > 1$ then the electrons can be significantly excited by the field to states $n' \gg n$, but few atoms are ionised.

The atomic beam leaving the cavity passes through an applied static field, after which ionised particles are counted by detectors. The static field is tuned to cause the ionisation of atoms that have been sufficiently excited by their interaction with the microwave field. Hence the experimental signal is a measure of both truly ionised hydrogen atoms and highly

excited atoms. For each substate there is a critical field above which ionisation occurs, so that by tuning the static field a criteria can be set for the selection of the highly excited atoms. The critical field depends predominantly on the principal quantum number, n, so to a first approximation ionisation occurs if $n > n_c$, where n_c is some cut-off value; however, for some experiments it is also necessary to take into account the dependence on all three quantum numbers specifying the substate.

The results from the experiments are typically plots of ionisation probability against field strength, or critical fields causing ionisation against frequency. Examples of each are given in [49] figures 8–13 and [24] figures 2 and 3.

The configuration just described was employed by Koch *et al* in 1974 and is detailed by Koch and Leeuwen [31]. In some experiments microwave wave guides have been used instead of the cavities; see for example, [7].

From an experimental perspective it is easier to vary the initial quantum number, n, than the field frequency, Ω, which is fixed by the geometry of the microwave cavity. Experiments are therefore typically performed by fixing the field frequency and using an appropriate choice of n to access different regions of behavioural interest.

The large quantum numbers involved mean that classical and semi-classical techniques can sometimes be employed, although for some fields and initial excited states, quantal effects dominate. In 1978 Leopold and Percival used classical dynamics [36, 37] to calculate ionisation probabilities that were found to be in good agreement with the original 1974 experiments. Fortunately these experiments were for frequencies and quantum numbers where the system's behaviour is well described classically.

The non-relativistic Hamiltonian describing the effect of the field on a hydrogen atom is,

$$H = \frac{\mathbf{p}^2}{2\mu} - \frac{e}{r} + zF(t),$$

where μ is the reduced electron mass, e is the electron charge and F is the applied electric field of frequency Ω. This is a non-linear system system perturbed by a uniform periodic force. A crude approximation to $F(t)$, ignoring the motion through the cavity ends, is $F(t) = F_\mu \sin \Omega t$, where F_μ is the field amplitude.

The dynamics of this system are determined by various time scales. In the absence of the applied field the unperturbed system is degenerate, with one characteristic frequency, ω_K, the Kepler frequency for the electron, $\omega_K = \mu e^4/n^3\hbar^3$. For an electron in an $n = 66$ excited state, $\omega_K \approx 23$GHz. The applied field introduces a set of resonances, $p\omega_K = q\Omega$, where p and q are incommensurate integers. In phase space, near any one of these resonances, the classical system behaves approximately like a simple pendulum: resonance islands containing librational orbits are separated by a boundary layer from surrounding rotational orbits. These resonance islands can lead to observed effects on the ionisation behaviour of the system. Unstable orbits near the separatrix are the source of chaotic motion. It is the resonances for small p and q that are most important, because for large p and q the resonance islands are small and the periodic motion within the islands is long compared to the field interaction times.

For the quantum mechanics, the energy separation between adjacent states is $\Delta E_n = E_{n+1} - E_n \approx \hbar\omega_K$, so when $\Omega = \omega_K$, there is approximately one photon energy separating the initial excited energy state from its immediate neighbours.

To recognise the effect of the resonances on the dynamics, it is useful to use scaled variables. The scaled frequency, $\Omega_0 = \Omega/\omega_K$, and the corresponding scaled field, $F_0 = a^2F/e^2$, where a is the unperturbed Kepler ellipse semi-major axis, $a = n^2\hbar^2/\mu e^2$. In scaled variables, the Coulomb force on the excited electron in an unperturbed circular orbit is, $F_0 = 1$.

The dynamics of the system is dominated by one frequency, Ω_0. From experiments and numerical calculations, the observed behaviour can be categorised by six overlapping regions with the following characteristic behaviours in each.

Region I: The Tunnelling Region For $\Omega_0 \lesssim 0.07$ the field changes little in one Kepler period of the unperturbed motion and so the classical motion is well described by the adiabatically changing action-angle variables for a static field. The electron follows an elliptical orbit that precesses around the axis of the applied field, with the z-component of the Runge-Lenz vector (or equivalently the electric action) approximately constant. For slowly switched fields, the adiabatic changes in the motion of the electron mean that most non-ionising hydrogen atoms entering the microwave cavity in an excited state with principal quantum number, n, leave the microwave cavity in a state with the same principal quantum number, n.

For scaled fields, $F_0 \gtrsim 0.13$, classical orbits for some values of the action do not exist. Hence, as the field is slowly switched on, some orbits ionise. For fields, $F_0 \gtrsim 0.38$, the majority of orbits ionise.

Quantally a similar behaviour is seen with the slowly switched-on field causing a number of states to ionise, with additional ionisation arising due to tunnelling through the barrier to the continuum. There is little coupling between the adiabatic states and, after the field switch-on, there is little ionisation other than by tunnelling from adiabatic states lying close to the top of the barrier. Experimentally ionisation is found to occur consistently below the classical ionisation limit and to be consistent with WKB tunnelling calculations described in [53] and [21]. There is a good match particularly for $\Omega_0 \lesssim 0.03$.

Region II: The Low Frequency Region This region is approximately given by $0.05 \lesssim \Omega_0 \lesssim 0.3$. This region is differentiated from region I by the appearance of quantal transitions between adiabatic states. Classically, there is greater variation in the adiabatic actions. The transitions between adiabatic states lead to the appearance of additional structure in experimental graphs of ionisation against field strength: for some values of Ω_0, additional peaks and troughs in ionisation probability arise. This is described, for example, in [49].

For lower scaled frequencies, $\Omega_0 \lesssim 0.05$, these features are not seen in the classical dynamics. One-dimensional quantal calculations [8, 9, 48, 49, 11, 22] suggest that the peaks correspond to resonances at $\Omega_0 \approx 1/p$. For large p, resonance effects are too small to have a noticeable effect in the classical dynamics, but quantally the resonances lead to stronger coupling between the adiabatic states causing excitations and de-excitations. These cause, for sufficiently strong fields, consequent changes in ionisation probability [49].

These resonances are also theoretically shown to extend into region I although the resonance widths become exponentially small with increasing p [22] and so do not cause observable changes in ionisation.

Region III: The Near Classical Region In the region, $0.1 \lesssim \Omega_0 \lesssim 1.2$, there is generally very good agreement between classical simulations and experimental results [24], par-

ticularly for 3-d simulations. Differences are seen at resonances values, where quantal descriptions are required. Experiments were carried out at 9.92GHz, 26.43GHz and 36.02GHz. Experimental results with initial states, n, chosen to correspond to the same scaled frequencies show a very close match (see for example, [31], figure 1b).

In region III, the ionisation region coincides with the onset of classical chaos, identified by Meerson *et al* [46]. This was shown for a one-dimensional model by Jensen [26, 27, 28] and by Leopold and Richards [38, 39] for the one-dimensional classical hydrogen atom [38] and the three-dimensional classical hydrogen atom [39]. For the Hamiltonians used they showed that as the perturbation size increases, the resonance islands become larger until the Chirikov 'resonance overlap condition' is met and the resonance islands are no longer distinct. When this condition is satisfied, some electron orbits become unstable. The motion of these electrons through phase space is approximately diffuse, allowing the population of higher energy regions of phase space. The onset of this unstable motion has been shown to have good agreement with the experimental onset of ionisation over much of region III.

Classical resonances occur when $\Omega_0 = 1/p$, $p = 2, 3, \ldots$. The effects for $p \gg 1$, were discussed for region II. For $p = 2$ and $p = 3$ classical simulations and experiments also differ, but the reasons for this are not yet clear; quantal effects are probably important.

Region IV: The Transition Region For $1 \lesssim \Omega_0 \lesssim 2$, the deviation between experimental results and classical 3-d simulations becomes more marked. The classical prediction for the threshold ionisation field, for which the ionisation probability is greater than 10%, is typically lower than that observed experimentally, although this is not always true near resonances. For some Ω_0 values, the quantal system is more stable than the classical system. Jensen [29] showed numerically that at these frequencies the stable states occupied by the system are associated with classical unstable periodic orbits. Leopold and Richards [42] showed that the enhanced stability was due to the quantal system selectively exciting to these 'scarred wave functions'. The longer period associated with these classical orbits is the same property that quantally causes the decoupling of the scarred wave functions from the continuum and hence reduces ionisation.

Region V: The High-frequency Region For $\Omega_0 > 2$, experimental ionisation thresholds are above the classical predictions. Casati *et al* [15] showed that quantum effects could inhibit the excitation process, inhibiting the diffusive occupation of quantum states, even though the corresponding classical motion is chaotic; this process is known as *quantum localisation.* This localisation breaks down above a critical field referred to as the *quantum delocalisation border.* In region V this critical field is above the classical critical field for which the resonance overlap condition is met; hence, the quantal ionisation requires a higher field. A review of quantum localisation is provided in [16].

The ionisation threshold fields calculated from the quantum localisation theory are at some variance to those observed experimentally. More accurate estimates for ionisation threshold fields were given by Leopold and Richards [40] from detailed quantal calculations.

Region VI: The Photoelectric Region For $\Omega_0 \gtrsim n/2$, the energy gap to the continuum is one photon. This is the domain of the photoelectric effect, for which Einstein originally introduced the concept of the photon in 1905. Classical behaviour is expected to be entirely absent in this domain, at least for weak intensity fields.

A number of approaches to solve the quantum mechanics for the ionisation of atoms by microwave and laser fields have been developed. The large principal quantum number, the consequent high density of states and the need to include the continuum make the problem computationally intensive. Partly for this reason, almost all of the models developed to describe the system are one-dimensional.

Susskind and Jensen [55] compare one-dimensional calculations using different basis: a finite set of unperturbed hydrogenic states and a discretised set of continuum states is compared with a finite set of Sturmian states, which overlap the continuum states.

Blümel and Smilansky [9] use a finite basis set of unperturbed one-dimensional hydrogenic states. The calculations include bound-bound and bound-continuum transitions, but exclude continuum-continuum transitions. The effects of the field switch are ignored so that a Floquet method can be used to speed the calculations. The results show reasonable matches against experimental data [43], for $\Omega_0 \ll 1$, with an initial state in the interval $36 \leq n \leq 42$ and the

basis set including states in the interval $31 \leq n \leq 120$.

A more efficient approach for low frequencies is given by Richards [48] using an adiabatic basis of bound Stark states and including ionisation to the continuum by the introduction of complex energies. The choice of basis requires fewer states to be included in the calculations. The method is compared with experimental results and the calculations of Blümel and Smilansky in [49].

For high scaled frequencies, $\Omega_0 > 1$, Leopold and Richards [41] give an efficient method using a truncated basis of one-dimensional hydrogenic Stark states. Ionisation is introduced by the inclusion of complex energies which are calculated using semi-classical methods. The method includes for the presence of a static field, in order to make the number of bound states finite. The calculation of the complex energies is modified in [50] to apply to lower scaled frequencies.

The behaviour and theory just described apply to the excited hydrogen atom subjected to a microwave field. There is one fundamental frequency for this system, Ω_0, which is why the system can be described reasonably well by one-dimensional approximations. However, the physics of the system is changed by the introduction of an additional static electric field, which we describe in the following section.

1.2 Microwave and Static Fields

The Hamiltonian for the electron of a hydrogen atom in a static field parallel to a microwave linearly polarised field is approximated by,

$$H = \frac{\mathbf{p}^2}{2\mu} - \frac{e}{r} + z(F_\mu \sin \Omega t + F_s),$$

where F_μ is the microwave field amplitude and F_s is the static field. In this thesis we consider the low frequency region, $\Omega_0 \ll 1$.

The presence of the static field introduces another time scale to the system. In classical mechanics, the additional static field causes the axis of the orbital ellipse to precess in the plane of the orbit. The frequency of precession varies with the static field, so that for some static field values resonances arise between the applied microwave field and the frequency of

the precession. The dynamics are now determined by two frequencies: the scaled frequency, Ω_0, and the frequency of precession caused by the static field.

The additional timescale leads to observable differences in the ionisation behaviour of the system with distinct peaks in ionisation sometimes arising near resonances between the applied field frequency and the frequency of the precession of the ellipse, the latter depending on the static field strength, F_s.

For low frequencies, $\Omega_0 \ll 1$, a good match to the experimental results is obtained using classical mechanics [51]. However, in this frequency range tunnelling is known to be important in the absence of a static field, as described for region I in the previous section. This motivates the development of a quantum description for the system, but this is complicated by the presence of the two time scales and the large quantum numbers involved.

Classically, the separatrix plays an important part in the dynamics of the system, leading to complex ionisation behaviour, particularly for slowly switched fields. As the separatrix occupies a relatively small area of phase space it is unclear how it will affect the quantum mechanics, or how large the quantum numbers must be before there is a clear correspondence between the classical and quantum behaviour. To examine this requires a quantum approximation that can be applied for high quantum numbers.

This thesis is concerned primarily with the classical and quantum physics of a parallel static and linearly polarised microwave field, with scaled frequencies lying in region I described above. In this region, in the absence of a static field, resonances between the Kepler frequency and the microwave frequency have a negligible effect. Hence, when a static field is introduced we expect that resonance effects will be primarily due to resonances between the frequency of precession and the microwave field frequency.

The Hamiltonian is time-dependent, but is axially symmetric, so the magnetic quantum number, m, is constant and the system has 2 degrees of freedom. The classical physics of this was described by Richards [51] for low scaled frequencies, $\Omega_0 \ll 1$. Good agreement was found with experimental results for the locations and widths of resonance ionisation peaks, although many of the comparisons between experiment and theory remain unpublished [33].

The quantal methods described in the previous section cannot be applied to the problem considered here. For low scaled frequencies in the presence of a static field, the orbital

ellipse of the electron precesses and the electron motion is not one-dimensional; hence the one-dimensional methods just described cannot be used. We are aware of only two methods that can be used to solve Schrödinger's equation for excited states that can also account for variation in the electron angular momentum. Buchleitner *et al* [12, 13, 14] apply Floquet techniques using a Sturmian basis for the three-dimensional Hamiltonian for a linearly polarised microwave field, although the techniques are applied only for $n \sim 20$. The case of a circularly polarised microwave is also considered [56]. These techniques cannot be straightforwardly adapted to describe slowly-switched fields, which can have appreciable effects on the dynamics and are important for the system considered here.

The most direct method, although computationally intensive, is the numerical integration of the time-dependent Schrödinger equation on a space-time lattice. Robicheaux *et al* [52] use a space-time lattice approach for excited hydrogen atoms subjected to microwave and static fields. Their results are compared with the experimental results of Koch *et al* [32] in the vicinity of a resonance for $\Omega_0 = 0.073$. We compare their results with the method described here in §2.2.2 and §3.2.2 (pages 56 and 110) for ionisation probabilities and in §5.5 (page 172) for ionisation times.

The quantum method developed here is valid for low frequency linearly polarised microwave fields with parallel static fields and can be used for slowly-switched fields. The approach is computationally efficient, allowing a wide range of parameters to be explored and for very high quantum numbers to be tackled. Results for principal quantum numbers up to $n = 800$ are presented, with calculations possible for at least $n = 1600$. These calculations were carried out on a desktop PC with one Q6600 2.4GHz CPU.

1.3 Outline of Thesis

For the region of interest, $\Omega_0 \ll 1$; the period of the applied field is much longer than the Kepler period. This fact is essential to the development of a classical approximation for the system by Richards [51], which is the starting point for the work described here. For clarity we include in this thesis a summary of the elements from [51] that we use; these are: the analysis leading to the *Averaged Hamiltonian* in §2.1.1 and §2.1.2, the *Resonance Hamiltonian* in §2.1.4

and the classical ionisation mechanism described in §2.1.6. All other work presented here is the work of the author, unless stated otherwise within the text.

In the following, we provide an outline of the contents of this thesis. In chapter 2.1.2 we develop the classical theory. For the region of interest, $\Omega_0 \ll 1$, the period of the applied field is much longer than the Kepler period. This fact is essential in the development of an approximate Hamiltonian to describe the system, see Richards [51].

The approach taken is to reduce the number of degrees of freedom and separate the faster and slower time scales of the system, allowing averaging methods to be used to ultimately give a more computationally efficient approximate Hamiltonian.

For a hydrogen atom in a static electric field, the Hamiltonian is separable in parabolic coordinates and for bound motion can be re-formulated in terms of action variables. These are most usefully expressed as the principal action, I_n, the axial angular momentum action, I_m, and the electric action, I_e, which corresponds to the z-component of the Runge-Lenz vector for the orbital ellipse. For parallel static and microwave fields, axial symmetry means that I_m is constant.

When the applied field varies slowly with time, the Hamiltonian gains an additional term in the canonical transformation to action-angle variables. The term depends on the angle variables, causing the action variables, I_n and I_e, to evolve. For $\Omega_0 \ll 1$, the frequency associated with the Kepler motion is much faster than the frequency associated with the evolution of the electric action, I_e. A simpler approximation to the motion is therefore obtained by averaging over this faster motion, reducing the system to a one-dimensional time-dependent Hamiltonian, the *Mean Motion Hamiltonian*. This averaging approximation is equivalent to ignoring transitions between adiabatic states with different principal quantum numbers. In the absence of static fields, this is known to be a reasonable approximation for low frequencies, $\Omega_0 \ll 1$. We apply the theory over a range of frequencies $\Omega_0 < 0.1$; the theory is expected to be more accurate in region I for $\Omega_0 < 0.05$.

The static field cause a precession in the orbital ellipse, the frequency of which depends on the static field strength and hence for particular static field strengths, resonances can arise between the frequency of the precession and the applied frequency, Ω. This effect can be isolated by an appropriate canonical transformation of the Mean Motion Hamiltonian, after

which the action variable, I_e, and its canonically conjugate angle are both slowly varying compared to the external field frequency allowing a further simplifying approximation to be made to give the *Averaged Hamiltonian.* This Hamiltonian forms the basis for most of the calculations described here.

For most field values, the action, $I_e(t)$, is changed little by the presence of the applied field. However, in the vicinity of resonances, the resonance islands that appear in the phase space can cause larger changes in $I_e(t)$, which can result in increases in ionisation. To show this effect on the dynamics, an appropriate canonical transformation of the Averaged Hamiltonian is made to give the *Resonance Hamiltonian*, a time-independent Hamiltonian valid in the vicinity of a resonance when the applied field is at constant amplitude. The Resonance Hamiltonian proves useful in explaining the resonance structures seen in calculated ionisation probabilities and ionisation times.

Action-angle variables describe only the dynamics of bound motion. Ionisation therefore has to be included as an additional approximation. For given values of (I_n, I_m, I_e) there is a critical static field in scaled variables, $F_c(I_m/I_n, I_e/I_n)$ such that if $F_0 > F_c$ this state cannot exist. Banks and Leopold [2, 3] obtained an approximate algebraic formula for this critical field. Because the motion is approximately adiabatic for low scaled frequencies, these limits can also be incorporated into the ionisation tests used here and applied to each calculated orbit: all orbits for which $F_c(I_m/I_n, I_e/I_n) < F_0$ are assumed to ionise — this is referred to as 'over the barrier' ionisation.

To validate the derived classical approximation, comparison is made with ionisation probabilities calculated using regularised dynamics for the exact Hamiltonian (see [47]). The comparisons are made for both single substates for specified $(I_m, I_e(0))$ with a uniform distribution of the initial conjugate angle of $I_e(0)$, $\{\psi_e(0)\}$, and for microcanonical distributions of initial conditions. Experiments have so far provided data only for the latter. To confirm that the equations of motion and their numerical evaluation are correct, we compare curves, $I_e(t)$, calculated using the equations of motion with analytic expressions derived from the Averaged Hamiltonian using classical perturbation theory, which are valid for field values away from resonance.

For the exact Hamiltonian, a number of features were identified in the structure of the

ionisation probability [51]:

- In the vicinity of resonances, some peaks are seen in the ionisation probability as a function of static field. However, for some resonances, these are missing [25].
- The height and width of the resonance ionisation peaks vary considerably.
- Resonance ionisation peaks are usually displaced from the exact static field at which the resonance occurs and their shapes are difficult to predict.

We show that these features also occur for the approximate Averaged Hamiltonian and derive properties of the resonance islands that predict and explain some of these features. The calculations also show the important effect that the field switch-on has on the dynamics of the system.

For low scaled frequencies in the absence of a static field we know tunnelling to be an important contributor to ionisation. A quantal approximation is therefore required to properly describe the problem. This is developed in chapter 3.

A quantal formulation is obtained from the classical Hamiltonians by rewriting them as suitably symmetrised operator equations. Quantum equations of motion are derived for the Averaged Hamiltonian and the Resonance Hamiltonian.

Because the quantum equations of motion are derived from the action-angle variable classical Hamiltonian, they can only describe bound states. Ionisation is introduced as a further approximation by the inclusion of complex energies.

In the absence of static fields, tunnelling is a significant contributor to ionisation for low scaled frequencies, $\Omega_0 \ll 1$. We therefore expect that in addition to ionisation due to excitation 'over the barrier', tunnelling will be a significant contributor to ionisation.

Corresponding to the classical 'over the barrier' ionisation, states (n, m, k) such that the classical critical field, in scaled variables, $F_c(m/n, k/n) > F_0$ are expected to ionise. Tunnelling will also include ionisation from states below this critical limit.

Semi-classical techniques were used by Dando [21] to calculate tunnelling rates for excited hydrogen atoms in the presence of a low frequency microwave field. The approach uses tunnelling rates calculated for a static field that are assumed to also be valid when the field is slowly varying. It is not known how the accuracy of this theory varies with frequency, but for

the low frequencies of region I, a good match was found with experiments [53] for $\Omega_0 \lesssim 0.05$, with the best match found for $\Omega_0 \lesssim 0.033$. Here we derive a computationally efficient decay function suitable, fitted to semi-classically determined decay rates in the vicinity of the classical ionisation limit, for use over a range of field values.

The limited availability of published quantal calculations and experimental data restricts the validation checks that we can make for our quantal approximation. Comparison is made with classical calculations for the Averaged Hamiltonian and the exact Hamiltonian using regularised dynamics to confirm that the behaviour is consistent. Later calculations for very high quantum numbers (see §6 on page 177) confirm the expected high quantum number correspondence with classical dynamics. However, as far as we are aware, the only other published quantal calculations in the region of interest are those of Robicheaux *et al* [52], who compare their calculations with the experiments of Koch *et al* [32]. The essential features seen in these limited results are consistent with our quantal calculations, although we identify and discuss a number of differences between their calculations, the ionisation probabilities presented here and exact classical calculations using regularised dynamics.

Resonances cause broadly similar effects in the quantal and classical ionisation probabilities as functions of static field, with ionisation peaks occurring in the vicinity of the classical resonances. However, we find that tunnelling plays an important part in ionisation even for relatively high quantum numbers, such as $n = 100$. We show these effects for low quantum numbers in §3.4 (page 126) and for high quantum numbers in §6.2 (page 179).

Quantally, additional local maxima and minima are seen in ionisation probability curves, particularly for low quantum numbers. Floquet treatments show that these correspond to 'avoided crossings' where the eigenvalues of neighbouring states become nearly degenerate. For low quantum numbers we show that the eigenvalues and eigenstates of the quantised Resonance Hamiltonian correspond to Floquet quasi-energies and states and that the locations of the avoided crossings correspond to the observed peaks and troughs in the ionisation probabilities.

In chapter 4 we apply the classical and quantum theory developed in the preceding chapters to provide insight into the effects that resonances have on ionisation behaviour. Two neighbouring resonances are examined for the scaled frequency, $\Omega_0 = 0.0528$. Much of the observed quantal behaviour echoes the corresponding classical behaviour, which is traced to

the effect of the resonance island on the classical orbits. For the second resonance, for short field durations, two ionisation peaks are seen both classically and quantally. This structure is shown to be a consequence of ionisation contributions from both librational and rotational orbits near the resonance, but only arises for gradually switched-on fields.

The time scales associated with classical orbits near resonances are determined by the librational orbits of the resonance island. Orbits close to the separatrix have long periods and consequently in the vicinity of a resonance, ionisation times are longer if the orbits contributing to ionisation lie close to the separatrix. In chapter 5 we derive analytic expressions for ionisation times and show how the classical ionisation times of individual orbits lead to characteristic peaks in ionisation times at resonance for systems prepared in single substates of $(I_m, I_e(0))$.

The influence of the separatrix is also seen in quantal ionisation times, even for relatively small quantum numbers, $n = 39$. We examine ionisation times for high quantum numbers and confirm that for sufficiently high quantum numbers all of the classical features are also observed.

When ionisation times are calculated for microcanonical distributions of initial conditions, averaging hides much of the structure; however, a clear peak in ionisation times is still seen in the vicinity of a resonance. This behaviour is also seen in the calculations of Robicheaux *et al* [52] and their figure 2 in particular, where they plot the ionisation probability as a function of time, although this is not conclusive as the results are only given for three field values. We calculate similar plots and confirm that the behaviour for our quantum approximation is very similar and is a consequence of the behaviour seen for individual substates.

The quantum approximation we have derived is computationally efficient and can be applied to high quantum numbers with relatively modest computational resources, which we exploit in chapter 6. The quantal matrices to solve are tri-diagonal and for a single substate the computational time varies approximately as $n^{1.7}$, where n is the principal quantum number. In contrast, calculations using unperturbed hydrogenic states vary as n^3.

We show that although the fraction of states contributing to tunnelling ionisation reduces with increasing quantum number, there are still appreciable differences in ionisation behaviour for $n = 100$ and that for small resonance islands, tunnelling is important for very large quantum

numbers, up to $n = 400$ for the island sizes considered.

Classically, near a resonance when the external field is slowly switched on, the presence of the separatrix causes tangles to develop in the evolving phase curves. The slower the field is switched on, the more complex the tangles become. The effects of this on the classical ionisation probability were explored by Richards [51] for the exact classical system. As the field switch duration is extended, the increasingly tangled initial phase curves cause more complex features to be seen in plots of ionisation probability against static field. Multiple ionisation peaks appear and for some switch-on durations ionisation is missing entirely. These effects are also demonstrated for the classical Averaged Hamiltonian.

The separatrix curves occupy a relatively small region in phase space and so we do not expect the same structures to appear in the quantum mechanics for low quantum numbers. However, as the quantum number is increased, the increasing state density should lead to mimicked behaviour in the quantum mechanics. We confirm that this is the case for high quantum numbers ($n = 800$) and show that, although less clear, the effects are still present at $n = 100$.

Chapter 2

The Averaged Hamiltonian

2.1 Classical Theory

2.1.1 The Mean Motion Hamiltonian

Experiments on the ionisation of excited hydrogen atoms by microwave fields have been carried out by two groups using slightly different configurations. Koch and co-workers use a microwave cavity with a linearly polarised field coincident and parallel electric field coincident with the direction of travel of the atoms through the cavity. Bayfield and co-workers pass the atomic beam through a TE mode waveguide in a direction perpendicular to the waveguide axis.

Leopold and Richards [41] showed that if, in the rest frame of the hydrogen atom, the field is switched on and off gradually then for both experimental configurations the Hamiltonian can be approximately written as,

$$H = \frac{1}{2\mu}\mathbf{p}^2 - \frac{e^2}{r} + F(t)z \tag{2.1}$$

where μ is the reduced atomic mass, e is the electron charge and F is the applied field.

The numerical evaluation of the equations of motion for this Hamiltonian are complicated by the presence of the Coulomb singularity. Suitable equations can be obtained by a regularisation method described by Rath and Richards [47]. For the sake of brevity, hereafter we will refer to these regularised dynamics for the exact Hamiltonian as the *exact classical dynamics.*

The applied field is of the form,

$$F(t) = \lambda(t)\left(F_s + F_\mu \cos(\Omega t)\right), \tag{2.2}$$

where F_s is the static field, F_μ and Ω are the amplitude and frequency of the microwave field. The function $\lambda(t)$ determines the shape of the field envelope; this approximation for the field is valid only for $\dot{\lambda}/\lambda \ll \Omega$.

The field envelope for the Bayfield experiments is $\sin(\pi t/T)$ where T is the time taken for the atoms to pass through the waveguide. The envelope function we will consider here applies to the Koch experiments. In the hydrogen atom rest frame the field is seen to rise monotonically from zero to one over a switch-on period lasting N_a field periods, remain approximately constant for a period of N_b field cycles and fall monotonically to zero over a matching switch-off period lasting N_a field cycles. The envelope will be referred to using the notation N_a–N_b–N_a. A suitable form for the envelope is taken to be,

$$\lambda(t) = \begin{cases} x^2(2-x^2), & x = \dfrac{t}{N_a T}, & 0 \le \dfrac{t}{T} < N_a, \\ 1, & & N_a \le \dfrac{t}{T} < N_a + N_b, \\ x^2(2-x^2), & x = \dfrac{(2N_a + N_b)T - t}{N_a T}, & N_a + N_b \le \dfrac{t}{T} < 2N_a + N_b, \\ 0, & & \text{otherwise}, \end{cases} \tag{2.3}$$

where $T = 2\pi/\Omega$. The suitability of this approximation was checked originally by solving Maxwell's equations numerically for the microwave cavity, including the end caps. For the original experiments the best fit was obtained for $N_a = 13$ and $N_b = 116$. Whilst the field in the cavity is axially symmetric, there is variation radially. The approximation therefore allows for an averaging over a small field range near the axis centre.

Much of the analysis is more convenient in scaled units defined in terms of the unperturbed Kepler ellipse semi-major axis, $a = I_n^2/(\mu e^2)$ and the Kepler frequency, $\omega_K = \mu e^4/I_n^3$, where $I_n = n\hbar$ and n is the principal quantum number for the unperturbed atom. Where it is necessary to make clear that the quantities are scaled, the subscript 0 will be used. Scaled

and unscaled frequencies and field values are related by

$$\Omega_0 = \frac{\Omega}{\omega_K} = \frac{\Omega}{\text{GHz}}(0.00533757n)^3 \quad \text{and} \quad F_0 = \frac{a^2F}{e^2} = \frac{F}{\text{V/cm}}(0.00373535n)^4.$$

For a uniform static field the Hamiltonian is separable in squared parabolic coordinates (see [10]),

$$x = \xi\eta\cos\phi, \quad y = \xi\eta\sin\phi, \quad z = \frac{1}{2}(\xi^2 - \eta^2), \quad \xi \geq 0, \eta \geq 0,$$

with the conjugate momenta,

$$p_\xi = \mu\dot{\xi}(\xi^2 + \eta^2), \quad p_\eta = \mu\dot{\eta}(\xi^2 + \eta^2) \quad \text{and} \quad p_\phi = \mu\dot{\phi}\xi^2\eta^2.$$

In these coordinates, the Hamiltonian becomes

$$H = \frac{1}{2\mu(\xi^2+\eta^2)}\left[p_\xi^2 + p_\eta^2 + \left(\frac{1}{\xi^2} + \frac{1}{\eta^2}\right)p_\phi^2 + \mu F(\xi^4 - \eta^4) - 4\mu e^2\right] = E, \tag{2.4}$$

where the energy E is constant. Since $\partial H/\partial\phi = 0$, p_ϕ is constant — the axial angular momentum is conserved.

In the following we assume that $F > 0$ and $E < 0$. The Hamilton-Jacobi equation is

$$\left(\frac{\partial S}{\partial \xi}\right)^2 + \frac{1}{\xi^2}\left(\frac{\partial S}{\partial \phi}\right)^2 + \mu F\xi^4 - 2\mu\xi^2 E + \left(\frac{\partial S}{\partial \eta}\right)^2 + \frac{1}{\eta^2}\left(\frac{\partial S}{\partial \phi}\right)^2 - \mu F\xi^4 - 2\mu\xi^2 E = 4\mu e^2, \tag{2.5}$$

where $S(\mathbf{q}, \mathbf{I})$ is the generating function for the canonical transformation from the coordinates $(\mathbf{q}, \mathbf{p})$ to action-angle variables. The symbol $\mathbf{q}$ denotes the original coordinates, (ξ, η, ϕ). This equation is separable, so the generating function can be written as

$$S = S_1(\xi) + S_2(\eta) + I_m\phi, \tag{2.6}$$

where

$$S_1(\xi) = \int p_\xi \, \mathrm{d}\xi = \int \frac{\mathrm{d}\xi}{\xi}(-\mu F\xi^6 + 2\mu E\xi^4 + 2\alpha_1\mu e^2\xi^2 - I_m^2)^{1/2}, \tag{2.7}$$

$$S_2(\eta) = \int p_\eta \, \mathrm{d}\eta = \int \frac{\mathrm{d}\eta}{\eta}(\mu F\eta^6 + 2\mu E\eta^4 + 2\alpha_2\mu e^2\eta^2 - I_m^2)^{1/2} \tag{2.8}$$

The dimensionless terms α_1 and α_2 are the separation constants for the Hamilton-Jacobi equation (2.5), satisfying $\alpha_1 + \alpha_2 = 2$.

Before deriving the action variables, it is useful to examine the effective potentials for the ξ-motion and η-motion. From the Hamilton-Jacobi equation, expressed in terms of the original parabolic coordinate momenta,

$$\frac{p_\xi^2}{2\mu e^2} + V_1(\xi) = \alpha_1 \quad \text{and} \quad \frac{p_\eta^2}{2\mu e^2} + V_2(\eta) = \alpha_2$$

where

$$V_1(\xi) = \frac{F\xi^4}{2e^2} - \frac{E\xi^2}{e^2} + \frac{p_\phi^2}{2\mu e^2\xi^2} \quad \text{and} \quad V_2(\eta) = -\frac{F\eta^4}{2e^2} - \frac{E\eta^2}{e^2} + \frac{p_\phi^2}{2\mu e^2\eta^2}. \tag{2.9}$$

Plots of $V_1(\xi)$ and $V_2(\eta)$ are shown in figures 2.1 and 2.2, assuming that $F > 0$.

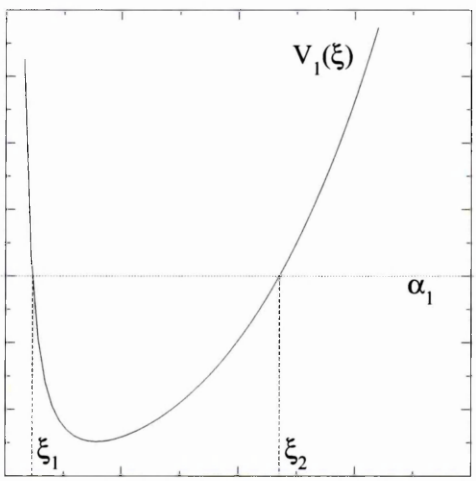

Figure 2.1 $V_1(\xi)$.

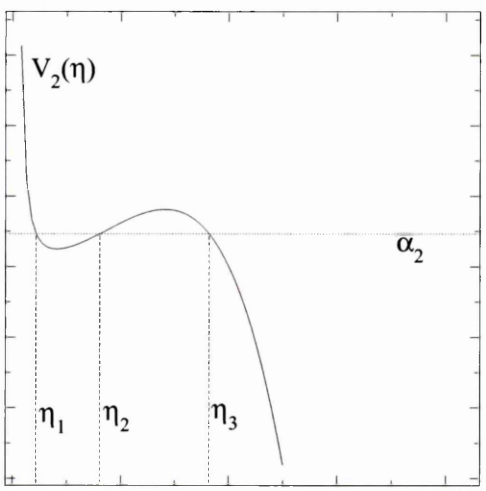

Figure 2.2 $V_2(\eta)$.

For all $F > 0$, the ξ-motion is bound, such that $\xi_1 \leq \xi \leq \xi_2$. The η-motion is only bound for certain values of E, F and α_2. From figure 2.2 it can be seen that bound motion satisfies $\eta_1 \leq \eta \leq \eta_2$ and the unbound motion, $\eta > \eta_3$. If E is kept fixed and α_2 increased, the turning

points η_2 and η_3 approach each other and eventually coalesce; for larger α_2 there is no bound motion. Changing the sign of F effectively swaps the potentials $V_1(\xi)$ and $V_2(\eta)$, so that the η-motion becomes bound for all values of E, F and α_1, whereas the ξ-motion can be bound or unbound.

From equations (2.7) and (2.8), the action variables are

$$I_1 = \frac{1}{\pi}\int_{\xi_1}^{\xi_2} \frac{\mathrm{d}\xi}{\xi}(-\mu F\xi^6 + 2\mu E\xi^4 + 2\alpha_1\mu e^2\xi^2 - I_m^2)^{1/2} \tag{2.10}$$

and

$$I_2 = \frac{1}{\pi}\int_{\eta_1}^{\eta_2} \frac{\mathrm{d}\eta}{\eta}(\mu F\eta^6 + 2\mu E\eta^4 + 2\alpha_2\mu e^2\eta^2 - I_m^2)^{1/2} \tag{2.11}$$

where ξ_1, ξ_2, η_1 and η_2 are the classical turning points. The action variables only exist for bound-motion.

For much of the analysis, it is more convenient to work with the equivalent canonical variables,

$$\begin{aligned} I_n &= I_1 + I_2 + I_m, & \theta_1 &= \phi_n - \phi_e, \\ I_e &= I_2 - I_1, & \theta_2 &= \phi_n + \phi_e, \\ J_m &= I_m, & \theta_m &= \phi_n + \phi_m, \end{aligned}$$

where I_n is the principal action is associated with the orbital motion of the electron around the nucleus and I_m is is the axial angular momentum action. The electric action, I_e, corresponds to the z-component of the Runge-Lenz vector for the electron orbital ellipse.

The system is semi-classically quantised by

$$I_k = \left(n_k + \frac{1}{2}\right)\hbar, \quad k = 1, 2 \quad \text{and} \quad I_m = m\hbar \tag{2.12}$$

where n_k are integers satisfying $n_k \geq 0$. These quantum numbers satisfy,

$$n = n_1 + n_2 + |m| + 1 \quad \text{and} \quad n_e = n_2 - n_1,$$

where n is the principal quantum number and n_e is named the electric quantum number.

The integrals (2.10) and (2.11) implicitly relate (E, α_1) to (I_1, I_2). An evaluation of these integrals as series expansions in F is given by Richards [51], from which much of the following is quoted. From the series expansions for I_1 and I_2, the energy can be expressed as

$$E(I_e, F) = -\frac{\mu e^4}{2I_n^2} + \sum_{k=1}^{\infty} E_k(\mathbf{I}) F^k, \tag{2.13}$$

where the first five perturbation terms for the energy are:

$$\begin{aligned}
E_1(\mathbf{I}) &= -\frac{3}{2}\frac{I_n I_e}{\mu e^2}, \\
E_2(\mathbf{I}) &= -\frac{I_n^4}{16\mu^3 e^8}(17I_n^2 - 3I_e^2 - 9I_m^2), \\
E_3(\mathbf{I}) &= -\frac{3I_n^7 I_e}{32\mu^5 e^{14}}(23I_n^2 - I_e^2 + 11I_m^2), \\
E_4(\mathbf{I}) &= -\frac{3I_n^{10}}{1024\mu^7 e^{20}}(1829I_n^4 - 1134I_m^2 I_n^2 - 183I_m^4 + \\
&\qquad (602I_n^2 - 378I_m^2)I_e^2 + 49I_e^4), \\
E_5(\mathbf{I}) &= -\frac{3I_n^{13} I_e}{1024\mu^9 e^{26}}(10563I_n^4 + 772I_m^2 I_n^2 + 725I_m^4 + \\
&\qquad (98I_n^2 + 220I_m^2)I_e^2 - 21I_e^4).
\end{aligned}$$

Some higher terms in the expansion for $E(I_e, F)$ are given in [51], but here we truncate all expansions to $O(F^5)$ as later approximations to derive the Hamiltonian for a time-varying field are made to $O(F)$ only. The radius of convergence of the series sets an upper limit on the scaled field, $|F_0|$. Calculating the ratio of consecutive perturbation terms and using Richardson extrapolation, an estimate can be obtained for the radius of convergence. Using this method applied to the first 17 terms in the perturbation expansion, Richards [51] calculated that for $I_m/I_n = 0, 0.8$ and 1, the radius of convergence was approximately, 0.17, 0.19 and 0.21.

The angle variables, (θ_1, θ_2), corresponding to the action variables (I_1, I_2) can be expressed in terms of the auxiliary angles ψ and χ as

$$\theta_1 = \psi + P_1(\psi) + Q_1(\chi) \quad \text{and} \quad \theta_2 = \chi + P_2(\psi) + Q_2(\chi), \tag{2.14}$$

where ψ and χ are defined by

$$\xi^2 = \xi_2^2 \sin^2 \frac{\psi}{2} + \xi_1^2 \cos^2 \frac{\psi}{2} \quad \text{and} \quad \eta^2 = \eta_2^2 \sin^2 \frac{\chi}{2} + \eta_1^2 \cos^2 \frac{\chi}{2},$$

and

$$\begin{aligned} P_1 &= -\sigma_1 \sin\psi + O(F), \quad P_2 = -\sigma_1 \sin\psi + O(F), \\ Q_1 &= -\sigma_2 \sin\chi + O(F) \quad \text{and} \quad Q_2 = -\sigma_2 \sin\chi + O(F), \end{aligned}$$

where

$$\sigma_1 = \frac{\sqrt{I_1(I_1 + I_m)}}{I_n} \quad \text{and} \quad \sigma_2 = \frac{\sqrt{I_2(I_2 + I_m)}}{I_n}.$$

In the presence of a time-dependent field, $F(t)$, the generating function (2.6) becomes $S(\boldsymbol{q}, \boldsymbol{I}, t)$ and the Hamiltonian in these new coordinates gains an additional term, $\partial S/\partial t$,

$$K = E(\boldsymbol{I}, F(t)) + \frac{\partial S}{\partial F}\frac{\mathrm{d}F}{\mathrm{d}t}.$$

When $\lambda(t) = 1$, $\mathrm{d}F/\mathrm{d}t = -F_\mu \Omega \sin\Omega t$. During field switch-on and switch-off, it is

$$\frac{\mathrm{d}F}{\mathrm{d}t} = -F_\mu \Omega \left[\lambda(x)\sin\Omega t + \frac{1}{2\pi N_a}\frac{\mathrm{d}\lambda(x)}{\mathrm{d}x}\left(\frac{F_s}{F_\mu} + \cos\Omega t\right)\right],$$

where x is given in equation (2.3). If the field switch-on and switch-off periods are sufficiently long, then the second term in the brackets can be ignored, so we use the approximation,

$$\dot{F} \approx -\lambda(t) F_\mu \Omega \sin\Omega t. \tag{2.15}$$

In scaled units F_μ and Ω are small, hence a second order approximation can be obtained for $\partial S/\partial t$ by expanding $\partial S/\partial F$ in F and ignoring all terms $O(F)$ or higher. From [51],

$$\frac{\partial S}{\partial F} = \frac{I_n^4}{2\mu^2 e^6} G,$$

where

$$G = (3I_2 + I_1 + 2|I_m|)\sigma_1 \sin\psi - (3I_1 + I_2 + 2|I_m|)\sigma_2 \sin\chi - \frac{I_n}{2}(\sigma_1^2 \sin 2\psi - \sigma_2^2 \sin 2\chi).$$

The resulting approximate Hamiltonian, which will be referred to as the *Adiabatic Hamiltonian*, is

$$K = E(\boldsymbol{I}, F) + \frac{I_n^4}{2\mu^2 e^6} F_\mu \Omega \sin(\Omega t)\, G(I_1, I_2, \psi, \chi). \tag{2.16}$$

This is the same as given by Richards [51] apart from a sign change for the second term. In most cases considered here the sign difference has no effect as the results are generated from averages over a uniform distribution of initial conditions for the angle variables.

The Adiabatic Hamiltonian is expected to be more accurate for small scaled values of F and Ω, and for sufficiently slowly changing field envelopes such that $\dot{\lambda}/\lambda \ll \Omega$.

In order to express $G(I_1, I_2, \psi, \chi)$ in terms of canonically conjugate angles, the terms in ψ and χ are obtained as multiple Fourier series expansions in θ_1 and θ_2,

$$\begin{pmatrix} \sin k\psi \\ \sin k\chi \end{pmatrix} = \sum_{s_1=-\infty}^{\infty} \sum_{s_2=-\infty}^{\infty} \begin{pmatrix} S_{s_1 s_2}^{(k)} \\ C_{s_1 s_2}^{(k)} \end{pmatrix} \exp\left[-i\left(s_1\theta_1 + s_2\theta_2\right)\right]. \tag{2.17}$$

The Fourier coefficients are obtained using (2.14),

$$S_{s_1 s_2}^{(k)} = \begin{cases} i\dfrac{k}{2s} J_{s_2}(s\sigma_2)[J_{s_1+k}(s\sigma_1) + J_{s_1-k}(s\sigma_1)], & s \neq 0, \\ \mp\dfrac{i\sigma_2}{4}, & s = 0,\ s_1 = \pm 1 \text{ and } k = 1, \\ 0, & \text{otherwise;} \end{cases}$$

and

$$C_{s_1 s_2}^{(k)} = \begin{cases} i\dfrac{k}{2s} J_{s_1}(s\sigma_1)[J_{s_2+k}(s\sigma_2) + J_{s_2-k}(s\sigma_2)], & s \neq 0, \\ \mp\dfrac{i\sigma_1}{4}, & s = 0,\ s_1 = \pm 1 \text{ and } k = 1, \\ 0, & \text{otherwise,} \end{cases}$$

where $s = s_1 + s_2$.

A further approximation can be made following examination of the angular frequencies for the I_n and I_e motions, which are

$$\omega_e = \frac{\partial K}{\partial I_e} = -\frac{3I_n}{2\mu e^2}F(t) + O(F^2)$$

and

$$\omega_n = \frac{\partial K}{\partial I_n} = \frac{\mu e^4}{I_n^3} - \frac{3I_n}{2\mu e^2}F(t) + O(F^2).$$

For small $|F|$, $\omega_e \ll \omega_n$. When ϕ_n changes by 2π there is little change in ϕ_e, hence an approximation can be obtained by averaging over ϕ_n. Averaging removes all terms containing $\exp(-is\phi_n)$ from equation (2.17) where $s \neq 0$. Hence

$$\langle \sin\psi \rangle = \frac{\sigma_2}{2}\sin 2\phi_e, \quad \langle \sin\chi \rangle = -\frac{\sigma_1}{2}\sin 2\phi_e$$

and

$$\langle \sin 2\psi \rangle = \langle \sin 2\chi \rangle = 0.$$

Inserting these expressions into $G(I_1, I_2, \psi, \chi)$, we obtain the mean motion Hamiltonian,

$$K_m = E(I_e, F(t)) + \frac{1}{4}\frac{I_n^3}{\mu^2 e^6}\frac{\mathrm{d}F}{\mathrm{d}t}A(I_e)B(I_e)\sin(2\phi_e), \tag{2.18}$$

where

$$A(I_e) = \sqrt{(I_n + |I_m|)^2 - I_e^2}, \quad B(I_e) = \sqrt{(I_n - |I_m|)^2 - I_e^2} \quad \text{and} \quad |I_e| \leq I_n - |I_m|.$$

The mean motion approximation reduces the system to a one-dimensional time dependent problem in (ϕ_e, I_e), with I_n constant due to the averaging over ϕ_n. Quantum mechanically this is equivalent to ignoring all transitions between different n states. This is a reasonable assumption for the low frequency fields considered, because the energy difference between neighbouring principal quantum number states is relatively large compared with the photon

energy, $\hbar\Omega$, of the applied field. As a first approximation,

$$E \approx E_n = -\frac{\mu e^4}{2I_n^2},$$

hence the difference between energy levels is

$$\Delta E_n = |E_{n+1} - E_n| \approx \frac{\mu e^4}{\hbar^2 n^3}$$

and the number of photons required to bridge the gap is

$$\left|\frac{\Delta E_n}{\hbar\Omega}\right| \approx \frac{1}{\Omega_0} \gg 1.$$

For the low frequencies considered here, $\Omega_0 \leq 0.1$ and $|\Delta E_n/E_{ph}| > 10$.

2.1.2 The Averaged Hamiltonian

For low scaled frequencies the ϕ_e-dependent term in the mean motion Hamiltonian (2.18) is relatively small. Consequently, for most values of F_s, F_μ and Ω, I_e executes small amplitude oscillations. There are however, values of F_s, F_μ and Ω for which resonances occur and the variation in I_e can become much larger. Examples of this variation are shown in figure 2.4 (page 42), later in this section.

The energy (2.13) contains terms linear in I_e; taken alone these terms cause a simple evolution in ϕ_e which is independent of I_e. This can be seen by examining the Hamiltonian $E_L(I_e, F(t))$ obtained by ignoring all components of E other than those linear in I_e. The equation of motion for ϕ_e is

$$\dot{\phi_e} = \frac{\partial E_L}{\partial I_e},$$

which is independent of I_e and can therefore be immediately integrated to give

$$\phi_e(t) = \phi_e(0) - \frac{3}{2} I_n g(t)$$

where

$$\begin{aligned} g(t) &= -\frac{2}{3I_n}\int_0^t \frac{\partial E_L}{\partial I_e}\,\mathrm{d}t \\ &= \int \mathrm{d}t\left[F + \frac{I_n^6 F^3}{16}(23I_n^2 + 11I_m^2) + \right. \\ &\qquad \left. \frac{I_n^{12}F^5}{512}(10563I_n^4 + 772I_n^2I_m^2 + 725I_m^4) + \ldots\right]. \end{aligned} \tag{2.19}$$

In the above expression and for the rest of this section we have set $\mu = e = 1$. The function $g(t)$ can be written as $g(t) = \overline{g}t + \tilde{g}(t)$ where $\overline{g}$ is constant and $\tilde{g}(t)$ is periodic in t with zero mean. Restricting attention to times when $\lambda(t) = 1$, $F(t) = F_s + F_\mu \cos\Omega t$ gives

$$\begin{aligned} \overline{g} &= F_s + \frac{I_n^6}{16}(23I_n^2 + 11I_m^2)F_s\left(F_s^2 + \frac{3}{2}F_\mu^2\right) \\ &+ \frac{I_n^{12}}{512}(10563I_n^4 + 772I_n^2I_m^2 + 725I_m^4)F_s\left(F_s^4 + 5F_s^2F_\mu^2 + \frac{15}{8}F_\mu^4\right) + \ldots\ldots \end{aligned} \tag{2.20}$$

The periodic function $\tilde{g}(t)$ can be written as a Fourier series,

$$\tilde{g}(t) = \frac{F_\mu}{\Omega}\sum_{k=1}^{\infty}\tilde{g}_k \sin k\Omega t \tag{2.21}$$

where

$$\begin{aligned} \tilde{g}_1 &= 1 + \frac{3I_n^6}{16}(23I_n^2 + 11I_m^2)\left(F_s^2 + \frac{F_\mu^2}{4}\right) + O(F^4), \\ \tilde{g}_2 &= \frac{3I_n^6F_sF_\mu}{64}(23I_n^2 + 11I_m^2) + O(F^4), \\ \tilde{g}_3 &= \frac{I_n^{12}F_\mu^2}{192}(23I_n^2 + 11I_m^2) + O(F^4) \end{aligned}$$

and all other $\tilde{g}_k$ are $O(F^4)$.

The canonical transformation $F_2(\phi_e, P) = P(\phi_e + 3I_n g(t))$ transforms to a rotating reference frame, $\psi_e = \phi_e + 3I_n g(t)$ and $P = I_e$, which removes the terms linear in I_e. The new Hamiltonian is

$$K'_m = E_R(I_e, F(t)) - \frac{1}{4}I_n^3\lambda(t)F_\mu\Omega A(I_e)B(I_e)\sin\Omega t\sin\left(2\psi_e - 3I_n g(t)\right) \tag{2.22}$$

where $E_R(I_e, F(t)) = E(I_e, F(t)) - E_L(I_e, F(t))$.

From this expression we see that for F and Ω in scaled coordinates, $\dot{I}_e = O(F\Omega)$ and $\dot{\psi}_e = O(F^2)$, hence the (ψ_e, I_e) variables evolve slowly compared to the applied field. The energy expression used in the mean motion Hamiltonian, equation (2.18), can therefore be approximated by averaging over a period of the applied field,

$$E(I_e, F(t)) \approx \overline{E}(I_e, F_s, F_\mu, t) = -\frac{1}{2I_n^2} + \sum_{k=1}^{\infty} E_k(\mathbf{I})\overline{F^k} \tag{2.23}$$

where $\overline{F^k}$ are the averages over one field period of $F(t)^k$,

$$\overline{F^k(t)} \approx \frac{\lambda^k(t)}{T}\int_0^T (F_s + F_\mu \cos(\Omega t'))^k \, \mathrm{d}t', \quad T = \frac{2\pi}{\Omega},$$

where we assume that $\lambda(t)$ varies little during one field oscillation. The resultant Hamiltonian, which will be referred to as the *Averaged Hamiltonian*, is

$$\overline{K}_m = \overline{E}_R(I_e, F_s, F_\mu, t) - \frac{1}{4}I_n^3\lambda(t)F_\mu\Omega A(I_e)B(I_e)\sin\Omega t \sin\left(2\psi_e - 3I_n g(t)\right) \tag{2.24}$$

where to $O(F^5)$ and ignoring terms independent of I_e,

$$\begin{aligned}
\overline{E}_R(I_e, F_s, F_\mu, t) &= \frac{3I_n^4 I_e^2 \lambda^2(t)}{16}\left(F_s^2 + \frac{F_\mu^2}{2}\right) + \frac{3I_n^7 I_e^3 \lambda^3(t)}{32}F_s\left(F_s^2 + \frac{3F_\mu^2}{2}\right) \\
&- \frac{I_n^{10} I_e^2 \lambda^4(t)}{512}\left(903I_n^2 - 567I_m^2 + \frac{147I_e^2}{2}\right)\left(F_s^4 + 3F_s^2F_\mu^2 + \frac{3F_\mu^4}{8}\right) \\
&- \frac{I_n^{13} I_e^3 \lambda^5(t)}{256}\left(\frac{147I_n^2}{2} + 165I_m^2 - \frac{63I_e^2}{4}\right)F_s\left(F_s^4 + 5F_s^2F_\mu^2 + \frac{15F_\mu^4}{8}\right)
\end{aligned} \tag{2.25}$$

and $\lambda(t)$ is given by equation (2.3), page 28.

This Hamiltonian forms the basis for much of the analysis and results given throughout the remainder of this thesis. It provides a one-dimensional approximation to the three-dimensional exact Hamiltonian (2.1), page 27, for a hydrogen atom in a parallel static and linearly polarised microwave field. A number of approximations have been made in its derivation, which we summarise for clarity:

1. The energy expression (2.13), page 32, is a perturbation expansion in F. The expansion has a finite radius of convergence in $|F|$. Here we terminate the expansion at $O(F^5)$.

2. The adaptation of the static field Hamiltonian to the case of a time-varying field requires the inclusion of a time dependent perturbation term, $\partial S/\partial t$, calculated as a first order expansion in F.

3. The microwave field frequency is small relative to the Kepler frequency, allowing the fast oscillation terms in ϕ_n to be averaged over.

4. The field switch-on and switch off are assumed to be sufficiently long so that $\mathrm{d}F/\mathrm{d}t \approx -\lambda(t)F_\mu\Omega\sin\Omega t$.

5. Terms linear in I_e cause a secular change in the angle variable. The canonical transformation, $F_2(\phi_e, P) = P(\phi_e + 3I_n g(t))$ removes this secular change. A further approximation is introduced in the expansion for $g(t)$.

6. From the resultant Hamiltonian, Hamilton's equations, in scaled variables, are $O(F^2)$ and $O(F\Omega)$, hence the variables (ϕ_e, I_e) evolve slowly allowing the term $E_R(t)$ to be approximated as $\overline{E}_R$, obtained by averaging over a period of the applied field.

From these assumptions we expect the Averaged Hamiltonian to be most accurate for small Ω and F. For the results shown later, typically in scaled variables, $\Omega < 0.1$, $F_\mu \leq 0.15$ and $F_s \leq 0.08$. From [53, 21], it was shown that for $\Omega \gtrsim 0.05$ transitions between different n states need to be taken into account, so we expect the Averaged Hamiltonian to become less accurate in this domain.

The approximation for $\mathrm{d}F/\mathrm{d}t$ is of less importance. For $N_a \geq 5$, the approximation is a fairly close match, as can be seen in figure 2.3. In practice, the limited evolution of $I_e(t)$ observed during short duration field means that the inaccuracies in the approximation are not important, as is seen later in §6.4, page 191; hence, the approximation can reasonably be applied for all N_a.

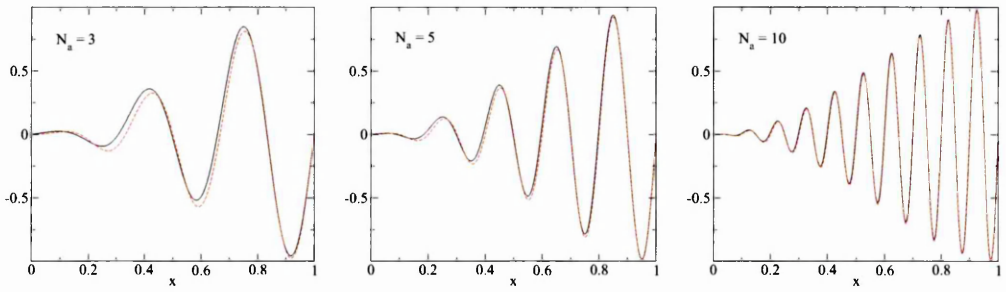

Figure 2.3 Plots comparing $(F_\mu\Omega)^{-1}\,\mathrm{d}F/\,\mathrm{d}t$ calculated exactly (solid line) and using the approximation $(F_\mu\Omega)^{-1}\,\mathrm{d}F/\,\mathrm{d}t \approx -\lambda(t)\sin\Omega t$ (dashed line) for $x = t\Omega/2\pi N_a$ and various N_a.

2.1.3 Classical Equations of Motion

The numerical integration of Hamilton's equations derived from equation (2.24) is complicated by the presence of the $B(I_e)$ factor in the time dependent term, which introduces a singularity into the equations of motion when $I_e = \pm(I_n - |I_m|)$. To avoid this the equations of motion can be rewritten in terms of the three dimensional vector,

$$\mathbf{Z} = (B(I_e)\cos(2\psi_e - 3g(t)), B(I_e)\sin(2\psi_e - 3g(t)), I_e)\,.$$

The components of $\mathbf{Z}$ satisfy commutation relations $[Z_i, Z_j] = 2\epsilon_{ijk}Z_k$, where ϵ_{ijk} is the completely antisymmetric tensor. The length $|\mathbf{Z}| = I_n - |I_m|$ is constant. The equations of motion,

$$\dot{Z}_i = [Z_i, \overline{K}_m] + \frac{\partial Z_i}{\partial t}\,,$$

become

$$\begin{aligned}
\frac{\mathrm{d}Z_1}{\mathrm{d}t} &= 2\alpha A Z_3 + Z_2\left(3\dot{g} - 2\frac{\partial \overline{E}_R}{\partial I_e}\right) - 2\alpha\frac{\partial A}{\partial Z_3}Z_2^2, \\
\frac{\mathrm{d}Z_2}{\mathrm{d}t} &= 2Z_1\frac{\partial \overline{E}_R}{\partial I_e} - 3\dot{g}Z_1 + 2\alpha Z_1 Z_2\frac{\partial A}{\partial Z_3}, \\
\frac{\mathrm{d}Z_3}{\mathrm{d}t} &= -2\alpha A Z_1,
\end{aligned} \tag{2.26}$$

where

$$\alpha(t) = -\frac{\lambda(t)}{4}\frac{I_n^3}{\mu^2 e^6}F_\mu\Omega\sin(\Omega t) \quad \text{and} \quad A(Z_3) = \sqrt{(I_n + |I_m|)^2 - Z_3^2}. \tag{2.27}$$

These equations can be easily integrated numerically. Numerical calculations provided here are performed either in Fortran using the NAG routine D02CJF for the integration of the equations of motion, or in Maple. All numerical calculations are done in scaled variables, setting $I_n = e = \mu = 1$, so that $I_e \to I_e/I_n$ and $I_m \to I_m/I_n$.

In figure 2.4, the equations of motion, (2.26), are integrated using the method described above for the scaled variables, $F_\mu = 0.13$, $\Omega_0 = 0.011414$, $I_m = 0.2$, field envelope 16-50-16 and $I_e(0) = -0.5$. Two values for F_s are chosen to exhibit the typical behaviour of $I_e(t)$ for the Averaged Hamiltonian. For each F_s value, results for two initial conditions for $\psi_e(0)$ are provided.

For $F_s = 0.026$ the behaviour is characteristic of 'off-resonance' field parameters. It can be seen that for both initial conditions for $\psi_e(0)$, only a small variation in $I_e(t)$ occurs, with the motion centred on value close to $I_e(0)$.

Examining $I_e(t)$ at the end of integration for a sample of 600 orbits with $\psi_e(0)$ uniformly distributed in the range $(0, \pi)$ confirms this behaviour: the mean value is -0.505, the standard deviation is 0.0096 and all final I_e values lie in the narrow range $(-0.52, -0.49)$. Off resonance behaviour is examined in more detail in §2.4 using classical perturbation theory.

In contrast, $F_s = 0.02464$ is chosen to lie near a resonance between the applied field and the system. There are large underlying oscillations in $I_e(t)$, with superimposed smaller fluctuations. The amplitude and centre of the oscillation depend on the initial value $\psi_e(0)$. For a similar sample of final $I_e(t)$ values for 600 orbits, the mean is -0.439, the standard deviation is 0.108 and the range is $(-0.60, -0.17)$. Resonance behaviour is explored further in the following section.

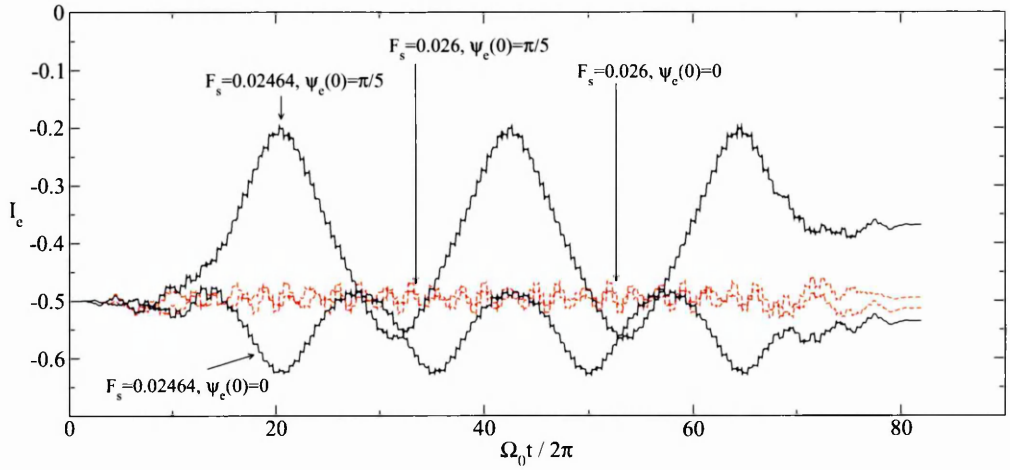

Figure 2.4 $I_e(t)$ for $O(F^5)$ Hamiltonian $\overline{K}_m$, $F_\mu = 0.13, \Omega_0 = 0.011414$, $I_m = 0.2$, $I_e(0) = -0.5$ and envelope 16-50-16. All quantities are given in scaled variables.

2.1.4 The Resonance Hamiltonian

In general the time-dependent perturbation term in the Averaged Hamiltonian, equation (2.24), page 38, changes rapidly and hence when integrated causes only small changes in $I_e(t)$. However, for certain field parameters resonances arise and the perturbation term becomes a more slowly varying function of time. When the equations of motion are integrated the slower changes can, as observed in figure 2.4, have significant effects on $I_e(t)$.

The nature of the resonances and the behaviour of the system at resonance can be shown by a further transformation of the Averaged Hamiltonian. In this section, we assume that the field amplitude is fixed so that $\lambda(t) = 1$. Fourier expanding the ψ_e-dependent term in equation (2.24) yields

$$\sin\left(2\psi_e - 3I_n g(t)\right) = \sum_{k=-\infty}^{\infty} \mathcal{J}_k \sin(2\psi_e - \nu_k t + k\pi),$$

where

$$\nu_k = 3I_n\overline{g} - k\Omega. \tag{2.28}$$

The Fourier coefficients, $\mathcal{J}_k$, depend on $\tilde{g}_k$ and to $O(F^2)$ are (from [51], equation (28))

$$\begin{aligned}\mathcal{J}_k &= J_k(z_1)J_0(z_2)J_0(z_3) + J_0(z_2)\sum_{s=1}^{\infty} J_s(z_3)\left[J_{k-3s}(z_1) + (-1)^s J_{k+3s}(z_1)\right] \\ &+ J_0(z_3)\sum_{s=1}^{\infty} J_s(z_2)\left[J_{k-2s}(z_1) + (-1)^s J_{k+2s}(z_1)\right] \\ &+ \sum_{s=1}^{\infty} J_s(z_2)\sum_{r=1}^{\infty} J_r(z_3)\left[J_{k-2s-3r}(z_1) + (-1)^r J_{k-2s+3r}(z_1)\right. \\ &\qquad \left. + (-1)^s J_{k+2s-3r}(z_1) + (-1)^{s+r} J_{k+2s+3r}(z_1)\right], \end{aligned} \tag{2.29}$$

where $z_k = 3\tilde{g}_k I_n F_\mu/\Omega$. Expanding in powers of F, the leading term is

$$\mathcal{J}_k \approx J_k\left(\frac{3I_n F_\mu}{\Omega}\right). \tag{2.30}$$

This expression is exact if the series expansion for $g(t)$ is terminated at $O(F^2)$. Defining

$$\widetilde{\mathcal{J}}_j = (\mathcal{J}_{j-1} - \mathcal{J}_{j+1})/2, \tag{2.31}$$

the Hamiltonian (2.24) can be rewritten as,

$$\overline{K}_m \approx \overline{E}_R(I_e, F) - \frac{1}{4} I_n^3 F_\mu \Omega A(I_e) B(I_e) \sum_{k=-\infty}^{\infty} \widetilde{\mathcal{J}}_k \cos(2\psi_e - \nu_k t + k\pi).$$

The nature of the solutions to Hamilton's equations changes in the regions where for some j, $|\nu_j| \approx 0$; i.e. when the field amplitudes, F_s and F_μ, satisfy

$$3I_n \overline{g}(F_s, F_\mu) = j\Omega, \quad j = 1, 2, \ldots. \tag{2.32}$$

For fixed F_μ and Ω, the static field values, $F_s^{(j)}(F_\mu, \Omega)$, satisfying this equation will be referred to as the dynamical resonances. To a first approximation, including terms up to $O(F)$ only, $F_s^{(j)} \approx j\Omega_0/3$ in scaled units. It will be seen later that near $F_s = F_s^{(j)}$, the ionisation probability can have local maxima. The maxima usually do not lie exactly at $F_s = F_s^{(j)}$; the reason for this is explained in §2.3.

When a comparison is made between the exact classical dynamics and the approximations

described here, it is seen that the locations of the ionisation probability maxima are slightly different. Including higher order terms in the calculation of the dynamical resonances, $F_s^{(j)}$ reduces the differences. This is discussed further in §2.2.1.

Ignoring the rapidly oscillating terms for $k \neq j$, the Averaged Hamiltonian can be approximated by

$$K_R \approx \overline{E}_R(I_e, F) - \frac{1}{4} I_n^3 F_\mu \Omega A(I_e) B(I_e) \widetilde{\mathcal{J}}_j \cos(2\psi_e - \nu_j t + j\pi).$$

Applying the canonical transformation,

$$\theta_R = \psi_e - \nu_j t/2 + j\pi/2, \tag{2.33}$$

with I_e unchanged, the resultant time-independent Hamiltonian, which will be referred to as the *Resonance Hamiltonian*, is

$$\overline{K}_R = \overline{E}_R(I_e, F) - \frac{\nu_j}{2} I_e - \frac{1}{4} I_n^3 F_\mu \Omega A(I_e) B(I_e) \widetilde{\mathcal{J}}_j \cos(2\theta_R), \tag{2.34}$$

or equivalently,

$$\overline{K}_R = \overline{E}(I_e, F) - \frac{j\Omega_0}{2} I_e - \frac{1}{4} I_n^3 F_\mu \Omega A(I_e) B(I_e) \widetilde{\mathcal{J}}_j \cos(2\theta_R),$$

where $\overline{E}$ and $\overline{E}_R$ are given in equations (2.23)and (2.25) on page 38.

If terms higher than $O(F^2)$ are ignored in the energy expansion, the Hamiltonian is

$$\overline{K}_R = \frac{3}{16}\left(F_s^2 + \frac{F_\mu^2}{2}\right)(I_e - \alpha_j)^2 - \frac{1}{4} I_n^3 F_\mu \Omega A(I_e) B(I_e) J_j'\left(\frac{3 I_n F_\mu}{\Omega}\right) \cos(2\theta_R). \tag{2.35}$$

where

$$\alpha_j = \frac{8}{3 I_n^4}\left(\frac{3 I_n F_s - j\Omega}{F_\mu^2 + 2F_s^2}\right).$$

The Resonant Hamiltonian is time-independent and has a number of similarities with the Hamiltonian for the simple pendulum, with librational and rotational motion phase curves separated by a separatrix curve. The size of the librational island can have a significant effect on the dynamics and on observed ionisation behaviour.

For certain values of j, F_μ and Ω, $\widetilde{\mathcal{J}}_j = 0$, removing the θ_R-dependent term from the Resonance Hamiltonian. This can affect the observed ionisation behaviour, suppressing the appearance of ionisation probability peaks. This effect is observed in the exact classical dynamics and in experimental results, see for example [25].

It is generally more useful to work in scaled variables. From here on, unless stated otherwise, all scaled variables are used.

2.1.5 Resonance Islands

The behaviour of the system in the vicinity of a resonance is dominated by the presence of resonance islands in phase space. In this section we calculate some properties of the resonance islands that are useful later to understand and predict ionisation behaviour.

Figures 2.5 and 2.6 show phase curves of the $O(F^5)$ Resonance Hamiltonian given by equation (2.34) for the dynamical parameters $F_\mu = 0.13$ and $\Omega_0 = 0.011414$. The values of F_s are 0.0357 and 0.0363 for figures 2.5 and 2.6 respectively, chosen to bracket the tenth resonance, $F_s^{(10)} = 0.03615$. The phase spaces contain both librational and rotational periodic orbits. The resonance island appears at the bottom of the phase space as F_s is increased and approaches $F_s^{(j)}$, with the centre of the resonance island lying at $I_e = 0$ when $F_s = F_s^{(j)}$.

It can be seen that the resonance island can, for particular dynamical values and particular initial conditions $(\theta_R(0), I_e(0))$, have significant effects on the range of values taken by $I_e(t)$. This in turn can lead to observable effects on ionisation behaviour.

The equilibrium points satisfy the conditions

$$\frac{\partial \overline{K}_R}{\partial I_e} = 0 \quad \text{and} \quad \frac{\partial \overline{K}_R}{\partial \theta_R} = 0.$$

For the parameters chosen the librational centre of the resonance island lies at $\theta_R = \pi/2$ as $\widetilde{\mathcal{J}}_j < 0$. For $\widetilde{\mathcal{J}}_j > 0$, the centre of the island lies at $\theta_R = 0$.

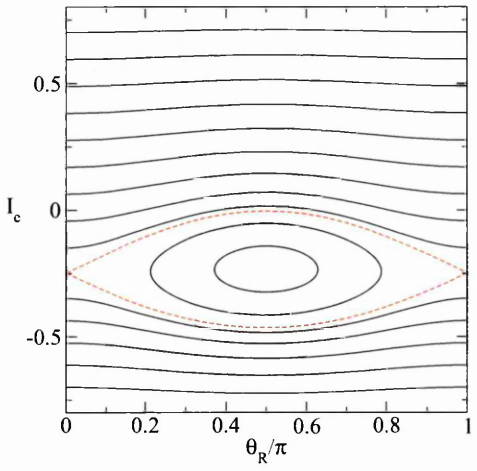

Figure 2.5 Phase curves for $O(F^5)$ $\overline{K}_R$ Hamiltonian, $F_\mu = 0.13$, $\Omega_0 = 0.011414$, $F_s = 0.0357$ and $I_m = 0.2$. The separatrix curves are shown with dashed lines.

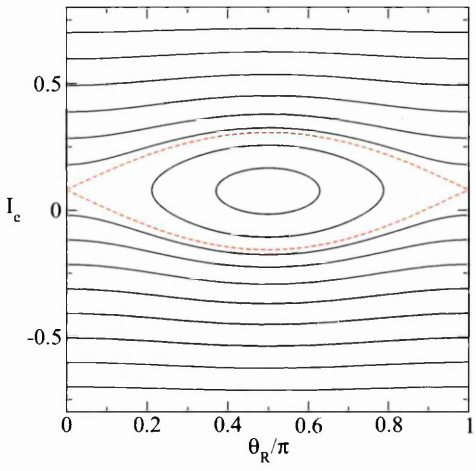

Figure 2.6 As for figure 2.5, except $F_s = 0.0363$.

Ionisation probabilities are calculated from averages over initial values of θ_R uniformly distributed in the range $(0, \pi)$ and are therefore unaffected by the sign of $\widetilde{\mathcal{J}}_j$. If $\widetilde{\mathcal{J}}_j < 0$ the separatrix unstable equilibrium points lie at $(0, I_{sep})$ and (π, I_{sep}), whereas if $\widetilde{\mathcal{J}}_j > 0$ the separatrix unstable equilibrium points lie at (π, I_{sep}). In both cases I_{sep} satisfies

$$\frac{\partial \overline{E}_R}{\partial I_e}(I_{sep}) - \frac{\nu_j}{2} - \epsilon \frac{\partial}{\partial I_e}\left(A(I_{sep})B(I_{sep})\right) = 0$$

and $\epsilon = -F_\mu \Omega_0 |\widetilde{\mathcal{J}}_j|/4$. An approximate solution for I_{sep} can be derived by noting that for small I_e,

$$\overline{E}_R \approx \beta I_e^2,$$

where to $O(F^5)$,

$$\beta = \frac{3}{16}\left(F_s^2 + \frac{F_\mu^2}{2}\right) - \frac{3}{512}\left(301 - 189 I_m^2\right)\left(F_s^4 + 3F_s^2 F_\mu^2 + \frac{3F_\mu^4}{8}\right) \tag{2.36}$$

and by using the Taylor expansion,

$$A(I_e)B(I_e) \approx \epsilon\left[1 - I_m^2 - I_e^2\left(\frac{1 + I_m^2}{1 - I_m^2}\right)\right].$$

This gives

$$I_{sep} \approx \frac{\nu_j}{4}\left[\beta + \epsilon\left(\frac{1+I_m^2}{1-I_m^2}\right)\right]^{-1}. \tag{2.37}$$

Figure 2.7 compares this approximation with the numerically calculated value for a range of F_s values in the vicinity of the $j = 10$ resonance for $F_\mu = 0.13$, $I_m = 0.2$ and $\Omega_0 = 0.011414$. There is a reasonable match for much of the region around the point $F_s = F_s^{(10)} = 0.03615$. Towards $I_e = \pm(1 - I_m)$ the approximation diverges. This is a consequence of the singularity in $B(I_e)'$ at these limits, where the Taylor expansion is invalid.

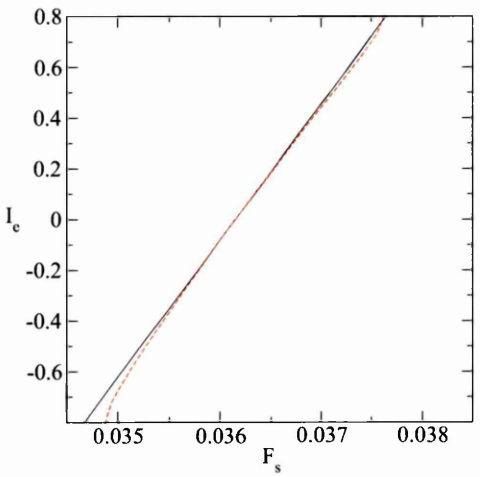

Figure 2.7 Comparison between I_{sep} calculated using approximation (2.37) (solid line) and I_{sep} calculated numerically (dashed line) for $F_\mu = 0.13$, $\Omega_0 = 0.011414$ and $I_m = 0.2$.

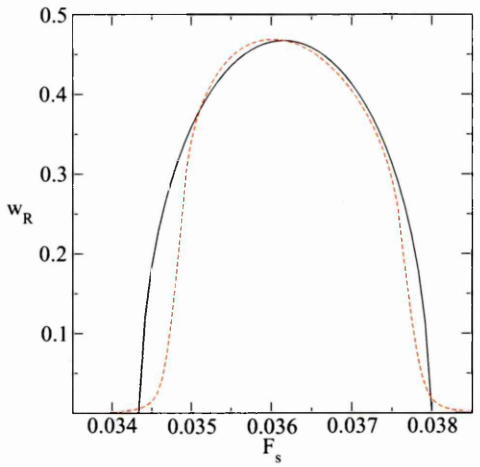

Figure 2.8 Approximate island width, w_R (solid line) and numerically calculated island width (dashed line) for $O(F^5)$ $\overline{K}_R$ Hamiltonian, $F_\mu = 0.13$, $\Omega_0 = 0.011414$ and $I_m = 0.2$.

The energy on the separatrix is given by

$$E_s \approx \beta I_{sep}^2 - \frac{\nu_j}{2} I_{sep} - \epsilon\left[1 - I_m^2 - I_{sep}^2\left(\frac{1+I_m^2}{1-I_m^2}\right)\right].$$

Denoting the I_e values lying on the separatrix curves at $\theta_R = \pi/2$ by $\mathcal{I}_1$ and $\mathcal{I}_2$, their values are obtained from the energy equation,

$$\mathcal{I}_i^2\left[\beta - \epsilon\left(\frac{1+I_m^2}{1-I_m^2}\right)\right] - \frac{\nu_j}{2}\mathcal{I}_i - E_s + \epsilon(1-I_m^2) = 0$$

and are

$$\begin{aligned}\mathcal{I}_1 &= \frac{\nu_j}{4}\left[\beta-\epsilon\left(\frac{1+I_m^2}{1-I_m^2}\right)\right]^{-1}-\frac{w_R}{2},\\ \mathcal{I}_2 &= \frac{\nu_j}{4}\left[\beta-\epsilon\left(\frac{1+I_m^2}{1-I_m^2}\right)\right]^{-1}+\frac{w_R}{2}.\end{aligned} \tag{2.38}$$

The resonance width, w_R, is defined as the maximum separation between the separatrix curves and given by

$$w_R = 2\sqrt{\frac{-2\epsilon}{\beta-\epsilon\gamma}\left(1-I_m^2-\frac{\nu_j^2\gamma}{16(\beta^2-\epsilon^2\gamma^2)}\right)},\quad \gamma=\left(\frac{1+I_m^2}{1-I_m^2}\right). \tag{2.39}$$

A comparison between this approximate expression and the resonance island width calculated numerically is shown in figure 2.8 for the $j = 10$ resonance for $F_\mu = 0.13$, $I_m = 0.2$ and $\Omega_0 = 0.011414$. The match is closest for F_s in $(0.035, 0.0375)$, corresponding to the region where the calculated value for I_{sep} is valid. Outside this region, the Taylor expansion for $A(I_e)B(I_e)$ is increasingly inaccurate. In general we therefore expect the approximation for w_R to be more accurate for F_s values near the dynamical resonance, $F_s^{(j)}$.

At the dynamical resonance $F_s = F_s^{(j)}$, $\nu_j = 0$ and the width in scaled variables is

$$w_R = 2\sqrt{\frac{-2\epsilon}{\beta-\epsilon\gamma}(1-I_m^2)} = 2\sqrt{\frac{2F_\mu\Omega_0|\widetilde{\mathcal{J}}_j|\,(1-I_m^2)}{4\beta+F_\mu\Omega_0|\widetilde{\mathcal{J}}_j|\gamma}}, \tag{2.40}$$

which to $O(F^2)$ is

$$w_R = 8\sqrt{\frac{F_\mu\Omega_0|\widetilde{\mathcal{J}}_j|\,(1-I_m^2)}{3(2F_s^2+F_\mu^2)+8F_\mu\Omega_0|\widetilde{\mathcal{J}}_j|\gamma}}. \tag{2.41}$$

At low frequencies, the resonance width will be small; this in turn can lead to characteristic narrow peaks in the ionisation probability, $P_i(F_s)$ at low frequencies. It can be also be seen that the resonance width is dependent upon the term, $\widetilde{\mathcal{J}}_j$. As $\widetilde{\mathcal{J}}_j \to 0$, $w_R \propto \sqrt{|\widetilde{\mathcal{J}}_j|}$. Hence, if $\widetilde{\mathcal{J}}_j = 0$, the island width is zero and the resonance has no effect on the dynamics. Because $\widetilde{\mathcal{J}}_j \propto \Omega_0^{-1}$, for low frequencies it is sensitive to the number of terms included in its expansion. The effect of the resonance island width on ionisation is discussed further in §2.3.1.

2.1.6 The Inclusion of Ionisation

The equations of motion for the Averaged Hamiltonian, equation (2.24), (page 38), are derived using action-angle variables, which can only describe bound-motion.

The domain where the action angle variables are valid determines a bound region in the phase space of the exact dynamics. Inside this region, the exact dynamics are approximated by the action-angle orbits, whilst outside the region the orbits are assumed to be unbound. Ionisation is included in the approximation by determining the boundary location and treating all orbits that reach the boundary as ionising orbits. It should be understood that this is an approximation only. The equations of motion for the approximate Hamiltonian describe the averaged classical motion of the electron and do not include the faster fluctuations of the exact motion that can, for some orbits, allow the electron to stray into the 'ionising' region of phase space even though the averaged motion remain bound. Similarly, an electron could temporarily stray into the 'ionising' region but remain sufficiently close to the atom to remain bound as the field changes. Hence, the boundary determined for the Averaged Hamiltonian is expected to be an approximation only: rather than a discrete boundary separating ionising and bound orbits, it marks the approximate location of a finite thickness region in phase space containing both bound and ionising orbits.

In the case of a static field, bound motion is only possible for $0 \leq F < F_c$, where F_c is a critical field depending on the values of I_m and I_e (in scaled variables). From an examination of figure 2.2 on page 30 it can be seen that the η-motion becomes unbound when the field magnitude is such that the turning points η_2 and η_3 coalesce.

For a given I_e (or equivalently, a given value of I_2), a maximum value of $F = F_c$ can be found at which the turning points coalesce. For $F \geq F_c$, no bound motion is possible and ionisation is assumed to occur. There is no simple way to invert the action integrals, (2.7) and (2.8) to obtain an expression for F_c. The critical fields were calculated by Banks and Leopold [2, 3]. The approximations used here for the numerical calculation of F_c are given in [3].

In the present application, it is assumed that the field changes sufficiently slowly that the change can be treated as adiabatic and hence that the same ionisation criteria can be applied

to determine whether a specific state ionises, i.e. ionisation occurs if

$$F(t) > F_c(I_e(t), I_m) \quad \text{for} \quad F(t) > 0.$$

For an oscillating field, if $F_\mu > F_s$, $F(t)$ changes sign during each oscillation. In §2.1.1, it was found that ξ-motion is always bound and that the η-motion can be bound or unbound if $F \geq 0$. It can be seen by examining the potentials, $V(\xi)$ and $V(\eta)$ in equation (2.9) that when F changes sign, the nature of the two motions is effectively swapped; the η-motion becomes bound for all values of η, whilst the ξ-motion can now be bound or unbound. Physically, the case $F < 0$ is equivalent to the case $F > 0$ with the z-axis reflected and the direction of axial rotation, $\dot{\phi}(t)$, reversed. This transforms $(\eta, \xi, F) \rightarrow (-\eta, -\xi, -F)$, which is equivalent to $(I_e, I_m, F) \rightarrow (-I_e, -I_m, -F)$; however, the transformation in I_m is immaterial as it only appears in the equations of motion as $|I_m|$. The ionisation condition for $F < 0$ is therefore

$$-F(t) > F_c(-I_e(t), I_m) \quad \text{for} \quad F(t) < 0.$$

Assuming that $I_e(t)$ changes relatively little over a field period, a further approximation can be made, replacing $F(t)$ with its maximum value over a field period; hence for F_s and F_μ positive, the ionisation criteria are

$$\begin{aligned} \lambda(t)(F_s + F_\mu) &> F_c(I_e(t), I_m) \quad \text{for all values of } F_\mu \text{ and } F_s; \text{ and} \\ \lambda(t)(F_\mu - F_s) &> F_c(-I_e(t), I_m) \quad \text{if } F_\mu > F_s. \end{aligned} \tag{2.42}$$

For $I_m = 0.2$, F_c is in the range $(0.136, 0.281)$.

Ionisation probabilities for a particular choice of field parameters, I_m and $I_e(0)$, are calculated using the Monte Carlo method and N initial conditions for $\psi_e(0)$, then integrating the equations of motion (2.26) over the field envelope. The ionisation conditions (2.42) are checked throughout the orbit and if satisfied at any point on the orbit, the orbit is assumed to have ionised. The overall ionisation probability is the fraction of orbits for which ionisation occurs. Each of the initial values of $\psi_e(0)$ are uniformly distributed throughout the interval $(0, 2\pi]$; hence initial values for $\psi_e(0)$ are selected by stratified sampling — dividing up the

range of ψ_e into N equal sub-intervals and selecting a $\psi_e(0)$ value randomly from each. The use of a Monte Carlo method places a limit on the accuracy for each calculated ionisation value. If M orbits ionise out of a sample size of N, the ionisation probability is estimated to be $P_i = M/N$ and with no stratification, the standard deviation of this estimate is (see [23])

$$\sigma = \sqrt{\frac{P_i(1-P_i)}{N}},$$

implying a 95% probability of the true result lying in the interval $(P_i - 2\sigma, P_i + 2\sigma)$. Stratification of the samples reduces the statistical errors further, but with only one point per stratified interval, there is no estimate for the standard deviation: the above formula gives an upper bound for this case.

2.2 Validation of the Classical Approximation

The Averaged Hamiltonian is an approximation to the exact Hamiltonian, equation (2.1) and is expected to be applicable in the case of low frequency fields. In this section we compare ionisation probabilities calculated using equations of motion for the approximate Averaged Hamiltonian (2.24) together with the ionisation criteria (2.42), and the exact classical dynamics to examine the validity of the approximation.

2.2.1 Single Substate Results

In figures 2.9 and 2.10 we compare the ionisation probability calculated using the Averaged Hamiltonian with exact classical dynamics results for varying F_s, using the parameters, $\Omega_0 = 0.0528$, $F_\mu = 0.13$, $I_m = I_2(0) = 0.2$ and a field envelope of 16-50-16. These parameters are selected for comparison with the exact classical dynamics of Richards (see [51], figure 2).

The Hamiltonian for figure 2.9 includes terms up to and including $O(F^2)$, while the Hamiltonian for figure 2.10 includes terms up to and including $O(F^5)$. We used $N = 250$ grid points in the initial values of $\psi_e(0)$. For the exact classical dynamics, 1600 initial values are used.

Peaks in ionisation probability can occur in the vicinity of the dynamical resonances, $F_s = F_s^{(j)}$, discussed in §2.1.2. The peaks are labelled in the diagrams by their corresponding

j value (obtained from equation (2.32) on page 43).

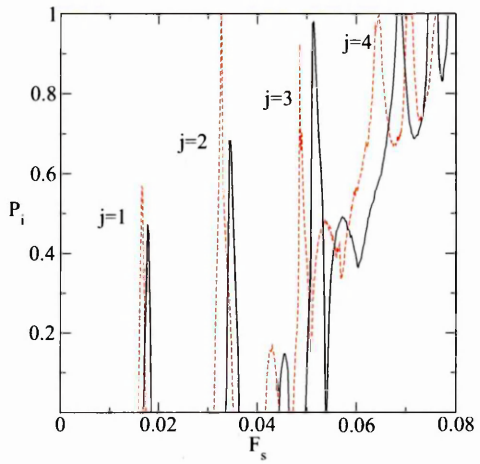

Figure 2.9 Ionisation probabilities, $P_i(F_s)$, for $\Omega_0 = 0.0528$, $F_\mu = 0.13$, $I_m = I_2(0) = 0.2$ for the $O(F^2)$ Averaged Hamiltonian (solid line) and the exact classical dynamics (dashed line) (Richards [51], figure 2).

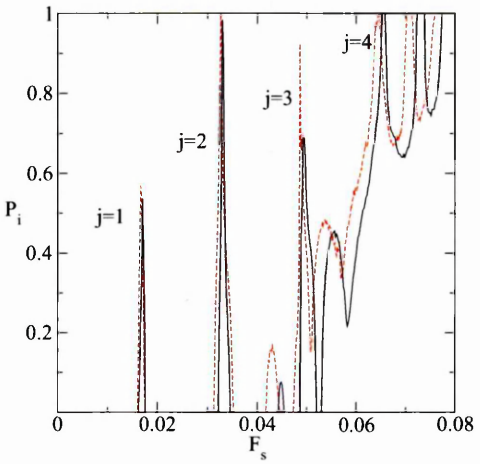

Figure 2.10 Ionisation probabilities, $P_i(F_s)$, for $\Omega_0 = 0.0528$, $F_\mu = 0.13$, $I_m = I_2(0) = 0.2$ for the $O(F^5)$ Averaged Hamiltonian (solid line) and the exact classical dynamics (dashed line) (Richards [51], figure 2).

The figures show a good correspondence between the Averaged Hamiltonian results and those for the exact classical dynamics. In particular, the following key characteristics are observed:

1. Each of the four resonance peaks calculated for the exact classical dynamics occur also for the Averaged Hamiltonian results, although the locations and heights of the peaks are slightly different.

2. Local maxima observed in $P_i(F_s)$ for the exact classical dynamics at $F_s = 0.0430, 0.0535$ and 0.0705 also occur for the Averaged Hamiltonian, although at slightly different values of F_s. These peaks are not associated with known resonances.

3. The exact Hamiltonian and the Averaged Hamiltonian results both show an underlying increase in ionisation probability for $F_s \gtrsim 0.045$.

It can be seen that the locations of the resonance ionisation probability peaks are closer to those of the exact classical dynamics for the $O(F^5)$ than for the $O(F^2)$ Averaged Hamiltonian. This suggests that the differences in locations are a consequence of ignoring higher order F

Table 2.1: Comparison of measured locations for the local maxima in $P_i(F_s)$, denoted by $\mathcal{F}_s^{(j)}$, for exact classical dynamics, $O(F^2)$ and $O(F^5)$ Averaged Hamiltonians, with $F_\mu = 0.13$, $\Omega_0 = 0.0528$ and $I_m = I_2(0) = 0.2$. Dynamical resonance locations, $F_s^{(j)}$, are shown for the Averaged Hamiltonians.

	Exact Hamiltonian	$O(F^2)$ Averaged Hamiltonian		$O(F^5)$ Averaged Hamiltonian	
j	$\mathcal{F}_s^{(j)}$	$\mathcal{F}_s^{(j)}$	$F_s^{(j)}$	$\mathcal{F}_s^{(j)}$	$F_s^{(j)}$
1	0.0166	0.0178	0.0176	0.0170	0.0168
2	0.0327	0.0344	0.0352	0.0330	0.0335
3	0.0486	0.0514	0.0528	0.0492	0.0500
4	0.0645	0.0686	0.0704	0.0654	0.0662

terms in the Averaged Hamiltonian. The measured locations of the maxima in ionisation probability peak in the vicinity of each of the four dynamical resonances are shown in table 2.1. The measured location is the value of F_s for which P_i has a locally maximum value. Where $P_i(F_s) = 1$ for a range of sampled F_s values, the value of F_s in the middle of the range is used. The dynamical resonances, $F_s^{(j)}$, are also given, showing that the peaks in ionisation probability do not necessarily coincide with the dynamical resonances. This behaviour is also seen for the exact classical dynamics [51].

We note the presence of the small peak at $F_s = 0.0430$; this was also observed for the exact classical dynamics [51]. The cause of this peak is not understood; it was suggested, but not proven, by Richards that the peak might be due to a non-integer resonance at $j = 2\frac{2}{3}$.

Figure 2.11 shows the ionisation probabilities, $P_i(F_s)$ at the lower frequency of $\Omega_0 = 0.011414$ for the $O(F^5)$ Averaged Hamiltonian and the exact Hamiltonian. All other parameters are same as for figure 2.10. Figure 2.12 shows the corresponding ionisation probability, $P_i(F_s)$, in the case of the $O(F^2)$ Averaged Hamiltonian. The resonance location labels refer to the locations of the exact classical dynamics; the $O(F^2)$ resonance locations occur at different values of F_s, in some cases lying close to exact resonance locations with different j values. For clarity figure 2.13 is included to show the $O(F^2)$ ionisation probability curve with the corresponding $O(F^2)$ resonance locations marked.

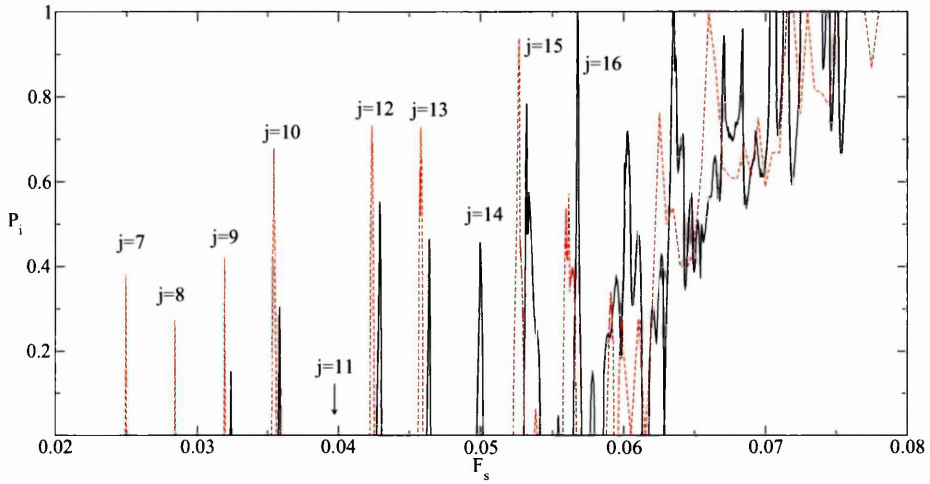

Figure 2.11 Ionisation probabilities, $P_i(F_s)$, for $F_\mu = 0.13$, $\Omega_0 = 0.011414$ and field envelope 16-50-16 for the $O(F^5)$ Averaged Hamiltonian (solid line) and the exact classical dynamics (dashed line).

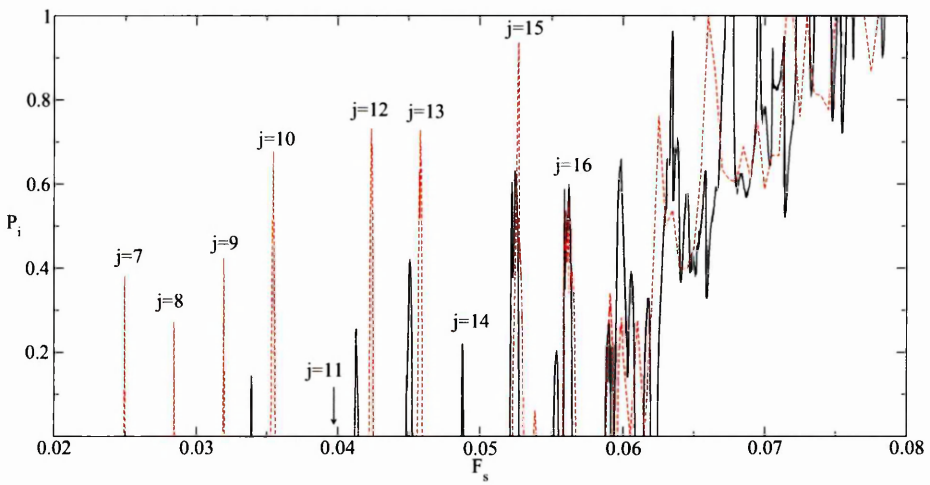

Figure 2.12 Ionisation probabilities, $P_i(F_s)$, for $F_\mu = 0.13$, $\Omega_0 = 0.011414$ and field envelope 16-50-16 for the $O(F^2)$ Averaged Hamiltonian (solid line) and the exact classical dynamics (dashed line), with exact resonance locations marked.

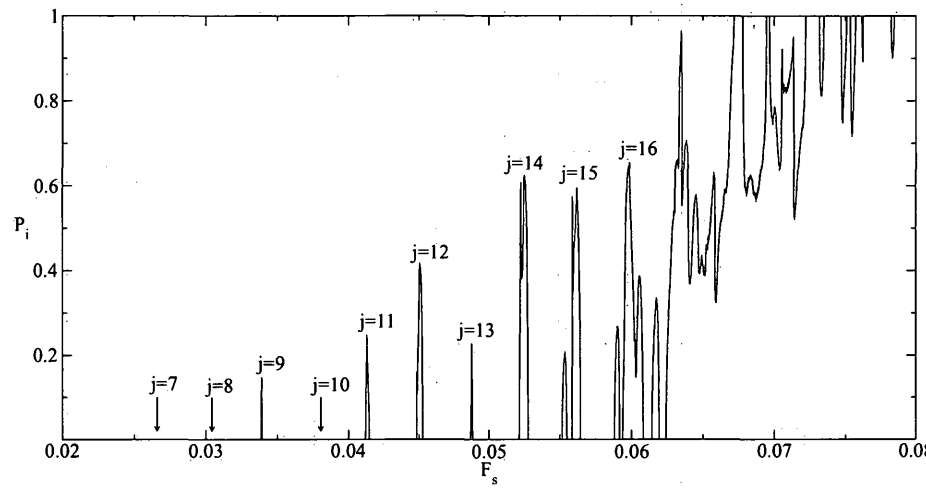

Figure 2.13 Ionisation probabilities, $P_i(F_s)$, for $F_\mu = 0.13$, $\Omega_0 = 0.011414$ and field envelope 16-50-16 for the $O(F^2)$ Averaged Hamiltonian with corresponding $O(F^2)$ resonance locations marked.

As for the higher frequency comparison, the Averaged Hamiltonian results show a reasonable match against those for the exact classical dynamics:

1. Up to $F_s \approx 0.06$, the ionisation behaviour for both the exact and Resonant Hamiltonian cases are broadly similar, characterised by narrow ionisation probability peaks near the location of the dynamical resonances.

2. For $F_s \gtrsim 0.06$ there is a general underlying trend of increased ionisation probability for both the exact and the Averaged Hamiltonian results.

3. For the Averaged Hamiltonian, where resonance ionisation peaks occur, they are reasonably close to the locations of resonance peaks for the exact case. The locations are closer for the $O(F^5)$ Averaged Hamiltonian than for the $O(F^2)$ Averaged Hamiltonian.

The following key differences are observed:

1. Some of the resonance ionisation peaks present in the exact case are missing for the Resonant Hamiltonian and vice versa. For the exact case, the first eight ionisation peaks occur near $F_s^{(j)}$ for $j = 7, 8, 9, 10, 12, 13, 15$ and 16; in comparison, for the $O(F^5)$ Averaged Hamiltonian, the $j = 7$ and $j = 8$ resonance peaks are missing while the

$j = 14$ resonance peak is present. For the $O(F^2)$ case, the $j = 9, 11, 12, 13, 14, 15$ and 16 resonance peaks are present, but the $j = 10$ peak is missing. The presence or absence of ionisation peaks near dynamical resonances is analysed in §2.3.

2. There is no obvious match between the exact and Resonant Hamiltonians for the height of each of the resonance ionisation peaks.

3. For $F_s \gtrsim 0.06$, the underlying ionisation trend is broadly similar between the Resonant and exact cases, the detailed behaviour is different.

We conclude that the Averaged Hamiltonian captures the general characteristics observed for the exact classical dynamics ionisation probabilities, with clear peaks in ionisation probability occurring near resonance locations and an underlying increase in ionisation probability occurring as F_s passes a threshold value. For both frequencies considered, the location of the ionisation peaks is better for the higher order approximation. In the exact case it is observed that for isolated resonance ionisation peaks, the peaks are typically narrower for lower frequencies; this is also observed in the approximation.

As the frequency is reduced, the approximation is not as good at predicting the height, or presence of ionisation peaks at resonance. The reasons for this are discussed in §2.3.

2.2.2 Averaged Substate Results

In the preceding section, the values of I_m and $I_e(0)$ were fixed.

The experimental data is for ionisation of excited hydrogen atoms averaged over an initial distribution of substates of n. The exact distribution is not known, but there are good reasons, see Koch *et al* [31], to assume that it is a microcanonical distribution, that is there is an equal distribution of the unperturbed (free field) substates. In classical mechanics, this means that I_m, $I_e(0)$ and $\psi_e(0)$ are uniformly distributed in the intervals,

$$\begin{array}{ccccc} -I_n & < & I_m & < & I_n, \\ |I_m| - I_n & < & I_e(0) & < & I_n - |I_m|, \\ 0 & \leq & \psi_e(0) & < & \pi. \end{array}$$

Figure 2.14 shows ionisation probabilities calculated for the $O(F^5)$ Averaged Hamiltonian

for $\Omega_0 = 0.0980$, $F_\mu = 0.1$ and a field envelope of 16-80-16, averaged over a distribution of initial conditions. The field parameters are selected for comparison with Richards [51] figure 1. For the Averaged Hamiltonian results, 39000 orbits are used for each F_s value, obtained from 780 values of $(I_m, I_e(0))$ with 50 initial values of $\psi_e(0)$ considered for each. The initial values are taken to match the possible (m, k_i) quantum values for a given n; in this case, $n = 39$. The exact classical dynamics ionisation probabilities are shown for comparison, derived using 1296 orbits for each F_s value. The adiabatic ionisation curve is also shown, calculated in the absence of the perturbation, for which $I_e(t)$ is constant, hence from equations (2.42), page 50, ionisation occurs if $F_\mu + F_s > F_c(I_e(0), I_m)$ or $F_\mu - F_s > F_c(-I_e(0), I_m)$. The distribution of initial values $(I_m, I_e(0))$ is taken in the same way as for the Averaged Hamiltonian, in this case with $n = 39$ and hence with 780 initial values of $(I_m, I_e(0))$ for each F_s.

The match between resonance locations is good, although the ionisation probability is generally lower for the Averaged Hamiltonian when compared with the exact classical dynamics ionisation probability. For the majority of F_s values, the ionisation is seen to be close to the adiabatic curve. The cause of this underestimation is assumed to be the location of the phase space boundaries between bound and ionising orbits. The actual orbits for the exact dynamics only approximately follow those of the Averaged Hamiltonian, allowing some orbits for the exact dynamics to ionise whilst the equivalent orbits for the Averaged Hamiltonian lie within a region where the orbits are bound.

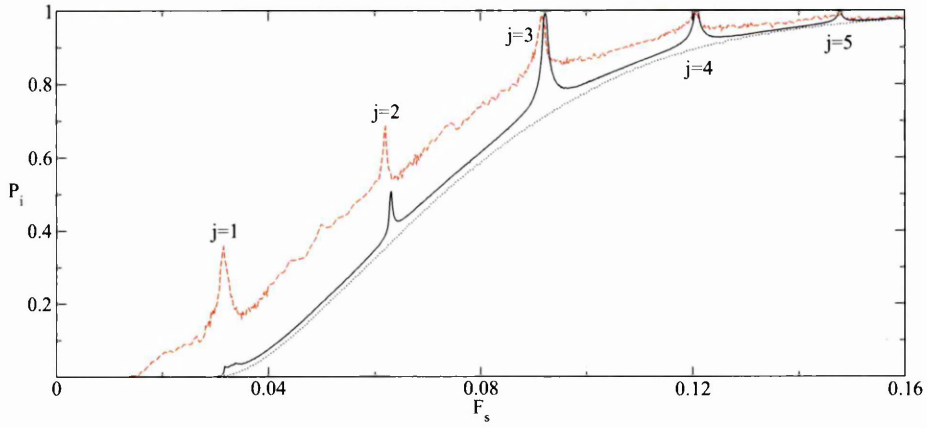

Figure 2.14 Ionisation probabilities, $P_i(F_s)$, for $F_\mu = 0.1$ and $\Omega_0 = 0.0980$, field envelope 16-80-16 $O(F^5)$ Averaged Hamiltonian (solid line) and the exact classical dynamics (dashed line) from [51] figure 1). The adiabatic ionisation curve is shown by a dotted line.

Robicheaux *et al* [52] numerically obtained quantum and classical ionisation probabilities for comparison with the experimental results of Koch *et al* [32] from quantal and classical approximations using the parameters: $n = 39$, $F_\mu = 319\,\mathrm{Vcm}^{-1}$, $\Omega = 8.1\,\mathrm{GHz}$ and an overall field envelope of 150 cycles. The corresponding scaled parameters are $F_\mu = 0.14372$ and $\Omega_0 = 0.0730$. These are the only other available quantal results.

The overall field envelope used by Robicheaux *et al* was created by multiplying the field by functions of the form $(1 + \mathrm{erf}(t/5T))/2$ for the switch-on and $(1 - \mathrm{erf}((t - T_e)/5T))/2$ for the switch-off. It appears from the description provided by Robicheaux that the integration is made for t in the interval $(0, T_e)$; if so then the envelope function starts at $1/2$ meaning that the field is instantaneously applied. This physically different initial condition would be expected to affect the evolution of the system.

The field envelope used here is given by equation (2.3) with envelope parameters, 16-113-16. A better fit to the Robicheaux envelope could be obtained using envelope parameters 16-134-16 with $t = 0$ for Robicheaux occurring after 8 field cycles for the envelope function defined here. We have compared the results generated using both the envelope 16-113-16 and 16-134-16 and confirmed that this has only a minimal effect on the calculated ionisation probabilities.

In figure 2.15 we compare the ionisation probabilities in the region of the $j = 1$ resonance

using the $O(F^5)$ Averaged Hamiltonian, over the scaled range F_s = 0.0180–0.0262 (corresponding to F_s =39.97–58.17 Vcm^{-1}) with those for the exact classical dynamics. For the results presented here, the ionisation probabilities were calculated as averages over a uniform distribution of 780 values of $(I_m, I_e(0))$ with each ionisation value determined from a microcanonical array of 250 initial ψ_e values. The exact classical dynamics ionisation probabilities — derived using 4096 initial orbits — are also shown in the figure. Robicheaux classical results taken from figure 1 of [52] are shown for comparison and are for the scaled F_s range (0.018, 0.0234).

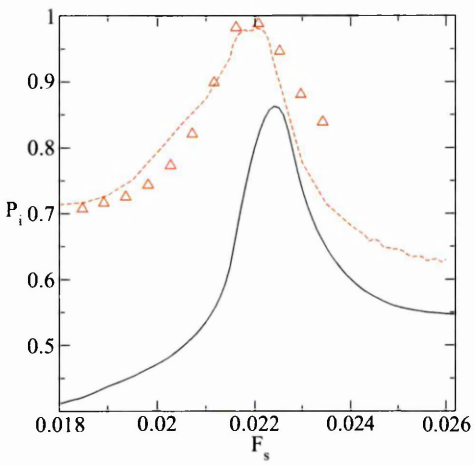

Figure 2.15 $P_i(F_s)$ for the $j = 1$ resonance averaged over substates, F_μ = 0.14372, Ω_0 = 0.0730 and envelope of 16-113-16 for the $O(F^5)$ Averaged Hamiltonian (solid line) and exact classical dynamics (dashed line). Comparison Robicheaux classical results taken from [52] are shown using triangles.

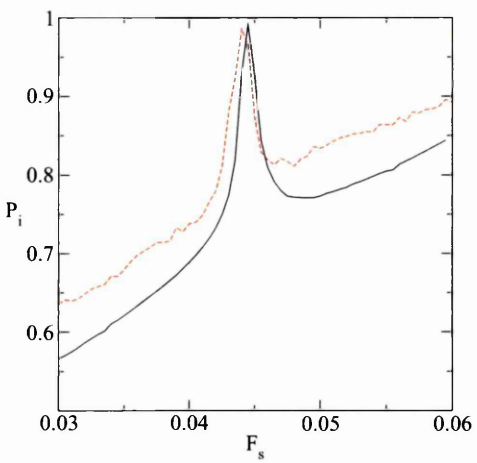

Figure 2.16 $P_i(F_s)$ for the $j = 2$ resonance averaged over substates, F_μ = 0.14372, Ω_0 = 0.0730 and envelope of 16-113-16 for the $O(F^5)$ Averaged Hamiltonian (solid line) and exact classical dynamics (dashed line).

The exact classical dynamics ionisation probability is generally higher than the Robicheaux calculations for F_s values to the right of the ionisation maximum, and lower for values to the left. The location of the probability peaks is similar. We would expect the two sets of results to be a better match. Two possible sources of the difference are:

1. Different envelope functions were used; in particular, the Robicheaux envelope has an initial value of 1/2 at $t = 0$. If integration was started at $t = 0$ then this is equivalent to

the instantaneous application of the applied field.

2. It is unclear from the Robicheaux description how numerical problems when the electron passes close to the nucleus were avoided. Calculations for the exact Hamiltonian shown here use regularisation methods to prevent numerical problems. Robicheaux also reports that some of the orbits are chaotic. Whilst for $\Omega_0 \to 1$ chaos is significant, for the low frequencies considered here the orbits are generally stable hence allowing the development of the one dimensional approximation described here. The averaged Hamiltonian, $\overline{K}_m$, is derived assuming that I_n is constant. From exact classical calculations at $F_s = 0.018$ for $\Omega_0 = 0.0730$, $P_i \approx 0.71$ and 1173 of the original 4096 orbits remain bound. The final values of I_n lie in the interval $(0.979, 1.028)$, have a mean of 1.002 and standard deviation of 0.004. These results confirm the applicability of the assumption that I_n is constant and do not suggest that the orbits behave chaotically. It is possible that the chaotic behaviour reported by Robicheaux in fact is a consequence of numerical instabilities.

The classical Averaged Hamiltonian results considered here provide a reasonable match for the location of the ionisation peak. The small difference, as discussed in the previous section, is assumed to be a consequence of the exclusion of higher order terms in F from the Averaged Hamiltonian. Overall the results for the Averaged Hamiltonian underestimate the ionisation probability, with the difference being more marked for F_s values below the ionisation peak; for the range of F_s values shown, the largest difference in ionisation probability between the exact classical dynamics and the Averaged Hamiltonian classical approximation is approximately 0.34.

The observed ionisation differences for low F_s values is probably partly a consequence of underestimating ionisation along the I_1 axis for the adiabatic ionisation tests used here (see §2.1.3, page 40 and equation (2.42) in particular). At $F_s = 0.0180$, $F_\mu - F_s = 0.12572$, which is close to the minimum critical field value, $F_c = 0.12944$ for $I_m = 0$. Whilst in the Averaged Hamiltonian approximation considered here this is insufficient to cause ionisation, there is significant ionisation for the exact classical dynamics. This is because the approximation used here smooths the dynamics, removing oscillations that can lead to ionisation in the exact

system. This smoothing increases as Ω_0 increases and decreases P_i.

In figure 2.16 we compare the calculated ionisation probabilities in the vicinity of the $j = 2$ resonance. In this case, $F_\mu - F_s$ is sufficiently small to exclude ionisation associated with the I_1 axis for the exact classical system as well. It can be seen that in this case there is a better match. For the range of F_s values shown, the largest difference in ionisation probability between the exact classical dynamics and the Averaged Hamiltonian classical approximation is approximately 0.11.

The underestimation of ionisation for small F_s is also observed in comparisons of single state initial conditions. In figure 2.17 ionisation curves are compared between the exact classical dynamics and Averaged Hamiltonian for $\Omega = 0.0528$, $I_m = 0.2$, $I_e(0) = -0.4$ and field envelope 16-50-16. In the first figure $F_\mu = 0.14$ for the exact and Averaged Hamiltonians, whilst in the second figure $F_\mu = 0.147$ for the Averaged Hamiltonian. When $F_\mu = 0.14$, ionisation is observed in both cases for small F_s but is appreciably less for the Averaged Hamiltonian. It is only when F_μ is increased to 0.147 that there is a reasonable match for smaller F_s, but the ionisation differences are now greater for larger F_s values; the peak at $F_s \approx 0.0165$ is also now absent.

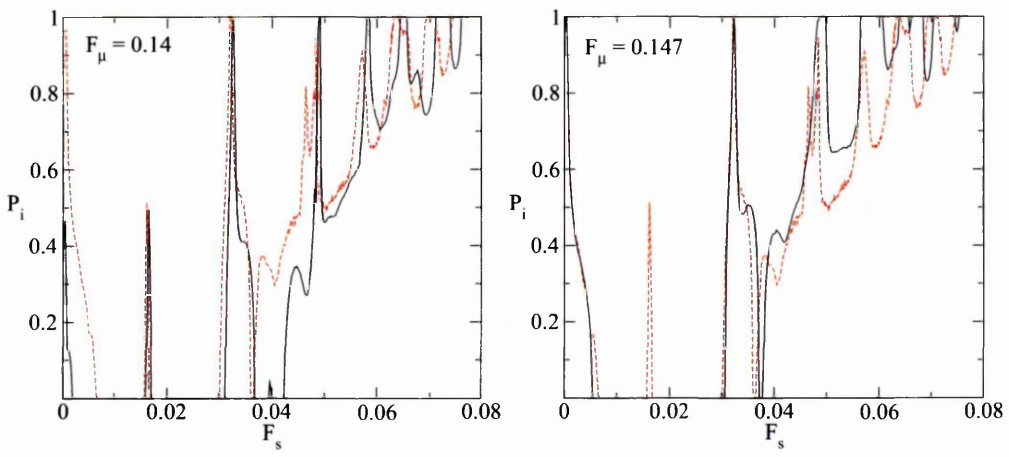

Figure 2.17 Ionisation probabilities, $P_i(F_s)$, for $\Omega = 0.0528$, $I_m = 0.2$, $I_e(0) = -0.4$ and envelope 16-50-16. The solid lines are for the Averaged Hamiltonian with F_μ values as marked. In each figure the dashed line is calculated for exact classical dynamics with $F_\mu = 0.14$.

2.2.3 Conclusions

From the comparisons discussed in the preceding sections, we have shown that for low scaled field frequencies the Averaged Hamiltonian reproduces most of the ionisation behaviour observed for the exact classical system. This includes the presence of ionisation probability peaks near resonances and the underlying increase in ionisation probability for sufficiently large $|F|$ and in some cases (when $F_\mu - F_s$ is sufficiently large) for small F_s.

A number of characteristic differences were observed between the Averaged Hamiltonian results and those for the exact classical dynamics. These are as follows:

1. The locations of dynamical resonance ionisation probability peaks are shifted relative to the exact results. It is assumed that this is a consequence of excluding higher order terms in F from the Averaged Hamiltonian. Consistent with this assumption, the $O(F^5)$ Averaged Hamiltonian provides a better match to exact results than the $O(F^2)$ Averaged Hamiltonian.

2. The Averaged Hamiltonian generally predicts a lower ionisation probability than observed for the exact case for most F_s values. This is seen most clearly in the case of results averaged over substates. This is assumed to be caused by differences between the exact and the approximate location of the ionisation boundary, as discussed in §2.1.6 on page 49; this discrepancy increases with increasing Ω_0.

3. For small F_s values when $F_\mu - F_s$ is sufficiently large, ionisation can occur for the exact classical system. This ionisation probability is underestimated by the Averaged Hamiltonian approximation.

4. For low frequencies, ionisation probability peaks do not occur at all values of $F_s^{(j)}$. This is observed for both the exact and the approximation Averaged Hamiltonians; however, there are differences between which peaks are present in the exact and approximation cases.

The last item is discussed further in the next section.

2.3 Analysis of Classical Results

2.3.1 Missing Ionisation Probability Peaks

In §2.2.1 the ionisation probability, $P_i(F_s)$, was calculated for the low frequency field, $\Omega_0 = 0.011414$, comparing $P_i(F_s)$ for the Averaged Hamiltonian, $\overline{K}_m$, equation (2.24) on page 38, with those for the exact classical dynamics (see figures 2.11 and 2.12 on pages 54 and 54 in particular). It was observed that in some cases ionisation probability peaks occur near the dynamical resonance values, $F_s^{(j)}$, although the presence or absence of peaks was different for the three Hamiltonians considered: exact classical dynamics, $O(F^5)$ and $O(F^2)$ Averaged Hamiltonian.

Whether an ionisation peak is observed near a resonance depends on the initial value, $I_e(0)$, the resonance island width and the effects of the field switch-on. These effects are shown in the following sections. Particularly for small Ω_0, the island width is sensitive to the number of terms included in the energy expansion, $\overline{E}$, equation (2.23) (page 38). Calculations are made to $O(F^2)$ and $O(F^5)$ to show this.

The $O(F^2)$ Averaged Hamiltonian

The presence and the locations of ionisation peaks can be largely explained by an examination of $\overline{K}_R$, the Resonance Hamiltonian described in §2.1.4, page 42. Results for the presence and location of resonance ionisation peaks are derived in this section using properties derived for the $O(F^2)$ Resonance Hamiltonian, equation (2.35) (page 44).

We consider first the dynamics of the Resonance Hamiltonian, $\overline{K}_R$ for an instantaneously applied field. It was shown in §2.1.5 (page 45) that near the dynamical resonances, which for the $O(F^2)$ Hamiltonian are at $F_s^{(j)} = j\Omega_0/3$, resonance islands appear in the phase space, the presence of which can cause significant changes in $I_e(t)$ for certain initial conditions. If the value of F_s is increased from a value initially below $F_s^{(j)}$, the resonance island initially appears with its centre, the stable librational equilibrium point, $I_e = I_s$, initially at $I_s \approx |I_m| - I_n$. As F_s increases, I_s increases, with $I_s = 0$ at $F_s = F_s^{(j)}$ and $I_s \approx I_n - |I_m|$ for F_s sufficiently large. Therefore, as F_s increases, the resonance island passes through both $I_e(0)$ and $I_c(F_s, F_\mu)$, the critical value above which ionisation occurs. The maximum change in $I_e(t)$ is given by the

resonance width, w_R, which is the maximum separation between the resonance separatrix. The resonance width varies with F_s, but has a maximum near $F_s = F_s^{(j)}$. For an instantaneously applied field, ionisation is only possible for the Resonance Hamiltonian if

$$w_R \geq I_c - I_e(0), \tag{2.43}$$

where the island width, w_R, is given by equation (2.41) on page 48.

The Resonance Hamiltonian, $\overline{K}_R$, is derived from the Averaged Hamiltonian, $\overline{K}_m$, by ignoring higher Fourier terms for frequencies ν_k where $k \neq j$. These terms introduce small fluctuations in $I_e(t)$ superimposed on the general behaviour that modify this ionisation criteria slightly. A more significant modification to the ionisation criteria is required when the effects of a gradually switched on field are included. During the field switch-on significant changes can occur in $I_e(t)$ requiring condition (2.43) to be modified to ionisation only being possible if

$$w_R \geq I_c - I_e(T_a, \psi_e(0)),$$

for at least some of the initial values of $\psi_e(0)$ and where T_a is the time at the end of the field switch-on. Without knowing the exact values of $I_e(T_a, \psi_e(0))$ for each of the initial conditions $\{\psi_e(0)\}$, this condition is less useful in predicting the presence of resonance peaks.

The effects of field switch-on can be removed by calculating ionisation probability in the case of an applied field which is instantaneously switched on and off, i.e. we set $\lambda(t) = 1$ throughout the period of integration. Figure 2.18 shows the ionisation probability calculated for the $O(F^2)$ Averaged Hamiltonian, equation 2.24 (page 38), with $\overline{E}_R(I_e, F_s, F_\mu, t)$ and $g(t)$ expanded to $O(F^2)$ for a 0-50-0 field envelope, with all other parameters chosen to match those of figure 2.12. The dynamical resonance locations, $F_s^{(j)}$, are marked with arrows.

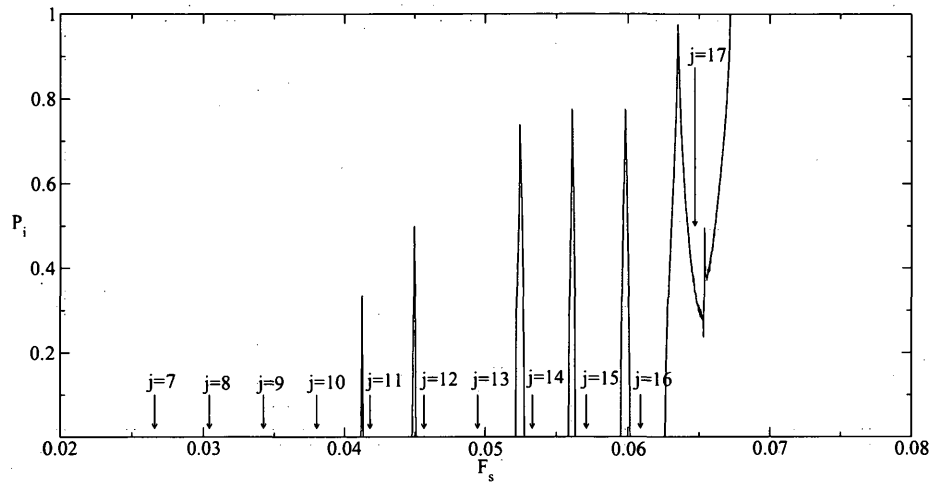

Figure 2.18 Ionisation probabilities, $P_i(F_s)$, for $F_\mu = 0.13$, $\Omega_0 = 0.011414$, $I_m = 0.2$ and $I_e(0) = -0.4$ for the $O(F^2)$ Averaged Hamiltonian with field envelope 0-50-0. Arrows mark the dynamical resonance locations, $F_s^{(j)} = j\Omega_0/3$.

Table 2.2 compares $I_c - I_e(0)$ with w_R at each of the first 17 dynamical resonances. If $I_e(0) + w_R - I_c$ is positive then condition (2.43) is satisfied, indicating that $I_e(t)$ may vary sufficiently to cause ionisation. For $j = 1$, no ionisation is possible for any value of $I_e(t)$. It can be seen by comparison with figure 2.18 that for each j value an ionisation probability peak occurs if and only if $I_e(0) + w_R - I_c \geq 0$.

If we compare the ionisation probability curve of figure 2.12 on page 54 with figure 2.18 we observe that when the field envelope includes a slow switch then two other ionisation peaks are introduced at $j = 9$ and $j = 13$. From table 2.2 we see that $I_e(0) + w_R - I_c$ is negative but small. In these cases, the changes in $I_e(t)$ occurring during the switch-on time are sufficient to permit ionisation.

The $O(F^5)$ Averaged Hamiltonian

Figure 2.19 shows $P_i(F_s)$ for the $O(F^5)$ Averaged Hamiltonian, equation 2.24, page 38, for a 0-50-0 field envelope, with all other parameters chosen to match those of figure 2.12. The dynamical resonances, $F_s^{(j)}$, are marked with arrows.

Table 2.2: Comparison of $I_c - I_e(0)$ with resonance width, w_R, at each of the dynamical resonances, $F_s^{(j)} = j\Omega_0/3$, for the $O(F^2)$ Resonance Hamiltonian with $F_\mu = 0.13$, $\Omega_0 = 0.011414$, $I_m = 0.2$ and $I_e(0) = -0.4$ for a suddenly switched field.

j	$F_s^{(j)}$	w_R	$I_c(F_s, F_\mu)$	$I_e(0) + w_R - I_c$
1	0.00380	0.315	No ionisation	No ionisation
2	0.00761	0.459	0.735	-0.675
3	0.01141	0.349	0.613	-0.664
4	0.01522	0.431	0.503	-0.472
5	0.01902	0.400	0.402	-0.402
6	0.02283	0.365	0.309	-0.343
7	0.02663	0.444	0.223	-0.180
8	0.03044	0.218	0.144	-0.326
9	0.03424	0.453	0.070	-0.017
10	0.03805	0.250	0.002	-0.152
11	0.04185	0.396	-0.061	0.057
12	0.04566	0.392	-0.120	0.112
13	0.04946	0.203	-0.175	-0.022
14	0.05327	0.411	-0.227	0.237
15	0.05707	0.310	-0.275	0.184
16	0.06087	0.271	-0.319	0.190
17	0.06468	0.387	-0.361	0.348

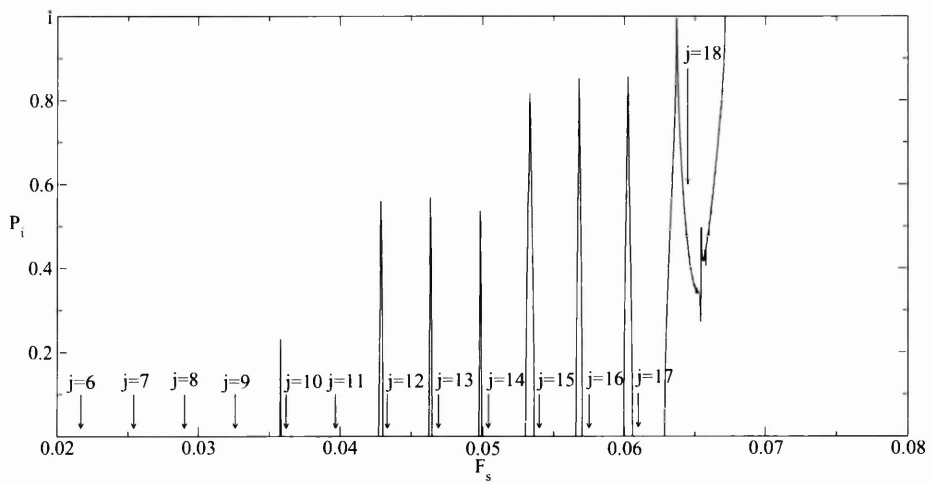

Figure 2.19 Ionisation probabilities, $P_i(F_s)$, for $F_\mu = 0.13$, $\Omega_0 = 0.011414$, $I_m = 0.2$ and $I_e(0) = -0.4$ for the $O(F^5)$ Averaged Hamiltonian with field envelope 0-50-0. Arrows mark the dynamical resonance locations, $F_s^{(j)}$, satisfying $3\overline{g}(F_s^{(j)}, F_\mu) = j\Omega_0$.

Table 2.3 contains resonance data calculated for the $O(F^5)$ Averaged Hamiltonian for each of the resonances, $j = 6 - 14$ with $\Omega_0 = 0.011414$ and $F_\mu = 0.13$. Data is calculated with

Table 2.3: Resonance width, w_R, dynamical resonance location, $F_s = F_s^{(j)}$, critical ionisation action, I_c, and critical $I_e(0) = \mathcal{I}_i$ for the start of ionisation field envelopes 16-50-16 and 0-50-0 for the $O(F^5)$ Resonance Hamiltonian with $F_\mu = 0.13$ and $\Omega_0 = 0.011414$.

j	$F_s^{(j)}$	w_R	I_c	$\mathcal{I}_i$ for 16-50-16 envelope	$\mathcal{I}_i$ for 0-50-0 envelope	$\mathcal{I}_i + w_R - I_c$ for 16-50-16 envelope	$\mathcal{I}_i + w_R - I_c$ for 0-50-0 envelope
6	0.0217	0.098	0.335	0.101	0.167	-0.135	-0.070
7	0.0254	0.493	0.251	-0.205	-0.245	0.037	-0.002
8	0.0290	0.357	0.174	-0.238	-0.192	-0.055	-0.009
9	0.0326	0.407	0.102	-0.423	-0.318	-0.118	-0.013
10	0.0362	0.467	0.036	-0.460	-0.422	-0.028	0.010
11	0.0397	0.100	-0.026	-0.293	-0.184	-0.166	-0.058
12	0.0433	0.461	-0.084	-0.577	-0.540	-0.032	0.005
13	0.0469	0.399	-0.138	-0.531	-0.501	0.006	0.036
14	0.0504	0.255	-0.189	-0.597	-0.498	-0.153	-0.054

and without field switch-on, using the corresponding field envelopes, 16-50-16 and 0-50-0. The dynamical resonance locations, $F_s^{(j)}$, are calculated by solving equation (2.32) on page 43,

$$3\overline{g}(F_s^{(j)}, F_\mu) = j\Omega_0,$$

to find $F_s^{(j)}$ for each j value. An approximation to the resonance island width, w_R, is found using equation (2.39), page 48, at $F_s = F_s^{(j)}$.

For each of the resonances, there is a critical initial value, which we denote by $\mathcal{I}_i$, such that ionisation is first observed for increasing $I_e(0)$ when $I_e(0) = \mathcal{I}_i$. This is estimated numerically for both field envelopes. Ionisation probabilities are calculated from a sample array of 100 orbits with a grid size of $\delta F_s = 2 \times 10^{-5}$.

In the previous section it was demonstrated that in the absence of field switch-on, the appearance of ionisation peaks depends primarily on whether the island size is sufficiently large for some orbits to reach above the critical ionisation limit, i.e. when $I_e(0) + w_R \geq I_c$. In table 2.3 it can be seen that this condition applies in the $O(F^5)$ Hamiltonian as well — for each resonance in the case of the 0-50-0 envelope , $|\mathcal{I}_i + w_R - I_c| \ll 1$ and $I_c - w_R$ is therefore a reasonable estimate for the $I_e(0)$ value for the onset of ionisation.

Tables 2.2 and 2.3 show that for each resonance, there are significant differences between the island widths for the $O(F^2)$ and $O(F^5)$ Hamiltonians. These differences can have an appreciable effect on whether ionisation occurs near each dynamical resonance.

For the $j = 10$ resonance, $w_R = 0.24972$ for the $O(F^2)$ Hamiltonian and $w_R = 0.46749$ for the $O(F^5)$ Hamiltonian. In the former case the island size is too small to allow ionisation for the initial action, $I_e(0) = -0.4$, but in the latter case the larger island size allows ionisation from $I_e(0) < -0.4$; hence the ionisation peak is missing for the $O(F^2)$ Hamiltonian but present for the $O(F^5)$ Hamiltonian.

For the $j = 11$ resonance, the ionisation peak is missing for the $O(F^5)$ Hamiltonian, but present for the $O(F^2)$ Hamiltonian. Again, this is caused by the different island sizes, with $w_R = 0.39615$ for the $O(F^2)$ Hamiltonian and $w_R = 0.09964$ in the $O(F^5)$ Hamiltonian.

An approximation to the island size was derived in §2.1.5, equation (2.40),

$$w_R = 2\sqrt{\frac{-2\epsilon}{\beta - \epsilon\gamma}(1 - I_m^2)}, \quad \gamma = \left(\frac{1 + I_m^2}{1 - I_m^2}\right), \quad \epsilon = -\frac{F_\mu \Omega_0 |\widetilde{\mathcal{J}}_j|}{4}$$

and

$$\beta = \frac{3}{16}\left(F_s^2 + \frac{F_\mu^2}{2}\right) - \frac{3}{512}\left(301 - 189I_m^2\right)\left(F_s^4 + 3F_s^2F_\mu^2 + \frac{3F_\mu^4}{8}\right).$$

In table 2.4 the measured island sizes for each of the resonances are compared with the approximate island size calculated using this expression for both the $O(F^2)$ and $O(F^5)$ Hamiltonians. It can be seen that the approximation provides a close match for each of the $O(F^2)$ resonances and a reasonable match for the $O(F^5)$ resonances.

The approximation for w_R is fairly insensitive to the small differences in F_s caused by the difference in locations of the dynamical resonances, $F_s^{(j)}$, for the different order Hamiltonians. However, the calculation of $\widetilde{\mathcal{J}}_j$ is sensitive to the order of the Hamiltonian. To $O(F^5)$, $\widetilde{\mathcal{J}}_j$ is given by equation (2.29) on page 43, whereas to $O(F^2)$, $\widetilde{\mathcal{J}}_j = J_j(3F_\mu/\Omega_0)$, from equation (2.30). The difference between the two expansions is dependant upon F_μ/Ω_0, which for the dynamical parameters considered is relatively large.

Figure 2.20 compares the $\widetilde{\mathcal{J}}_j$ expressions for $O(F^2)$ and $O(F^5)$ expansions for varying F_μ in the vicinity of the $j = 10$ resonance for $\Omega_0 = 0.011414$. The value $F_s = 0.03615$ is chosen to match the $O(F^5)$ dynamical resonance location, but the small difference between the locations

Table 2.4: Resonance widths, w_R, at each dynamical resonance, $F_s = F_s^{(j)}$, measured from the Resonance Hamiltonian orbits and estimated using equation (2.40) for the $O(F^2)$ and $O(F^5)$ Resonance Hamiltonians with $F_\mu = 0.13$ and $\Omega_0 = 0.011414$.

	$O(F^2)$			$O(F^5)$		
j	$\lvert\widetilde{\mathcal{J}}_j\rvert$	Estimated w_R	Actual w_R	$\lvert\widetilde{\mathcal{J}}_j\rvert$	Estimated w_R	Actual w_R
1	-0.05591	0.31459	0.31458	-0.11406	0.47382	0.47393
2	0.12186	0.45951	0.45947	0.06870	0.36956	0.36962
3	0.06997	0.34898	0.34897	0.12313	0.48990	0.49002
4	-0.10896	0.43094	0.43091	-0.04222	0.28920	0.28923
5	-0.09493	0.40000	0.39999	-0.13363	0.50604	0.50620
6	0.08033	0.36536	0.36535	-0.00491	0.09821	0.09821
7	0.12202	0.44362	0.44359	0.12947	0.49324	0.49342
8	-0.02960	0.21826	0.21826	0.06738	0.35651	0.35660
9	-0.13404	0.45333	0.45330	-0.08972	0.40731	0.40744
10	-0.04098	0.24972	0.24972	-0.12086	0.46728	0.46749
11	0.10776	0.39616	0.39615	0.00542	0.09963	0.09964
12	0.10886	0.39193	0.39191	0.12135	0.46038	0.46063
13	-0.02961	0.20262	0.20262	0.09199	0.39863	0.39882
14	-0.12832	0.41065	0.41063	-0.03792	0.25517	0.25523

for $F_s^{(10)}$ for the different order expansions has only a small effect when compared to the F_μ dependence. From the figure it can be seen that the difference between the two curves increases as F_μ is increased. In particular, at $F_\mu = 0.13$, for $O(F^2)$, $\widetilde{\mathcal{J}}_{10} = -0.04098$, whilst for $O(F^5)$, $\widetilde{\mathcal{J}}_{10} = -0.12086$.

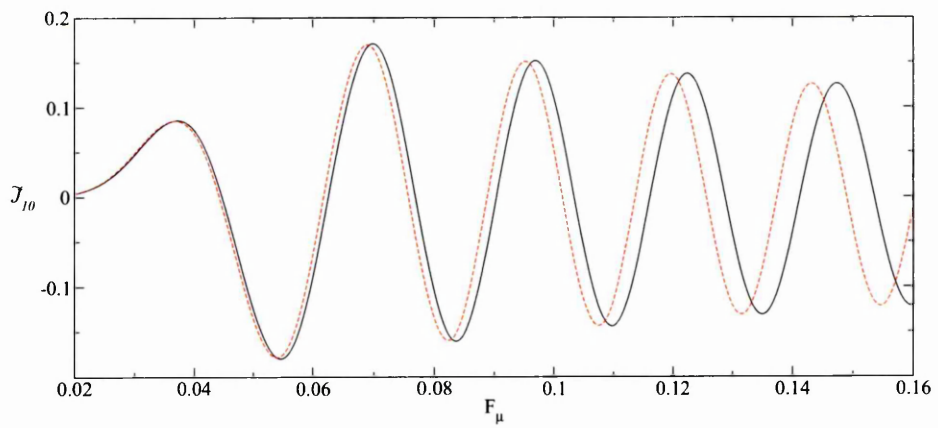

Figure 2.20 Comparison between $\widetilde{\mathcal{J}}_{10}(F_\mu)$ for $O(F^2)$ (solid) and $\widetilde{\mathcal{J}}_{10}(F_\mu)$ for $O(F^5)$ (dashed) for $F_s = 0.03615$ and $\Omega = 0.011414$.

The effect of the field switch on ionisation can be seen by examining table 2.3 for the 16-50-16 envelope. For each resonance, $\mathcal{I}_i$ is smaller for the gradually switched on field than for the instantaneously applied field, apart from for $j = 7$. The variation in $I_e(t)$ during switch-on means that in many cases orbits with smaller values of $I_e(0)$ can be sufficiently excited in the presence of the resonance island that they ionise. The difference between $\mathcal{I}_i$ values for the 16-50-16 and the 0-50-0 envelopes gives an indication of the amount of change in $I_e(t)$ occurring during the switch-on; this can be seen in particular for $j = 9, 11$ and 14.

The changes in $I_e(t)$ during switch-on do not always increase ionisation. For $j = 7$ the evolution of $I_e(t)$ is such that $\mathcal{I}_i$ for the slowly switched field is higher than for the instantaneously applied field. The reason for this can be seen in figures 2.21 and 2.22. The first figure shows the initial line, $I_e(0) = -0.24450$, and the evolved line $I_e(T_a)$ for this initial condition, calculated for a 16-50-16 field envelope at $F_s = 0.02537$, chosen to be close to the F_s value at which ionisation starts. The separatrix curves form the boundary of the resonance island at $t = T_a$ and are calculated from the Resonance Hamiltonian, equation (2.34), page 44. In addition, two extra phase curves are shown for the Averaged Hamiltonian, evaluated for the 0-50-0 envelope with different $\psi_e(0)$. Curve (A) lies sufficiently close to the island to be captured and follow a librational orbit before ionising; Curve (B) falls outside the island and follows a rotational orbit that does not ionise. For clarity, only segments of the whole phase curves are shown. The angle coordinates for the $I_e(T_a)$ curve are translated using the transformation (2.33) on page 44, modified to account for the switch-on period,

$$\phi_e = \psi_e - \frac{\nu_j t}{2} + j\frac{\pi}{2} - \frac{3}{2}G_A, \tag{2.44}$$

where $G_A = g(T_a) - \overline{g}T_a$ and $g(t)$ and $\overline{g}$ are given by equations (2.19) and (2.20) on page 37. This transformation is valid for times after the switch-on when the field envelope is at its maximum amplitude, $\lambda(t) = 1$. The curve $I_e(T_a)$ is significantly deformed during the switch-on with respect to the initial phase curve, $I_e(0)$, but in contrast to the instantaneously applied field, this phase curve lies wholly outside the resonance island; hence no ionisation occurs for the 16-50-16 field with $I_e(0) = -0.24450$. Figure 2.22 shows $I_e(T_a)$ generated for $I_e(0) = -0.20491$, chosen to lie just above $\mathcal{I}_i$ for the 16-50-16 envelope. Ionisation occurs for

orbits lying within the small segment of $I_e(T_a)$ lying inside the resonance island, marked on the figure with a triangle.

The behaviour observed for the $j = 7$ resonance shows that although the field switch can have significant effects on the evolution of $I_e(t)$, the effects on the observed ionisation can be subtle. Switch effects are explored further in §6.4, page 191, where they are shown to have a significant effect on ionisation.

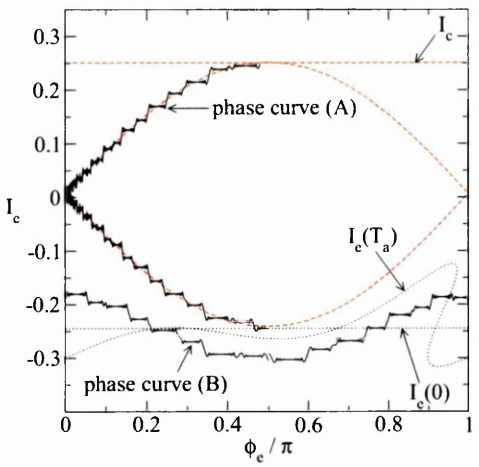

Figure 2.21 Phase curves near the $j = 7$ resonance for $F_\mu = 0.13$, $\Omega_0 = 0.011414$, $F_s = 0.02537$ and $I_m = 0.2$ are shown with solid lines. The separatrix and the ionisation critical value, I_c, are shown by dashed lines. Dotted lines show the initial action, $I_e(0) = -0.24450$, and the evolved action, $I_e(T_a)$. Phase curves (A) and (B) are examples of ionising and non-ionising orbits calculated for $\overline{K}_m$ and a suddenly applied field (envelope 0-50-0).

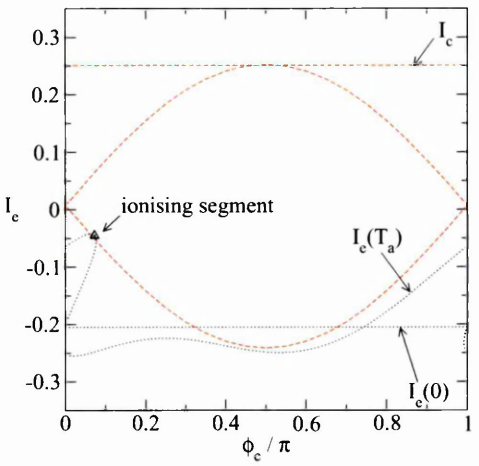

Figure 2.22 Dynamical parameters as for figure 2.21, but with $I_e(0) = -0.20491$ and $I_e(T_a)$ calculated for this initial value. The triangle lying on the $I_e(T_a)$ line marks the only segment that ionises.

Comparison with Exact Hamiltonian Results

Figures 2.23–2.26 show approximate contour plots for $P_i(F_s, I_e(0))$ at a number of resonances for the exact classical dynamics with $F_\mu = 0.13$, $\Omega_0 = 0.011414$, $I_m = 0.2$ and a 16-50-16 field envelope. The figures are calculated from 225 orbits at each $(F_s, I_e(0))$ point, with 400 orbits for the $j = 11$ plot. Contours are plotted at $P_i = 0.1, 0.2, \ldots, 1.0$ for figures 2.23–2.26,

with additional contours at $P_i = 0.01$ and $P_i = 0.02$ in figures 2.24–2.26. The statistical error introduced are significant for this sample size, causing the small fluctuations observed in the contours, which would otherwise be smooth. These resonances are very narrow, with widths of order $\Delta F_s = 10^{-4}$ for large j; hence we have magnified the scale and shifted the origin to $F_s = F_s^{(j)}$.

Comparison contour plots for the Averaged Hamiltonian, $\overline{K}_m$, are shown in figures 2.27–2.30. These are calculated using 250 orbits for each $(F_s, I_e(0))$ point. The contours are plotted at $P_i = 0.1, 0.2, \ldots, 1.0$ in each case.

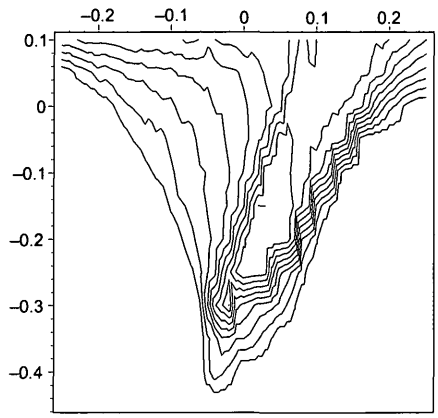

Figure 2.23 Contour plots, $P_i(x, I_e(0))$, near the $j = 8$ resonance for the exact classical dynamics with $\Omega_0 = 0.011414$, $F_\mu = 0.13$, $I_m = 0.2$ and field envelope, 16-50-16; $x = 1000(F_s - 0.02845)$. The horizontal axis is x and the vertical axis is $I_e(0)$.

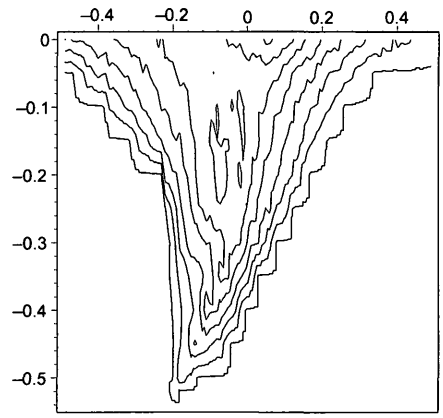

Figure 2.24 Contour plots, $P_i(x, I_e(0))$, near the $j = 9$ resonance for the exact classical dynamics with $\Omega_0 = 0.011414$, $F_\mu = 0.13$, $I_m = 0.2$ and field envelope, 16-50-16; $x = 1000(F_s - 0.031935)$.

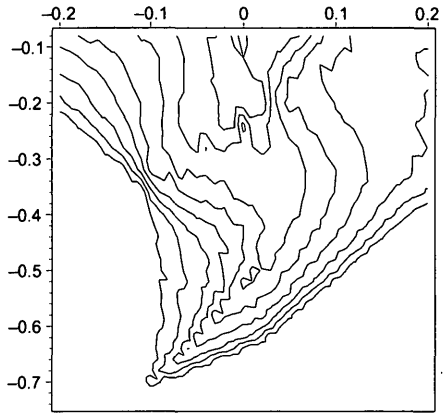

Figure 2.25 Contour plots, $P_i(x, I_e(0))$, near the $j = 10$ resonance for the exact classical dynamics with $\Omega_0 = 0.011414$, $F_\mu = 0.13$, $I_m = 0.2$ and field envelope, 16-50-16; $x = 1000(F_s - 0.03540)$.

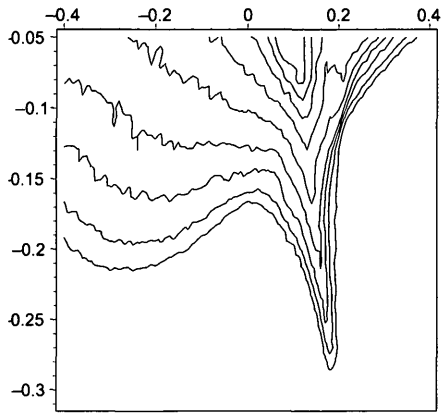

Figure 2.26 Contour plots, $P_i(x, I_e(0))$, near the $j = 11$ resonance for the exact classical dynamics with $\Omega_0 = 0.011414$, $F_\mu = 0.13$, $I_m = 0.2$ and field envelope, 16-50-16; $x = 1000(F_s - 0.03870)$.

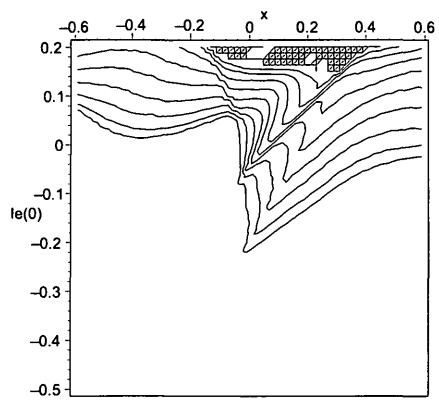

Figure 2.27 Contour plots, $P_i(x, I_e(0))$, near the $j = 8$ resonance for the Averaged Hamiltonian, $\overline{K}_m$, with $\Omega_0 = 0.011414$, $F_\mu = 0.13$, $I_m = 0.2$ and field envelope, 16-50-16; $x = 1000(F_s - 0.02896)$.

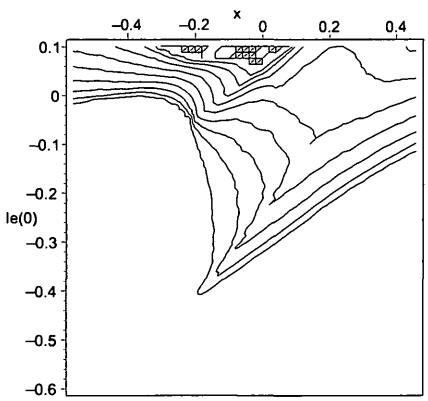

Figure 2.28 Contour plots, $P_i(x, I_e(0))$, near the $j = 9$ resonance for the Averaged Hamiltonian, $\overline{K}_m$, with $\Omega_0 = 0.011414$, $F_\mu = 0.13$, $I_m = 0.2$ and field envelope, 16-50-16; $x = 1000(F_s - 0.03256)$.

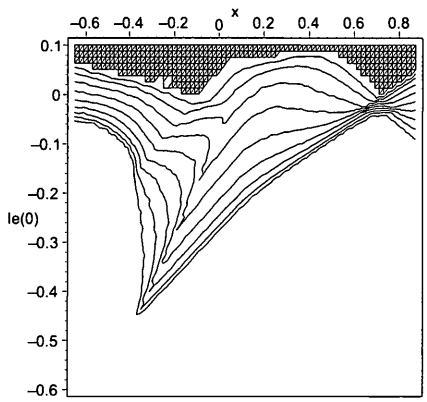

Figure 2.29 Contour plots, $P_i(x, I_e(0))$, near the $j = 10$ resonance for the Averaged Hamiltonian, $\overline{K}_m$, with $\Omega_0 = 0.011414$, $F_\mu = 0.13$, $I_m = 0.2$ and field envelope, 16-50-16; $x = 1000(F_s - 0.03615)$.

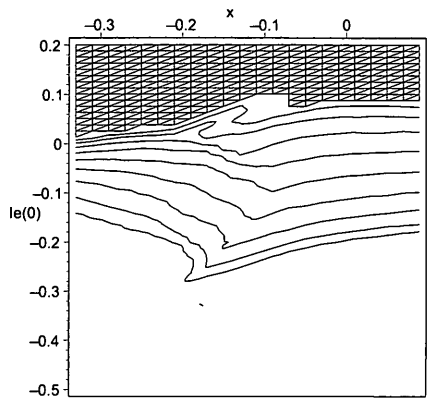

Figure 2.30 Contour plots, $P_i(x, I_e(0))$, near the $j = 11$ resonance for the Averaged Hamiltonian, $\overline{K}_m$, with $\Omega_0 = 0.011414$, $F_\mu = 0.13$, $I_m = 0.2$ and field envelope, 16-50-16; $x = 1000(F_s - 0.03973)$.

Whilst the details are different for each resonance, a number of general characteristics are observed in both the exact classical dynamics and the approximation that apply to all of the resonances except the $j = 10$ exact resonance:

1. The value of $I_e(0)$ at which ionisation starts is sensitive to j.

2. From the minimum $I_e(0)$ value at which ionisation starts, the region for which $P_i \neq 0$ forms a peninsula with its left side bounded by an approximately constant static field value, $F_s = F_s^{(start)}$, although in the figures this feature is less clear, because the minimum contour shown is at $P_i = 0.1$. The F_s range for which $P_i \neq 0$ increases as $I_e(0)$ is increased.

3. Above a certain value of $I_e(0)$, there is also ionisation for $F_s < F_s^{(start)}$. The difference between this and the minimum $I_e(0)$ value at which ionisation starts varies significantly between resonances — this is due to the difference in resonance island widths.

Taking figure 2.27 for $j = 8$ as an example, the onset of ionisation occurs at $F_s \approx 0.02893$ for $-0.25 < I_e(0) < 0.0$. For $I_e(0) > 0$ ionisation occurs for all F_s values shown. In the

following section we derive an analytic expression for the start of ionisation, $F_s = F_s^{(start)}$. From equation (2.49) (page 80), for this resonance, $F_s^{(start)} = 0.02893$.

This behaviour can be understood by considering the effect of the resonance island on the phase curves. When F_s is increased the maximum I_e value on the upper separatrix boundary of the resonance island also increases. Upon reaching the critical ionisation value, I_c, ionisation becomes possible for librational orbits trapped in the resonance island. This can be seen in figure 2.21 on page 71: a phase curve starting near the bottom of the resonance island follows a librational curve before ionising close to the top of the separatrix.

For the $j = 11$ resonance for the exact Hamiltonian shown in figure 2.26 the behaviour seems to be the mirror of that seen for other resonances for the start of ionisation: for $-0.28 < I_e(0) < -0.13$, ionisation stops at approximately the same F_s value. The reasons for this are not understood.

The resonance island width, w_R, is the main factor determining the range in $I_e(0)$ for which orbits can be trapped in the resonance island, although as previously discussed changes in $I_e(t)$ during the field switch-on also have an effect. Comparison between the Averaged Hamiltonian contour plots and w_R from table 2.4 on page 69 shows a broad correlation between island size and the length of the straight line segment, $F_s \approx F_s^{(start)}$, in the contour plots. For the j values shown, the smallest 'peninsula' for the Average Hamiltonian occurs for $j = 11$. From table 2.4 this also has the smallest island width.

For sufficiently large $I_e(0)$, rotational phase curves lying above the separatrix can also ionise. Ionisation then can become possible over a broader range of F_s values; as an example, for $j = 8$ shown in figure 2.27, this occurs for $I_e(0) \gtrsim 0$.

The contributions to ionisation from librational and rotational orbits are shown in figures 2.31 and 2.32 for the $j = 9$ resonance, chosen for comparison with figure 2.28. The probabilities are calculated by integrating orbits for 50 equally spaced initial conditions for $\psi_e(0)$ in the interval $(0, \pi)$ at each $(F_s, I_e(0))$ point. Ionising orbits are classified as librational or rotational if the point $I_e(T_a, \psi_e(0))$ lies inside or outside the resonance island calculated from the Resonance Hamiltonian. This test is approximate only as trajectories of the Averaged and exact Hamiltonians execute small oscillations around an underlying rotational or librational curve; so points lying near the separatrix could be either librational or rotational.

Contours are drawn at $P_i = 0.1, 0.2, \ldots, 1.0$; this excludes some small ionisation contributions incorrectly classified as rotational in librational-only ionisation regions. Their incorrect classification was confirmed by examining individual trajectories which were confirmed to follow librational orbits within the resonance island. The figures confirm the earlier assertions: as $I_e(0)$ is increased ionisation initially occurs from librational orbits only, with the smallest F_s value for the onset of ionisation approximately constant; rotational ionisation starts at larger values of $I_e(0)$ and over a broader range of F_s values.

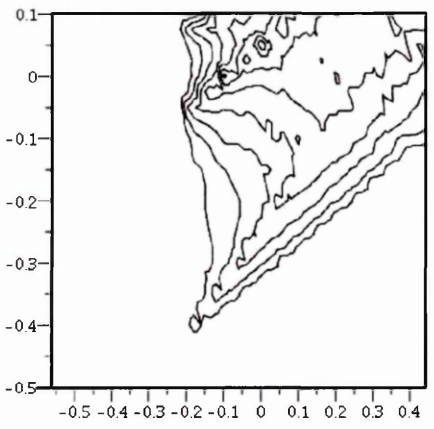

Figure 2.31 Contour plots, $P_i(x, I_e(0))$, resulting from librational orbits near the $j = 9$ resonance for the Averaged Hamiltonian, $\overline{K}_m$, with $\Omega_0 = 0.011414$, $F_\mu = 0.13$, $I_m = 0.2$ and field envelope, 16-50-16; $x = 1000(F_s - 0.03256)$.

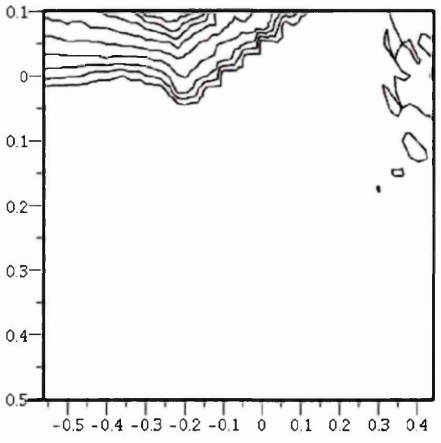

Figure 2.32 Contour plots, $P_i(x, I_e(0))$, resulting from rotational orbits near the $j = 9$ resonance for the Averaged Hamiltonian, $\overline{K}_m$, with $\Omega_0 = 0.011414$, $F_\mu = 0.13$, $I_m = 0.2$ and field envelope, 16-50-16; $x = 1000(F_s - 0.03256)$.

The dynamical process we have outlined — of resonance islands causing significant changes in $I_e(t)$ such that ionisation can occur — is assumed to also occur in the case of the exact Hamiltonian. However, whilst the general characteristics are seen in both the exact classical dynamics and the approximate mechanics, the results do not exactly match at each resonance. A cause of this may be the termination to $O(F^5)$ of the series for $\widetilde{g}(t)$, equation (2.21), page 37. Particularly for low frequencies the island width is sensitive to the number of terms, as can be seen by comparing $O(F^2)$ and $O(F^5)$ widths in table 2.3 and the results outlined earlier in this section.

Conclusions

We have shown that ionisation can be significantly affected by the presence of resonance islands, the width of which has an important effect on observed behaviour: much of the observed behaviour can be understood from the behaviour of phase curves for the approximate Resonance Hamiltonian, $\overline{K}_R$. The key points are as follows:

1. The resonance island width, w_R, strongly affects the onset of ionisation. In the case of an instantaneously applied field, the onset of ionisation for librational orbits is independent of $I_e(0)$ and this causes the characteristic straight edge, $F_s = F_s^{(start)}$, seen in each of the contour plots (except for the $j = 10$ exact classical dynamics). In the following section an estimate for $F_s^{(start)}$ is derived.

2. Depending on $I_e(0)$, w_R and I_c, both librational and rotational orbits can contribute to ionisation. As $I_e(0)$ increases from $-(I_n - I_m)$ the first curves to ionise are those inside the resonance island.

3. The island size, w_R, depends on the coupling term in the Resonance Hamiltonian, $\overline{K}_R$. In particular, the term $\widetilde{\mathcal{J}}_j$ depends on F_μ/Ω_0 and becomes increasingly sensitive to the number of terms in the expansion for $\widetilde{g}(t)$ as $\Omega \to 0$. This might be the cause of the observed differences between the exact and approximate mechanics in the size of ionisation peaks and the onset of ionisation, $I_e(0) = I_c$.

4. Field envelope effects are important and can have subtle effects on observed ionisation behaviour. A slow switch-on of the field causes a spread in I_e values at $t = T_a$, which may either increase or decrease the ionisation probability.

2.3.2 Location of Resonance Ionisation Probability Peaks

It can be seen from figures 2.18 (page 65) and 2.35 (page 82) that while the ionisation probability peak associated with each dynamical resonance lies close to the corresponding dynamical resonance value, $F_s^{(j)}$, the ionisation peak occurs at a slightly different value of F_s and in fact there is no ionisation at $F_s = F_s^{(j)}$ in these particular examples.

The conditions leading to the beginning and end of ionisation as F_s is varied can be understood by examining the location and width of the resonance island and the effect of the island on the orbits.

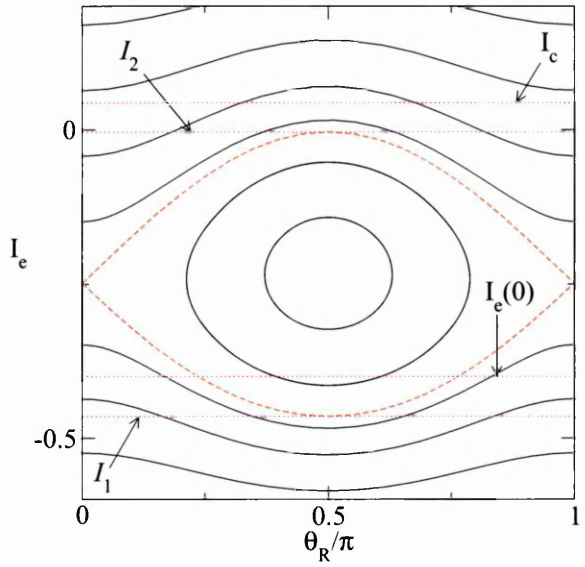

Figure 2.33 Phase curves near the $j = 10$ dynamical resonance for the $O(F^5)$ Averaged Hamiltonian with $F_\mu = 0.13$, $I_m = 0.2$, $F_s = 0.0357$ and $\Omega_0 = 0.011414$. The separatrix curves at $t = T_a$ are shown by dashed lines. Dotted lines show the initial value, $I_e(0)$, the ionisation critical value, I_c and the minimum and maximum separatrix curve I_e values, $\mathcal{I}_1$ and $\mathcal{I}_2$.

Figure 2.33 shows a number of phase curves for $\Omega = 0.011414$, $F_\mu = 0.13$ and $F_s = 0.0357$, lying near the dynamical resonance, $F_s^{(10)} = 0.03615$. The separatrix is shown by dashed lines. Dotted lines are used to show a number of important I_e values: the critical value for ionisation, I_c; the initial action, $I_e(0)$; and the minimum and maximum separatrix values, $\mathcal{I}_1$ and $\mathcal{I}_2$. For the selected dynamical parameters no ionisation is observed for either a 16-50-16 or a 0-50-0 field envelope. The greatest change in $I_e(t)$ occurs for librational orbits lying close to the separatrix and hence these are the first orbits to ionise[1] when F_s is increased to values

[1]This assumes that only librational orbits contribute to the observed ionisation. If the resonance island is sufficiently large, rotational orbits can also contribute to ionisation. The effect of rotational orbits on ionisation is explored further in §5.

such that

$$\mathcal{I}_2 \geq I_c. \tag{2.45}$$

For ionisation to take place it is necessary that some of the initial orbits have been captured in the resonance island. As F_s is increased further, the location of the resonance island changes until a point is reached when there are no orbits captured and consequently ionisation from librational orbits ceases. The F_s value at which this occurs depends upon the distribution of phase points, $\{(\theta_R(T_a), I_e(T_a))\}$, at the end of the field switch-on, $t = T_a$. However, for the case of an instantaneously applied field the condition is simpler:

$$\mathcal{I}_1 \geq I_e(0). \tag{2.46}$$

When this condition is satisfied, ionisation is expected to cease.

Approximate expressions can be obtained to find the F_s values for which conditions (2.45) and (2.46) are satisfied. We start by deriving an approximate expression for ν_j near $F_s = F_s^{(j)}$. The Taylor expansion of ν_j from equation (2.28) in terms of $\Delta F_s = F_s - F_s^{(j)}$ yields

$$\nu_j(\Delta F_s) = 3\overline{g}^{(1)}\Delta F_s + O(\Delta F_s^2), \tag{2.47}$$

where

$$\overline{g}^{(1)} = \left.\frac{\partial \overline{g}}{\partial F_s}\right|_{F_s = F_s^{(j)}}.$$

The condition (2.45) is met when $I_c = \mathcal{I}_2$, hence, from equation (2.38),

$$I_c = \frac{3\Delta F_s \overline{g}^{(1)}}{4}\left[\beta(\Delta F_s) + \frac{F_\mu \Omega_0 |\widetilde{\mathcal{J}}_j|}{4}\left(\frac{1+I_m^2}{1-I_m^2}\right)\right]^{-1} + \frac{w_R(\Delta F_s)}{2}, \tag{2.48}$$

where β and w_R are given in equations (2.36) and (2.39) on pages 46 and 48. We wish to evaluate β and w_R as functions of ΔF_s. The function $\beta(\Delta F_s)$ is slowly varying in the vicinity of the dynamical resonance, particularly for low frequencies, where the ionisation peak is narrow in F_s. Because $|\Delta F_s| \ll F_s$, we can assume that $\beta(\Delta F_s) \approx \beta_0 = \beta(0)$. To $O(F^5)$,

$$\beta_0 = \frac{3}{16}\left((F_s^{(j)})^2 + \frac{F_\mu^2}{2}\right) - \frac{3}{512}\left(301 - 189I_m^2\right)\left((F_s^{(j)})^4 + 3(F_s^{(j)})^2 F_\mu^2 + \frac{3F_\mu^4}{8}\right).$$

The island width is then given by

$$w_R(\Delta F_s) = 2\sqrt{\frac{-2\epsilon}{\beta_0 - \epsilon\gamma}\left(1 - I_m^2 - \frac{9\left(\overline{g}^{(1)}\right)^2 \Delta F_s^2 \gamma}{16(\beta_0^2 - \epsilon^2\gamma^2)}\right)}$$

where $\epsilon = -F_\mu \Omega_0 |\widetilde{\mathcal{J}}_j|/4$ and $\gamma = (1 + I_m^2)/(1 - I_m^2)$.

With these expressions for $\beta(\Delta F_s)$ and $w_R(\Delta F_s)$, expression (2.48) can be solved for ΔF_s and hence an approximation for the start of ionisation is given by

$$F_s^{(start)} = F_s^{(j)} + \frac{4(\beta_0 + \epsilon\gamma)}{3\overline{g}^{(1)}}\left(I_c - \sqrt{\frac{-2\epsilon}{\beta_0 + \epsilon\gamma}(1 - I_m^2 - I_c^2\gamma)}\right). \tag{2.49}$$

This expression is independent of $I_e(0)$, which is consistent with the observed onset of ionisation from librational orbits observed in the previous section.

Repeating the analysis for the end of ionisation condition, (2.46), using the expression for $\mathcal{I}_1$ from equation (2.38), the approximate end of ionisation is given by

$$F_s^{(end)} = F_s^{(j)} + \frac{4(\beta_0 + \epsilon\gamma)}{3\overline{g}^{(1)}}\left(I_e(0) + \sqrt{\frac{-2\epsilon}{\beta_0 + \epsilon\gamma}(1 - I_m^2 - I_e(0)^2\gamma)}\right). \tag{2.50}$$

This expression is expected to be most accurate when the field is instantaneously applied for the reason given above.

Ionisation only occurs if the resonance width is sufficiently large that both $\mathcal{I}_2 > I_c$ and $\mathcal{I}_1 < I_e(0)$ are simultaneously met. When the first condition is met, orbits within the resonance island can be excited sufficiently to allow ionisation. The second condition determines whether any of the initial orbits fall within the resonance island. That both conditions are satisfied can also be expressed as the condition that ionisation can occur if $F_s^{(start)} < F_s^{(end)}$.

Table 2.5 shows $F_s^{(start)}$ values calculated from equation (2.49) for $\Omega_0 = 0.011414$, $F_\mu = 0.13$ and $I_m = 0.2$ for each of the resonances $j = 2 \ldots 14$ (ionisation is not possible for $j = 1$). The results are compared with start values found by numerically solving the separatrix equations to find $\mathcal{I}_2 = I_c$ and the measured start of ionisation found by examining $P_i(F_s)$ for the $O(F^5)$ Averaged Hamiltonian, calculated for a grid of $\delta F_s = 2 \times 10^{-5}$ and a field envelope of 0-50-0. The onset of ionisation is calculated for $I_e(0)$ values chosen such that ionisation occurs,

Table 2.5: Calculated start of ionisation at each resonance for $O(F^5)$ Averaged Hamiltonian, $\Omega_0 = 0.011414$, $F_\mu = 0.13$ and $I_m = 0.2$. Comparison results are shown by numerical calculations of $\mathcal{I}_2 = I_c$ and measured results by calculating $P_i(F_s)$.

j	I_c	w_R	$F_s^{(j)}$	$F_s^{(start)}$ (equation (2.49))	$F_s^{(start)}$ (numerical)	$F_s^{(start)}$ (measured)
2	0.746	0.370	0.0073	0.0084	0.0083	0.0083
3	0.630	0.490	0.0109	0.0116	0.0116	0.0116
4	0.523	0.289	0.0145	0.0152	0.0152	0.0152
5	0.425	0.506	0.0181	0.0185	0.0185	0.0185
6	0.335	0.098	0.0217	0.0223	0.0223	0.0222
7	0.251	0.493	0.0254	0.0254	0.0254	0.0254
8	0.174	0.357	0.0290	0.0290	0.0290	0.0289
9	0.102	0.407	0.0326	0.0324	0.0324	0.0324
10	0.036	0.467	0.0362	0.0358	0.0358	0.0358
11	-0.026	0.100	0.0397	0.0396	0.0396	0.0395
12	-0.084	0.460	0.0433	0.0427	0.0427	0.0427
13	-0.138	0.399	0.0469	0.0462	0.0462	0.0462
14	-0.189	0.255	0.0504	0.0498	0.0498	0.0497

but only from librational orbits. The value of $I_e(0)$ does not affect the start of ionisation to the accuracy of the selected F_s grid size so long as this condition is met, which is consistent with the explanation that ionisation starts when $\mathcal{I}_2 \geq I_c$.

The calculated results show a good match in all cases with the numerically calculated and measured results.

In figures 2.34–2.37 calculated $F_s^{(start)}$, $F_s^{(end)}$, and $F_s^{(j)}$ values are compared with $P_i(F_s)$ calculated for an instantaneously applied field and gradually switched-on field at a number of resonances.

It can be seen that the field envelope has little effect on the start of ionisation and $F_s^{(start)}$ is generally a good approximation, although slightly less accurate for $j = 13$. The calculated $F_s^{(stop)}$ value is reasonably close to the instantaneous field result but is a less accurate approximation than $F_s^{(start)}$. It generally underestimates the end of ionisation for the 16-50-16 field, which is expected.

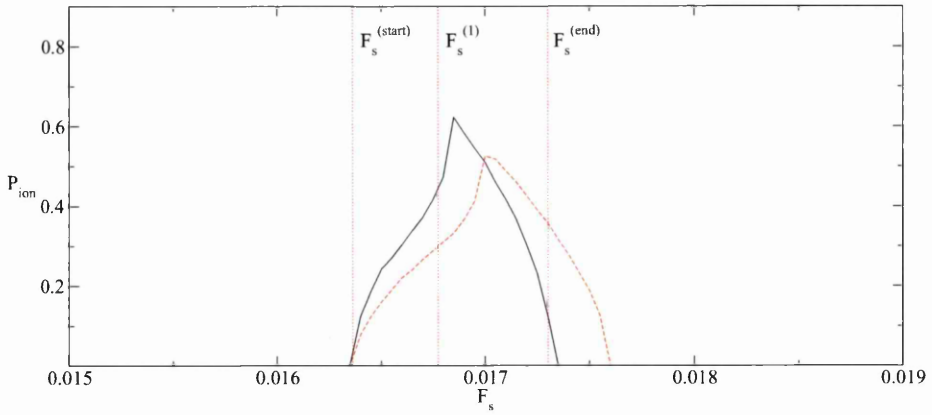

Figure 2.34 $P_i(F_s)$, for the $F_\mu = 0.13$, $I_m = 0.2$ and $\Omega_0 = 0.0528$ $O(F^5)$ Averaged Hamiltonian, field envelope 0-50-0 (solid line) and 16-50-16 (dashed line) in the region of the $j = 1$ resonance.

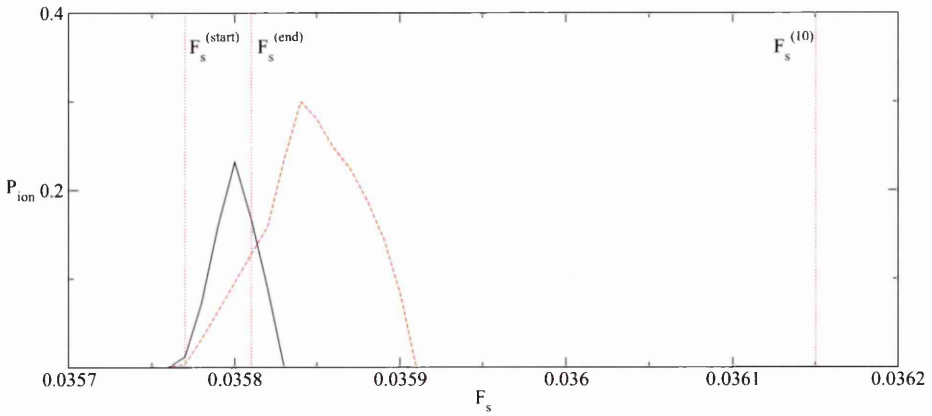

Figure 2.35 $P_i(F_s)$, for the $F_\mu = 0.13$, $I_m = 0.2$ and $\Omega_0 = 0.011414$ $O(F^5)$ Averaged Hamiltonian, field envelope 0-50-0 (solid line) and 16-50-16 (dashed line) in the region of the $j = 10$ resonance.

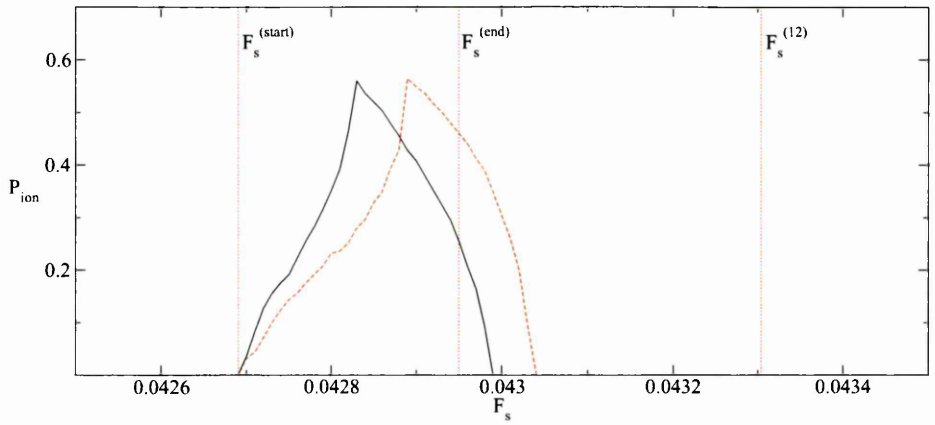

Figure 2.36 $P_i(F_s)$, for the $F_\mu = 0.13$, $I_m = 0.2$ and $\Omega_0 = 0.011414$ $O(F^5)$ Averaged Hamiltonian, field envelope 0-50-0 (solid line) and 16-50-16 (dashed line) in the region of the $j = 12$ resonance.

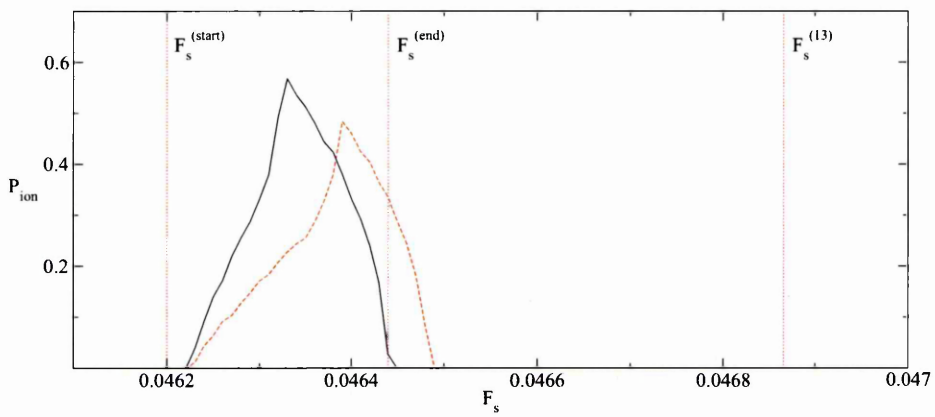

Figure 2.37 $P_i(F_s)$, for the $F_\mu = 0.13$, $I_m = 0.2$ and $\Omega_0 = 0.011414$ $O(F^5)$ Averaged Hamiltonian, field envelope 0-50-0 (solid line) and 16-50-16 (dashed line) in the region of the $j = 13$ resonance.

2.4 Off-resonance Analysis

2.4.1 Classical Perturbation Theory

Away from resonances changes in the action, $I_e(t)$, are small and a perturbation analysis can be used to determine higher order invariant actions of the motion. This analysis is motivated on two grounds: firstly the solutions obtained provide an independent check on the solutions

derived numerically using the equations of motion, (2.26); and secondly the solutions provide information on the size of fluctuations in $I_e(t)$ away from resonance.

The effects of the field switch-on are excluded in this section, as the method can only be applied to periodic perturbations. The results obtained are therefore only applicable for times during which the field envelope is constant, when $\lambda(t) = 1$.

The method used in this section is described, for example, in [45].

Under the canonical transformation $F_2(\psi_e, P) = (\psi_e - 3\overline{g}(t)/2)P$, the Averaged Hamiltonian (equation (2.24)) is transformed to be

$$\mathcal{K} = \mathcal{K}_0(I_e) + \epsilon\mathcal{K}_1(I_e, \phi_e, t)$$

where

$$\mathcal{K}_0(I_e) = \overline{E}_R(I_e) - \frac{3}{2}\overline{g}I_e, \quad \mathcal{K}_1 = A(I_e)B(I_e)\sin\Omega_0 t\sin(2\phi_e - 3\tilde{g}(t)) \tag{2.51}$$

and $\epsilon = -F_\mu\Omega_0/4$. The functions $\overline{g}$ and $\tilde{g}(t)$ are given by equations (2.20) and (2.21). This canonical transformation is chosen to ensure that $\mathcal{K}_1(I_e, \phi_e, t)$ is periodic in ϕ_e and t.

We wish to find a transformation $(\phi_e, I_e) \to (\chi, J)$, $\mathcal{K} \to \mathcal{K}'$ such that J is constant to $O(\epsilon)$. Defining the generating function

$$S(J, \phi_e) = J\phi_e + \epsilon S_1(J, \phi_e, t),$$

then

$$I_e = J + \epsilon\frac{\partial S_1}{\partial \phi_e}, \tag{2.52}$$

$$\chi = \phi_e + \epsilon\frac{\partial S_1}{\partial J} \tag{2.53}$$

$$\text{and} \quad \mathcal{K}'(J, \chi, t) = \mathcal{K}(I_e(J, \chi, t), \phi_e(J, \chi, t), t) + \frac{\partial S}{\partial t}.$$

Taylor expanding $\mathcal{K}'$,

$$\mathcal{K}' = \mathcal{K}_0(J) + \epsilon\left(\omega\frac{\partial S_1(J, \chi, t)}{\partial \chi} + \frac{\partial S_1(J, \chi, t)}{\partial t} + \mathcal{K}_1(J, \chi, t)\right) + O(\epsilon^2), \tag{2.54}$$

where

$$\omega = \omega(J) = \frac{\partial \mathcal{K}_0(J)}{\partial J} = \frac{\partial \overline{E}_R(J)}{\partial J} - \frac{3}{2}\overline{g} = \frac{\partial \overline{E}(J)}{\partial J} \tag{2.55}$$

and $\overline{E}(J)$ is given by equation 2.23. To $O(F^5)$,

$$\begin{aligned}
\omega(J) &= -\frac{3I_nF_s}{2} + \frac{3I_n^4J}{8}\left(F_s^2 + \frac{F_\mu^2}{2}\right) - \frac{3I_n^7(23I_n^2 - J^2 + 11I_m^2)}{32}F_s\left(F_s^2 + \frac{3F_\mu^2}{2}\right) \\
&- \frac{21I_n^{10}J(2(43I_n^2 - 27I_m^2) + 14J^2)}{512}\left(F_s^4 + \frac{3F_\mu^4}{8} + 3F_\mu^2F_s^2\right) \\
&- \left[\frac{3I_n^{13}(10563I_n^4 + 772I_m^2I_n^2 + 725I_m^4 + 3(98I_n^2 + 220I_m^2)J^2 - 105J^4)}{1024} \times \right. \\
&\left. \left(F_s^4 + \frac{15F_\mu^4}{8} + 5F_\mu^2F_s^2\right)\right].
\end{aligned}$$

The perturbing Hamiltonian term, $\mathcal{K}_1(J, \chi, t)$, is periodic in χ and t with zero mean value. If S_1 is chosen such that

$$\omega\frac{\partial S_1}{\partial \chi} + \frac{\partial S_1}{\partial t} = -\mathcal{K}_1 \tag{2.56}$$

then we see from equation (2.54) that to $O(\epsilon)$, $\mathcal{K}'$ is independent of χ. Hence J is an invariant of the motion to first order in ϵ.

The generating function S_1 can be found by expressing $\mathcal{K}_1$ and S_1 as Fourier series,

$$\begin{aligned}
\mathcal{K}(J, \phi_e, t) &= A(J)B(J)\sum_{l=-\infty}^{\infty}\sum_{m=-\infty}^{\infty}\mathcal{K}_{lm}e^{i(l\phi_e + m\Omega_0 t)}, \\
S_1(J, \phi_e, t) &= A(J)B(J)\sum_{l=-\infty}^{\infty}\sum_{m=-\infty}^{\infty}S_{lm}e^{i(l\phi_e + m\Omega_0 t)}
\end{aligned}$$

and solving equation (2.56) term by term, so that

$$S_{lm} = -\frac{i\mathcal{K}_{lm}}{l\omega + m\Omega_0}.$$

The resulting generating function is

$$S_1(J, \phi_e, t) = \frac{A(J)B(J)}{2}\sum_{k=-\infty}^{\infty}\left(\frac{a_k - a_{k+2}}{2\omega(J) + k\Omega_0}\right)\sin(2\phi_e + k\Omega_0 t) \tag{2.57}$$

where

$$a_k = \frac{1}{\pi}\int_0^\pi \cos\left((1-k)s - 3\tilde{g}\left(\frac{s}{\Omega_0}\right)\right) \mathrm{d}s.$$

The series is only convergent if $2\omega(J)+k\Omega_0 \neq 0$ for all k. Resonances occur when this equality is satisfied, which is the same as the condition given by equation (2.32) on page 43.

For the $O(F^2)$ Averaged Hamiltonian,

$$\tilde{g}(t) = \frac{F_\mu}{\Omega_0}\sin\Omega_0 t + O(F^2)$$

and the generating function is

$$S_1(J,\phi_e,t) = -A(J)B(J)\sum_{k=-\infty}^{\infty}\left(\frac{J'_{-k}(3F_\mu/\Omega_0)}{2\omega(J)+k\Omega_0}\right)\sin(2\phi_e + k\Omega_0 t).$$

Hamilton's equation for $\dot{\chi}(t)$ is trivially solved,

$$\chi(t) = \omega(J)t + \delta,$$

where δ is an arbitrary phase factor. Hence from equations (2.52), (2.53) and (2.57), to first order,

$$\begin{aligned} I_e(t) &= J - \frac{F_\mu\Omega_0}{4}A(J)B(J)\sum_{k=-\infty}^{\infty}\left(\frac{a_k - a_{k+2}}{2\omega(J)+k\Omega_0}\right)\cos(2\phi_e(t)+k\Omega_0 t), \qquad (2.58)\\ \chi(t) &= \phi_e(t) + \frac{F_\mu\Omega_0 J}{8}\left(\frac{A(J)}{B(J)}+\frac{B(J)}{A(J)}\right)\sum_{k=-\infty}^{\infty}\left(\frac{a_k - a_{k+2}}{2\omega(J)+k\Omega_0}\right)\sin(2\phi_e(t)+k\Omega_0 t). \end{aligned}$$

Assuming $|\epsilon\partial S_1/\partial J| \ll 1$ the second expression can be inverted approximately to give

$$\phi_e(t) \approx \omega t + \delta - \frac{F_\mu\Omega_0 J}{8}\left(\frac{A(J)}{B(J)}+\frac{B(J)}{A(J)}\right)\sum_{k=-\infty}^{\infty}\left(\frac{a_k - a_{k+2}}{2\omega+k\Omega_0}\right)\sin((2\omega+k\Omega_0)t+2\delta).$$

From expression (2.58) it can be seen that $I_e(t) - I_e(0)$ is $O(F_\mu\Omega_0)$, confirming that for low frequency fields away from resonance, the fluctuations in $I_e(t)$ are small.

2.4.2 Off-resonance Results

Diagrams 2.38–2.40 compare the first order perturbation solutions for $I_e(t)$ against numerical solutions of the classical equations of motion (see equations (2.26)), for $\Omega_0 = 0.0528$, $F_s = 0.026$, $I_m = 0.2$, $I_e(0) = -0.4$ and $\psi_e(0) = 0$. The equations were integrated over 82 field cycles with $\lambda(t) = 1$ throughout for various values of F_μ including terms up to $O(F^5)$ in the Hamiltonian. The dynamical parameters are chosen for comparison with figure 2.9 with F_s chosen to lie between the $j = 1$ and $j = 2$ resonances. The diagrams show the calculated $I_e(t)$ values in the ranges $0 \leq t/T_e \leq 0.3$ and $0.7 \leq t/T_e \leq 1$, where T_e is the overall integration time.

The graphs show a good correspondence between the numerical and perturbation theory results. The difference between the numerically determined $I_e(t)$ and the perturbation theory $I_e(t)$ for $F_\mu = 0.0325$ is almost imperceptible on the figure. Over the full integration time the maximum absolute difference between the perturbation and numerically integrated values for $I_e(t)$ is approximately 0.6% of the maximum variation in numerically calculated $I_e(t)$. As F_μ is increased the difference grows, although there is still a close match, even for $F_\mu = 0.13$. Calculations for the $O(F^2)$ Averaged Hamiltonian also showed a good match.

The perturbation theory results also provide some validation of the numerical results presented elsewhere in this thesis for the Averaged Hamiltonian (equation (2.24), page 38), as they are derived independently of the equations of motion (2.26), page 40, and their computational evaluation.

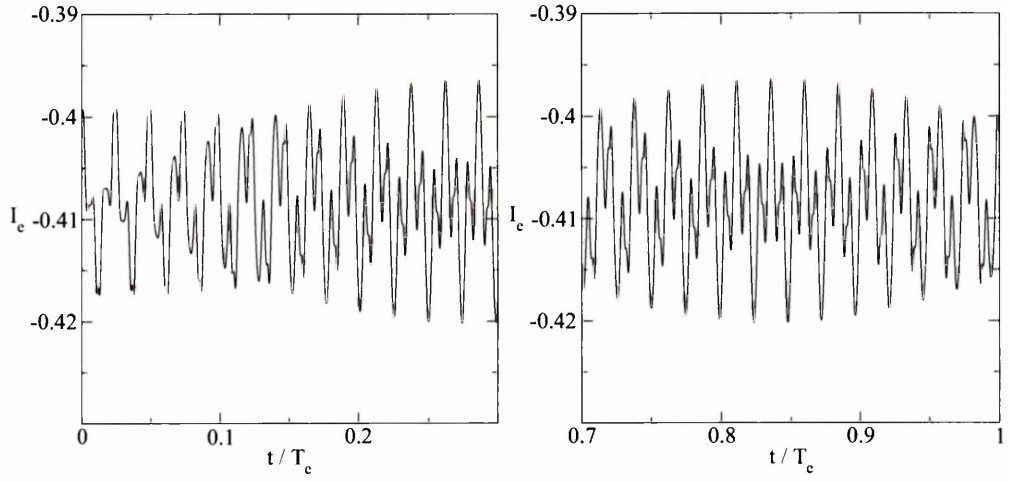

Figure 2.38 $I_e(t)$ determined from perturbation theory (solid line) and numerical integration (dashed line) for $F_\mu = 0.0325$, $\Omega_0 = 0.0528$, $I_m = 0.2$, $F_s = 0.026$, envelope 0-82-0, $I_e(0) = -0.4$ and $\psi_e(0) = 0$ for the $O(F^5)$ Averaged Hamiltonian. The time is scaled by $T_e = 82 \times 2\pi/\Omega_0$.

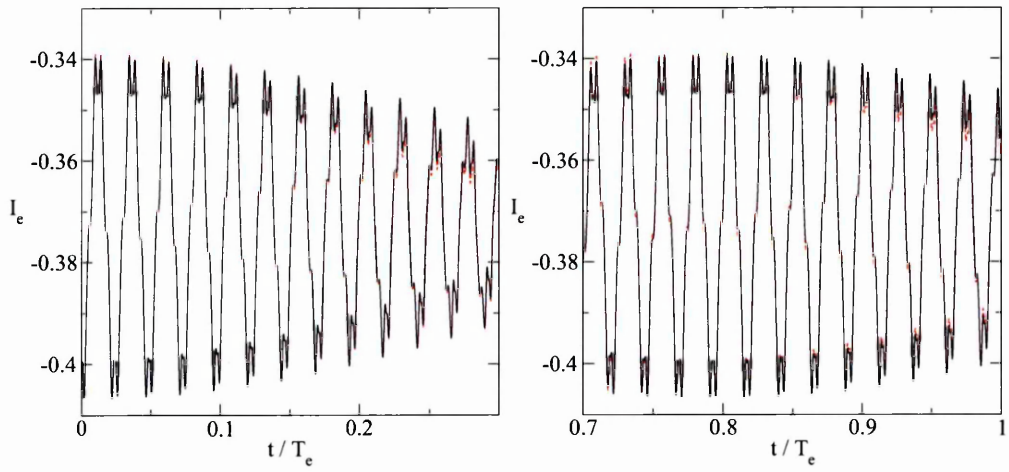

Figure 2.39 $I_e(t)$ determined from perturbation theory (solid line) and numerical integration (dashed line) for $F_\mu = 0.065$, $\Omega_0 = 0.0528$, $I_m = 0.2$, $F_s = 0.026$, envelope 0-82-0, $I_e(0) = -0.4$ and $\psi_e(0) = 0$ for the $O(F^5)$ Averaged Hamiltonian. The time is scaled by $T_e = 82 \times 2\pi/\Omega_0$.

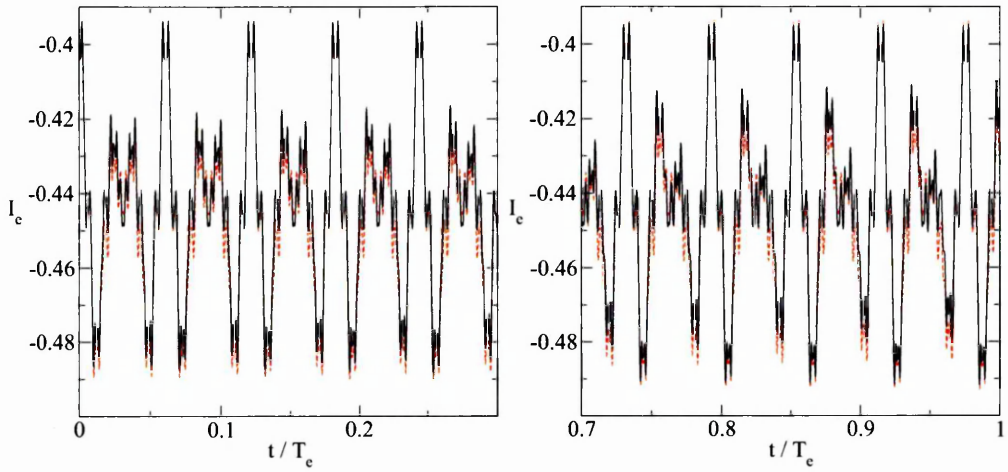

Figure 2.40 $I_e(t)$ determined from perturbation theory (solid line) and numerical integration (dashed line) for $F_\mu = 0.13$, $\Omega_0 = 0.0528$, $I_m = 0.2$, $F_s = 0.026$, envelope 0-82-0, $I_e(0) = -0.4$ and $\psi_e(0) = 0$ for the $O(F^5)$ Averaged Hamiltonian. The time is scaled by $T_e = 82 \times 2\pi/\Omega_0$.

Chapter 3

Quantum Mechanics

3.1 Quantum Theory

3.1.1 Quantum Equations of Motion

The Averaged Hamiltonian is quantised by rewriting equation (2.24) (page 38), replacing I_e by the operator $\hat{p} = -i\hbar\partial/\partial\psi_e$, so that

$$\hat{H} = \overline{E}_R(\hat{p}, F_s, F_\mu, t) + \alpha(t)A(\hat{p})B(\hat{p})\sin(2\psi_e - 3I_n g(t))$$

The function $\alpha(t)$ is given by equation (2.27) on page 40. The presence of non-commuting factors of $\hat{p}$ and ψ_e mean that in its current form, the Hamiltonian is not Hermitian. This can be addressed in the normal way by taking a symmetric combination of the non-commuting terms, giving

$$\begin{aligned}\hat{H} &= \overline{E}_R(\hat{p}, F_s, F_\mu, t) \\ &+ \frac{\alpha}{2}\Big[A(\hat{p})B(\hat{p})\sin(2\psi_e - 3I_n g(t)) \\ &+ \sin(2\psi_e - 3I_n g(t))\,A(\hat{p})B(\hat{p})\Big]. \end{aligned} \tag{3.1}$$

The normalised eigenfunctions of the unperturbed Hamiltonian obtained by setting $\alpha = 0$

in equation 3.1 are

$$\langle \psi_e | k \rangle = \frac{e^{ik\psi_e}}{\sqrt{2\pi}}.$$

The wave function is 2π-periodic in ψ so k is an integer. The classical action is constrained by the requirement that $|I_e| \leq I_n - I_m$. In the quantum case the allowed states are constrained such that,

$$|k| \leq N, \quad N = n - m. \tag{3.2}$$

The quantal equations of motion can be derived by expanding the wave function in terms of the momentum eigenfunctions. Rewriting equation (3.1) as $\hat{H} = \hat{H}_0 + \hat{H}_1$ where $\hat{H}_0$ is the unperturbed energy term, the eigenfunctions of $\hat{H}_0$ are the eigenfunctions of $\hat{p}$ and from $\hat{H}_0|k\rangle = E_k|k\rangle$ the eigenvalues are

$$E_k = \overline{E}_R(\hbar k, F_s, F_\mu, t),$$

where the values of k are subject to the constraint equation (3.2).

Writing the equation of motion for the full Hamiltonian as

$$\hat{H}|t\rangle = i\hbar \frac{\partial}{\partial t}|t\rangle \tag{3.3}$$

the wave function, $|t\rangle$, can be expanded in terms of the momentum eigenfunctions

$$|t\rangle = \sum_{k=-N}^{N} a_k(t)|k\rangle.$$

Multiplying equation (3.3) by $\langle l|$ gives

$$i\hbar \dot{a}_l = E_l a_l + \sum_{k=-N}^{N} a_k \langle l|\hat{H}_1|k\rangle. \tag{3.4}$$

Writing $f(\psi_e) = \sin(2\psi_e - 3I_n g(t))$, the off-diagonal matrix elements are

$$\langle l|\hat{H}_1|k\rangle = \frac{\alpha}{2}\Big(A(l\hbar)B(l\hbar) + A(k\hbar)B(k\hbar)\Big)\langle l|f(\psi_e)|k\rangle \tag{3.5}$$

$$
\begin{aligned}
&= \frac{\alpha}{2}\Big(A(l\hbar)B(l\hbar) + A(k\hbar)B(k\hbar)\Big) \iint \mathrm{d}\theta\,\mathrm{d}\phi \langle l|\theta\rangle\langle\theta|f(\theta)|\phi\rangle\langle\phi|k\rangle \\
&= \frac{\alpha}{2}\Big(A(l\hbar)B(l\hbar) + A(k\hbar)B(k\hbar)\Big)\frac{1}{2\pi}\int_{-\pi}^{\pi} \mathrm{d}\theta\, e^{i(k-l)\theta} f(\theta) \\
&= \frac{\alpha}{4i}\Big(A(l\hbar)B(l\hbar) + A(k\hbar)B(k\hbar)\Big) \times \begin{cases} \exp\left(-3iI_n g(t)\right), & k = l-2, \\ -\exp\left(3iI_n g(t)\right), & k = l+2, \\ 0, & \text{otherwise.} \end{cases}
\end{aligned}
$$

The perturbation matrix, $\hat{H}_1$ is banded, with non-zero coupling between neighbouring states only[1].

The equations of motion (3.5) must be modified to satisfy constraint (3.2) on page 92. This is done by removing the off-diagonal matrix elements corresponding to the transitions $k = N \to k = N+2$ and $k = -N \to k = -N-2$. The final equations of motion are

$$
\begin{aligned}
i\hbar\dot{a}_N &= a_N \overline{E}_R(N\hbar, F_s, F_\mu, t) \\
&\quad + a_{N-2}\frac{\alpha}{4i}\Big[A(N)B(N) + A(N-2)B(N-2)\Big] \times \\
&\quad \exp\left(-3iI_n g(t)\right),
\end{aligned} \tag{3.6}
$$

$$
\begin{aligned}
i\hbar\dot{a}_{-N} &= a_{-N} \overline{E}_R(-N\hbar, F_s, F_\mu, t) \\
&\quad - a_{-N+2}\frac{\alpha}{4i}\Big[A(N)B(N) + A(N+2)B(N+2)\Big] \times \\
&\quad \exp\left(3iI_n g(t)\right)
\end{aligned} \tag{3.7}
$$

and

$$
\begin{aligned}
i\hbar\dot{a}_k &= a_k \overline{E}_R(k\hbar, F_s, F_\mu, t) \\
&+ \frac{\alpha}{4i}\Big\{a_{k-2}[A(k)B(k) + A(k-2)B(k-2)]\exp\left(-3iI_n g(t)\right) \\
&- a_{k+2}[A(k)B(k) + A(k+2)B(k+2)]\exp\left(3iI_n g(t)\right)\Big\},
\end{aligned} \tag{3.8}
$$

for $-N < k < N$.

[1]The electric quantum number k is defined as $n_2 - n_1$. Because n_1 and n_2 are constrained by $n_1 + n_2 + |m| + 1 = n$ a change of ± 1 in n_2 corresponds to a change of ± 2 in k.

The equivalent scaled equations of motion are

$$\begin{aligned}\frac{i}{n}\frac{\mathrm{d}a_N}{\mathrm{d}t_0} &= a_N\overline{E}_R\left(\left(\frac{N}{n}\right),F_{s0},F_{\mu 0},t_0\right)\\ &\quad +a_{N-2}\frac{\alpha(t_0)}{4i}\Big[A_0(N)B_0(N)+A_0(N-2)B_0(N-2)\Big]\times\\ &\quad \exp\left(-i3g(t_0)\right),\end{aligned}\tag{3.9}$$

$$\begin{aligned}\frac{i}{n}\frac{\mathrm{d}a_{-N}}{\mathrm{d}t_0} &= a_{-N}\overline{E}_R\left(\left(\frac{-N}{n}\right),F_{s0},F_{\mu 0},t_0\right)\\ &\quad -a_{-N+2}\frac{\alpha(t_0)}{4i}\Big[A_0(N)B_0(N)+A_0(N+2)B_0(N+2)\Big]\times\\ &\quad \exp\left(i3g(t_0)\right)\end{aligned}\tag{3.10}$$

and

$$\begin{aligned}\frac{i}{n}\frac{\mathrm{d}a_k}{\mathrm{d}t_0} &= a_k\overline{E}_R\left(\left(\frac{k}{n}\right),F_{s0},F_{\mu 0},t_0\right)\\ &+ \frac{\alpha(t_0)}{4i}\Big\{a_{k-2}\Big[A_0(k)B_0(k)+A_0(k-2)B_0(k-2)\Big]\exp\left(-i3g(t_0)\right)\\ &- a_{k+2}\Big[A_0(k)B_0(k)+A_0(k+2)B_0(k+2)\Big]\exp\left(i3g(t_0)\right)\Big\},\end{aligned}\tag{3.11}$$

for $-N < k < N$. Because $\hat{H}$ is Hermitian, $|\mathrm{a}(t)|^2$ is constant. As only bound states are included, ionisation must be added as an additional approximation; this is considered in §3.1.3, page 97.

For each of the scaled equations of motion I_n is set to one in $E_R((k/n),F_{s0},F_{\mu 0},t_0)$ and $\alpha(t_0)$. The functions $A_0(k)$ and $B_0(k)$ are defined by

$$A_0(k)=\sqrt{\left(1+\frac{m}{n}\right)^2-\left(\frac{k}{n}\right)^2}\quad\text{and}\quad B_0(k)=\sqrt{\left(1-\frac{m}{n}\right)^2-\left(\frac{k}{n}\right)^2}.$$

3.1.2 The Quantum Resonance Hamiltonian

The Resonance Hamiltonian, equation (2.34) (page 44), can be quantised to give the Hamiltonian

$$\hat{H}_R=\overline{E}_R(\hat{p},F_s,F_\mu)-\frac{\nu_j}{2}\hat{p}+\alpha_R A(\hat{p})B(\hat{p})\cos(2\psi_R)$$

where $[\psi_R, \hat{p}] = i\hbar$, $\alpha_R = -I_n^3 F_\mu \Omega \widetilde{\mathcal{J}}_j / 4\mu^2 e^6$ and ν_j is given by equation (2.28), page 42. The quantised equations of motion are derived in the same way as described in the previous section, to give

$$i\hbar\dot{a}_l = \left(\overline{E}_{Rl} - \frac{\nu_j}{2}\hbar l\right) a_l + \sum_{k=-N}^{N} a_k \langle l|\hat{H}_{R1}|k\rangle \tag{3.12}$$

where the symmetrised perturbing term is

$$\hat{H}_{R1} = \frac{\alpha_R}{2}\Big[A(\hat{p})B(\hat{p})\cos(2\psi_R) + \cos(2\psi_R)A(\hat{p})B(\hat{p})\Big].$$

The off-diagonal matrix elements are given by

$$\langle l|\hat{H}_{R1}|k\rangle = \frac{\alpha_R}{4i}\Big[A(l\hbar)B(l\hbar) + A(k\hbar)B(k\hbar)\Big] \times \begin{cases} 1, & k = l-2, \\ -1, & k = l+2, \\ 0, & \text{otherwise.} \end{cases}$$

We shall use the Resonance Hamiltonian to understand the behaviour of the quantum mechanical system in the vicinity of resonances, as will be seen later (see §3.3.2).

Equation (3.12) can be rewritten as $\dot{\mathbf{a}} = -i\mathbf{R}\mathbf{a}$ where the matrix elements are

$$\mathbf{R}_{lk} = \frac{1}{\hbar}\left[\delta_{lk}(\overline{E}_{Rl} - \frac{\nu_j}{2}\hbar l) + \langle l|\hat{H}_{R1}|k\rangle\right]. \tag{3.13}$$

If decay terms are excluded from $\overline{E}_{Rl}$ and for times other than switch-on and switch-off, the matrix $\mathbf{R}$ is Hermitian and time-independent. Denoting its eigenvalues and eigenfunctions by $\{\lambda_k\}$ and $\{\mathbf{b}_k\}$, the state vector is therefore given by

$$\mathbf{a}(t) = \sum_{k=-N}^{N} e^{-i\lambda_k t} c_k \mathbf{b}_k, \quad c_k = \mathbf{b}_k^\dagger \mathbf{a}(0). \tag{3.14}$$

The Resonance Hamiltonian approximation was obtained by excluding Fourier components of frequencies other than ν_j. If frequencies ν_k, for $k \neq j$, are retained, the resultant

Hamiltonian, $\mathbf{H}'_{\mathbf{R}}$, is no longer time-independent, but satisfies the periodic condition,

$$\mathbf{H}'_{\mathbf{R}}\left(t+\frac{2\pi}{\Omega_0}\right)=\mathbf{H}'_{\mathbf{R}}\left(t\right)$$

and can be analysed using Floquet theory. The eigenvalues, λ_k, obtained above correspond to the Floquet quasi-energies when the non-resonant frequencies are removed as will be shown.

The monodromy matrix $\mathbf{U}$ for $\mathbf{H}'_{\mathbf{R}}$ can be obtained by integrating the equation

$$\dot{\mathbf{\Phi}}(t)=-i\mathbf{H}'_{\mathbf{R}}(t)\mathbf{\Phi}(t) \tag{3.15}$$

over one period $2\pi/\Omega_0$ with the initial condition, $\mathbf{\Phi}(0)=\mathbf{I}$, so that $\mathbf{U}=\mathbf{\Phi}(2\pi/\Omega_0)$.

Writing the eigenvalues of $\mathbf{U}$ as $\exp(-i2\pi\rho_k/\Omega_0)$, ρ_k are the Floquet quasi-energies. Denoting the corresponding eigenvectors by $\mathbf{d}_k$, the vectors

$$\mathbf{v}_k(t)=\mathbf{\Phi}(t)\mathbf{d_k}$$

satisfy equation (3.15) and have the property,

$$\mathbf{v}_k\left(t+\frac{2\pi}{\Omega_0}\right)=e^{-i\frac{2\pi\rho_k}{\Omega_0}}\mathbf{v}_k\left(t\right).$$

When the non-resonant frequency components are removed from $\mathbf{H}'_{\mathbf{R}}$ it is time-independent and equation (3.15) can be integrated to give the formal solution,

$$\mathbf{\Phi}(t)=\mathbf{\Phi}(0)\exp(-i\mathbf{H}'_{\mathbf{R}}t).$$

The eigenvalues of $\mathbf{\Phi}(2\pi/\Omega_0)$ for the initial conditions $\mathbf{\Phi}(0)=I$ are the eigenvalues of

$$\exp\left(-i\frac{2\pi}{\Omega_0}\mathbf{H}'_{\mathbf{R}}\right).$$

Hence, if $\mathbf{H}'_{\mathbf{R}}=\mathbf{R}$, the quasi-energies ρ_k are the eigenvalues, λ_k, of $\mathbf{R}$.

3.1.3 Decay Terms for the Quantum Approximation

Because the quantum equations described in the preceding sections are derived from the action-angle classical Hamiltonians, all states are bound and $|\mathbf{a}(t)|^2$, satisfying equations (3.9–3.11) is constant. As for the classical approximation, ionisation must be introduced as a further approximation. In the quantum case this is done by the addition of a complex part to the eigen-energies. States corresponding to the classical case of $F > F_c$ are effectively above the potential barrier and would be expected to decay rapidly. For states below but close to the top of the barrier, ionisation is also expected by tunnelling. Two forms of the decay function are considered:

- Step decay function, for which a constant decay term is included for all states above the barrier, that is $F > F_c$. This excludes all ionisation due to tunnelling.
- Tunnelling decay function, where ionisation due to tunnelling from states below the classical barrier are included by fitting the decay function to ionisation rates obtained using semi-classical approximations for the case of a static field.

Step Decay Function

Ionisation is introduced into the equations of motion by the substitution,

$$\overline{E}_R(k\hbar, F, t) \rightarrow \varepsilon(k,t) = \overline{E}_R(k\hbar, F, t) - i\frac{\Gamma(k,t)}{2n} \tag{3.16}$$

where $\Gamma(k,t) \geq 0$. The decay term in equation (3.16) is scaled by the factor $1/2n$ so that a particular value of D causes the same amount of ionisation over one Kepler period irrespective of n, as we show below.

The step decay function takes the form

$$\Gamma_s(k,t) = \begin{cases} 0, & k < k_c(t), \\ D, & k \geq k_c(t), \end{cases} \tag{3.17}$$

where $k_c(t)$ is the critical value at which ionisation occurs in the classical system and D is a constant.

In the case of $F_\mu > F_s$, classically ionisation is possible along the ξ-axis, as can be seen by the substitution, $F \to -F$ in the potential expressions given in equation (2.9) on page 30: effectively interchanging the form of the potentials for $V_1(\xi)$ and $V_2(\eta)$. Quantally, this corresponds to ionisation along the n_1 axis, where n_1 is given by equation (2.12) on page 31, so that ionisation is also possible for

$$\Gamma_s(k,t) = \begin{cases} 0, & -k < k_c'(t), \\ D, & -k \geq k_c'(t), \end{cases}$$

where k_c' is the critical ionisation value in the classical case for the field $F_\mu - F_s$.

A suitable value for D is obtained by assuming that for a state expected to ionise the decay function should result in a halving of $|a_k|^2$ over one Kepler orbit (for which $t = 2\pi$ in scaled coordinates). Ignoring oscillatory terms in the phase and coupling terms between states, the scaled equations of motion are

$$\dot{a}_k = -\frac{1}{2}\Gamma(k,t)a_k,$$

with solutions

$$a_k(t) \propto \exp\left(-\frac{\Gamma t}{2}\right)$$

if $\Gamma(k,t)$ is treated as a constant. Hence over one Kepler period,

$$\exp(-2\pi D) = \frac{1}{2}, \quad \text{that is,} \quad D \approx 0.11.$$

The ionisation behaviour is unchanged for a wide range of D values, although some differences are observed in the magnitude of ionisation probabilities, particularly at resonances. For very large or very small values, the ionisation probability can be significantly reduced. The reasons for this are provided in appendix A.

Figure 3.1 shows the ionisation probability calculated for a number of different D values for varying F_s for the Hamiltonian (2.24) including terms up to $O(F^5)$. The system is prepared in an initial state $a_k = 1$ for $k = k_i$, and $a_k = 0$ for $k \neq k_i$.

The parameters chosen are: $n = 39$, $m = 10$, $k_i = -14$, $F_\mu = 0.14$, $\Omega_0 = 0.07311$, a field envelope of 16–50–16 and a grid size of $\Delta F_s = 0.0001$.

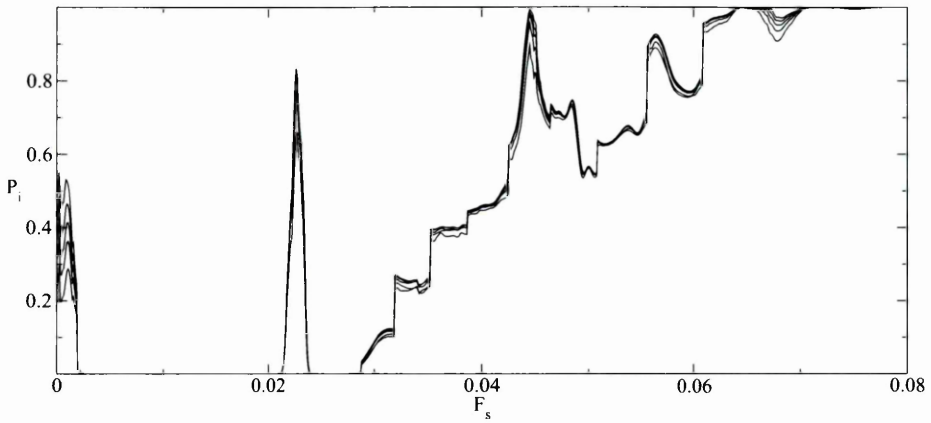

Figure 3.1 Ionisation probabilities $P_i(F_s)$ for $D = 0.055, 0.11, 0.22, 0.44$ and 0.88.

The largest differences in $P_i(F_s)$ occur for the ionisation near $F_s = 0$. Table 3.1 compares the difference ΔP_i between the ionisation probability for $D = 0.11$ and other values of D. Although there are significant differences in the height of ionisation peaks for low F_s, the underlying ionisation behaviour does not show any marked differences for these values of D. As a measure of the overall difference, the integrated area,

$$\int_0^{0.08} P_i(D, F_s)\,\mathrm{d}F_s,$$

was calculated for each D value. The difference between the integrated area for each D value when compared with that for $D = 0.11$ is less than 3% for each of the D values considered.

In figure 3.1, the ionisation probability is seen to apparently undertake step changes at a number of F_s values, for example, $F_s = 0.0318, 0.0351$ and 0.0386. These non-physical changes are a limitation of the step decay approximation. As F_s is increased, the classical critical value, k_c, above which ionisation occurs, changes continuously; however, for the quantum step decay function, the number of ionising states will change by integer amounts as k_c falls below each allowed state, k. The step changes observed in the ionisation probability correspond to each change in the number of ionising states.

Table 3.1: Comparison of maximum difference between ionisation probabilities, $P_i(D, F_s)$, for various step sizes, D, with $P_i(0.11, F_s)$. The difference, $\Delta P_i(D)$, is calculated as the maximum value of $|P_i(D, F_s) - P_i(0.11, F_s)|$ for $0 \leq F_s \leq 0.08$. The F_s value at this maximum is denoted by F_s^M. The dynamical parameters are: $n = 39$, $m = 10$, $k_i = -14$, $F_\mu = 0.14$, $\Omega_0 = 0.07311$ and a field envelope of 16-50-16.

D	F_s^M	$P_i\left(0.11, F_s^M\right)$	ΔP_i	$\Delta P_i / P_i\left(0.11, F_s^M\right)$
0.055	0.057	0.887	0.033	0.037
0.22	0.00	0.387	0.059	0.151
0.44	0.001	0.455	0.115	0.252
0.88	0.001	0.455	0.195	0.430

Semi-classical Decay Function

In quantum mechanics, ionisation by tunnelling is expected for states below the classical barrier. It is assumed that the field is sufficiently slowly varying that at any point in time the decay term can be approximated by the time-independent decay term calculated at the corresponding field value, $F(t)$.

As the principal quantum number is increased, the relative contribution of tunnelling to overall ionisation is expected to reduce; however, for the relatively low frequencies considered, tunnelling is still significant for relatively high values of n. For example, for $\Omega_0 = 0.011414$, tunnelling is still important for $n \geq 50$ (see figure 3.11 for F_s in the range $(0.05, 0.065)$). For small resonance islands, tunnelling can have an appreciable effect for quantum numbers as large as $n = 200$. This is shown in §6.3, page 184 and in particular in figures 6.11–6.14 on page 188.

Damburg and Kolosov [19] determined the following semi-empirical expression for the decay term in the case of a static field, expressed in atomic units:

$$n^3 \Gamma_{DK} = \frac{(4R)^{2n_2+m+1}}{n_2!(n_2+m)!} \exp\left(-\frac{2}{3}R - \frac{1}{4}n^3 F g(\mathbf{n})\right), \quad m \geq 0, \tag{3.18}$$

where

$$g(\mathbf{n}) = 34n_2(n_2+m) + 46n_2 + 7m^2 + 23m + \frac{53}{3} \quad \text{and} \quad R = \frac{(-2E_{DK})^{3/2}}{F}$$

and n_2 is given by equation (2.12) on page 31 and can be determined from the electric quantum

number, n_e, by the following equation.

The energy levels, E_{DK}, were calculated using fourth order perturbation theory (see [19], equation 40). In scaled units, $E_{DK_0} = n^2 E_{DK}$, which is given by

$$\begin{aligned} -2E_{DK_0} &= 1 + 3\frac{n_e}{n}F_0 + \frac{F_0^2}{8}\left(17 - 3\left(\frac{n_e}{n}\right)^2 - 9\left(\frac{m}{n}\right)^2 + \frac{19}{n^2}\right) \\ &+ \frac{3n_e}{16n}F_0^3\left(23 - \left(\frac{n_e}{n}\right)^2 + 11\left(\frac{m}{n}\right)^2 + \frac{39}{n^2}\right) \\ &+ \frac{F_0^4}{512}\left\{5487 - 1134\left(\frac{mn_e}{n^2}\right)^2 + 1806\left(\frac{n_e}{n}\right)^2 - 3402\left(\frac{m}{n}\right)^2\right. \\ &+ 147\left(\frac{n_e}{n}\right)^4 - 549\left(\frac{m}{n}\right)^4 \\ &\left. + \frac{1}{n^2}\left(35182 + 5754\left(\frac{n_e}{n}\right)^2 - 8622\left(\frac{m}{n}\right)^2 + \frac{16211}{n^2}\right)\right\}. \end{aligned}$$

For large n_2 and m, the Damburg and Kolosov decay term can be approximated using Stirling's approximation to give

$$n^3\Gamma_{DK} = n\Gamma_{DK_0} = \frac{1}{2\pi}\sqrt{\frac{n^2}{n_2(n_2+m)}}\exp\left(-nG_{DK}(\mathbf{n}, F_0)\right) \tag{3.19}$$

where

$$\begin{aligned} G_{DK} &= \frac{2}{3}R_0 - \left(1 + \frac{n_e}{n}\right)\ln(4R_0) + \frac{n_2}{n}\ln\left(\frac{n_2}{en}\right) + \frac{n_2+m}{n}\ln\left(\frac{n_2+m}{en}\right) \\ &+ \frac{F_0}{4}\frac{g(\mathbf{n})}{n^2} \end{aligned}$$

and Γ_{DK_0} is expressed in scaled coordinates. R_0 is defined by $nR_0 = R$ and F_0 is the scaled field.

The Damburg and Kolosov decay expression given by equation (3.18) is accurate for a restricted range of the parameters, n, m and n_e, with better accuracy for smaller values of $|m|$ and n_1. For example, Damburg and Kolosov compared numerically determined decay rates with their semi-empirical formula for $n = 30, m = 0$ and $n_e = 29$ (see [19] table 2.17) and showed good agreement for a number of field values. However, experimental results [30] show that for $n = 40$ the Damburg Kolosov formula overestimates the decay factor significantly for $|m| > 3$.

Table 3.2: Comparison between classical critical field and $G_{DK}(F_{DK}) = 0$ in the limit $n \to \infty$.

I_m	I_2	I_e	F_{DK}	F_c	$(F_{DK} - F_c)/F_c$
0.2	0.2	-0.4	0.1828	0.1984	-0.0786
0.2	0.4	0.0	0.1544	0.1682	-0.0820
0.2	0.6	0.4	0.1390	0.1491	-0.0677
0.4	0.2	-0.2	0.1694	0.1848	-0.0833
0.4	0.4	0.2	0.1471	0.1593	-0.0766
0.4	0.6	0.6	0.1349	0.1425	-0.0533

The accuracy of expression (3.19) reduces as the barrier top is approached, which unfortunately is where ionisation due to tunnelling is greatest. This can be seen in the limit $n \to \infty$, when the quantum ionisation behaviour should approach that of the classical case. In this limit, physical considerations suggest that $G_{DK}(F)$ should have the behaviour

$$G_{DK} \begin{cases} > 0, & F_0 < F_c, \\ = 0, & F_0 = F_c, \\ < 0, & F_0 > F_c. \end{cases} \tag{3.20}$$

Table 3.2 compares the value of F at which $G_{DK}(F) = 0$ with F_c for a number of I_m and I_e values in the limit $n \to \infty$; it can be seen that the Damburg and Kolosov approximation gives a consistently low estimate of the critical field value.

More accurate estimates for the decay value near the top of the barrier can be obtained using semi-classical methods, as described by Dando [21]. The technique was used to calculate ionisation rates for hydrogen in a microwave field in the absence of a static field and provides a good match with experimental results for sufficiently low scaled frequency for which ionisation is assumed to result primarily from tunnelling [53].

The method used by Dando for the calculation of the semi-classical decay rates requires the calculation of a decay rate for each set of parameters, (n, m, n_e, F). This calculation is complex and too computationally intensive for direct inclusion in the calculations considered here. Instead we derive semi-empirical formulae for particular values of n, m and n_e suitable for use over a range of F values; the formulae use parameters calculated by the semi-classical methods.

Table 3.3: Example decay parameters obtained using semi-classical methods for a static field.

n	m	n_e	n_1	n_2	F_c	a	b	c
39	0	38	0	38	0.130135	0.025309	1.119521	9.918105
39	0	28	5	33	0.137840	0.024067	1.055912	9.644235
39	0	18	10	28	0.146922	0.024660	0.952032	9.804940
39	0	8	15	23	0.157681	0.027769	0.950593	9.057639
39	0	-2	20	18	0.170890	0.034152	0.992983	8.193732
39	0	-12	25	13	0.188302	0.044012	1.035137	7.273361
39	0	-22	30	8	0.214117	0.057068	1.017246	6.339353
39	0	-32	35	3	0.261821	0.079321	0.837856	5.218557
39	0	-38	38	0	0.335513	0.062887	0.559475	2.462048

We start by writing the decay function in a similar form to that of Damburg and Kolosov as

$$\Gamma_{SC} = k(\mathbf{n}) \exp\left(-nG_{SC}(\mathbf{n}, F_0)\right) \tag{3.21}$$

and fitting $G_{SC}(\mathbf{n}, F_0)$ to match the decay factors calculated using semi-classical methods at values of F near F_c satisfying $F < F_c$. The value of $k(\mathbf{n})$ depends upon m and n_2,

$$k(\mathbf{n}) = \begin{cases} \dfrac{1}{2\pi}\sqrt{\dfrac{n^2}{n_2(n_2+m)}}, & n_2 \neq 0, \quad m \geq 0, \\ \sqrt{\dfrac{n}{2\pi m}}, & n_2 = 0, \quad m > 0, \\ 1, & n_2 = m = 0. \end{cases} \tag{3.22}$$

G_{SC} is expressed as a quadratic expansion about $F_0 = F_c$,

$$G_{SC}(\mathbf{n}, F_0) = a(\mathbf{n}) + b(\mathbf{n})\left(\frac{F_c - F_0}{F_c}\right) + c(\mathbf{n})\left(\frac{F_c - F_0}{F_c}\right)^2, \quad F_0 < F_c. \tag{3.23}$$

Values for $a(\mathbf{n})$, $b(\mathbf{n})$ and $c(\mathbf{n})$ are obtained by matching the approximation against values obtained using the semi-classical method. Examples are provided in table 3.3.

As for the Damburg and Kolosov case, in the limit of $n \to \infty$, the behaviour of G_{SC} should be given by equation (3.20). Taking quantum values to match the classical parameters, $I_m = 0.2$, $I_2 = 0.2$, table 3.4 shows the calculated critical field value, F_{SC}, where $G_{SC}(F_{SC}) = 0$ for increasing n. It can be seen that as n increases, the difference between F_{SC} and F_c decreases,

Table 3.4: Comparison between classical critical field and $G_{SC}(F_{SC}) = 0$ for increasing n corresponding to $I_m = 0.2$ and $I_2 = 0.2$.

n	m	n_2	n_e	F_{SC}	F_c	$(F_{SC} - F_c)/F_c$
50	10	10	-19	0.2051	0.1965	-0.0440
100	20	20	-39	0.2013	0.1975	-0.0193
200	40	40	-79	0.1995	0.1979	-0.0078
400	80	80	-159	0.1988	0.1982	-0.0030
800	160	160	-319	0.1986	0.1983	-0.0012

as required.

The quadratic decay function approximation is inaccurate for $F \ll F_c$. However, little ionisation will result from any sufficiently large value of G_{SC}; inaccuracies for $F \ll F_c$ will therefore have little impact on the results of ionisation calculations.

For the time-dependent field (2.2), a further approximation can be made by averaging the decay function over a field period,

$$\Gamma_{SC}(t) \approx \overline{\Gamma}_{SC}(t) = \frac{1}{T}\int_{t-\pi/\Omega_0}^{t+\pi/\Omega_0} \mathrm{d}s\, k(\mathbf{n}) \exp\left(-nG_{SC}(\mathbf{n}, F_0(s))\right). \tag{3.24}$$

This approximation reduces the computational complexity of numerically evaluating the quantum equations of motion. The integral (3.24) can be approximated by expanding about the maximum of $F(t)$ at

$$t = 2\pi M/\Omega_0 + s,$$

where M is an integer and $|s| < 2\pi/\Omega_0$,

$$F\left(\frac{2\pi M}{\Omega_0} + s\right) = \lambda\left(\frac{2\pi M}{\Omega_0} + s\right)\left(F_s + F_\mu - \frac{1}{2}F_\mu(\Omega_0 s)^2\right) + O(s^4).$$

Hence,

$$G_{SC} = \overline{a} + \overline{b}(\Omega_0 s)^2 + O(s^4),$$

where

$$\overline{a}(\mathbf{n}) = a(\mathbf{n}) + \left(1 - \frac{\lambda(t)(F_s + F_\mu)}{F_c}\right) b(\mathbf{n}) + \left(1 - \frac{\lambda(t)(F_s + F_\mu)}{F_c}\right)^2 c(\mathbf{n}) \tag{3.25}$$

and

$$\bar{b}(\mathbf{n}) = \frac{1}{2}\frac{\lambda(t)F_\mu}{F_c}\left[b(\mathbf{n}) + \left(1 - \frac{\lambda(t)(F_s+F_\mu)}{F_c}\right)c(\mathbf{n})\right]. \quad (3.26)$$

Substituting for $G_{SC}(t)$ in expression (3.24), we obtain the approximation

$$\Gamma_{SC} \approx \frac{k(\mathbf{n})\exp(-n\bar{a})}{2\sqrt{\pi n\bar{b}}}\mathrm{erf}\left(\sqrt{\pi n\bar{b}}\right) \quad \text{for} \quad \lambda(t)(F_s+F_\mu) \leq F_c.$$

For $F > F_c$, this approximation is not valid, but from physical considerations rapid ionisation is expected; hence a step value is assumed for the decay value for $F > F_c$. The combined expression for the decay function is

$$\Gamma_{SC} = \begin{cases} \dfrac{k(\mathbf{n})\exp(-n\bar{a})}{2\sqrt{\pi n\bar{b}}}\mathrm{erf}\left(\sqrt{\pi n\bar{b}}\right), & \lambda(t)(F_s+F_\mu) \leq F_c, \\ D, & \lambda(t)(F_s+F_\mu) > F_c, \end{cases} \quad (3.27)$$

where $D = 0.11$.

For the case of $F_\mu > F_s$ ionisation is also possible along the n_1 quantisation axis, as can be seen by examining $V_1(\xi)$ for $F < 0$ (see equation (2.9)). The additional decay coefficient is obtained from the expressions (3.22), (3.25), (3.26) and (3.27) by making the substitutions $(n_e, F_s) \rightarrow (-n_e, -F_s)$.

Numerical tests confirm that the calculated ionisation probability is reasonably insensitive to the value of Γ_{SC} for $F > F_c$. The effect of different values of D in equation (3.27) is demonstrated by repeating the quantum ionisation calculations of the previous section for $F_\mu = 0.14$, $\Omega_0 = 0.07311$, field envelope 16-50-16, $n = 39$, $m = 10$, $k_i = -14$ and grid size $\Delta F_s = 0.0001$ using the semi-classical decay function and varying D. Figure 3.2 compares the ionisation probability $P_i(F_s)$ for $D = 0.055, 0.11, 0.22, 0.44$ and 0.88. The maximum difference in ionisation probability calculated for varying D is shown in table 3.5. Contrasting these results with those for the step decay function, it can be seen that the effect of the decay value for $F > F_c$ is much less for the semi-classical case. The worst case difference, comparing $D = 0.11$ and $D = 0.88$ is approximately 4% and the overall difference in integrated area varies by less than 0.3% for the D values considered.

Table 3.5: Comparison of maximum difference between ionisation probabilities, $P_i(D, F_s)$, for a semi-classical decay function with various step sizes, D, with $P_i(0.11, F_s)$. The difference, $\Delta P_i(D)$, is calculated as the maximum value of $|P_i(D, F_s) - P_i(0.11, F_s)|$ for $0 \leq F_s \leq 0.08$. The F_s value at this maximum is denoted by F_s^M. The dynamical parameters are: $n = 39$, $m = 10$, $k_i = -14$, $F_\mu = 0.14$, $\Omega_0 = 0.07311$ and a field envelope of 16-50-16.

D	F_s^M	$P_i\left(D = 0.11, F_s^M\right)$	ΔP_i	$\Delta P_i / P_i\left(0.11, F_s^M\right)$
0.055	0.0750	0.9992	0.0001	0.0001
0.22	0.0437	0.8636	0.0081	0.0093
0.44	0.0437	0.8636	0.0214	0.0247
0.88	0.0438	0.8980	0.0369	0.0410

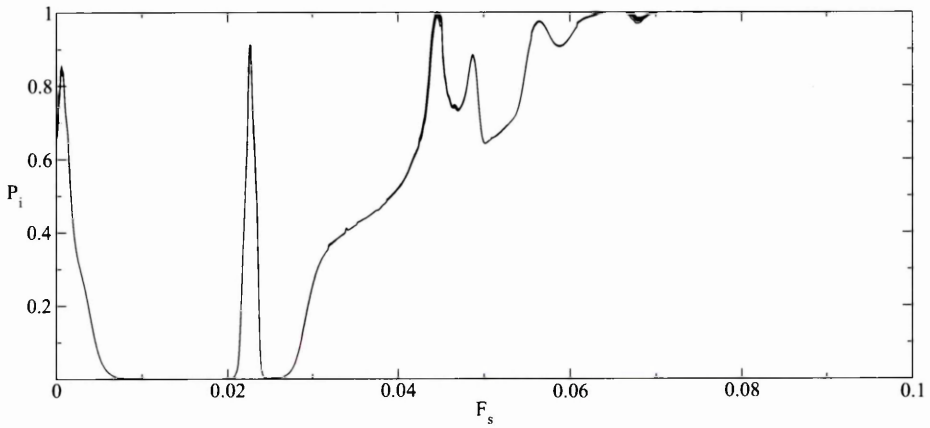

Figure 3.2 Ionisation probabilities, $P_i(F_s)$, for the $O(F^5)$ Averaged Hamiltonian with $\Omega_0 = 0.07311$, $F_\mu = 0.14$, field envelope 16-50-16, $n = 39$, $m = 10$ and $k_i = -14$. A semi-classical decay function is used with separate curves for $D = 0.055, 0.11, 0.22, 0.44$ and 0.88.

The Effect of Tunnelling on Ionisation

Tunnelling can make a significant contribution to ionisation for surprisingly high quantum numbers. The effect of tunnelling can be isolated by modifying equations (3.9)–(3.11) to remove the inter-state interaction terms. Figure 3.3 shows the ionisation probabilities obtained by integrating the resultant equations of motion for varying F_s and F_μ, for $n = 39$, $k_i = -10$ and $m = 10$. The period of integration is set to match that of a field envelope of 16-50-16, for a scaled frequency of $\Omega_0 = 0.0528$. The lines show the values of F_s and F_μ for which the ionisation probability passes through $P_i = 0.5$, for the two decay functions, $\Gamma_s(k, t)$ and $\Gamma_{SC}(k, t)$. For $F_\mu - F_s$ sufficiently large ionisation can also occur along the n_1 axis.

Figure 3.4 shows the effect of tunnelling on ionisation for different n values. For these cases, $m = 0$ and $k_i = 0$ for n odd and $k_i = 1$ for n even. It can be seen that the area for which $P_i(F_s, F_\mu) < 0.5$ reduces for the semi-classical decay function as n is reduced; hence tunnelling becomes an increasingly significant contributor to ionisation as the quantum number is reduced. In the contrast, for the step decay function, the curves for which $P_i(F_s) = 0.5$ lie very close together; the differences are due only to the differences in initial conditions, k_i/n and m/n, which vary slightly as n is changed. For all n values, ionisation for the semi-classical decay function is higher than for the step function.

The effect of tunnelling means that in general, we expect quantum ionisation probabilities to be greater than for the classical mechanics, with the differences becoming larger for smaller principal quantum number, although this is not always true; at resonances, the different underlying dynamic mechanisms can lead to lower quantum ionisation probabilities.

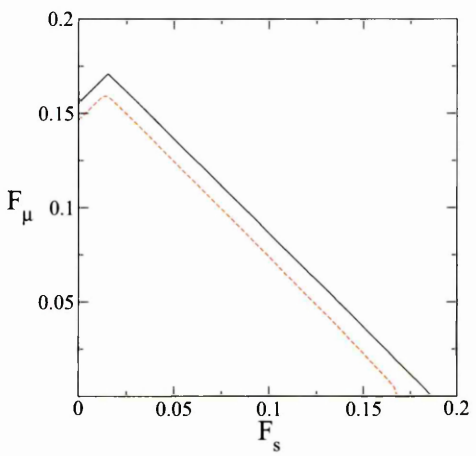

Figure 3.3 Ionisation probability, $P_i(F_s, F_\mu) = 0.5$, for $n = 39$, $m = 10$ and no interaction terms with Γ_s (solid line) and Γ_{SC} (dotted line).

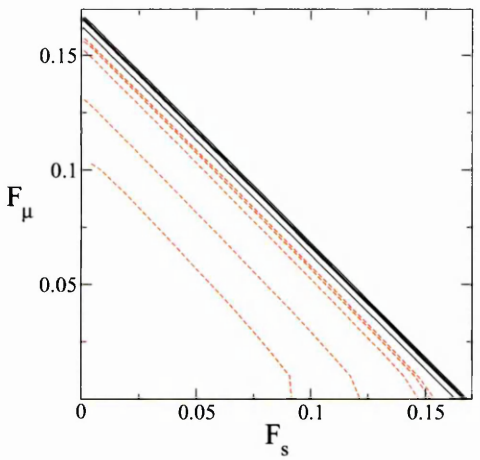

Figure 3.4 $P_i(F_s, F_\mu) = 0.5$ for $m = 0$, no interaction terms and $n = 5, 10, 30, 39$ and 50. For each n, $P_i(F_s) = 0.5$ is shown with a solid line for the step decay function, Γ_s, and a dotted line for the semi-classical decay function, Γ_{SC}.

Tunnelling makes a significant contribution for relatively large n, although the effect becomes smaller with increasing n. Table 3.6 shows ionisation thresholds for $F_\mu = 0.13$ for various n, comparing the value of F_s for which the ionisation probability rises to 50% for a step decay function and for the semi-classical decay function. The initial state is chosen to

Table 3.6: 50% Ionisation thresholds, F_s for which $P_i = 0.5$; for $F_\mu = 0.13$ and $m = 0$ for step decay, $\Gamma_S(F_s)$, and semi-classical decay, $\Gamma_{SC}(F_s)$, functions for various n in the absence of inter-state interactions. See text for k_i values.

n	Step decay F_s	Semi-classical F_s	$F_s(\Gamma_s)/F_s(\Gamma_{SC})$ %
10	0.03282	0.00202	6.16
30	0.03623	0.02319	64.02
39	0.03807	0.02748	72.19
50	0.03702	0.02862	77.31

be $k_i = 0$ for n odd and $k_i = 1$ for n even. For all values of n shown there is an appreciable contribution from tunnelling.

3.2 Validation of the Quantum Approximation

In this section we provide some validation for the quantum approximation, comprising the equations of motion, (3.9–3.11) on page 94 and the ionisation mechanism detailed in §3.1.3, page 97. Unless otherwise stated, the semi-classical decay function given by equation (3.27) (page 105) is used.

Validation of the quantum approximation is made difficult by the limited availability of published data in the region of interest.

We check the consistency of the quantal calculations with classical calculations to ensure that there are no major errors in the calculations. Comparison is made with the classical Resonance Hamiltonian results for a single initial substate $(I_e(0), I_m)$ and for a microcanonical distribution of initial states. The parameters are chosen to allow comparison with [51]. Later calculations for high quantum numbers provided in chapter 6 confirm the expected correspondence with the classical dynamics.

At this time, the only comparative quantum calculations for low frequency linearly polarised microwave fields in a parallel static field are Robicheaux *et al* [52]. We compare the quantum calculations described here with those of Robicheaux *et al* and the exact classical dynamics. Comparison with ionisation times calculated by Robicheaux *et al* are provided in §5.5 on page 172.

3.2.1 Quantum Results for Single Substates

Figures 3.5 and 3.6 compare the ionisation probabilities calculated using the quantum approximation for the Averaged Hamiltonian with the classical ionisation ionisation probabilities calculated in §2.2.1, figures 2.9 and 2.10 which were calculated for $F_\mu = 0.13$, $\Omega_0 = 0.0528$, $I_m = 0.2$, $I_e(0) = -0.4$ and field envelope 16-50-16. For the quantum calculations, $n = 50$ and $m = 10$. The corresponding best match initial state is chosen to be $k_i = -19$.

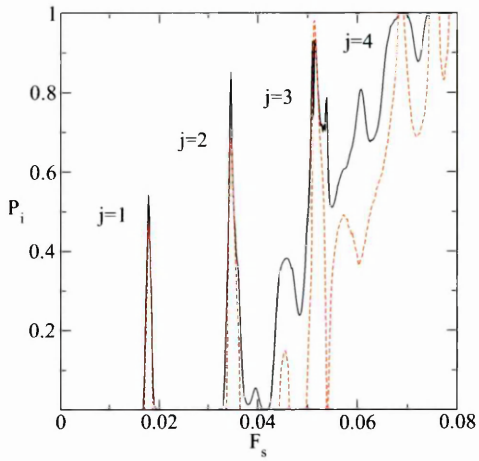

Figure 3.5 Ionisation probabilities, $P_i(F_s)$, for $\Omega_0 = 0.0528$, $F_\mu = 0.13$, envelope 16-50-16, $I_m = I_2(0) = 0.2$ (classical), $n = 50$, $m = 10$, $k_i = -19$ (quantum) for the $O(F^2)$ Averaged Hamiltonian quantum (solid line) and classical (dashed line) approximations.

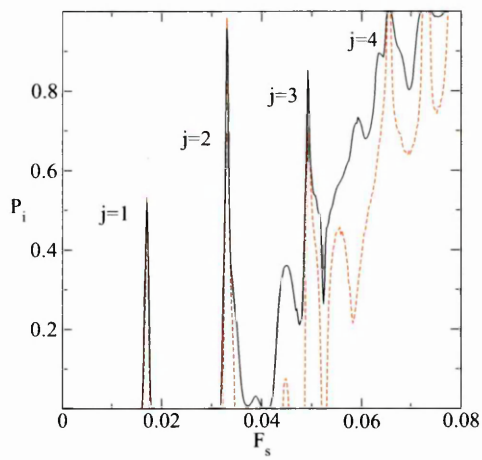

Figure 3.6 Ionisation probabilities, $P_i(F_s)$, for $\Omega_0 = 0.0528$, $F_\mu = 0.13$, envelope 16-50-16, $I_m = I_2(0) = 0.2$ (classical), $n = 50$, $m = 10$, $k_i = -19$ (quantum) for the $O(F^5)$ Averaged Hamiltonian quantum (solid line) and classical (dashed line) approximations.

The quantum approximations are seen to be consistent with the classical approximation, generating ionisation probability peaks at the same locations as the classical approximations for each of the resonances, $j = 1 \ldots 4$. Generally the ionisation probabilities for the quantum case are higher than the corresponding classical case, due primarily to the effects of tunnelling.

Figure 3.7 compares the ionisation probability, $P_i(F_s)$ for the $n = 39$ quantum Averaged Hamiltonian with the classical results shown in figure 2.11, §2.2.1 for $F_\mu = 0.13$, $\Omega_0 = 0.011414$ and the field envelope 16-50-16. The quantum numbers, $m = 8$ and $k_i = -16$ are chosen to match as closely as possible the classical parameters, $I_m = 0.2$ and $I_e(0) = -0.4$. It can be seen that where resonance ionisation peaks occur, the classical and quantum results are

broadly similar, particularly for $0 < F_s \lesssim 0.045$. For higher values of F_s, there is an underlying trend of higher ionisation probability for the quantum approximation due to tunnelling.

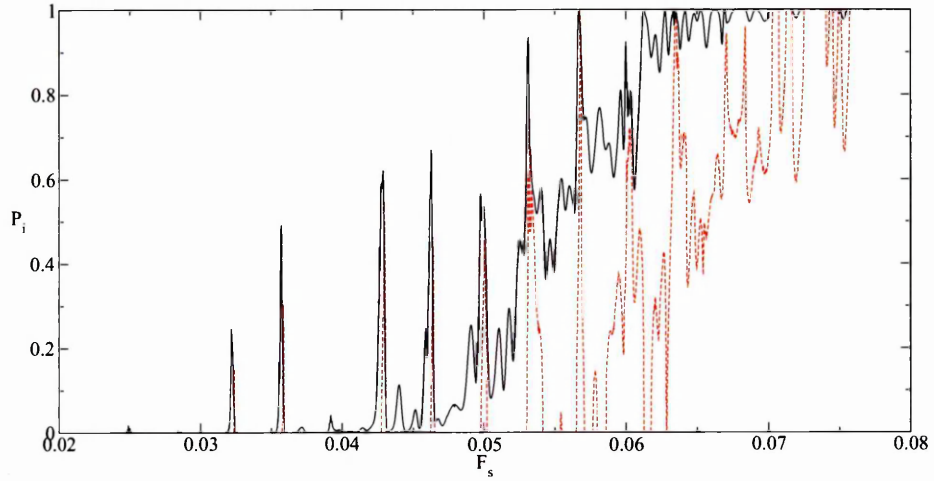

Figure 3.7 Ionisation probabilities, $P_i(F_s)$, for the $O(F^5)$ Averaged Hamiltonian, $F_\mu = 0.13$ and $\Omega_0 = 0.011414$ for the $n = 39$, $m = 8$ and $k_i = -16$ quantum (solid line) and classical (dashed line) approximations.

3.2.2 Quantum Ionisation Probabilities for Averaged Substates

Repeating the calculations of §2.2.2 using the quantum equations of motion, figure 3.8 shows the ionisation probability calculated by averaging the ionisation probabilities calculated for each possible initial substate (m, k_i) for $n = 39$. The classical results generated previously for the Averaged Hamiltonian and the exact classical dynamics results are also shown for comparison.

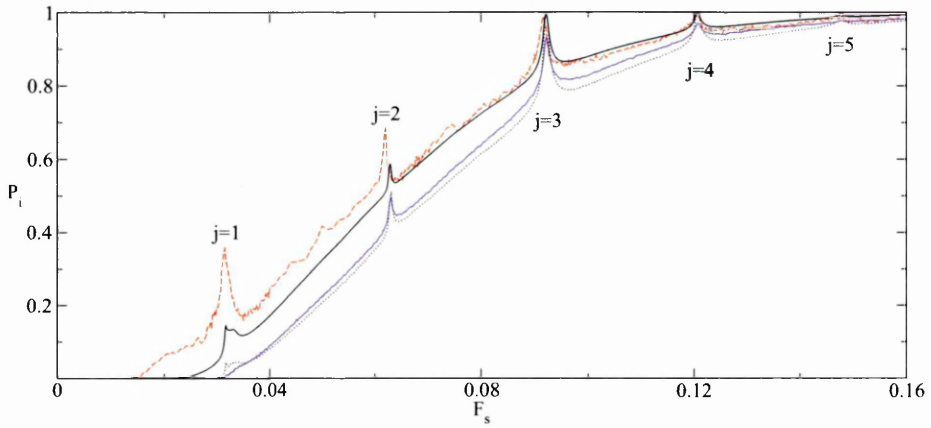

Figure 3.8 $P_i(F_s)$, for $F_\mu = 0.1$ and $\Omega_0 = 0.0980$, field envelope 16-50-16 $O(F^5)$ Averaged Hamiltonian quantum approximation (solid line), classical approximation (dotted line) and exact classical dynamics (dashed line). The blue line shows the quantum approximation calculated using a step decay function.

As for the single substate comparison, the locations of ionisation probability peaks for each of the resonances are seen to coincide for the classical and quantum results. Overall, the quantum ionisation probability is higher at each F_s value than in the corresponding classical Averaged Hamiltonian case.

Classically, away from resonance the action, $I_e(t)$, undergoes little change after the initial field switch-on. The observed ionisation is close to the adiabatic ionisation curve as is seen in figure 2.14 on page 58. The quantum dynamics behave similarly and in the absence of tunnelling the quantum and classical ionisation probabilities are similar away from resonance, as can be seen from the step decay quantum curve also shown. When tunnelling is present ionisation can also occur from states below the classical critical ionisation limit, increasing the observed ionisation.

Figures 3.9 and 3.10 compare the averaged quantum ionisation probability calculated for field parameters to match figures 2.15 and 2.16, selected for comparison with the results of Robicheaux *et al* [52].

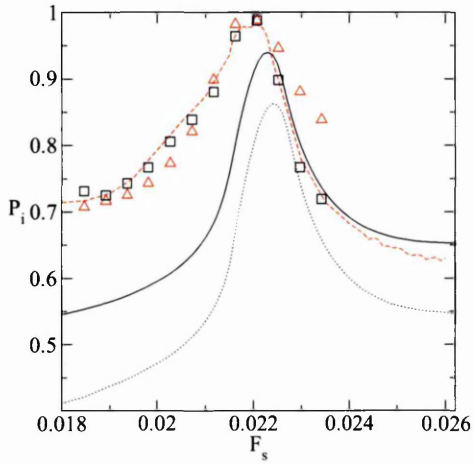

Figure 3.9 $P_i(F_s)$ for the $j = 1$ resonance averaged over substates, $F_\mu = 0.14372$, $\Omega_0 = 0.0730$ and envelope of 16-113-16 for the $O(F^5)$ $n = 39$ quantum approximation (solid line), classical approximation (dotted line) and exact classical dynamics (dashed line). Robicheaux comparison results, taken from [52], are shown using triangles for the classical results and squares for the quantum results.

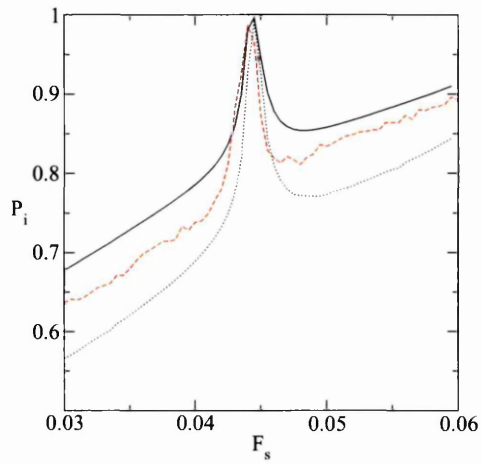

Figure 3.10 $P_i(F_s)$ for the $j = 2$ resonance averaged over substates, $F_\mu = 0.14372$, $\Omega_0 = 0.0730$ and envelope of 16-113-16 for the $O(F^5)$ $n = 39$ quantum approximation (solid line), classical approximation (dotted line) and exact classical dynamics (dashed line).

The differences between the exact classical dynamics, averaged Hamiltonian and Robicheaux classical results were discussed in §2.2.2, page 56. The quantum and classical ionisation peaks for the averaged Hamiltonian, $\overline{K}_m$ are coincident and generally, at each F_s value the quantum ionisation probability is higher than the classical ionisation probability. This is different to the Robicheaux results, where $P_i^{(quant)} > P_i^{(class)}$ for $F_s < 0.021$ and $P_i^{(quant)} < P_i^{(class)}$ for $F_s > 0.021$. The reason for this is not understood: tunnelling is expected to enhance the ionisation and for the Averaged Hamiltonian we observe that $P_i^{(quant)} > P_i^{(class)}$ for most F_s values.

3.3 Analysis of Quantum Results

3.3.1 Ionisation Probability Dependence on Tunnelling

In figure 3.11, the effect of changing the principal quantum number on ionisation is shown. The ionisation probability, $P_i(F_s)$, is plotted using solid lines for $n = 10, 15, 20$ and 39 with field parameters the same as for figure 3.7 and quantum states specified in table 3.7, chosen to give the best match to the classical initial condition, $I_e(0) = -0.4$. The $n = 5$ case was also calculated but not plotted, because in that case the ionisation probability is close to 1 for all F_s.

To demonstrate the effect of tunnelling on ionisation probability, the adiabatic ionisation probabilities, $P_i^{(adia)}(F_s)$, are also shown in figure 3.11 using dotted red lines. They are calculated in the absence of inter-state coupling; this is equivalent to setting $\langle l|\hat{H}_1|k\rangle = 0$ in equation (3.4) (page 92). For each n value, the $P_i(F_s)$ and $P_i^{(adia)}(F_s)$ curves lie close together. As n decreases, the effect of tunnelling on ionisation becomes more significant at smaller F_s values and over a wider range in F_s. Tunnelling explains the underlying difference in $P_i(F_s)$ observed between the quantum and classical approximations in figure 3.7 on page 110 for $F_s \gtrsim 0.45$.

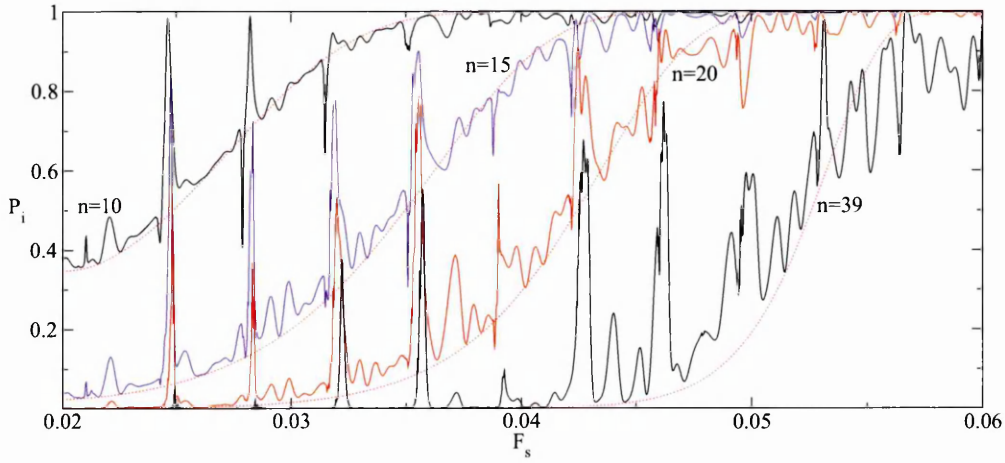

Figure 3.11 Quantum ionisation probabilities, $P_i(F_s)$, are shown using solid lines for the $O(F^5)$ Averaged Hamiltonian with $F_\mu = 0.13$, $\Omega_0 = 0.011414$ and $n = 10, 15, 20$, and 39. The field parameters are chosen to match those for figure 3.7. For each n, corresponding m and k_i values are given in table 3.7. The dotted red lines show the adiabatic ionisation probabilities, $P_i^{(adia)}(F_s)$, calculated by setting all off-diagonal matrix elements to zero.

For ionisation probabilities calculated with inter-state coupling, different behaviour is observed near resonance for the n values shown. As n decreases a number of resonance ionisation peaks appear, which are missing for higher quantum numbers and also in the classical dynamics. For example, the $j = 7$ resonance ($F_s^{(7)} = 0.02536$) peak is missing in the classical case (see figure 3.7 on page 110); there is a small ionisation probability peak at $F_s = 0.02490$ with $P_i = 0.017$ for $n = 39$, whilst for $n = 5, 10, 15$ and 20 there are strong ionisation peaks with maximum values, $P_i(F_s) > 0.66$. The differences between the observed classical and quantum ionisation probabilities at resonance are partly explained by tunnelling and partly by quantum resonance behaviour; the latter is discussed in the next section.

In §2.3 it was shown that ionisation occurs if classical orbits are captured by the resonance island and the top of the resonance island lies above the classical ionisation point I_c (see equation (2.43)). The field duration must also be sufficiently long. In the quantum case, ionisation by tunnelling can occur for states corresponding to $I_e < I_c$. Hence, dynamical effects due to resonances which do not have an observable effect in the classical case can manifest as ionisation probability peaks in the quantum dynamics because of tunnelling.

Table 3.7: Quantum parameters for varying n chosen to best match the classical parameters $I_m = 0.2$ and $I_e(0) = -0.4$.

n	m	k_i	m/n	k_i/n	n	m	k_i	m/n	k_i/n
5	1	-3	0.200	-0.600	50	10	-21	0.200	-0.420
10	2	-5	0.200	-0.500	100	20	-41	0.200	-0.410
15	3	-7	0.200	-0.467	200	40	-81	0.200	-0.405
20	4	-9	0.200	-0.450	400	80	-161	0.200	-0.402
39	8	-16	0.205	-0.410	800	160	-321	0.200	-0.401

3.3.2 Quantum Resonances

Whilst the presence of classical dynamical resonances are seen to have a similar general effect in the quantum dynamics — in the sense that ionisation probabilities can be enhanced in the region of classical dynamical resonances — the underlying mechanism by which the resonance causes changes in the quantum dynamics is distinctly different.

In the classical mechanics, the presence of the resonance island in phase space causes underlying periodic oscillations in $I_e(t)$, with periods and amplitudes determined by the initial conditions, $(I_e(0), \psi_e(0))$, and the relative location of the phase curve and the resonance island. For the quantum mechanics the resonance can cause enhanced couplings between substates which cause periodic underlying oscillations in the population of substates and can cause changes in the observed ionisation. The period of these oscillations is entirely quantal in nature.

In this section we examine an ionisation peak in the vicinity of a resonance and show how the observed ionisation behaviour is related to the coupling between substates. We consider the small quantum number, $n = 10$, as this allows the quantal resonance effects to be more easily seen. For higher quantum numbers, the same mechanisms outlined here also cause the ionisation behaviour, but there are increasing numbers of interacting states and the combined effect becomes closer to the observed classical behaviour. Higher quantum numbers are examined in more detail in §6 (page 177).

The effect of a resonance on the quantum dynamics can be seen by examining the state expectation value,

$$\langle n_e(t) \rangle = \sum_{k=-N}^{N} a_k^*(t)\, k\, a_k(t).$$

The ratio $\langle n_e(t)/n \rangle$ corresponds to the classical action, $I_e(t)$. Figure 3.12 plots $\langle n_e(t) \rangle$ for the $n = 10$ Averaged Hamiltonian at $F_s = 0.02464$, an ionisation peak; and at $F_s = 0.26$, a point not at resonance. To observe the underlying dynamics and the oscillations all decay terms are set to zero for the calculations shown in this figure. As for the classical case away from resonance, $\langle n_e(t) \rangle$ undergoes small oscillations only. At resonance, larger amplitude oscillations occur.

Figure 3.12 also shows the expectation values calculated by integrating the quantum Resonance Hamiltonian, equation (3.12). It can be seen that the behaviour described by this simplified Hamiltonian is a reasonable match to the behaviour observed for the Averaged Hamiltonian. The frequencies of oscillation are very close, although there is a slight difference in phase. This is due primarily to the evolution of the system during the field switch-on, which is not expected to be as well approximated by the Resonance Hamiltonian. The fact that the Resonance Hamiltonian provides a good approximation to the Averaged Hamiltonian behaviour at resonance can be used to provide a better understanding of the detailed resonance behaviour in the quantum mechanical case.

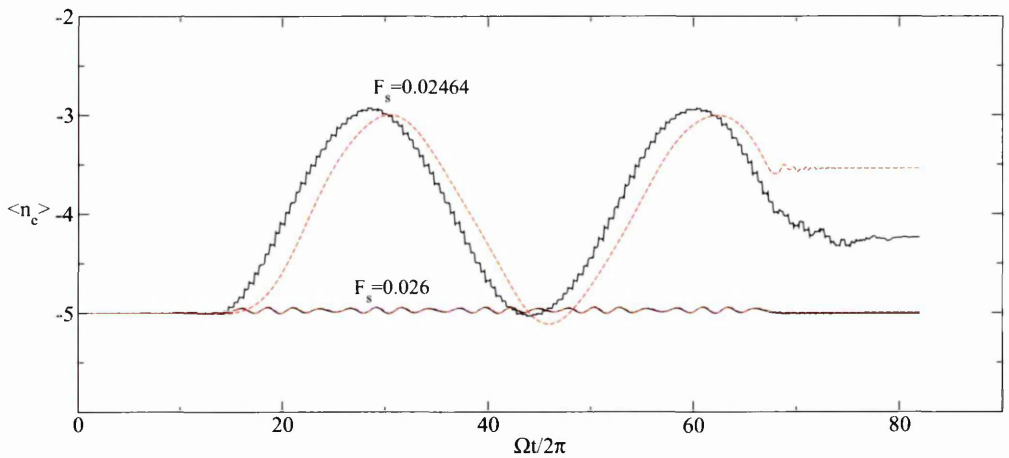

Figure 3.12 Expectation values $\langle n_e(t) \rangle$ for the $O(F^5)$ Resonance (solid lines) and Dynamical Resonance (dashed lines) Hamiltonians for $n = 10$, $m = 2$, $k_i = -5$, $F_\mu = 0.13$, $\Omega_0 = 0.011414$ and envelope 16-50-16 at two F_s values.

Figure 3.13 shows ionisation probabilities in the region of the $j = 7$ resonance, calculated for the Averaged Hamiltonian with ionisation now included, for two initial conditions, $k_i = -5$

and $k_i = -3$. The following features are observed regarding the ionisation probabilities:

1. for $k_i = -5$ there is a dip at $F_s = 0.02428$;
2. at $F_s = 0.02446$ there is a dip for $k_i = -3$ and a slight shoulder for $k_i = -5$; and
3. at $F_s = 0.02464$ there is a peak for $k_i = -5$.

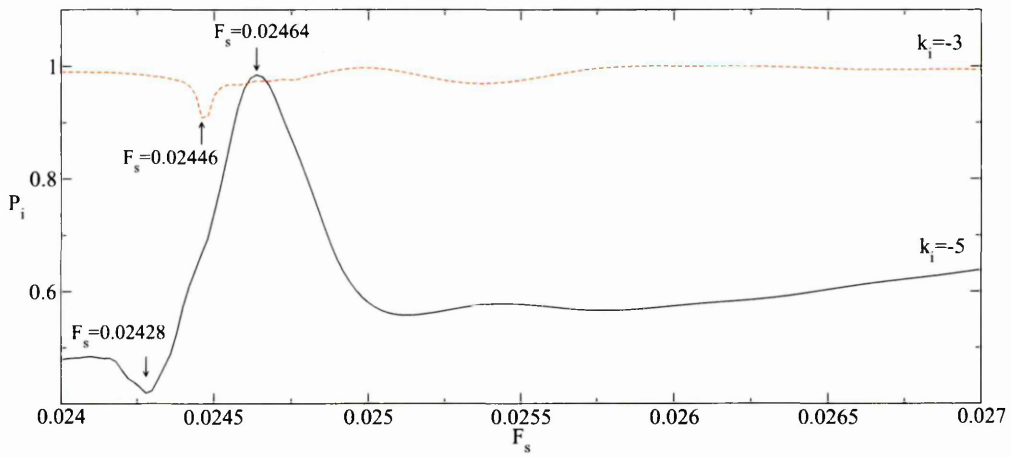

Figure 3.13 Ionisation probabilities $P_i(F_s)$ for the $O(F^5)$ Averaged Hamiltonian for $n = 10$, $m = 2$, $F_\mu = 0.13$, $\Omega_0 = 0.011414$ and envelope 16-50-16 around the $j = 7$ resonance; $k_i = -5$ (solid line) and $k_i = -3$ (dashed line).

These features are caused by the effect of the resonance on coupling between states, which can most easily be seen for the Resonance Hamiltonian. Whilst the field switch affects the dynamics and the observed ionisation, the general features described above are largely dependent upon state coupling occurring when the field is at its maximum amplitude.

From §3.1.2 in the absence of ionisation and ignoring the field switch, the state vector, $\mathbf{a}(t)$, satisfies $\dot{\mathbf{a}}(t) = -i\mathbf{R}\,\mathbf{a}(t)$, where the matrix $\mathbf{R}$ is given by equation (3.13) on page 95. The state vector can be represented in terms of the eigenvectors, $\{\mathbf{b}_k\}$, of $\mathbf{R}$. From equation (3.14) (page 95),

$$\mathbf{a}(t) = \sum_k e^{-i\lambda_k t} c_k \mathbf{b}_k, \quad c_k = \mathbf{b}_k^\dagger \mathbf{a}(0),$$

where $\{\lambda_k\}$ are the eigenvalues of $\mathbf{R}$.

When ionisation is included, the matrix $\mathbf{R}$ must be modified to include additional complex diagonal matrix elements. Denoting $\mathbf{R}'$ as the matrix including ionisation, $\mathbf{a}(t)$ now satisfies

$\dot{\mathbf{a}}(t) = -i\mathbf{R}'\,\mathbf{a}(t)$. The matrix, $\mathbf{R}'$ is not Hermitian, so care is required in the manipulation of its eigenvectors. An expansion can be obtained as,

$$\mathbf{a}(t) = \sum_k e^{-i\mu_k t} m_k \mathbf{d}_k, \tag{3.28}$$

where $\{\mathbf{d}_k\}$ and $\{\mu_k\}$ are the right eigenvectors and eigenvalues of $\mathbf{R}'$. The eigenvalues, $\{\mu_k\}$, can be complex. The coefficients, $\{m_k\}$, are given by, $m_k = \mathbf{d}_k^L \mathbf{a}(0)$, where $\{\mathbf{d}_k^L\}$ are the left eigenvectors of $\mathbf{R}'$, satisfying

$$\mathbf{d}_k^L \mathbf{R}' = \mu_k \mathbf{d}_k^L.$$

The eigenvectors satisfy orthogonality conditions, $\mathbf{d}_k^L \mathbf{d}_l = \delta_{kl}$.

We expect the introduction of ionisation to affect the quantum dynamics, but that the ionisation acts as a perturbation to the non-ionising system and hence that the non-ionising dynamics are a reasonable approximation. To test this assertion, we examine the ionisation for $\mathbf{R}'$ and compare this with an approximation for the ionisation for a system in terms of the non-ionising eigenvectors, $\{\mathbf{b}_k\}$, obtained using a perturbation expansion. We express $\mathbf{R}'$ as,

$$\mathbf{R}' = \mathbf{R} + i\varepsilon\mathbf{\Gamma},$$

where $\mathbf{\Gamma}$ is a real matrix with zero non-diagonal elements and ε is a small real expansion parameter. To $O(\varepsilon)$,

$$\mathbf{d}_k = \mathbf{d}_k^{(0)} + \varepsilon \mathbf{d}_k^{(1)} \quad \text{and} \quad \mu_k = \mu_k^{(0)} + \varepsilon \mu_k^{(1)}, \tag{3.29}$$

with solutions,

$$\mathbf{d}_k^{(0)} = \mathbf{b}_k, \quad \mu_k^{(0)} = \lambda_k, \quad \mu_k^{(1)} = i\mathbf{b}_k^\dagger \mathbf{\Gamma} \mathbf{b}_k \quad \text{and} \quad \mathbf{d}_k^{(1)} = \sum_{l \neq k} i \frac{\mathbf{b}_l^\dagger \mathbf{\Gamma} \mathbf{b}_k}{\lambda_k - \lambda_l} \mathbf{b}_l,$$

where, by appropriate choice of the phase of $\mathbf{b}_k$, ${\mathbf{d}_k^{(1)}}^\dagger \mathbf{b}_k = 0$ so that the normalisation condition, $\mathbf{d}_k^\dagger \mathbf{d}_k = 1$, is satisfied to $O(\varepsilon)$.

To $O(\varepsilon)$ the left eigenvector corresponding to $\mathbf{d}_k$ is,

$$\mathbf{d}_k^L = \mathbf{b}_k^\dagger - \varepsilon \mathbf{d}_k^{(1)^\dagger}.$$

In the presence of ionisation, from equation (3.28) and using the perturbation substitutions of equation (3.29),

$$|\mathbf{a}(t)|^2 = \mathbf{a}^\dagger(t)\ \mathbf{a}(t) = \sum_k |m_k|^2 \exp\left(2\Im\left(\mu_k\right) t\right) + O(\varepsilon),$$

where $\Im(x)$ is the imaginary component of x. The initial state, $\mathbf{a}(0)$ can be expanded in terms of the unperturbed eigenfunctions,

$$\mathbf{a}(0) = \sum_k c_k \mathbf{b}_k,$$

so that to $O(\varepsilon)$, $m_k \approx c_k$. Hence, if $p_k^b(t)$ is the ionisation at time t for a system in an initial state, $\mathbf{a}(0) = \mathbf{b}_k$, then an estimate for the ionisation at time t is given by,

$$P_i(t) \approx P_i^{(est)}(t) = \sum_k |c_k|^2 p_k^b(t). \tag{3.30}$$

In figure 3.14 estimated ionisation probabilities, $P_i^{(est)}(F_s)$, calculated using equation (3.30) at time $t = T_e$, where $T_e = 2\pi(2N_a + N_b)/\Omega_0$, are compared with $P_i(F_s)$, calculated from the Averaged Hamiltonian. The field parameters are the same as for figure 3.13, other than the field envelope, which is 0-50-0 instead. Comparing the red dashed curves in figure 3.14 with the curves in figure 3.13 shows that the field switch has only a small effect on the curve: the majority of features are still present for the instantaneously applied field.

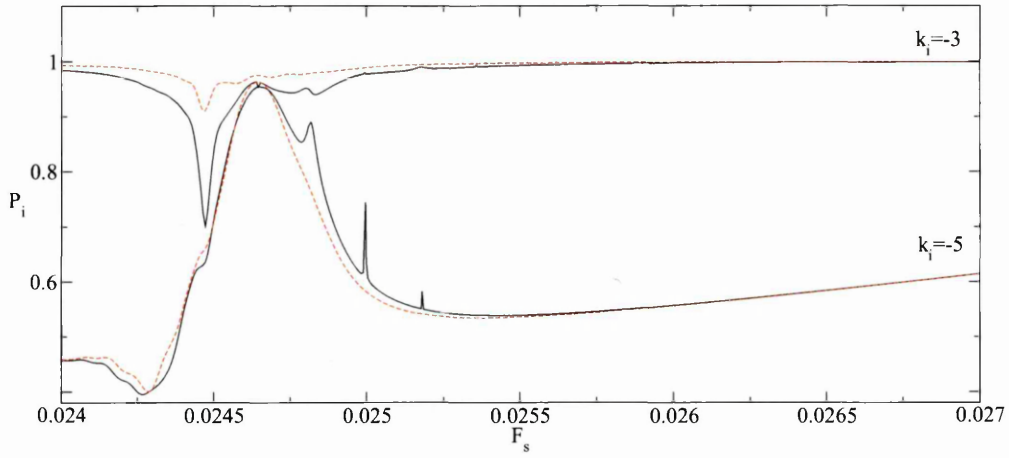

Figure 3.14 The solid lines show the estimated ionisation probabilities, $P_i^{(est)}(F_s)$, calculated using equation (3.30) with parameters chosen to be the same as for figure 3.13, but with an instantaneously applied field, envelope 0-50-0. For comparison the curves, $P_i(F_s)$, calculated from the Averaged Hamiltonian, are shown using dashed lines.

The estimated ionisation probabilities, $P_i^{(est)}(F_s)$, exhibits the same general features described in the list on page 117, although the dip at $F_s = 0.02446$ for $k_i = -3$ is much larger. However, $P_i^{(est)}(F_s)$ also has peaks at $F_s = 0.02482, 0.025$ and 0.02518 that are not present for $P_i(F_s)$. If we exclude these peaks, $P_i^{(est)}(F_s)$ captures the general features seen for $P_i(F_s)$. We can therefore understand these general features by considering the dynamics of the Resonance Hamiltonian in the absence of ionisation. The additional peaks in $P_i^{(est)}(F_s)$ are discussed later in this section.

The matrix $\mathbf{R}$ comprises diagonal elements and small off-diagonal perturbation elements. Away from resonances, the off-diagonal elements have little effect, the eigenvalues are non-degenerate and the normalised eigenvectors are approximated by $\mathbf{b}_{kl} \approx \delta_{kl}$; consequently for an initial state k,

$$\mathbf{a}(t) \approx e^{-i\lambda_k t}\mathbf{a}(0)$$

and hence $\langle n_e(t)\rangle \approx k$. The inclusion of off-diagonal elements introduces small additional oscillations from states, $l \neq k$, around the mean value, $\overline{\langle n_e\rangle}$.

The picture changes at resonances which correspond to eigenvalue near-degeneracies where,

for $k \neq l$, $\lambda_k - \lambda_l$ is small, but non-zero[2]. In these regions, $\mathbf{a}(t)$ is described by a superposition of the nearly degenerate states and $\langle n_e(t) \rangle$ will therefore oscillate. For two eigenstates with close eigenvalues, the angular frequency of oscillation will be $\lambda_k - \lambda_l$. In figure 3.12, for $F_s = 0.02464$, the dominant contributions are predominantly from two eigenstates. The calculated time period, expressed as $T\Omega_0/2\pi$, is

$$\frac{\Omega_0}{\lambda_k - \lambda_l} \approx 31.4,$$

which is reasonably consistent with the frequency of 31.9 measured for the Resonance Hamiltonian in figure 3.12. The amplitude of oscillation resulting from two dominant eigenvectors, $\mathbf{b}_i$ and $\mathbf{b}_j$, is

$$A_{ij} = 2|c_i^* c_j \langle \mathbf{b}_i | n_e | \mathbf{b}_j \rangle|.$$

In figure 3.12, taking just the two dominant eigenvectors, $A_{ij} \approx 2.05$; this is close to the measured amplitude of 2.11.

Figure 3.15 shows the eigenvalues as a function of F_s calculated for the Resonance Hamiltonian near the $j = 7$ resonance with all decay factors set to zero. It can be seen that at a number of F_s values, some of the eigenvalues become close although closer examination shows that they do not become identical, as is demonstrated in figure 3.16, focusing on a small region around a near-degeneracy. The effect that the near-degeneracies have on ionisation depends on the particular states mixed.

[2]Near-degeneracies are also referred to in the literature as "avoided crossings" and "avoided level crossings" (see, for example, [11]).

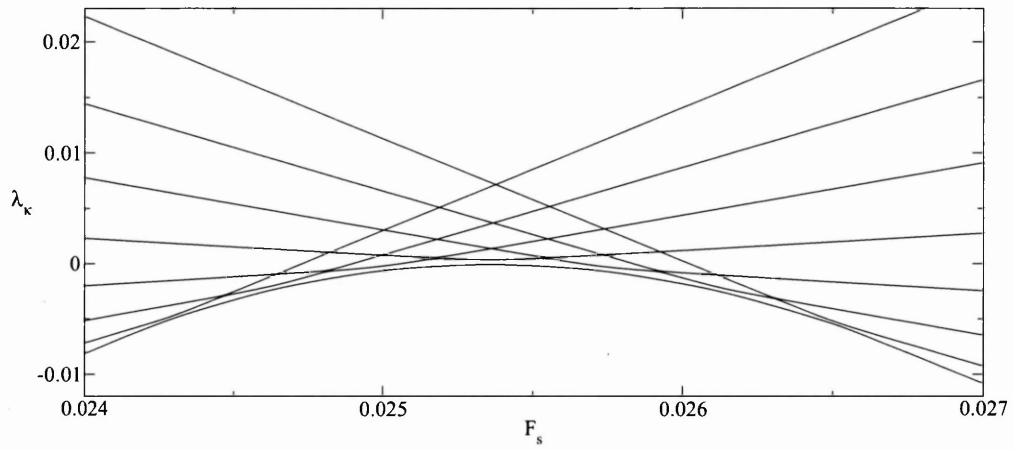

Figure 3.15 Eigenvalues of $\mathbf{R}$ for the $O(F^5)$ Resonance Hamiltonian with $n = 10$, $m = 2$, $F_\mu = 0.13$ and $\Omega_0 = 0.011414$.

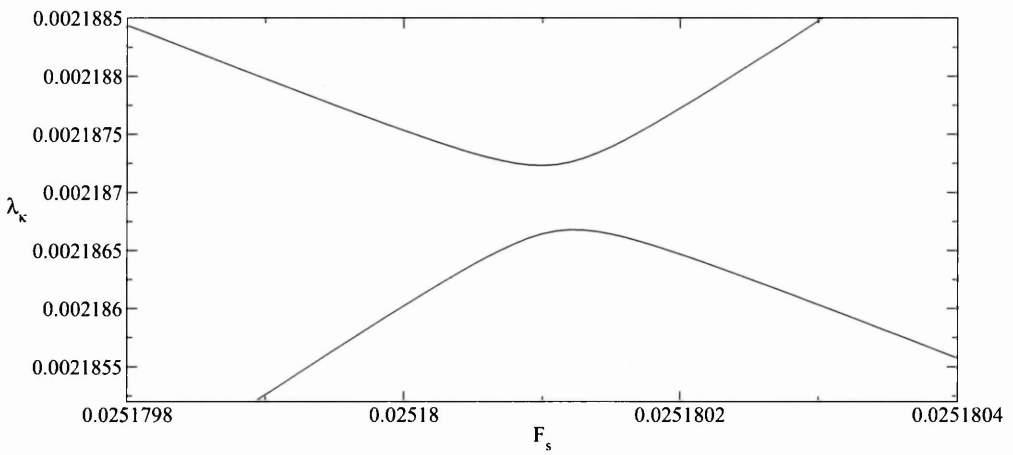

Figure 3.16 Eigenvalues of $\mathbf{R}$ for the $O(F^5)$ Resonance Hamiltonian with $n = 10$, $m = 2$, $F_\mu = 0.13$ and $\Omega_0 = 0.011414$ in the region of a near-degeneracy.

Tables 3.8–3.11 show the expectation values for each eigenvector, $\mathbf{b}_j$, and the modulus of the projection component of the initial state onto the eigenvector, c_j, at various F_s values. Tables 3.12 and 3.13 show the eigenvalues, λ_j and the ionisation probabilities, $p_j^b(T_e)$, calculated by integrating the equations of motion for an initial state $\mathbf{a}(0) = \mathbf{b}_j$ using the equations of motion for the Averaged Hamiltonian. The dynamical parameters used in the calculation of tables 3.8–3.13 are the same as those used for figures 3.12–3.17. At each F_s value, the eigenvectors, $\{\mathbf{b_j}\}$, are labelled in order of increasing expectation value, $\langle \mathbf{b}_j | n_e | \mathbf{b}_j \rangle$. From

Table 3.8: Expectation values, $\langle n_e(j)\rangle = \langle \mathbf{b}_j|n_e|\mathbf{b}_j\rangle$, for eigenvectors, $\mathbf{b}_j$, and projections, $c_j = \mathbf{b}_j^\dagger \mathbf{a}(0)$, for initial state $k_i = -3$ at various F_s values.

	F_s							
	0.024		0.02428		0.02446		0.02464	
j	$\langle n_e(j)\rangle$	$\lvert c_j\rvert$	$\langle n_e(j)\rangle$	$\lvert c_j\rvert$	$\langle n_e(j)\rangle$	$\lvert c_j\rvert$	$\langle n_e(j)\rangle$	$\lvert c_j\rvert$
-7	-6.96	0.01	-6.11	0.09	-6.15	0.45	-6.91	0.00
-5	-5.02	0.09	-5.84	0.13	-4.93	0.28	-4.05	0.66
-3	-3.01	0.99	-3.03	0.98	-3.89	0.84	-3.90	0.72
-1	-1.00	0.07	-1.01	0.10	-1.02	0.13	-1.12	0.19
1	1.00	0.00	1.00	0.00	0.99	0.00	0.99	0.01
3	3.00	0.00	3.00	0.00	3.00	0.00	3.00	0.00
5	5.00	0.00	5.00	0.00	5.00	0.00	5.00	0.00
7	7.00	0.00	7.00	0.00	7.00	0.00	7.00	0.00

Table 3.9: Expectation values, $\langle n_e(j)\rangle = \langle \mathbf{b}_j|n_e|\mathbf{b}_j\rangle$, for eigenvectors, $\mathbf{b}_j$, and projections, $c_j = \mathbf{b}_j^\dagger \mathbf{a}(0)$, for initial state $k_i = -3$ at various F_s values.

	F_s							
	0.02482		0.025		0.02518		0.027	
j	$\langle n_e(j)\rangle$	$\lvert c_j\rvert$	$\langle n_e(j)\rangle$	$\lvert c_j\rvert$	$\langle n_e(j)\rangle$	$\lvert c_j\rvert$	$\langle n_e(j)\rangle$	$\lvert c_j\rvert$
-7	-6.99	0.01	-6.99	0.00	-7.00	0.00	-7.00	0.00
-5	-3.38	0.39	-4.72	0.17	-4.69	0.11	-5.00	0.02
-3	-2.93	0.92	-2.08	0.72	-1.37	0.71	-3.00	1.00
-1	-2.67	0.08	-1.90	0.67	-0.97	0.28	-1.00	0.03
1	0.97	0.01	0.70	0.00	-0.66	0.64	1.00	0.00
3	2.99	0.00	2.99	0.00	2.68	0.02	3.00	0.00
5	5.00	0.00	5.00	0.00	4.99	0.00	5.00	0.00
7	7.00	0.00	7.00	0.00	7.00	0.00	6.99	0.00

tables 3.12 and 3.13 we note that the ionisation probability does not necessarily increase with increasing j.

Examination of figure 3.15 and tables 3.8–3.13 allows many of the features of the ionisation probability curves in figure 3.13 to be explained.

It can be seen from figure 3.15 and table 3.12 that at the point $F_s = 0.024$, the majority of eigenvalues are well separated apart from the lowest two and that the closest eigenvalues are for the lowest three; from table 3.12 we see that these correspond to the states $j = -7, -5$ and -3. The separation in eigenvalues is reflected in the expectation values of the eigenvectors, given in tables 3.8 and 3.10, where $\langle \mathbf{b}_j|n_e|\mathbf{b}_j\rangle \approx j$ apart from the lowest three states. States $j = -7$ and $j = -5$ have the closest eigenvalues and have the largest values of $|\langle \mathbf{b}_j|n_e|\mathbf{b}_j\rangle - j|$.

Table 3.10: Expectation values, $\langle n_e(j)\rangle = \langle \mathbf{b}_j|n_e|\mathbf{b}_j\rangle$, for eigenvectors, $\mathbf{b}_j$, and projections, $c_j = \mathbf{b}_j^\dagger \mathbf{a}(0)$, for initial state $k_i = -5$ at various F_s values.

	F_s							
	0.024		0.02428		0.02446		0.02464	
j	$\langle n_e(j)\rangle$	$\lvert c_j\rvert$	$\langle n_e(j)\rangle$	$\lvert c_j\rvert$	$\langle n_e(j)\rangle$	$\lvert c_j\rvert$	$\langle n_e(j)\rangle$	$\lvert c_j\rvert$
-7	-6.96	0.13	-6.11	0.65	-6.15	0.06	-6.91	0.11
-5	-5.02	0.99	-5.84	0.74	-4.93	0.94	-4.05	0.73
-3	-3.01	0.09	-3.03	0.16	-3.89	0.34	-3.90	0.68
-1	-1.00	0.00	-1.01	0.01	-1.02	0.01	-1.12	0.04
1	1.00	0.00	1.00	0.00	0.99	0.00	0.99	0.00
3	3.00	0.00	3.00	0.00	3.00	0.00	3.00	0.00
5	5.00	0.00	5.00	0.00	5.00	0.00	5.00	0.00
7	7.00	0.00	7.00	0.00	7.00	0.00	7.00	0.00

Table 3.11: Expectation values, $\langle n_e(j)\rangle = \langle \mathbf{b}_j|n_e|\mathbf{b}_j\rangle$, for eigenvectors, $\mathbf{b}_j$, and projections, $c_j = \mathbf{b}_j^\dagger \mathbf{a}(0)$, for initial state $k_i = -5$ at various F_s values.

	F_s							
	0.02482		0.025		0.02518		0.027	
j	$\langle n_e(j)\rangle$	$\lvert c_j\rvert$	$\langle n_e(j)\rangle$	$\lvert c_j\rvert$	$\langle n_e(j)\rangle$	$\lvert c_j\rvert$	$\langle n_e(j)\rangle$	$\lvert c_j\rvert$
-7	-6.99	0.08	-6.99	0.06	-7.00	0.05	-7.00	0.01
-5	-3.38	0.72	-4.72	0.96	-4.69	0.97	-5.00	1.00
-3	-2.93	0.25	-2.08	0.14	-1.37	0.08	-3.00	0.02
-1	-2.67	0.64	-1.90	0.09	-0.97	0.02	-1.00	0.00
1	0.97	0.00	0.70	0.20	-0.66	0.07	1.00	0.00
3	2.99	0.00	2.99	0.00	2.68	0.19	3.00	0.00
5	5.00	0.00	5.00	0.00	4.99	0.00	5.00	0.00
7	7.00	0.00	7.00	0.00	7.00	0.00	6.99	0.00

Table 3.12: Ionisation probabilities, $p_j^b(T_e)$, and eigenvalues, λ_j, at various F_s values. $p_j^b(T_e)$ values are calculated for $\mathbf{a}(0) = \mathbf{b}_j$ from the equations of motion for the Averaged Hamiltonian.

	F_s							
	0.024		0.02428		0.02446		0.02464	
j	$p_j^b(T_e)$	λ_j	$p_j^b(T_e)$	λ_j	$p_j^b(T_e)$	λ_j	$p_j^b(T_e)$	λ_j
-7	0.19	-0.0081	0.37	-0.0051	0.61	-0.0030	0.19	-0.0010
-5	0.46	-0.0072	0.39	-0.0049	0.61	-0.0036	0.97	-0.0020
-3	0.99	-0.0051	0.97	-0.0038	0.81	-0.0029	0.95	-0.0023
-1	1.00	-0.0020	1.00	-0.0016	1.00	-0.0013	0.99	-0.0010
1	1.00	0.0023	1.00	0.0019	1.00	0.0016	1.00	0.0013
3	1.00	0.0078	1.00	0.0064	1.00	0.0056	1.00	0.0047
5	1.00	0.0144	1.00	0.0122	1.00	0.0108	1.00	0.0094
7	1.00	0.0223	1.00	0.0192	1.00	0.0172	1.00	0.0152

Table 3.13: Ionisation probabilities, $p_j^b(T_e)$, and eigenvalues, λ_j, at various F_s values. $p_j^b(T_e)$ values are calculated for $\mathbf{a}(0) = \mathbf{b}_j$ from the equations of motion for the Averaged Hamiltonian.

	F_s							
	0.02482		0.025		0.02518		0.027	
j	$p_j^b(T_e)$	λ_j	$p_j^b(T_e)$	λ_j	$p_j^b(T_e)$	λ_j	$p_j^b(T_e)$	λ_j
-7	0.15	0.0010	0.14	0.0030	0.13	0.0050	0.08	0.0252
-5	0.88	-0.0006	0.61	0.0008	0.56	0.0022	0.61	0.0166
-3	0.96	-0.0014	0.98	-0.0002	0.99	0.0006	1.00	0.0091
-1	0.90	-0.0007	0.99	-0.0007	1.00	-0.0003	1.00	0.0027
1	1.00	0.0010	0.98	0.0007	0.99	0.0004	1.00	-0.0024
3	1.00	0.0039	1.00	0.0030	0.98	0.0022	1.00	-0.0065
5	1.00	0.0080	1.00	0.0065	1.00	0.0051	1.00	-0.0093
7	1.00	0.0133	1.00	0.0113	1.00	0.0093	1.00	-0.0108

Expectation values for the point $F_s = 0.027$ are also given (in tables 3.9 and 3.11) because of the generally large separation between eigenvalues at this point; again, $\langle \mathbf{b}_j | n_e | \mathbf{b}_j \rangle \approx j$. For both points, $F_s = 0.024$ and $F_s = 0.027$, the initial state, k_i has a projection dominated by the state $j = k_i$, consistent with the earlier assertion that $\langle n_e(t) \rangle \approx k_i$.

Returning to the earlier observations regarding ionisation probability for figure 3.13, these can now be understood as follows:

1. At $F_s = 0.02428$, from table 3.12 it can be seen that eigenvalues for the lowest two eigenstates, $j = -5$ and $j = -7$, are close. From table 3.10 it can be seen that the initial state $k_i = -5$ contains a significant contribution from the eigenstate $j = -7$ which has a lower ionisation probability, hence lowering the overall ionisation probability and causing the observed dip at this point.

2. In the region of $F_s \approx 0.02446$ the eigenvalues for the $j = -3$ and $j = -7$ eigenstates are closest, with $j = -5$ also close, causing a mixing of these states. The effect of this is most visible for $k_i = -3$, where the contribution from the $j = -5$ and $j = -7$ eigenstates — that have lower ionisation probabilities — causes a dip in the overall ionisation probability.

3. In the region of $F_s \approx 0.02464$ there is mixing between the eigenstates $j = -3$ and $j = -5$. Both states are strongly ionising. For both $k_i = -3$ and $k_i = -5$, the largest contributions come from these eigenstates, leading to significant ionisation.

It was noted earlier that the estimated ionisation curve, $P_i^{(est)}(F_s)$ for $k_i = -5$ has peaks at $F_s = 0.02482, 0.025$ and 0.02518 that are not present for $P_i(F_s)$. These peaks are seen to correspond to near-degeneracies. Their absence in the $P_i(F_s)$ curve may be a consequence of changes in the eigenvectors caused by the inclusion of ionisation terms in the matrix, $\mathbf{R}'$. In figure 3.17 ionisation curves are plotted for the Averaged Hamiltonian with a step decay function only; the perturbation of the eigenvectors is expected to be smaller in this case. Although very small, ionisation probability peaks can be seen at $F_s = 0.02482, 0.025$ and 0.02518, corresponding to locations of near-degeneracies.

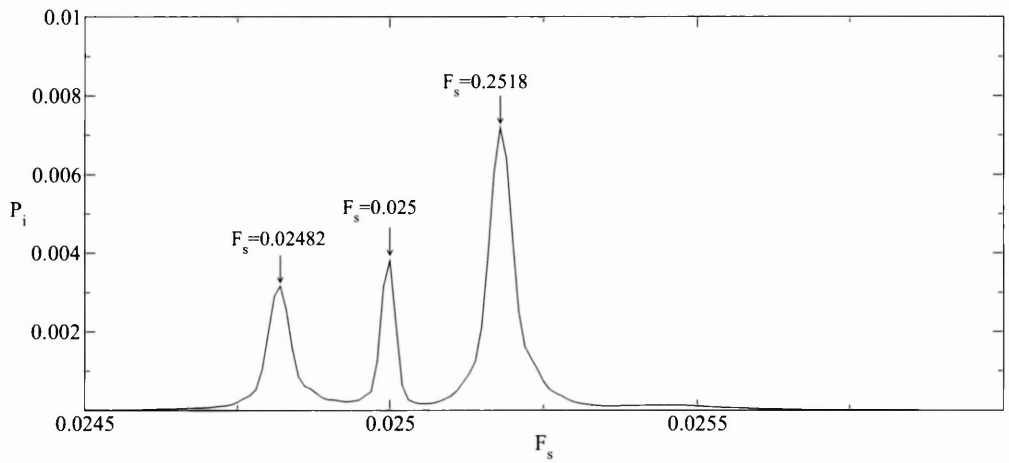

Figure 3.17 Ionisation probability curve, $P_i(F_s)$, for the $O(F^5)$ Averaged Hamiltonian for $n = 10$ using a step decay function. All other parameters are the same as for figure 3.13.

3.4 Low Quantum Numbers

The field parameters chosen for figure 3.6 on page 109 were selected for comparison with experimental results for hydrogen atoms excited such that $n = 50$. In this section, we examine the behaviour of the quantum system for lower quantum numbers.

We wish to select quantum parameters best matching the classical dynamical parameters chosen for figures 2.10 (page 52) and 3.6 (page 109), namely $\Omega_0 = 0.0528$, $F_\mu = 0.13$ and a field envelope of 16-50-16. The azimuthal quantum number, m, is selected such that $m/n = I_m = 0.2$. The initial state, k_i is selected to best match $I_e(0) = -0.4$; however, as the quantum number is decreased there is an increasing disparity between the best fit initial condition,

Table 3.14: Initial quantum states for various n selected to best fit the classical parameters, $I_m = 0.2$ and $I_e(0) = -0.4$.

n	m	k_i	Corresponding $I_e(0)$
100	20	-41	-0.41
50	10	-21	-0.42
40	8	-17	-0.425
20	4	-9	-0.45
10	2	-5	-0.5
5	1	-3	-0.6

$k = k_i$ and the required classical initial condition, as is shown in table 3.14.

In figure 3.18 we compare the quantum and classical ionisation probabilities for decreasing principal quantum number n, with the other quantum parameters selected from table 3.14. The decay terms include tunnelling. It can be seen that there is a general increase in ionisation probability as n is reduced and tunnelling becomes more significant, as discussed in §3.3.1. For the $n = 5$ case, $P_i(F_s) \approx 1$ for all F_s values.

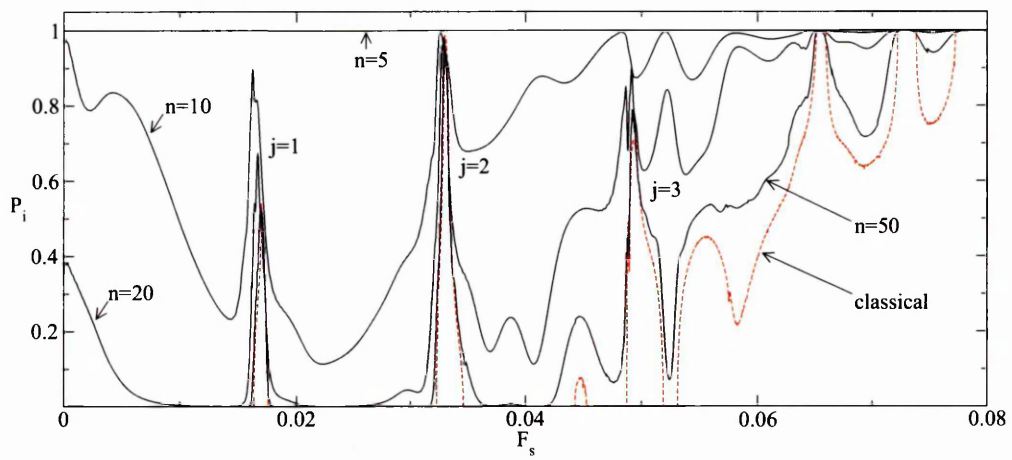

Figure 3.18 Ionisation probabilities for the quantum (solid) and classical (dashed) Averaged Hamiltonian for $\Omega_0 = 0.0528$, $F_\mu = 0.13$ and envelope 16-50-16. Various n values shown, with m and k_i chosen to best fit $I_m = 0.2$ and $I_e(0) = -0.4$

In figure 3.19 $P_i(F_s)$ is shown for a number of longer field durations of the form $16-N_b-16$. It would appear that the ionisation process continues indefinitely until all states are ionised. In figure 3.20 we plot $P_i(t)$ for $F_s = 0.026$, selected as a point away from resonance. The

decay curve is a close fit to an exponential decay curve after an initial period, suggesting that $P_i(t) \to 1$ as $t \to \infty$ and that the decay rate depends solely on the remaining population of states.

This behaviour contrasts markedly with that observed classically. Classically, for the field parameters considered, the orbits are regular and after the field amplitude has reached its maximum value, the orbits settle into periodic orbits that either ionise or remain as stable non-ionising orbits indefinitely. The ionisation probability, $P_i(t)$, tends to some constant value over time as the ionising orbits each reach the threshold ionisation limit.

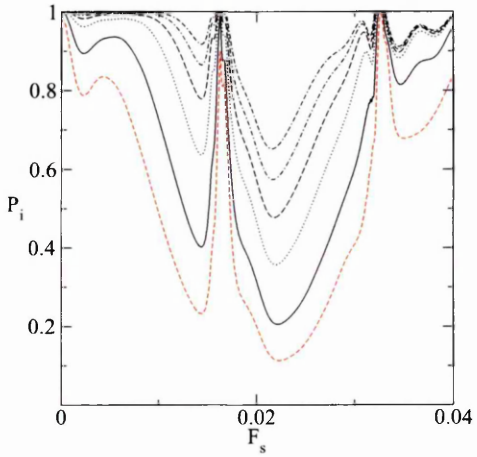

Figure 3.19 Ionisation probability, $P_i(F_s)$, for $n = 10$, $m = 2$ and $k_i = -5$, $F_\mu = 0.13$ and $\Omega_0 = 0.0528$ for field envelopes $16 - N_b - 16$ and $N_b = 50, 100, 200, 300, 400$ and 500. $P_i(F_s)$ increases with N_b.

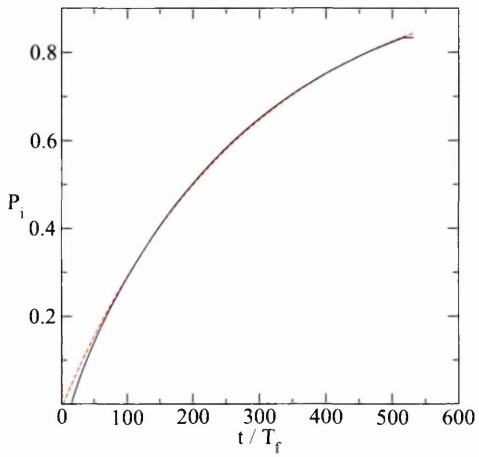

Figure 3.20 The solid line shows $P_i(t)$ for $n = 10$, $m = 2$ and $k_i = -5$, $F_\mu = 0.13$, $\Omega_0 = 0.0528$, $F_s = 0.026$ and field envelope 16-500-16, where $T_f = 2\pi/\Omega_0$. The dashed line is a numerically fitted exponential decay curve.

If an F_s value near resonance is chosen, additional features can be seen in $P_i(t)$. In figure 3.21 curves are shown for $n = 10$ and $n = 39$ for a 16-500-16 field envelope, although for clarity only the first 150 field cycles are shown. Ionisation due to tunnelling still dominates for $n = 10$, but additional bumps can also be seen, both for $n = 10$ and $n = 39$. These are due to the presence of the resonance island; their origin is explored further in §4. In particular, compare this figure with figure 4.4 on page 136.

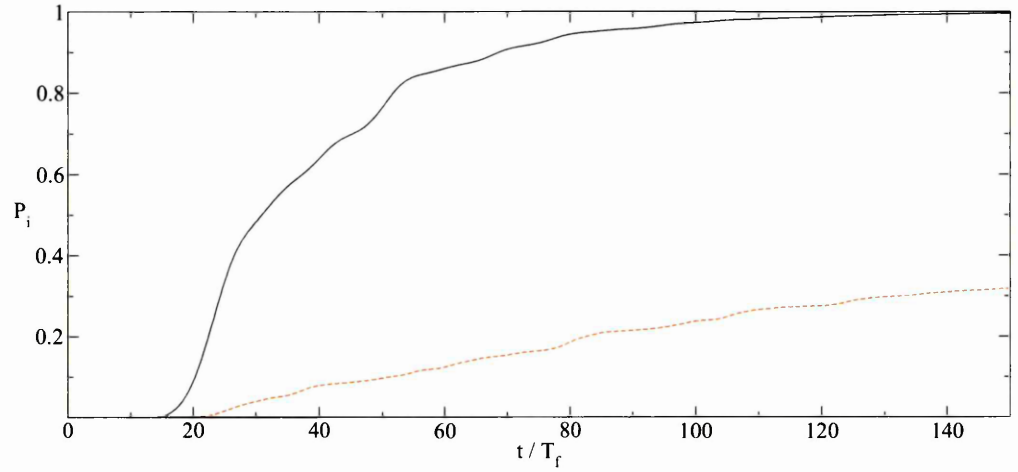

Figure 3.21 The solid line shows $P_i(t)$ for $n = 10$, $m = 2$ and $k_i = -5$, $F_\mu = 0.13$, $\Omega_0 = 0.0528$ at $F_s = 0.0163$ calculated for a field envelope of 16-500-16, where $T_f = 2\pi/\Omega_0$. The dashed line is for $n = 39$, $m = 8$ and $k_i = -16$.

Tunnelling obscures the underlying quantum dynamics for low quantum numbers. In figure 3.22, quantum ionisation probabilities are calculated in the absence of tunnelling, using a step decay function, which mimics the classical ionisation mechanism, in the vicinity of the $j = 1$ resonance. Whilst the $j = 1$ resonance ionisation probability peak is present for all n values shown, there is an increasing difference between the classical and the quantum results as n is reduced.

Part of this difference is due to the difference between the quantum initial condition, $k = k_i$, and the corresponding classical initial condition; however, this is not the principal cause. This is demonstrated in figure 3.23, where classical ionisation curves for $I_e = -0.4$ and $I_e = -0.6$ are compared with a quantum ionisation curve for $n = 5$ and $k_i = -3$.

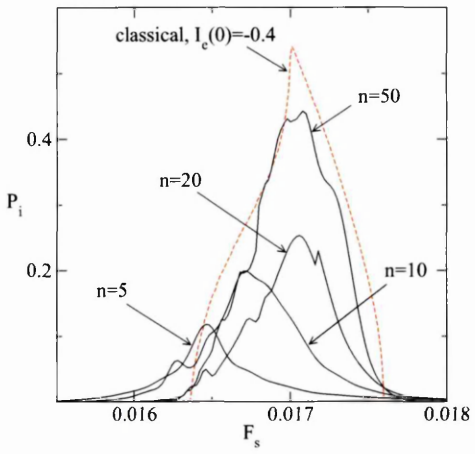

Figure 3.22 Ionisation probabilities for the quantum (solid) and classical (dashed) Averaged Hamiltonian for $\Omega_0 = 0.0528$, $F_\mu = 0.13$ and envelope 16-50-16 in the vicinity of the $j = 1$ resonance. A step decay function is used. Various n values are shown, with m and k_i chosen to best fit $I_m = 0.2$ and $I_e(0) = -0.4$; see table 3.14.

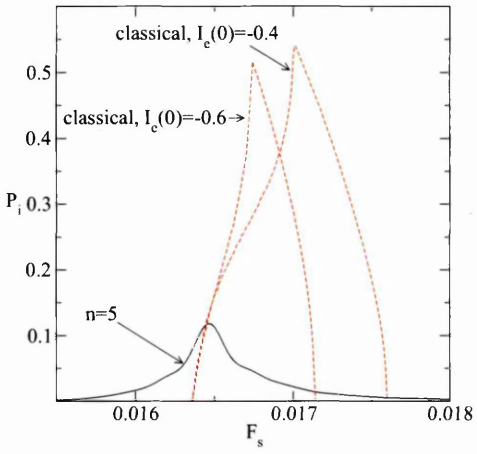

Figure 3.23 Ionisation probabilities for the quantum (solid) and classical (dashed) Averaged Hamiltonian for $\Omega_0 = 0.0528$, $F_\mu = 0.13$ and envelope 16-50-16 for $n = 5$, $m = 1$, $k_i = -3$, $I_e(0) = -0.6$ and $I_e(0) = -0.4$. A step decay function is used.

The changing behaviour in ionisation as n is reduced reflect the differences in underlying dynamical behaviour. This can be exhibited by comparing the quantum expectation value $\langle n_e(t) \rangle$ with the analogous classical case, obtained by generating an ensemble of orbits for the same initial value, $I_e(0)$, and a number of initial angles, $\{\psi_i\}$, taken from a uniform distribution over $[0, 2\pi)$. The classical expectation value is defined as

$$\langle I_e(t) \rangle = \frac{1}{N} \sum_{i=1}^{N} I_e(\psi_i, t).$$

Figures 3.24–3.26 compare this classical expectation value, calculated for $N = 300$ orbits, and the scaled quantum expectation value, $\langle n_e \rangle / n$, for various quantum numbers for the $O(F^5)$ Averaged Hamiltonian. The parameters are $\Omega_0 = 0.0528$, $F_\mu = 0.13$ and $I_m = 0.2$. For these comparisons the field envelope is 0-50-0. The quantum initial conditions are chosen to satisfy $m/n = I_m$ and to best fit $I_e(0) = -0.4$ according to table 3.14. To allow the classical and quantum behaviours to be accurately compared, the classical initial parameter, $I_e(0)$ is chosen to exactly match the quantum initial condition, $I_e(0) = k_i/n$. Two values of F_s are shown in

the vicinity of the $j = 1$ resonance; $F_s = 0.013$ is off-resonance and $F_s = 0.01685$ is near the classical ionisation probability peak. Ionisation channels are switched off in both the classical and quantum calculations.

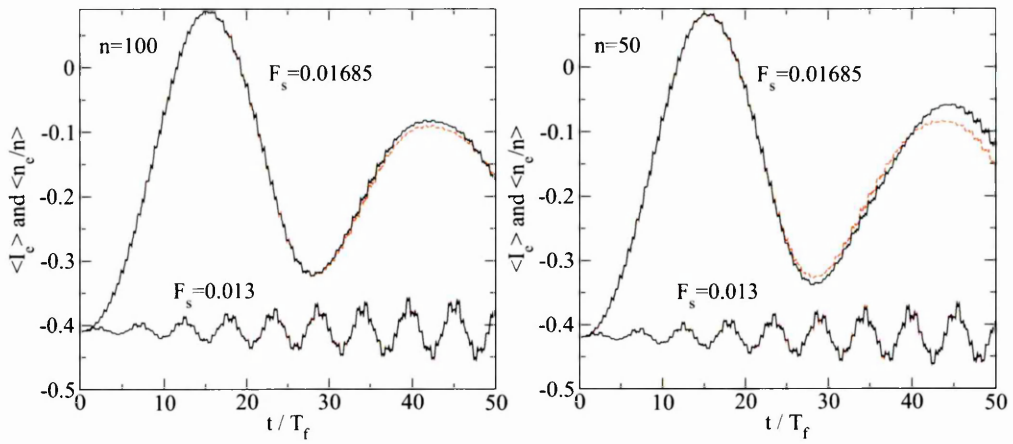

Figure 3.24 Expectation values for the quantum, $\langle n_e(t)/n \rangle$, (solid black lines) and classical, $\langle I_e(t) \rangle$, (dashed red lines) $O(F^5)$ Averaged Hamiltonian with $\Omega_0 = 0.0528$, $F_\mu = 0.13$ and envelope 0-50-0. Principal quantum numbers are shown on the figures, with values of m, k_i and $I_e(0)$ given in table 3.14.

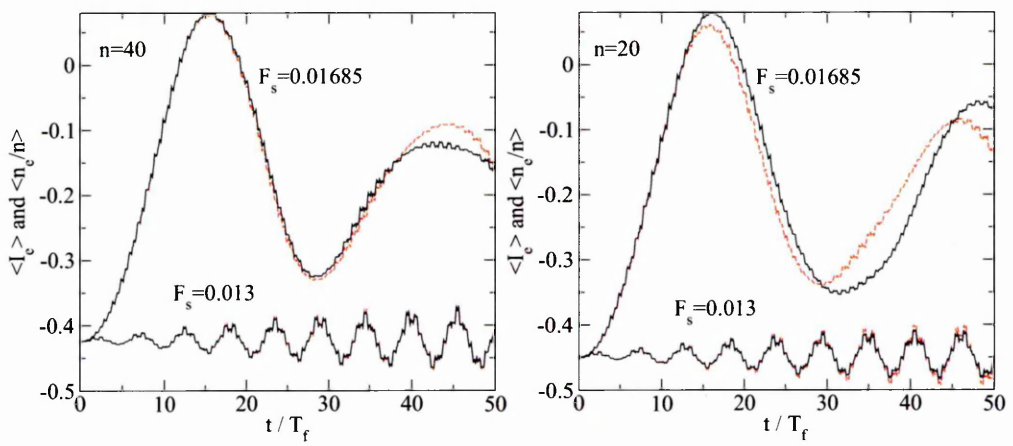

Figure 3.25 As for figure 3.24.

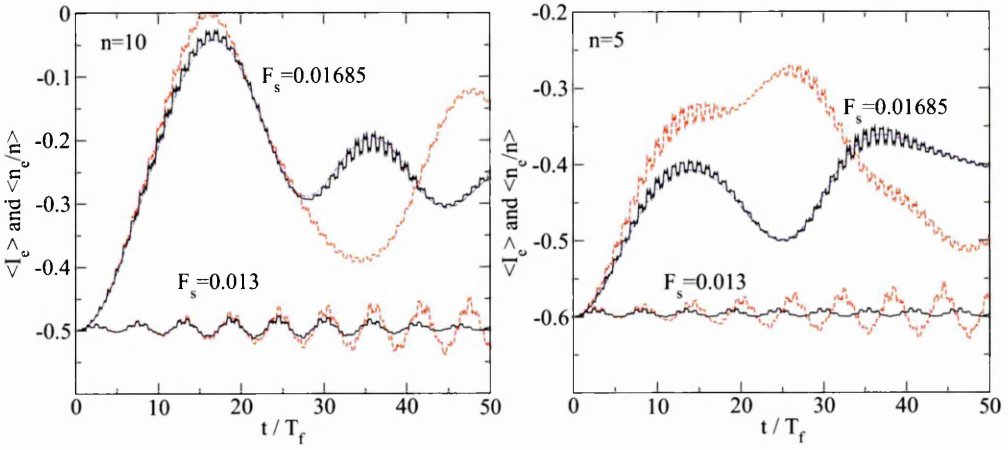

Figure 3.26 As for figure 3.24 with additional blue curves depicting $\langle n_e(t)/n \rangle$ for the quantum Resonance Hamiltonian.

For both the on and off resonance F_s values shown, there is a close match between $\langle I_e(t) \rangle$ and $\langle n_e(t)/n \rangle$ for $n = 100$. As n is reduced the differences increase, although even for n as small as 20 there is a reasonable match for $F_s = 0.013$, away from resonance. The differences between classical and quantum mechanics at smaller n reflect the fundamental differences in the mechanisms involved. In the figures for $n = 5$ and $n = 10$, $\langle n_e(t)/n \rangle$ curves are also shown using blue lines for the Resonance Hamiltonian, $\overline{K}_R$; these provide a good approximation to the quantum curves. Hence, the state vector, $\mathbf{a}(t)$, can be approximated by equation (3.14), page 95,

$$\mathbf{a}(t) = \sum_{k=-N}^{N} e^{-i\lambda_k t} c_k \mathbf{b}_k, \quad c_k = \mathbf{b}_k^\dagger \mathbf{a}(0),$$

where $\{\lambda_k\}$ and $\{\mathbf{b}_k\}$ are the eigenvalues and eigenvectors of the matrix $\mathbf{R}$ of equation (3.13). The expectation curve, $\langle n_e(t) \rangle$, is the sum of coupling terms between different states, p, q, of frequency $\lambda_p - \lambda_q$. For $n = 5$ and $m = 1$, there are 4 states and hence only 6 frequencies contributing to $\langle n_e(t)/n \rangle$. In contrast, the classical curve is calculated as an average over a large sample of trajectories. The time period of the trajectories vary continuously depending on the location of the trajectories in relation to the resonance island.

Chapter 4

Quantal Resonances

In chapter 2 and §2.3 in particular, we showed that for the classical mechanics, many of the features observed in the ionisation probabilities could be understood by examining the role that the resonance island has on determining the evolution of the classical trajectories.

Classically, initial conditions and the size of the resonance island affect the shape of the ionisation probability curves, determining whether rotational and librational orbits near the resonance contribute to ionisation.

In this chapter we will examine quantal ionisation probabilities calculated near two resonances and show how much of the observed behaviour can be understood by comparison with the corresponding classical mechanical system. Some of the differences between quantal and classical ionisation behaviour are identified and explained.

Two resonance locations are examined. For the $j = 1$ resonance and chosen initial conditions, classically only librational orbits contribute to ionisation. For the $j = 2$ resonance, both librational and rotational orbits contribute to ionisation leading to more complex ionisation behaviour.

4.1 The $j = 1$ Resonance

Figure 4.1 shows the $n = 39$ and $n = 100$ quantum and classical ionisation probabilities at the $j = 1$ resonance for $\Omega_0 = 0.0528$, $F_\mu = 0.13$ and field envelope 16-50-16 calculated using the

equations of motion for the Hamiltonians 3.1 (page 91) and 2.24 (page 38) respectively. The calculations use the grid size, $\delta F_s = 1 \times 10^{-5}$ and 300 orbits in the classical calculation. Both the quantal $n = 39$ and $n = 100$ ionisation probability curves are similar to the classical curve, with the $n = 100$ curve being the closer match. This suggests that the classical dynamics provide a good description of the observed quantum physics.

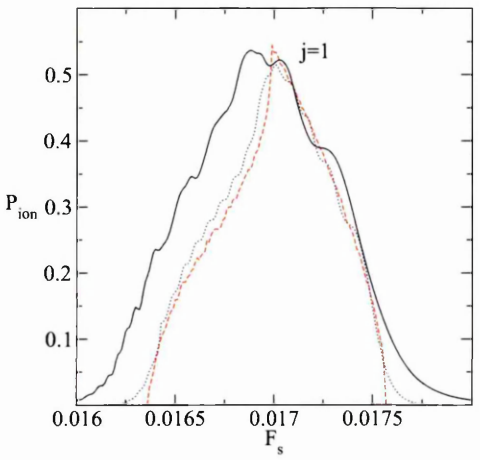

Figure 4.1 Ionisation probabilities, $P_i(F_s)$ for $F_\mu = 0.13$, $\Omega_0 = 0.0528$ and field envelope 16-50-16. Quantum ionisation probabilities for the Hamiltonian $\hat{H}_m$ for $n = 39$, $m = 8$ and $k_i = -16$ are shown with a solid line; for $n = 100$, $m = 20$ and $k_i = -41$ with a dotted line; and classical ionisation probabilities for matching I_m and $I_e(0)$ are shown with a dashed line.

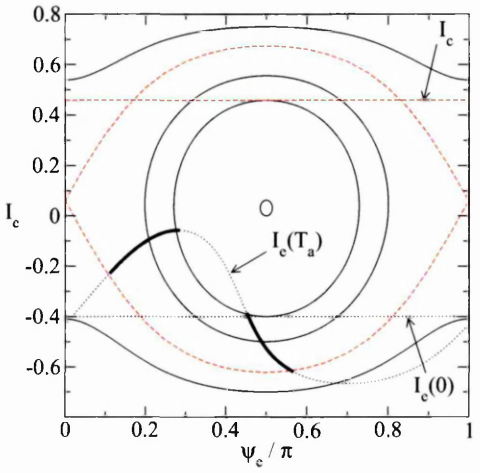

Figure 4.2 Resonance island for $F_\mu = 0.13$, $\Omega_0 = 0.0528$, $I_m = 8/39$ and $F_s = 0.01685$. The separatrix and the critical ionisation line, I_c, are shown by dashed lines. The initial line, $I_e(0)$ is shown by a horizontal dotted line and the evolved line, $I_e(T_a)$, is shown as a thick solid line and a dotted line.

Classically, the ionisation probability can be understood in terms of the effect of the resonance island upon the orbits. Figure 4.2 shows the resonance island for the Resonance Hamiltonian 2.34 (page 44) at the field $F_s = 0.01685$. The initial action, $I_e(0) = -16/39$, and the ionisation critical I_e value, $I_c = 0.459$, are marked with dashed lines. The island width, w_R, is 1.3. The ψ_e values are translated by $\pi/2$ so that the resonance island lies at the centre of the figure.

The resonance island divides the orbits into librational and rotational orbits. If the field is instantaneously applied such that $\lambda(t) = 1$ for $t > 0$, the rotational orbits will all lie below the

resonance island centre. The maximum change in $I_e(t)$ for a librational orbit is w_R, whereas for a rotational orbit the maximum change for $F_s \approx F_s^{(j)}$ is approximately $w_R/2$; for the $j = 1$ resonance, with $I_e(0) = -16/39$, this means that only librational orbits can change sufficiently to ionise. Further, for the given $I_e(0)$ and I_c, all of the librational orbits have sufficient amplitude to ionise with a sudden switch. For a set of initial conditions, $\{\psi_e(0)\}$ uniformly distributed in $(0, \pi)$, the ionisation probability is therefore the fraction of orbits lying within the island; this is confirmed by numerical integration of the classical equations of motion for a field envelope 0-50-0: the fraction of orbits lying in the island is 0.62 and the ionisation probability calculated by numerical integration is 0.61.

When the field amplitude is switched on gradually, the dynamics is changed by the appearance of the resonance island at the bottom of phase space and its subsequent motion through the initial line, $I_e(0)$. The effect of this is shown on the figure by the evolved line $I_e(T_a)$, where $T_a = 16 \times (2\pi/\Omega_0)$, shown as a thick line for the orbits that can ionise (given a sufficiently long duration applied field) and a dotted line for the non-ionising orbits. After the switch-on period the dynamical evolution of the quantum and classical systems is the same as for the instantaneously applied field but with the initial conditions given by $\{a_k(T_a)\}$ and $\{(\psi_e(T_a), I_e(T_a))\}$; hence the ionisation probabilities for a 16-50-16 field envelope are the same as for a 0-50-0 field envelope with a modified distribution of initial conditions, $\{I_e(0), \psi_e(0)\}$.

Ionisation begins at the time when the first orbit reaches $I_e(t) = I_c$. For the 0-50-0 field envelope, ionisation begins at $t/T_f = 10.26$ with P_i rising to 95% of its final value by $t/T_f = 21.73$. The first orbit to ionise is not from the librational orbit closest to the centre of the island. Although this orbit has the shortest period of oscillation, it is not the fastest orbit to cover the portion of phase space from $I_e = I_e(0)$ to $I_e = I_c$. The measured time for onset of ionisation is consistent with the calculated theoretical time for this portion of the orbit.

For the 16-50-16 envelope the onset of ionisation begins later at $t/T_f = 22.31$, as for much of the switch-on time the field has little effect on $I_e(t)$.

Much of the observed quantum ionisation behaviour is consistent with the classical description just given, with the differences appearing primarily because of the difference in ionisation mechanisms. Figure 4.3 compares the expectation value, $\langle n_e(t)/n \rangle$, with the classical expectation value, $\langle I_e(t) \rangle$, calculated as the average of $I_e(t)$ for the remaining bound orbits at

each time t. The expectation values are calculated at $F_s = 0.013$ and 0.01685 for the 0-50-0 field envelope with 300 orbits used to determine the classical curves. The off-resonance value, $F_s = 0.013$, has zero ionisation probability and it can be seen that the classical and quantum expectation curves are virtually indistinguishable, exhibiting small amplitude oscillations in the vicinity of $I_e(0)$. For $F_s = 0.01685$, if ionisation is excluded from the integration, there is a similar close match between classical and quantum expectation values; however, differences become evident when ionisation is included. In figure 4.3 for $F_s = 0.01685$, the classical and quantum expectation curves are very close until ionisation starts, at $t/T_f \approx 9$.

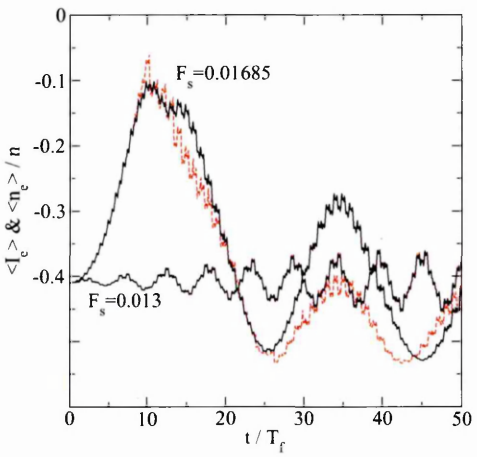

Figure 4.3 Expectation values for $F_\mu = 0.13$, $\Omega_0 = 0.0528$, $I_m = 8/39$ and $F_s = 0.01685$ for the 0-50-0 field envelope. The quantum parameters are $n = 39$, $m = 8$ and $k_i = -16$. The classical curves, $\langle I_e(t) \rangle$, are shown by dashed lines and the quantum curves, $\langle n_e(t)/n \rangle$, are shown by solid lines.

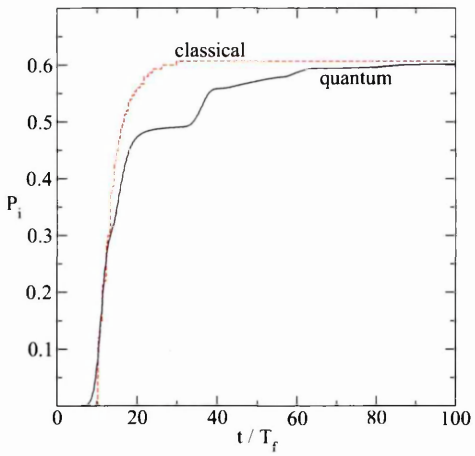

Figure 4.4 Ionisation probabilities, $P_i(t)$ for $F_\mu = 0.13$, $\Omega_0 = 0.0528$, $F_s = 0.01685$ and field envelope 0-100-0. Quantum ionisation probabilities for the Hamiltonian $\hat{H}_m$ for $n = 39$, $m = 8$ and $k_i = -16$ are shown with a solid line; classical ionisation probabilities for matching I_m and $I_e(0)$ are shown with a dashed line.

The different effects of ionisation on the classical and quantum systems can be seen by comparing the evolution of the quantum state distribution with the corresponding classical density for $I_e(t)$. We first consider the classical mechanics.

So that we can compare the classical and quantum mechanics, we define the classical orbit density, $\rho_e(k,t)$, as the fraction of orbits lying in the region, $\left(k - \frac{1}{2}\right)/n \leq I_e(t) < \left(k + \frac{1}{2}\right)/n$ at time t for the substate k.

In figure 4.5 classical contour plots of $\sqrt{\rho_e(k,t)}$ are shown for the 0-50-0 field envelope, with $I_e(0) = -16/39$. A sample of 300 orbits is taken and the k and n values are chosen to match the $n = 39$, $m = 8$ quantum parameters. The vertical axis shows k/n and the horizontal axis shows the time in units of field cycles, $2\pi/\Omega_0$. The contours are at 0.1, 0.2 and 0.3. The plotted points are smoothed for clarity, by averaging over 11 neighbouring time sample points for each (k,t) sample point, centred on the time t. The time grid size, $\delta t = 10$.

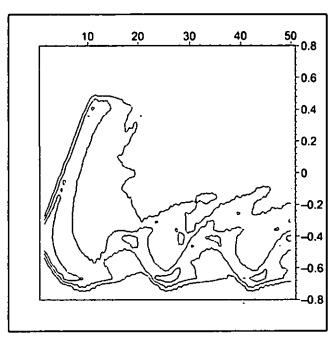

Figure 4.5 Classical $\sqrt{\rho_e(k,t)}$.

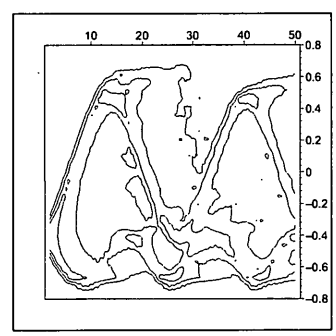

Figure 4.6 Classical $\sqrt{\rho_e(k,t)}$ in the absence of ionisation.

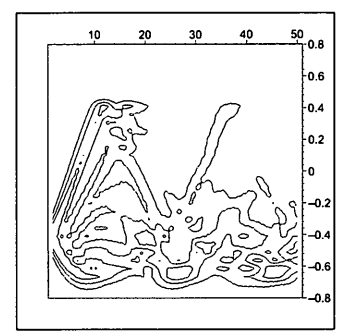

Figure 4.7 Quantum $|a_k(t)|$ with ionisation present.

Quantum $|a_k(t)|$ and classical $\sqrt{\rho_e(k,t)}$ contour plots for $F_s = 0.01685$, $F_\mu = 0.13$, $\Omega_0 = 0.0528$ and field envelope 0-50-0. Quantum parameters are $n = 39$, $m = 8$ and $k_i = -16$. Classical parameters are $I_m = 8/39$ and $I_e(0) = -16/39$. The vertical axis is shown as k/n. Time on the horizontal axis is shown in units of field cycles, $T_f = 2\pi/\Omega_0$. Contours are shown at $|a_k| = 0.1, 0.2$ and 0.3.

In figure 4.6, $\sqrt{\rho_e(k,t)}$ is shown in the absence of ionisation. The classical orbit density is seen to be composed of two components: a larger amplitude component of librational orbits that oscillate around the resonance island centre and a smaller amplitude component of rotational orbits oscillating about points below the separatrix unstable equilibrium points, $I_e = I_{sep} = 0.0605$. In the presence of ionisation, for the F_s value selected, all of the librational orbits ionise and from figure 4.5 it can be seen that after about 20 field cycles, few librational orbits remain. The effect of ionisation on the librational orbits can be seen by examining the fractions of non-ionised orbits above and below I_{sep}, which for a sample of N orbits, with initial conditions, $\{(\psi_i, I_e(0))\}$, are,

$$\rho_L(t) = \frac{1}{N}\sum_{i=1}^{N} H\big(I_e\big(\psi_i(0),t\big) - I_{sep}\big) \quad \text{and} \quad \rho_R(t) = \frac{1}{N}\sum_{i=1}^{N} H\big(I_{sep} - I_e\big(\psi_i(0),t\big)\big)$$

where $H(x)$ is the Heaviside step function. The subscript 'L' is used to denote the fraction of states above I_{sep} as only librational orbits can contribute to $\rho_L(t)$. The subscript 'R' is used as after a sufficient amount of time, only rotational orbits contribute to $\rho_R(t)$. In figure 4.9 these sums are plotted as functions of time. The librational component, $\rho_L(t)$, has a single peak whose maximum coincides with the onset of ionisation; after the peak its value quickly reduces to zero as all librational orbits ionise.

We now consider the quantum mechanics. Figure 4.7 shows the quantum state values, $|a_k(t)|$, for $n = 39$, calculated for the 0-50-0 envelope as a function of k and t. The vertical axis shows k/n and the horizontal axis shows the time in units of field cycles, $T_f = 2\pi/\Omega_0$. The contours and sampling are the same as for figures 4.5 and 4.6.

The initial evolution of $|a_k(t)|$ is similar to $\sqrt{\rho_e(k,t)}$ up to the start of ionisation. However, whereas classically the population of librational orbits has reduced to zero by $t/T_f \approx 30$, this is not the case quantally. In particular, a lobe is seen rising to a peak at $(t/T_f, k/n) \approx (35, 0.4)$ which corresponds with the stepped increase in ionisation seen in figure 4.4. If the field envelope duration is extended further then additional lobes are also seen, with accompanying rises in ionisation, although generally the successive lobes become smaller and less distinct.

The observed differences can be made clearer by examining the quantum analogue of $\rho_L(t)$ and $\rho_R(t)$: these are

$$\mathcal{P}_L(t) = \sum_{k \geq k_s} |a_k(t)|^2 \quad \text{and} \quad \mathcal{P}_R(t) = \sum_{k < k_s} |a_k(t)|^2.$$

Whereas classically $\rho_L(t)$ has one peak after which all ionisation is complete, for the quantum analogue, $\mathcal{P}_L(t)$, there are a series of peaks, as shown in figure 4.8. The peaks are associated with increases in ionisation shown in figure 4.4. As the quantum system evolves, there is a wider distribution of occupied k states so that not all 'librational' states ionise at the first ionisation event. The remaining population of states contribute to further ionisation. The second ionisation event occurs at $t/T_f \approx 35$, the contributing states being visible in figure 4.5 as the rising lobe discussed above; equivalently, the ionisation is associated with the second peak in $\mathcal{P}_L(t)$ seen in figure 4.8.

In figure 4.9, quantum density function, $\mathcal{P}_L(t)$, for $n = 400$ is also shown. It can be seen that the quantum curve for the first peak is similar to the classical curve and that the size of the subsequent peaks have become much smaller.

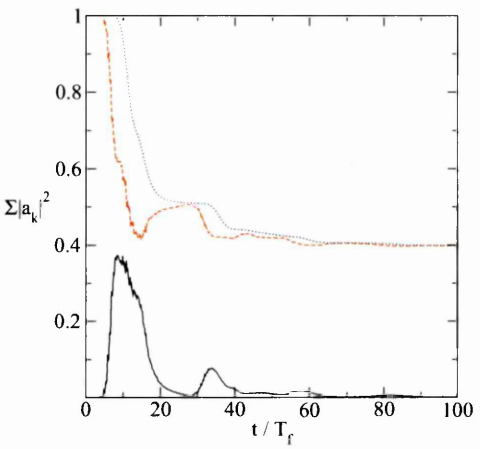

Figure 4.8 Probabilities, $\sum_k |a_k(t)|^2$ for $F_\mu = 0.13$, $\Omega_0 = 0.0528$, $F_s = 0.01685$, $n = 39$, $m = 8$, $k_i = -16/39$ and 0-100-0 field envelope. The sum $\mathcal{P}_R(t)$ is shown by the solid line; $\mathcal{P}_L(t)$ is given by the dashed line; and the dotted line is $\sum_k |a_k(t)|^2$ summed for all k.

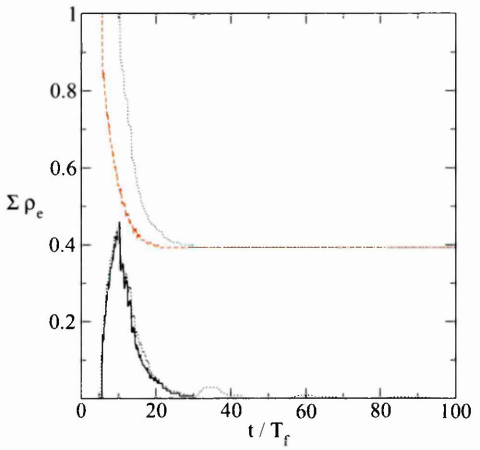

Figure 4.9 Classical densities, $\sum \rho_e(t)$ for $F_\mu = 0.13$, $\Omega_0 = 0.0528$, $F_s = 0.01685$, $I_m = 8/39$, $I_e(0) = -16/39$ and 0-100-0 field envelope. The sum $\rho_R(t)$ is shown as a solid line; the sum $\rho_L(t)$ is shown by a dashed line; and the upper dotted line is $\sum \rho_e(t)$ summed over all I_e. The lower dotted line shows the quantal function, $\mathcal{P}_L(t)$, for $n = 400$, $m = 80$ and $k_i = -161$.

In conclusion, the $n = 39$ quantal and corresponding classical ionisation probability curves at resonance share the same broad features, with peaks of similar size and with their maxima close together. The expectation values, $\langle n_e(t)/n \rangle$ and state densities $|a_k(t)|$ are similar to their classical counterparts up to the time when ionisation begins, indicating that the resonance island has a similar effect on the quantum dynamics to the classical dynamics. Differences arise primarily as a consequence of the different ionisation mechanisms. Classically, the mechanism is discrete — either an orbit will ionise or it will remain bound. For the chosen parameters, the rotational orbits are bound and all of the librational orbits ionise. Each librational orbit ionises within a time that is less than its librational period; for the parameters chosen here, each orbit ionises at a time that is approximately half its librational period.

For the quantum mechanics, ionisation leads to a reduction in the population of states below the classical critical ionisation limit, but the remaining population of bound states continues to evolve, with the dynamics driven by the resonance island. This leads to further ionisation events occurring at intervals after the initial ionisation peak.

4.2 The $j = 2$ Resonance

In this section we examine the $j = 2$ resonance. Although the resonance island width is similar to that of the $j = 1$ resonance, the larger static field means that the classical ionisation limit, I_c, is much smaller. The resonance island can cause sufficient variation in $I_e(t)$ that, for some F_s values near $F_s^{(2)}$, ionisation can also occur for rotational orbits. This causes some differences in the overall ionisation behaviour.

In figure 4.10 (a) the quantum and classical ionisation probabilities, $P_i(F_s)$, are shown for the $j = 2$ resonance; all other parameters are the same as for figure 4.1. There is a close match between the quantum and classical ionisation probabilities, $P_i(F_s)$, with the $P_i(F_s)$ curves reaching their maximum values at similar F_s values and having similar magnitude. The quantum and classical ionisation probabilities become closer as n is increased.

The dynamics causing ionisation is more complex for the $j = 2$ resonance than for the $j = 1$ resonance. This is exhibited in figure 4.10 (b), which shows $P_i(F_s)$ for the shorter field envelope, $16 - 5 - 16$, where there are two local maxima. The same does not occur for the $j = 1$ resonance: for a field envelope $16 - N_b - 16$ where $N_b \leq 50$, if ionisation occurs, only one peak is observed in the F_s interval (0.016,0.018).

Again, for the 16-5-16 envelope a good match is observed between these and classical ionisation probabilities, with a close match at the left ionisation peak. Quantum results are shown for $n = 39$ and $n = 100$ and it can be seen that for higher n the quantum curve becomes increasingly close to the classical curve, although there is still a noticeable difference at the second maxima. However, the close matches between the classical and quantum results suggests that the quantum behaviour can be understood in terms of the classical dynamics.

Classically, the more complex ionisation structure is a consequence of both librational and rotational motion ionising in contrast to $j = 1$ where only librational orbits ionise.

The resonance island width, $w_R = 1.2$ at $F_s = 0.0335$ and for F_s in the range $(0.030, 0.037)$, I_c is in the range $(0.021, 0.153)$. This reduces the change required in $I_e(t)$ to cause ionisation, so that for some F_s values near $F_s^{(2)}$ ionisation is possible from rotational orbits. The field switch-on also has an important effect on the observed ionisation — for field envelopes, $0 - N_b - 0$, there are no N_b values for which two peaks are observed.

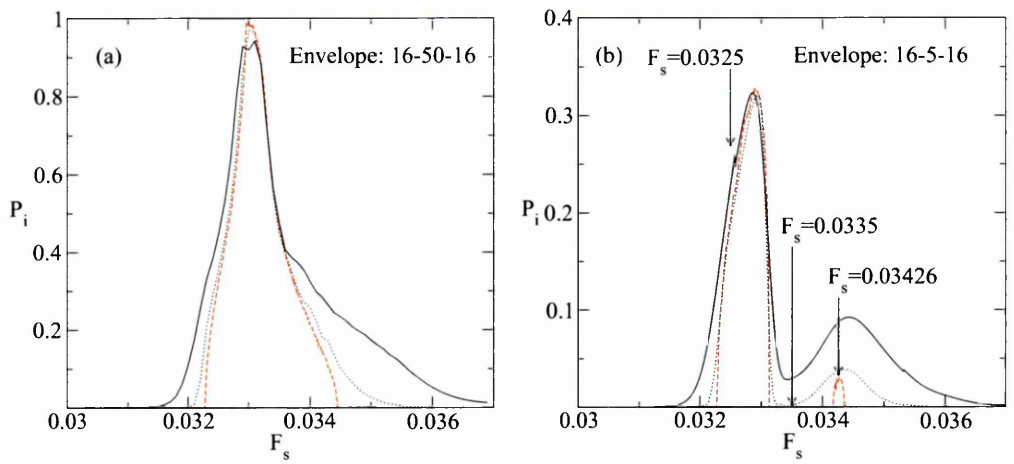

Figure 4.10 $P_i(F_s)$ for $F_\mu = 0.13$, $\Omega_0 = 0.0528$ and field envelopes given in the figures. Quantum results for the Hamiltonian $\hat{H}_m$ for $n = 39$, $m = 8$ and $k_i = -16$ are shown with a solid line; for $n = 100$, $m = 20$ and $k_i = -41$ with a dotted line; and classical results for $I_m = 8/39$ and $I_e(0) = -16/39$ are shown with a dashed line.

The appearance of the two ionisation peaks is most easily understood by examining the phase space plots shown in figures 4.11–4.13 for $F_s = 0.0325, 0.0335$ and 0.03426. These values are chosen by examining figure 4.10 (b): $F_s = 0.0325$ is for the first ionisation peak; $F_s = 0.0335$ is in the region of zero ionisation between the peaks; and $F_s = 0.03426$ is at the second ionisation peak. In each of figures 4.11–4.13 a number of phase curves are shown calculated from the Hamiltonian 2.24 (page 38) using a field envelope of 16-50-16 with the ψ_e values translated using the transformation (2.44) on page 70,

$$\phi_e = \psi_e - \frac{\nu_j t}{2} + j\frac{\pi}{2} - \frac{3}{2}\big(g(T_a) - \overline{g}T_a\big),$$

where $g(t)$ and $\overline{g}$ are given by equations (2.19) and (2.20) on page 37. This transformation is used only for $t \geq T_a$ when $\lambda(t) = 1$.

For clarity, the phase curves in figures 4.11–4.13 are shown only for times when $\lambda(t) = 1$ and to see the individual phase curves more clearly, only a few field periods are shown. On each diagram the curve shown as a dotted line with thick solid segments is the initial phase line $(\theta, I_e(0))$ evolved to time $t = T_a$. The thick line segments show the orbits that ionise if sufficient time is allowed. The horizontal dotted lines indicate the critical ionisation point, $I_e = I_c$. The curved dashed lines mark regions where ionisation would occur for orbits of the Resonance Hamiltonian 2.34 (page 44): above these lines all orbits would ionise, given sufficient time. In figure 4.12 the dashed line also marks the lower separatrix boundary.

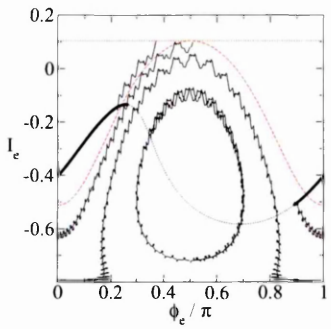

Figure 4.11 $F_s = 0.0325$

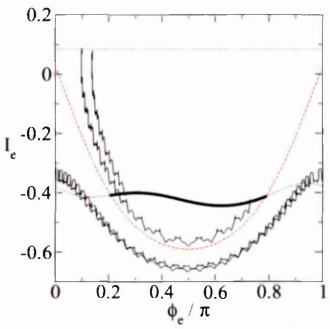

Figure 4.12 $F_s = 0.0335$

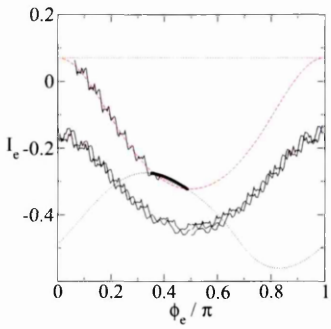

Figure 4.13 $F_s = 0.03426$

Phase curves for various F_s values, for $F_\mu = 0.13$, $\Omega_0 = 0.0528$, $I_m = 8/39$ and $I_e(0) = -16/39$. Phase curves are shown with solid black lines. The black curved dashed lines and solid black segments show the evolved line, $I_e(T_a)$, with the solid black segments showing orbits that ionise given sufficient time. The red horizontal dashed line marks the classical ionisation limit, I_c. All orbits above the curved dashed red lines ionise for the Resonance Hamiltonian.

From each of the figures the ionising sections of the evolved line $I_e(T_a)$ mostly lie within the ionising region expected for the Resonance Hamiltonian. The ionising orbits outside this region are a consequence of the small high frequency oscillations, produced by the additional higher frequency perturbations not present in the Resonance Hamiltonian.

For $F_s = 0.0325$ ionisation is possible only from rotational orbits. Two ionising orbits are shown; however, while the rotational orbit starting on the left ionises after $18.8T_f$ the rotational orbit starting on the right takes $41.8T_f$. Hence for a 16-5-16 envelope only the former contributes to the ionisation probability. It can be seen that for this F_s value the field switch-on has a significant effect on $I_e(t)$. In the absence of the switch-on none of the orbits have sufficient time to ionise.

For $F_s = 0.0335$, all the librational orbits ionise, but all rotational orbits remain bound. However, for a 16-5-16 envelope there is insufficient time for any of the librational orbits to reach ionisation and so $P_i = 0$. At $F_s = 0.03426$ the field envelope sufficiently distorts $I_e(T_a)$ to allow a small fraction of rotational orbits to ionise.

For the quantum mechanics, although two peaks in $P_i(F_s)$ are seen for the 16-5-16 envelope, ionisation occurs for all F_s values between the peaks, in contrast to the classical $P_i(F_s)$ curve. In figure 4.14, probabilities are shown for the 16-5-16 field envelope for $F_s = 0.0341$ where the classical ionisation is zero, whilst $P_i = 0.074$ for the $n = 39$ results. Probabilities are shown summed over states lying above the effective classical ionisation limit,

$$\mathcal{P}_1(t) = \sum_{k \geq k_c} |a_k(t)|^2, \tag{4.1}$$

and below the effective ionisation limit,

$$\mathcal{P}_2(t) = \sum_{k < k_c} |a_k(t)|^2, \tag{4.2}$$

where k_c is the lowest quantum state for which classical ionisation would occur. It can be seen that $\mathcal{P}_1(t) = 0$ until $t/T_f > 19$. The field switch-off begins at $t/T_f = 21$ leaving a relatively small time period for ionisation to occur. The dotted line shows the survival probability, $1 - P_i(t) = \mathcal{P}_1(t) + \mathcal{P}_2(t)$, and although the upper states included in $\mathcal{P}_1(t)$ are populated until $t/T_f > 28$, the reducing field amplitude means that the tunnelling probabilities rapidly reduce and by $t/T_f \approx 22$ all ionisation has ceased. The upper dashed black line shows the survival probability for a step decay function, where ionisation is only permitted for $k \geq k_c$.

Equivalent classical state occupation densities are shown in figure 4.15 calculated by determining the time dependent density of non-ionised orbits. For a sample of N orbits, with initial conditions, $\{(\psi_i, I_e(0))\}$, the fraction of orbits corresponding to substates $k \geq k_c$ is,

$$\rho_1(t) = \frac{1}{N} \sum_{i=1}^{N} H\left(I_e(\psi_i(0), t) - \frac{1}{n}\left(k_c - \frac{1}{2}\right)\right) \tag{4.3}$$

and the fraction of classical orbits corresponding to the substates $k < k_c$ is,

$$\rho_2(t) = \frac{1}{N}\sum_{i=1}^{N} H\left(\frac{1}{n}\left(k_c - \frac{1}{2}\right) - I_e\big(\psi_i(0), t\big)\right). \tag{4.4}$$

It can be seen that although the classical and quantum dynamics result in occupation of states close to the critical ionisation limit in similar times, $\rho_1(t)$ rises from zero slightly later than for the quantum system. Critically, although there are a small number of orbits that satisfy $I_e(t) \geq (k_c - 1/2)/n$, there is insufficient time for any orbit to reach $I_e(t) = I_c$ before the field switch-off begins; hence there is no ionisation.

The quantal ionisation depicted in figure 4.14 is a consequence of two quantal effects: ionisation due to tunnelling from states $k < k_c$; and the populating of states $k \geq k_c$ at earlier times than for the equivalent classical system. The dominant contribution is from the first effect, as can be seen by comparing the survival probability calculated with tunnelling — shown as a black dotted line in figure 4.14 — and the survival probability calculated for ionisation restricted to states $k \geq k_c$ — shown as the upper black dashed line in the same figure.

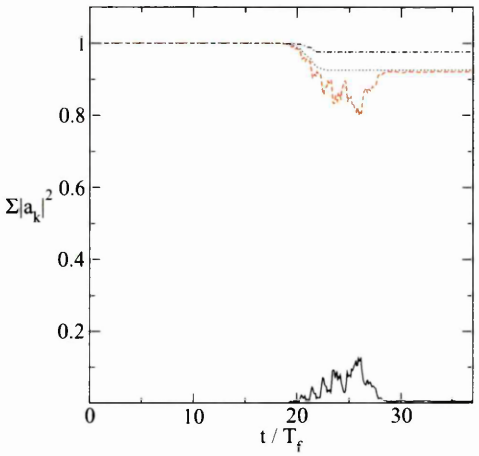

Figure 4.14 Quantum probabilities, $\sum |a_k(t)|^2$, for $F_\mu = 0.13$, $F_s = 0.0341$, $\Omega_0 = 0.0528$ and field envelope $16 - 5 - 16$. The solid line shows $\mathcal{P}_1(t)$ given by equation (4.1); the lower dashed line shows $\mathcal{P}_2(t)$ given by equation (4.2); and the survival probability, $1 - P_i(t)$, is shown by a dotted line. The upper dashed line is the survival probability if ionisation is only permitted from states, $k \geq k_c$.

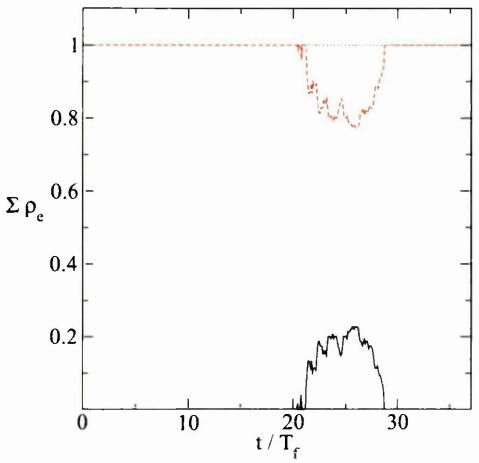

Figure 4.15 Classical probabilities, $\sum \rho_e(t)$, for $F_\mu = 0.13$, $F_s = 0.0341$, $\Omega_0 = 0.0528$ and field envelope $16 - 5 - 16$. The solid line shows $\rho_1(t)$ from equation (4.3); the lower dashed line shows $\rho_2(t)$ from equation (4.4); and the survival probability, $1 - P_i(t)$, is shown by a dotted line.

In summary, this examination of the $j = 2$ resonance has shown that for certain initial conditions both rotational and librational orbits can contribute to the classical ionisation. The different time scales associated with these types of orbits means that for short duration field envelopes, $16 - N_a - 16$ two separated ionisation peaks can arise, associated with the ionisation of rotational orbits, although we note that the peaks only arise if there is a gradual field switch-on, which sufficiently distorts the initial phase line, $(\theta, I_e(0))$ to allow subsequent ionisation during the short time, $t/T_f = N_b$.

The complex effects that the rotational and librational orbits have on the ionisation probability are also manifest in the quantum system, with two distinct maxima arising at similar locations to the classical peaks. As for $j = 1$, differences between classical and quantum ionisation behaviour are primarily a consequence of the different ionisation mechanisms.

Chapter 5

Ionisation Times

5.1 Introduction

The time taken for ionisation to occur is characteristically different on and off resonance. Away from resonances, when the field amplitude is constant (after switch-on), the action, $I_e(t)$, undergoes small oscillations around a constant value. During the field switch-on a greater variation in I_e is observed, but this is normally much less than the variation observed in the vicinity of a dynamical resonance.

Ionisation occurs when the field amplitude has risen to sufficient size to satisfy ionisation conditions (2.42), i.e. when

$$\lambda(t)(F_s + F_\mu) > F_c(I_e(t), I_n, I_m) \quad \text{and/or} \quad \lambda(t)(F_\mu - F_s) > F_c(-I_e(t), I_n, I_m) \quad \text{if} \quad F_\mu > F_s.$$

Away from resonances, $I_e(t) \approx I_e(0)$ and the orbits ionise at approximately the same time, so that $P_i(t)$ approaches a step function,

$$P_i(t) \approx \begin{cases} 0, & t < T_i, \\ 1, & t > T_t, \end{cases}$$

where T_i is the ionisation time. In figure 5.1, the ionisation probability, $P_i(t)$, is shown for

$F_s = 0.0168$, near the $j = 1$ resonance, and $F_s = 0.062$, away from resonance. Away from resonance, the ionisation probability rises from 0 to 97% of its final figure within $1.5T_f$. In contrast, for $F_s = 0.0168$, near the $j = 1$ resonance, the corresponding rise in $P_i(t)$ takes $18T_f$.

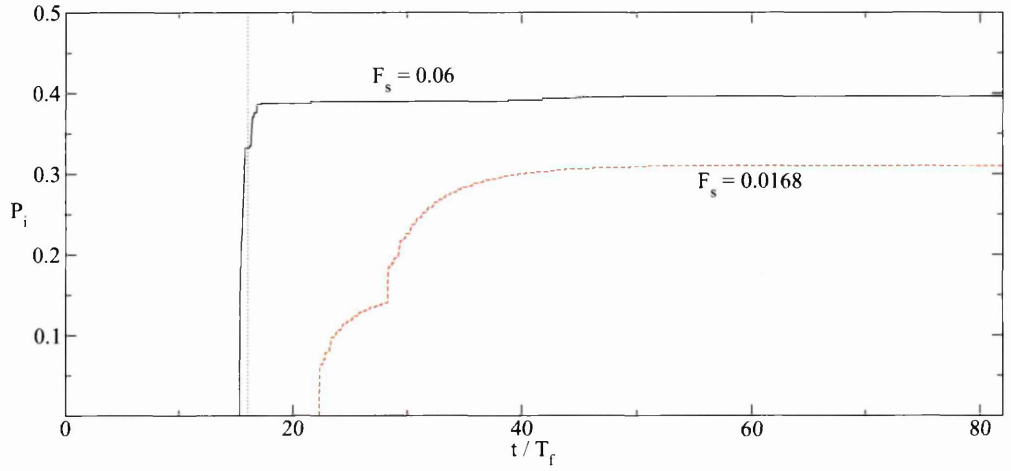

Figure 5.1 Classical ionisation probability, $P_i(t)$, for the Averaged Hamiltonian near resonance at $F_s = 0.0168$ (red dashed line) and away from resonance at $F_s = 0.06$ (solid black line). The field parameters are $F_\mu = 0.13$, $\Omega_0 = 0.0528$ and an envelope of 16-50-16. The end of the field switch-on, $T_a = 2\pi N_a/\Omega_0$, is marked with a blue dotted line.

Near a resonance, ionisation times depend upon the initial conditions and are generally larger than when there is no resonance; we will show that where orbits near the island separatrix are the principal contributors to ionisation, the ionisation time is larger. Further, we shall show numerically that quantum mechanics mimics this classical behaviour very well for $n = 400$, and even for $n = 39$ the ghost of the separatrix survives in the quantum mechanics.

Here we define the ionisation time, $T_i(F_s)$, as the time taken for half of the ionising orbits to have ionised. In the figures the ionisation time is scaled to lie in the range $[0, 1]$, by dividing $T_i(F_s)$ by T_e, where T_e is the time at the end of of the applied field envelope, $T_e = 2\pi(2N_a + N_b)/\Omega_0$. This definition allows later comparison with quantal ionisation times.

Figure 5.2 shows the ionisation time as the static field, F_s, is varied for the exact classical dynamics for $\Omega_0 = 0.0528$, $F_\mu = 0.13$ and a field envelope of 16-50-16. The ionisation probability is shown for comparison. The time at which the field envelope reaches its maximum amplitude, $2\pi N_a/\Omega_0$, is shown by a red dotted line.

Figure 5.3 shows the corresponding results for the Averaged Hamiltonian using using 1600 orbits and a grid size, $\delta F_s = 1 \times 10^{-5}$. The approximation shares much of the structure seen in the exact case and hence we can use the simpler approximation to understand the behaviour exhibited in figures 5.2 and 5.3.

The peaks in ionisation time shown in figure 5.3 are very sharp; for example, for the $j = 1$ resonance, the ionisation time falls from its peak value at $T_i/T_e = 0.73$ to $T_i/T_e = 0.56$ in one grid interval, $\delta F_s = 1 \times 10^{-5}$.

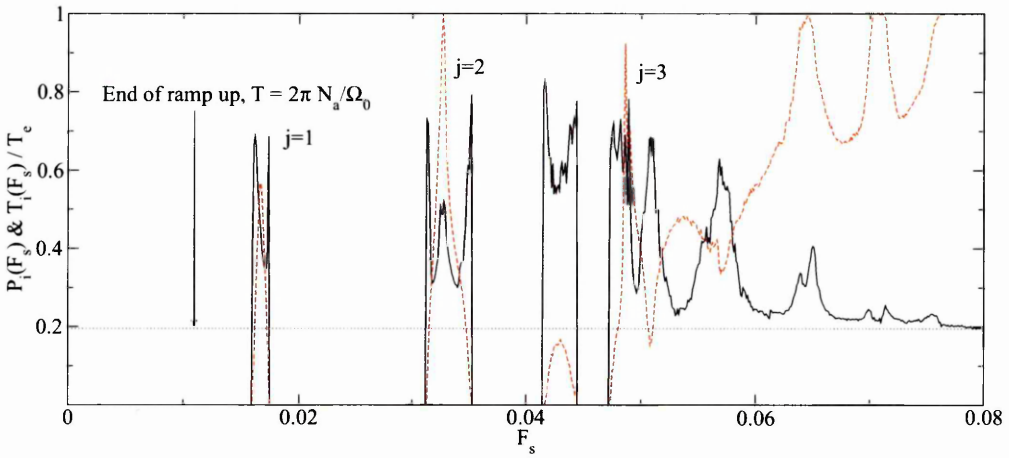

Figure 5.2 Ionisation time, $T_i(F_s)$ (solid line), and ionisation probability, $P_i(F_s)$ (dashed line), for $F_\mu = 0.13$, $\Omega_0 = 0.0528$, field envelope 16-50-16, $I_m = 0.2$ and $I_e(0) = -0.4$ for the exact dynamics. The end of the field switch-on, $T_a = 2\pi N_a/\Omega_0$, is marked with a blue dotted line.

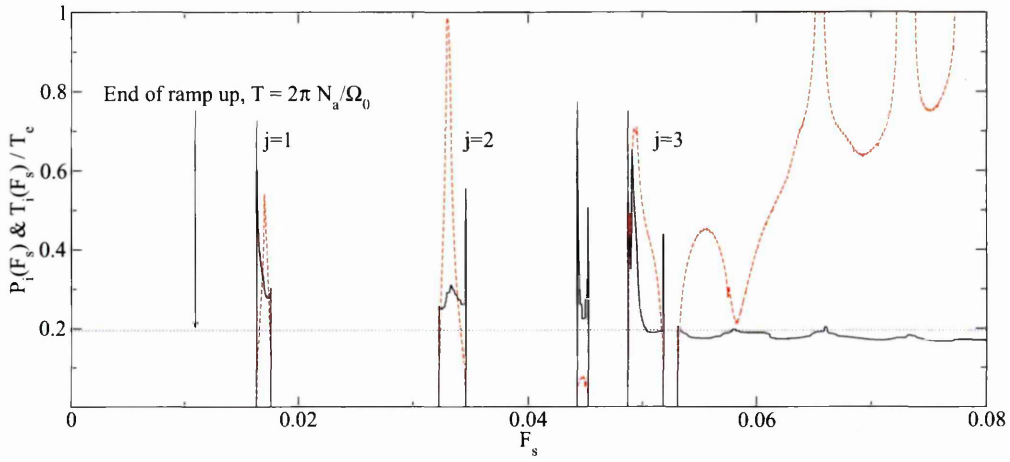

Figure 5.3 As for figure 5.2 for the $O(F^5)$ Averaged Hamiltonian.

The following general behaviour can be observed for the ionisation times for both the exact classical dynamics and the Averaged Hamiltonian:

1. Away from resonances if ionisation occurs then the ionisation times are similar to the switch-on times, consistent with the explanation outlined at the beginning of this section: $I_e(t)$ changes little with time with ionisation happening when $\lambda(t)$ has increased to an amplitude such that one of the conditions (2.42) are met. For the Averaged Hamiltonian ionisation occurs for all $F_s \geq 0.0531$ and the ionisation times are close to the end of the switch-on period, $T_a = 2\pi N_a/\Omega_0$.

2. For the exact and the $O(F^5)$ Averaged Hamiltonians, in the vicinity of the resonances, large ionisation times are observed, with the highest ionisation times occurring near edges of the ionisation probability peaks. For both the Averaged Hamiltonian and the exact Hamiltonian, an additional peak in ionisation time is observed for the $j = 2$ resonance. Figures 5.4 (a) and (b) show the $j = 1$ and $j = 2$ resonances in more detail for the Averaged Hamiltonian.

3. In general, the ionisation times at the edges of the resonance ionisation islands are higher for the exact case than for the approximate Averaged Hamiltonian.

4. There is an ionisation peak between the $j = 2$ and $j = 3$ peaks for the Averaged Hamiltonian (at $F_s = 0.045$) and the exact classical dynamics (at $F_s = 0.043$). The

cause of this peak is not known, but the fact that $T_i(F_s)$ has similar structure to the resonance peaks suggests that this is also caused by a resonance with an associated resonance island.

5. The ionisation times for the Averaged Hamiltonian are not as good an approximation for $F_s \gtrsim 0.52$. This might be due to the series truncation at $O(F^5)$ in the Averaged Hamiltonian, or because $F_s + F_\mu$ is close to the radius of convergence of the perturbation expansion in I_e.

5.2 Analysis

In this section we show that the behaviour of the ionisation times at the $j = 1$ and $j = 2$ resonances, seen in figures 5.2 and 5.3, is due to the large variation in the period of the librational and rotational motions near the resonance island separatrix.

The gradual switch-on of the field envelope also affects ionisation times, because a significant change in I_e can occur during the field switch-on and this can have an effect on ionisation. However, the general behaviour is the same for sudden and adiabatic switches, as can be seen by comparing the results shown in figures 5.4 (a) and (b) for a field envelope of 16-50-16, with figures 5.5 (a) and (b), calculated for constant amplitude field envelopes of 0-50-0, but otherwise identical dynamical parameters.

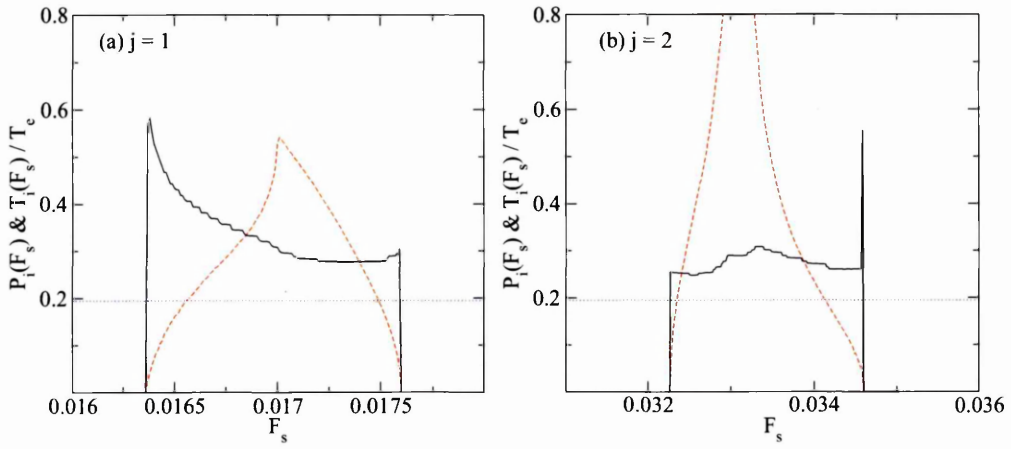

Figure 5.4 Ionisation times, $T_i(F_s)$ (black solid line), and ionisation probabilities, $P_i(F_s)$ (red dashed line), for the resonances $j = 1$ and $j = 2$, for $F_\mu = 0.13$, $\Omega_0 = 0.0528$ and field envelope 16-50-16 for the $O(F^5)$ Averaged Hamiltonian. The end of the field switch-on, $T_a = 2\pi N_a/\Omega_0$, is marked with a blue dotted line. The overall field duration is T_e.

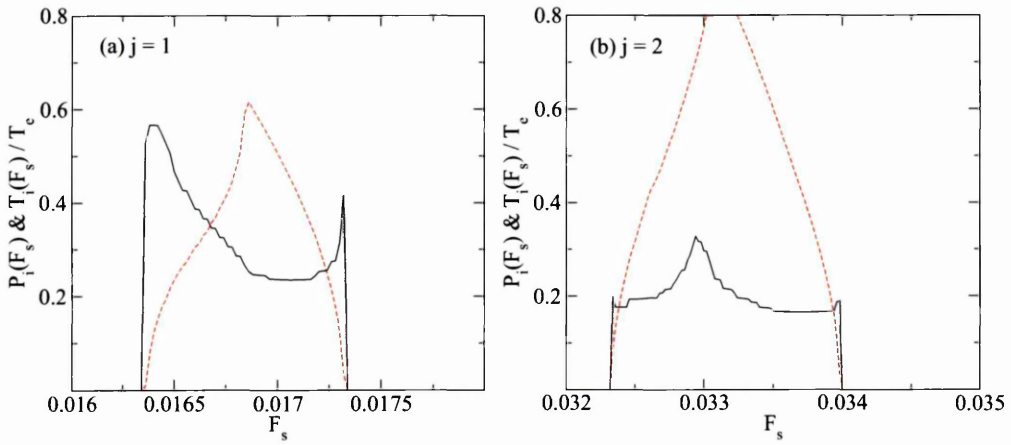

Figure 5.5 As for figure 5.4 with envelope 0-50-0.

It can be seen that the overall behaviour is similar, although there are the following differences:

1. The resonance peak widths are smaller for the 0-50-0 envelope field. The reason for this was provided in §2.3.

2. The ionisation times at the edges of the resonance island are generally higher in the

constant field amplitude case, with the exception of the $j = 2$ right hand edge.

The constant envelope behaviour can be explained by considering ionisation times for the simpler case of the Resonance Hamiltonian. In the following sections, an approximation for the period of librational and rotational orbits for the Resonance Hamiltonian is calculated and used to calculate the approximate ionisation time.

The sharp peak at the right edge of the ionisation time plot for $j = 2$ is not explained by the behaviour for a constant amplitude field. The cause of it is discussed in §5.3 on page 167.

5.2.1 Time Period for the Dynamical Resonance Hamiltonian

A simple approximation can be found for the librational time period at the stable equilibrium centre of the resonance island when $F_s = F_s^{(j)}$ when the centre of the island lies on the line $I_e = 0$. At this point, in scaled coordinates, the Resonance Hamiltonian, equation (2.34), page 44, becomes,

$$\overline{K}_R = \overline{E}_R(I_e, F) - \frac{F_\mu \Omega_0}{4} A(I_e) B(I_e) \widetilde{\mathcal{J}}_j \cos(2\theta_R).$$

Truncating $\overline{E}_R(I_e, F)$ to $O(F^2)$ and making the approximation, $A(I_e)B(I_e) \approx A(0)B(0)$, reduces the Hamiltonian to that a simple harmonic oscillator, from which the librational time period, T_l, is,

$$T_l = \frac{8\pi}{\sqrt{3F_\mu \Omega_0 |\widetilde{\mathcal{J}}_j| (1 - I_m^2)(2F_s^2 + F_\mu^2)}}. \tag{5.1}$$

The librational time period is at its minimum at the island centre, so this expression is useful for estimating the lower bound of librational time periods. If the field duration is comparable or shorter than half of this minimum librational period then the ionisation can be reduced. For smaller island sizes the librational period is longer, so long field durations are required for ionisation to occur for small islands. This is discussed further in §6.3 on page 184.

We wish to examine ionisation times across the ionisation peaks near resonances. To do this requires a more accurate expression than (5.1) that is valid at F_s values other than $F_s = F_s^{(j)}$. For a time independent Hamiltonian, the one dimensional Hamilton-Jacobi equation can be written in the form

$$H\left(q, \frac{\partial W}{\partial q}\right) = E,$$

where $W(q,E)$ is the characteristic function and $p = \partial W/\partial q$. The time may be calculated as

$$t - t_0 = \frac{\partial W}{\partial E}.$$

Hence,

$$t - t_0 = \frac{\partial}{\partial E}\int p(q,E)\,\mathrm{d}q, \tag{5.2}$$

where in the integration appropriate choice is made of the multivalued function, $p(q,E)$.

We wish to transform the Resonance Hamiltonian, (2.34), to a form more amenable to the calculation of the time period. Rewrite it as,

$$\overline{K}_R = \sum_{k=1}^{\infty} u_k I_e^k + \epsilon\widetilde{\mathcal{J}}_j \sum_{k=0}^{\infty} v_k I_e^k \cos(2\theta_R),$$

where $\epsilon = -F_\mu\Omega_0/4$ and the coefficients $\{u_k\}$ and $\{v_k\}$ are defined by

$$\overline{E}_R(I_e,F) = \sum_{k=1}^{\infty} u_k I_e^k, \quad \text{and} \quad A(I_e)B(I_e) = \sum_{k=1}^{\infty} v_k I_e^k.$$

Note that the function $A(I_e)B(I_e)$ is an even function of I_e, so for odd k, $v_k = 0$.

We seek a canonical transformation $F_2 = \theta_R(P+\alpha)$ such that the transformed Hamiltonian is of leading order P^2. The transformed Hamiltonian, $\overline{K}_T$, is

$$\begin{aligned}\overline{K}_T &= P\sum_{k=1}^{\infty} k u_k \alpha^{k-1} + P^2\sum_{k=2}^{\infty} u_k\binom{k}{2}\alpha^{k-2} + P^3\sum_{k=3}^{\infty} u_k\binom{k}{3}\alpha^{k-3} + \cdots \\ &+ \epsilon J_j'\left[\sum_{k=0}^{\infty} v_k\alpha^k + P\sum_{k=1}^{\infty} k v_k\alpha^{k-1} + P^2\sum_{k=2}^{\infty} v_k\binom{k}{2}\alpha^{k-2} + \cdots\right]\cos(2\theta_R),\end{aligned} \tag{5.3}$$

where terms independent of P and θ_R have been dropped.

Choosing α such that

$$\sum_{k=1}^{\infty} k u_k \alpha^{k-1} = 0, \tag{5.4}$$

where $|\alpha| < 1$, the leading energy term in $\overline{K}_T$ is $O(P^2)$. In the region $|\alpha| < 1$, the function is approximately linear and to a first approximation, $\alpha = -u_1/2u_2$.

To simplify the writing of the equations, we define the terms

$$U_r = \sum_{k=r}^{\infty} u_k \binom{k}{r} \alpha^{k-r} \quad \text{and} \quad V_r = \sum_{k=r}^{\infty} v_k \binom{k}{r} \alpha^{k-r}.$$

In the region of the resonance, it is numerically found that $|U_k P^k| \gg |U_{k+1} P^{k+1}|$ and hence the Hamiltonian, (5.3), can be approximated to reasonable accuracy by

$$\overline{K}_T \approx U_2 P^2 + \epsilon \widetilde{J}_j \sum_{k=0}^{\infty} V_k P^k \cos(2\theta_R).$$

The magnitude of the terms $\{V_k\}$ reduces more slowly as k is increased. However, for the purposes of calculating the time period, a reasonable approximation to the Hamiltonian can be obtained by truncating the sum in V_k after three terms, giving the final approximate Hamiltonian,

$$\overline{K}_T \approx U_2 P^2 + \epsilon \widetilde{J}_j \left(V_0 + V_1 P + V_2 P^2\right) \cos(2\theta_R) = E_T, \tag{5.5}$$

where E_T is the energy, which is constant. From this approximation, the momentum P can be expressed as $P(\theta_R, E_T)$. Substituting for P in equation (5.2) gives, for θ_R between the turning points,

$$t - t_0 = \int \frac{\mathrm{d}\theta_R}{\sqrt{a\cos^2 2\theta_R + b\cos 2\theta_R + c}}, \tag{5.6}$$

where $a = \epsilon^2 \widetilde{J}_j^2 (V_1^2 - 4V_0 V_2)$, $b = 4\epsilon \widetilde{J}_j (E_T V_2 - U_2 V_0)$ and $c = 4U_2 E_T$.

For librational motion, the period is

$$T_l = 4 \int_{\theta_0}^{\theta_1} \frac{\mathrm{d}\theta_R}{\sqrt{a\cos^2 2\theta_R + b\cos 2\theta_R + c}}, \tag{5.7}$$

For the resonances we will consider, J_j' is negative, which corresponds to motion around a librational centre at $\theta_R = \pi/2$ so that $\theta_0 = \pi/2$. The limit, θ_1, is determined from the maximum value of θ_R for the motion.

For rotational motion, the period is

$$T_r = 2 \int_{\pi/2}^{\pi} \frac{\mathrm{d}\theta_R}{\sqrt{a\cos^2 2\theta_R + b\cos 2\theta_R + c}}. \tag{5.8}$$

Each of the integrals, (5.6)–(5.8), is evaluated numerically.

5.2.2 Calculation of Approximate Ionisation Times at Resonance

The overall ionisation time is calculated by averaging the ionisation times for a set of phase curves for a chosen initial action, $I_e(0)$, and initial canonically conjugate angles uniformly distributed in the range $[0, 2\pi)$. Whilst the ionisation time depend on the time periods of the ionising phase curves, it also depends on where the phase curve is located relative to the resonance island and the ionisation critical limit, I_c.

The presence of ionisation in the vicinity of the dynamical resonances, $F_s^{(j)}$, depends on the size of the resonance island (see §2.1.2, page 36). For the Resonance Hamiltonian, assuming a constant amplitude field of the form 0-N_b-0, ionisation can only occur if the island size, w_R — defined as the maximum separation in I_e between the two separatrix curves — satisfies the criterion,

$$w_R \geq I_c - I_e(0).$$

In the case of the $j = 1$ resonance, this criterion is satisfied for a range of F_s values and ionisation is observed. However, whilst the island size is large enough to allow some of the librational phase curves to contribute to ionisation, it is too small to allow any rotational phase curves to be ionised. This is not the case for the $j = 2$ resonance where $I_c - I_e(0)$ is sufficiently small when compared to w_R that there are contributions to ionisation from both librational and rotational phase curves. It is this difference that causes the characteristic differences in behaviour seen in the ionisation times of the $j = 1$ and $j = 2$ resonances.

Ionisation Times for the $j = 1$ Resonance

Figure 5.6 shows a number of phase curves calculated for the $O(F^5)$ Resonance Hamiltonian in the region of the $j = 1$ resonance, with $F_s = 0.0167$, $F_\mu = 0.13$, $\Omega_0 = 0.0528$ and a field envelope of 0-50-0. Horizontal lines are marked on the figure showing the initial action, $I_e(0)$ and the critical action, $I_c = 0.463$. The phase curves are all calculated for $I_e(0) = -0.4$.

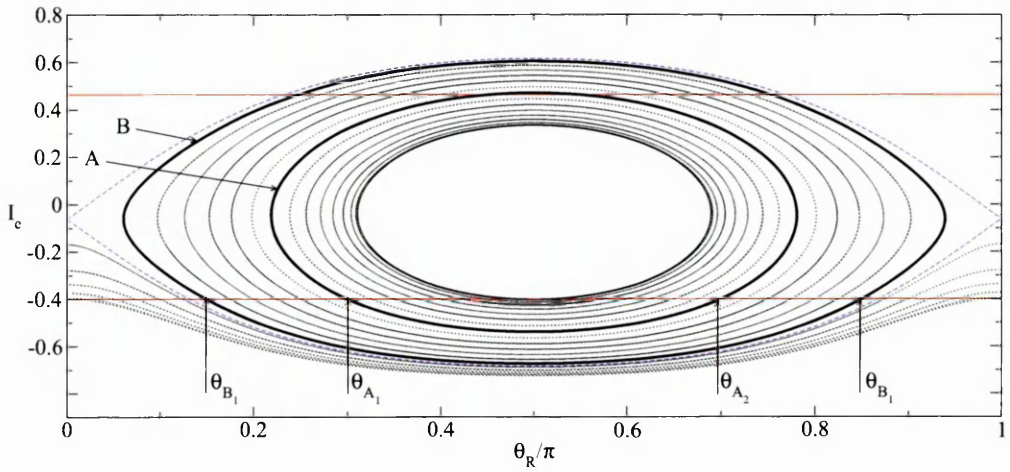

Figure 5.6 Phase curves, $I_e(\theta_R)$, for $F_\mu = 0.13$, $F_s = 0.0167$, $\Omega_0 = 0.0528$ and field envelope 0-50-0 for the $O(F^5)$ $j = 1$ Resonance Hamiltonian. Horizontal lines are shown for $I_e(0) = -0.4$ and the critical ionisation value, $I_e = I_c$. The separatrix is shown using blue dashed lines.

Two ionising phase curves are highlighted with bold lines, marked (A) and (B). The value $\max(I_e)$ for curve (A) lies just above the critical action. Two possible initial conditions for θ_R lie on the same phase curve, at θ_{A_1} and θ_{A_2} with, $\pi/2 - \theta_{A_1} = \theta_{A_2} - \pi/2$. The phase curve motion is clockwise around the resonance. If $\max(I_e) = I_c$ the ionisation times, T_i, for the two initial conditions are $(T_l - T_\delta)/2$ and $(T_l + T_\delta)/2$ respectively, where T_l is the librational time period and T_δ is the time taken to go from θ_{A_2} to θ_{A_1}.

For curve (B) there is an appreciable portion of the phase curve that lies above $I_e = I_c$. The ionisation times for the two phase curves with initial values, $(\theta_{B_1}, I_e(0))$ and $(\theta_{B_2}, I_e(0))$, are

$$T_i = \frac{T_l - T_c - T_\delta}{2} \quad \text{and} \quad T_i = \frac{T_l - T_c + T_\delta}{2},$$

where T_c is the time spent during one orbit such that $I_e(t) \geq I_c$ and T_δ is the time taken to go from θ_{B_2} to θ_{B_1}.

The time T_c can be calculated from equations (5.6–5.8), but in general its calculation depends on whether the motion is librational or rotational and whether the critical ionisation value, I_c, lies above or below the I_e value for the separatrix nodes at $\theta = 0$. The details of this calculation are provided in appendix B, page 221.

In earlier sections, the ionisation time was calculated as the time taken for half of the ionising orbits to have ionised; this will be referred to as the *median ionisation time.* Here we define the *mean ionisation time*, $\overline{T}_i$, as,

$$\overline{T}_i = \frac{1}{N_i} \sum_j T_i(\theta_j, I_e(0)), \tag{5.9}$$

where N_i is the number of ionising orbits, θ_j labels the initial values of θ_R at time $t = 0$ and the sum includes only those orbits which ionise. Any orbits whose ionisation times are longer than the applied field duration, $T_e = 2\pi(2N_a + N_b)/\Omega_0$, are also excluded.

Using this definition simplifies the calculation as we do not need to find T_δ. In general, for each closed curve in phase space intersecting both the critical line, $I_e = I_c$, and the initial line, $I_e = I_e(0)$, unless $\theta_R(0) = \pi/2$ there are two phase curves satisfying the initial condition $I_e(0)$: one with $\theta_R(0) < \pi/2$ and the other with $\theta_R > \pi/2$. The average ionisation time for these two curves is just $T_l - T_c$, which is independent of T_δ. Hence,

$$\overline{T}_i = \frac{\overline{T}_l - \overline{T}_c}{2}. \tag{5.10}$$

The mean librational time period, $\overline{T}_l$, and the mean time above the critical limit, $\overline{T}_c$, are calculated as the corresponding averages of the sets $\{T_l\}$ and $\{T_c\}$ calculated for orbits satisfying the criteria specified for equation (5.9).

The calculation of the time period is complicated by the calculation of T_c, which requires the evaluation of the intersection points, of the phase curve with the $I_e = I_c$ critical ionisation line. The phase curves calculated using the approximate Hamiltonian, $\overline{K}_T$, (5.5) are generally close to the corresponding phase curves for the Resonance Hamiltonian; however, in some cases where the maximum I_e value for the Resonance Hamiltonian phase curve only just satisfies $I_e \geq I_c$, the condition is not satisfied for the approximate Hamiltonian. In these cases, it is assumed that $T_c = 0$ in the calculation of the theoretical ionisation time.

Figure 5.7 compares half the averaged librational time period, $\overline{T}_l$, calculated from equation (5.7), with the numerical mean ionisation time for the $j = 1$ resonance. The numerical mean ionisation times are obtained by integrating the equations of motion for the Resonance

Hamiltonian and averaging the times taken for each ionising orbit to reach the critical value, $I_e(t) = I_c$.

In figure 5.8 we compare the theoretical mean ionisation time, $\overline{T}_i$, calculated using equation (5.9), with the numerical mean ionisation time. The graphs for $\overline{T}_l/2$ and $\overline{T}_i$ are calculated using 200 orbits at each F_s value, with the initial values, $\{\theta_R(0)\}$, equally spaced in the range $[0, \pi/2)$.

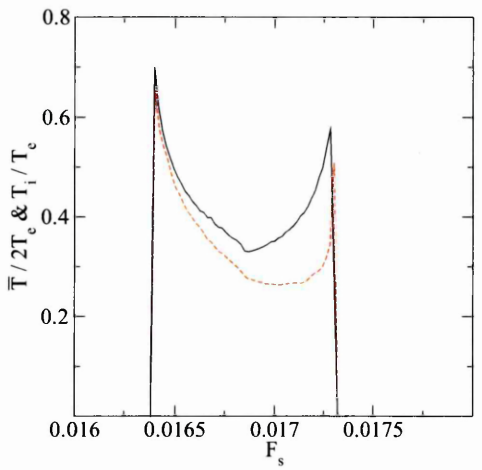

Figure 5.7 Half average librational time period, $\overline{T}_l(F_s)/2$, (solid) and numerical mean ionisation time (dashed) for the $O(F^5)$ $j = 1$ Resonance Hamiltonian, $F_\mu = 0.13$, $\Omega_0 = 0.0528$ and field envelope 0-50-0. The field duration is T_e.

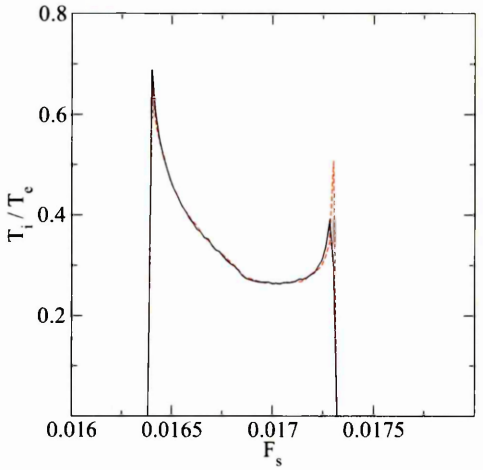

Figure 5.8 Mean theoretical ionisation time, $\overline{T}_i(F_s)$, (solid) and numerical mean ionisation time (dashed). Other parameters as for figure 5.7.

Comparing figures 5.7 and 5.8 with figure 5.5 the following is observed regarding ionisation times:

1. The general behaviour observed for the mean ionisation time for Resonance Hamiltonian is close to that of the median ionisation time calculated for the Averaged Hamiltonian[1].

2. There is a very good match between the numerical mean ionisation time and $\overline{T}_i$ for the Resonance Hamiltonian.

3. The $\overline{T}_l/2$ component is the dominant term in the theoretical ionisation time, particularly at the edges of the ionisation peak; this leads to the longer ionisation times seen there.

[1]The median ionisation times for the Resonance and Averaged Hamiltonians are also similar.

4. There is a close match between the averaged $\overline{T}_l/2$ curve and the numerical ionisation time at the start of the ionisation peak, with an increasing difference as F_s is increased, consistent with the explanation provided in §2.3.2 (page 77) that ionisation starts when F_s reaches a value such that the maximum value of $I_e(t)$ is just equal to I_c. At this point, $T_c = 0$ and hence $\overline{T}_i \approx \overline{T}_l/2$.

Ionisation Times for the $j = 2$ Resonance

For the $j = 2$ resonance, ionisation can occur for both librational and rotational phase curves. In this section we will show how this leads to a difference in ionisation time behaviour.

Although the island widths, w_R, for $j = 1$ and $j = 2$ are similar ($w_R = 1.30$ and $w_R = 1.20$ at $F_s^{(1)} = 0.0168$ and $F_s^{(2)} = 0.0335$ respectively), the required change in $I_e(t)$ to cause ionisation is much less for $j = 2$: for $j = 1$, $I_c - I_e(0) = 0.86$, whilst for $j = 2$, $I_c - I_e(0) = 0.50$.

Figure 5.9 depicts phase curves for the $j = 2$ Resonance Hamiltonian with $F_s = 0.03262$ and other parameters identical to those detailed for the $j = 1$ phase curves shown in figure 5.6. The line marked (C) is an example rotational orbit that ionises. Line (D) is a librational ionising phase curve.

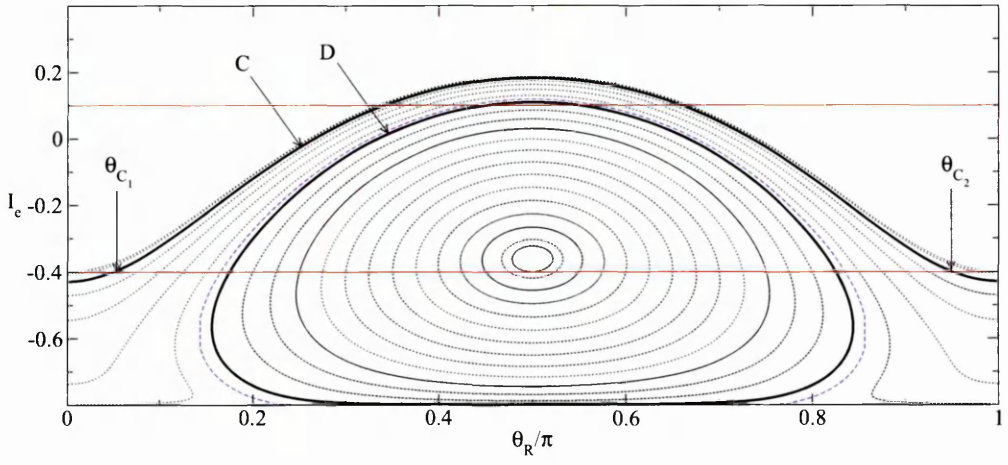

Figure 5.9 Phase curves, $I_e(\theta_R)$, for $F_\mu = 0.13$, $F_s = 0.03262$, $\Omega_0 = 0.0528$ and field envelope 0-50-0 for the $O(F^5)$ $j = 2$ Resonance Hamiltonian. Horizontal lines are shown for $I_e(0) = -0.4$ and the critical ionisation value, $I_e = I_c = 0.101$. The separatrix is shown using blue dashed lines.

The ionisation times for the two rotational orbits with initial conditions $(\theta_{C_1}, I_e(0))$ and $(\theta_{C_2}, I_e(0))$, are

$$T_i = \frac{T_r - T_c - T_\delta}{2} \quad \text{and} \quad T_i = \frac{T_r - T_c + T_\delta}{2},$$

where T_r is the rotational period given in equation (5.8), T_δ is the time taken to go from θ_{C_2} to θ_{C_1} and T_c was given previously.

For the reason described in the previous section, the times, T_δ, do not contribute to the mean ionisation time, $\overline{T}_i$, given by equation (5.9). With the inclusion of ionisation from rotational orbits, equation (5.10) is modified to become,

$$\overline{T}_i = \frac{\overline{T}_p - \overline{T}_c}{2}$$

where the mean time period, $\overline{T}_p$, is the average taken over both the librational ionising orbits periods, $\{T_l\}$, and the rotational ionising orbit periods, $\{T_r\}$.

Whereas for the $j = 1$ resonance the definition of the ionisation time, as either the mean or median, has little difference on the general behaviour, this is not the case for the $j = 2$ resonance. In figure 5.10 we compare the mean and median ionisation times calculated numerically from the equations of motion for the Resonance Hamiltonian.

In figure 5.11 the theoretical mean ionisation time, $\overline{T_i}$, is compared with the numerical mean ionisation time and is shown to be a reasonable approximation, although the differences between the curves are more marked than for the $j = 1$ resonance.

There are two main causes for the increased error. In the vicinity of the $j = 2$ resonance there are ionising orbits with larger $\max(|I_e(t)|)$ than for the $j = 1$ resonance. The approximate Hamiltonian, $\overline{K}_T$, is likely to be less accurate for larger $|I_e|$. The second source of errors is due to differences between the location of the separatrix curves calculated for $\overline{K}_T$ and the Resonance Hamiltonian, $\overline{K}_R$. Some initial conditions resulting in librational phase curves for the Resonance Hamiltonian correspond to rotational phase curves for the $\overline{K}_T$ Hamiltonian, hence contributing to errors in the calculation of the mean ionisation time.

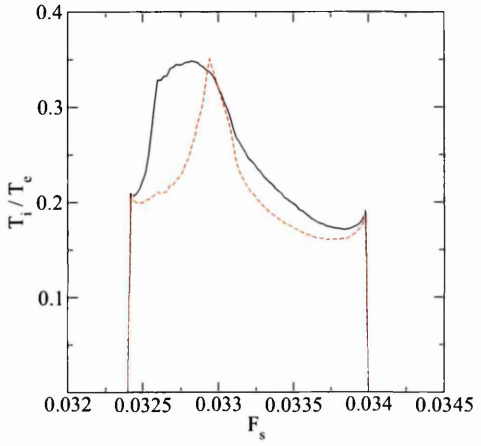

Figure 5.10 Numerical mean ionisation time, $\overline{T}_i(F_s)/2$, (solid black line) and numerical median ionisation time, $T_i(F_s)/2$, (dashed red line) for the $O(F^5)$ $j = 2$ Resonance Hamiltonian, $F_\mu = 0.13$, $\Omega_0 = 0.0528$, $I_m = 0.2$, $I_e(0) = -0.4$ and field envelope 0-50-0. The field duration is T_e.

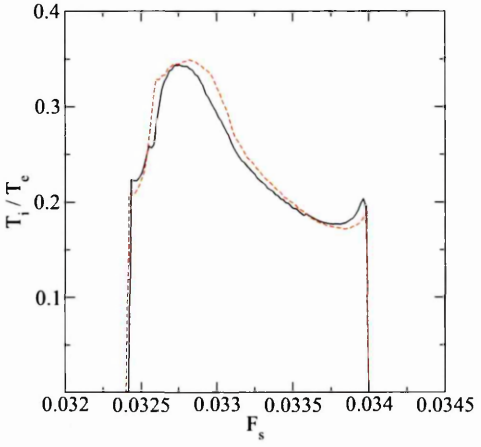

Figure 5.11 Theoretical mean ionisation time, $\overline{T}_i(F_s)$, (solid black line) and numerical mean ionisation time (dashed red line). The parameters are as for figure 5.10.

The separated contributions to ionisation from the librational and rotational phase curves are shown in figure 5.12. Figure 5.13 shows the mean ionisation times calculated separately for the librational and rotational phase curves. The location of the field, $F_s = 0.03274$, is marked on both figures. This is the location of $\max(\overline{T}_i(F_s))$ for the combined mean ionisation time in figure 5.11.

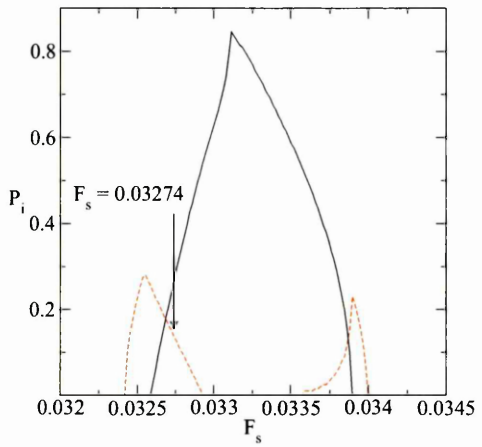

Figure 5.12 Ionisation probability, $P_i(F_s)$, for librational (solid) and rotational (dashed) phase curves for the approximate $j = 2$ Hamiltonian, $\overline{K}_T$, for $F_\mu = 0.13$, $\Omega_0 = 0.0528$ and field envelope 0-50-0.

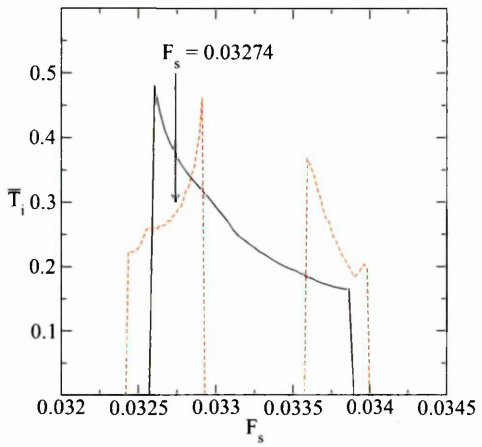

Figure 5.13 Mean theoretical ionisation time, $\overline{T}_i(F_s)$, for librational (solid) and rotational (dashed) phase curves for the approximate $j = 2$ Hamiltonian, $\overline{K}_T$, for $F_\mu = 0.13$, $\Omega_0 = 0.0528$ and field envelope 0-50-0.

The structures shown in figures 5.12 and 5.13 are complex and there are a number of features to note:

1. In the absence of contributions from the rotational phase curves, the ionisation time behaviour would be broadly similar to that observed for the $j = 1$ resonance.

2. The rotational phase curves contribute more towards the edges of the ionisation peak and are the sole contributors at the very edge.

3. In the central region, $0.03293 < F_s < 0.03359$, there is no ionisation from rotational orbits.

4. The ionisation times for rotational orbits increase as F_s increases in the region $0.03243 \leq F_s \leq 0.03293$.

5. As F_s increase in the region $0.03359 \leq F_s \leq 0.03398$ there is a general decrease in ionisation time although there is a small rise at the right hand edge.

These features can be understood by examining the effect the resonance island has on the phase curves for the Resonance Hamiltonian.

In figure 5.14, phase curves are shown for $F_s = 0.03245$ to demonstrate why rotational orbits are the first to ionise at the edges of the resonance. The location of the resonance island causes $I_e(t)$ for some rotational orbits to change sufficiently to ionise, but the separatrix boundary is below I_c so no librational orbits ionise.

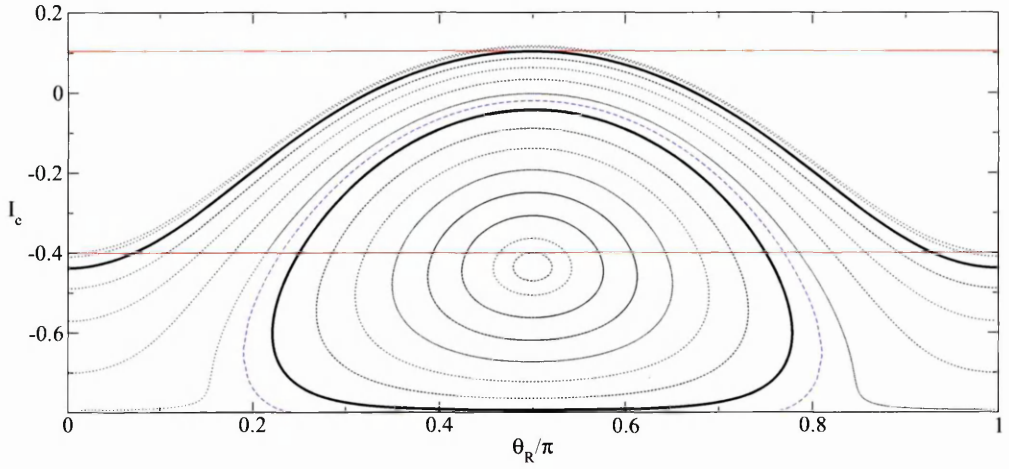

Figure 5.14 As for figure 5.9, except $F_s = 0.03245$ and $I_c = 0.104$. The thick black lines mark a rotational ionising orbit and a bound librational orbit.

From figures 5.14 and 5.9 we see that the rotational orbits that ionise all start in two regions along the $I_e(0)$ line: the first is bounded by $\theta_R = 0$ and the smallest θ_R value where the separatrix intersects $I_e(0)$; the second is bounded by the largest θ_R value where the separatrix intersects $I_e(0)$ and $\theta_R = \pi$. As F_s is increased the resonance island moves up through the phase space and these two regions become smaller, eventually disappearing when the separatrix unstable equilibrium point, $I_s(F_s)$, satisfies $I_s(F_s) = I_e(0)$ at $F_s = 0.03294$. Ionisation from rotational orbits reduces to zero as this limit is approached and the ionisation time increases because the remaining ionising orbits are closer to the separatrix and their period is longer. Because we exclude ionisation times that are greater than the field duration, ionisation will stop at an F_s field below the limit; in this case at $F_s = 0.03293$.

Figure 5.15 shows the phase space for $F_s = 0.0334$, selected to lie in the region $(0.03293, 0.03359)$ where no rotational orbits ionise. The figure shows that for the selected field value the only orbits to intersect both the initial line, $I_e(0)$, and the critical line, I_c, are librational orbits.

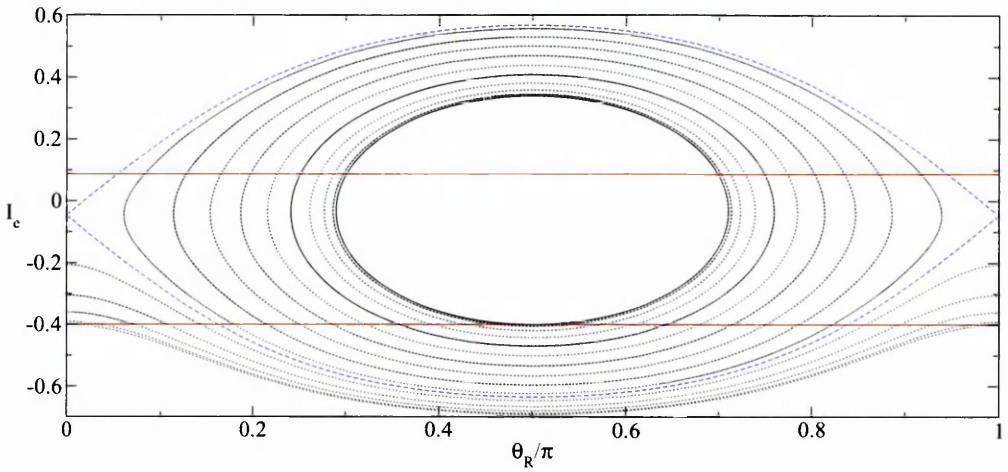

Figure 5.15 As for figure 5.9, except $F_s = 0.0334$ and $I_c = 0.086$. The thick black lines mark a rotational ionising orbit and a bound librational orbit.

For $F_s > 0.03358$, the separatrix unstable equilibrium point, $I_s(F_s)$, satisfies $I_s(F_s) > I_c$. When this condition is met the rotational orbits below the resonance island can be excited sufficiently to ionise. Figure 5.16 shows the phase curves for $F_s = 0.03361$, lying just above this limit. The bold black line shows a rotational orbit that ionises, but at this resolution is virtually indistinguishable from the separatrix border. All of the librational orbits shown also ionise. For F_s values just above 0.03358, the rotational orbits that ionise lie close to the separatrix and therefore have longer ionisation times. As F_s is increased, rotational orbits further from the separatrix can contribute; these have shorter periods, causing the mean ionisation time for the rotational orbits to reduce, as highlighted in item 5 listed on page 163.

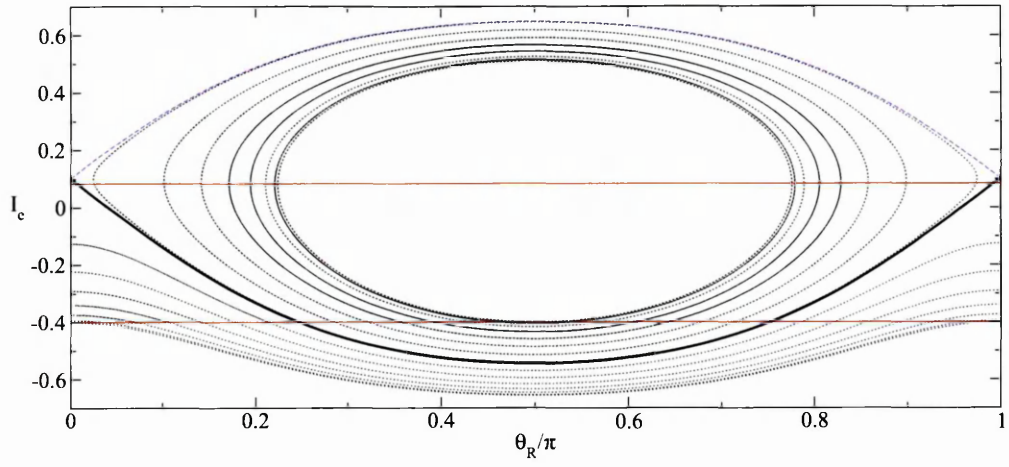

Figure 5.16 As for figure 5.9, except $F_s = 0.03361$ and $I_c = 0.082$. The thick black line marks an ionising rotational orbit.

For $F_s > 0.03390$, the minimum I_e value on the lower separatrix curve lies above $I_e(0)$ and there are no librational orbits for the given initial conditions. This coincides with the edge of librational ionisation seen in figure 5.12.

Figure 5.17 shows phase curves for $F_s = 0.03398$, lying close to the right edge of the ionisation peak. At this field only rotational orbits can ionise whose initial values lie close to $(\pi/2, I_e(0))$. These are the closest orbits to the separatrix curve, causing the slight rise seen in the mean ionisation time for the rotational orbits in figure 5.12 and noted in item 5 on page 163. The separation between the orbits and the separatrix is greater than at the onsets of ionisation for the two rotational ionisation peaks at $F_s = 0.03358$ and 0.03243, so the mean ionisation time peak is not as large.

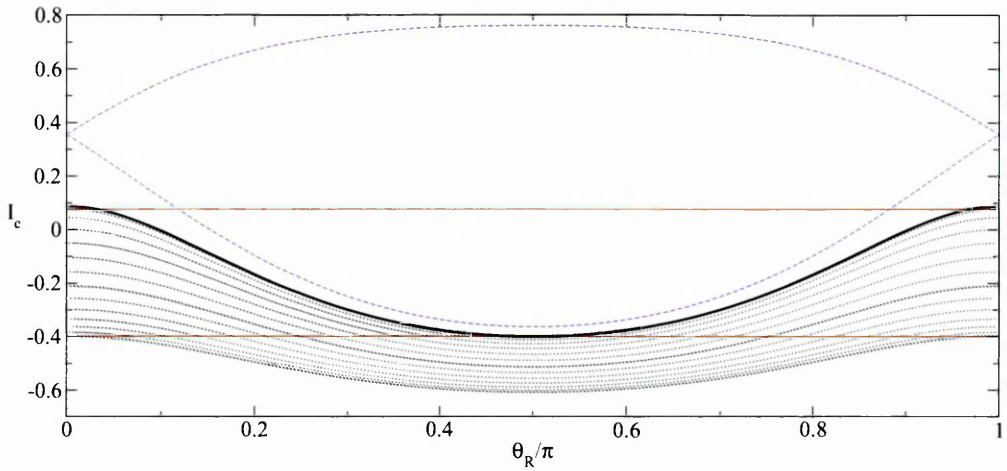

Figure 5.17 As for figure 5.9, except $F_s = 0.03398$ and $I_c = 0.075$. The thick black line marks an ionising rotational orbit.

5.3 Envelope Effects for $j = 2$

In the preceding section we showed that most of the features seen in ionisation times for $j = 2$ can be understood by examining the effect of the resonance island on phase curves when the field is at constant amplitude. From a comparison of figures 5.4 (b) on page 152 for a 16-50-16 envelope with figure 5.5 (b) on page 152 for a 0-50-0 envelope the following differences are seen:

1. For the gradual field switch, ionisation is present for a larger range in F_s.
2. For the gradually switched field a sharp peak in ionisation time is observed at the right hand side of the ionisation peak, at $F_s = 0.03459$. This is missing for the 0-50-0 envelope.

The first feature has been explained previously; see, for example, §2.3.2 on page 77. The second feature is explained in this section.

Figure 5.18 shows a typical ionising phase curve for the instantaneously applied field envelope, 0-50-0, at $F_s = 0.03398$, chosen to be close to the limit at which $P_i(F_s) = 0$. The time is scaled in units of the applied field period, $T_f = 2\pi/\Omega$; the critical ionisation limit, $I_e = I_c$, is shown as a dashed line. Ionisation commences at $t/T_f = 9.43$.

For the instantaneously applied field, 96% of the orbits ionise in the time $9.42 < t/T_f < 10.54$. This is the region where, in the absence of the smaller faster oscillations, $I_e(t)$ reaches its first maxima, as is seen in figure 5.18.

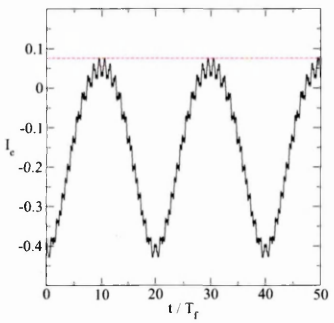

Figure 5.18 An ionising phase curve $I_e(t)$, for the $j = 2$ $O(F^5)$ Averaged Hamiltonian for $F_s = 0.03398$, $F_\mu = 0.13$, $\Omega_0 = 0.0528$ and field envelope 0-50-0.

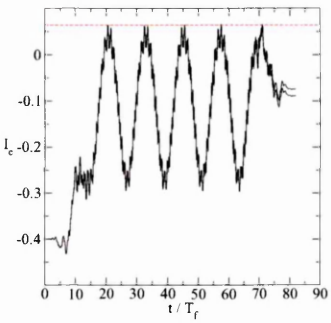

Figure 5.19 Two ionising phase curves, $I_e(t)$, for the $j = 2$ $O(F^5)$ Averaged Hamiltonian for $F_s = 0.03459$, $F_\mu = 0.13$, $\Omega_0 = 0.0528$ and field envelope 16-50-16.

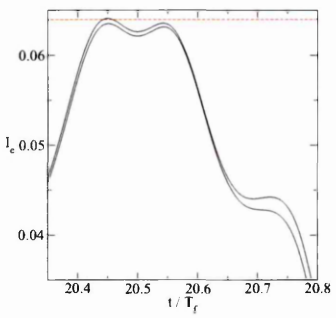

Figure 5.20 Close up of figure 5.19, in the vicinity of the first ionisation.

For comparison, figure 5.19 shows two ionising phase curves for the 16-50-16 field envelope at $F_s = 0.03459$, the field value chosen to lie at the edge of the ionisation region. The effect of the field switch-on clearly seen in the motion up to $t/T_f = 16$. For $16 < t/T_f < 66$ the behaviour is broadly similar to that of the instantaneously applied field phase curve, although with the orbits starting from a different region in phase space. However, whilst the trajectories for the two curves remain close, one orbit ionises at $t/T_f = 20.44$, whilst the other ionises at $t/T_f = 71.11$. Figure 5.20 shows the two phase curves in the vicinity of the first ionisation.

The dominant contribution to the motion for $16 < t/T_f < 66$ is caused by the presence of the resonance island and is closely approximated by the motion for the Resonance Hamiltonian. However, the small oscillations caused by the higher frequency terms present in the Averaged Hamiltonian become significant for field values near the edge of the ionisation region, leading to longer ionisation times.

For the 16-50-16 envelope field, although the ionising phase curves make a number of close approaches to the critical limit, I_c, only 5.3% ionise at the first peak. Further ionisation takes place at time intervals determined by the rotational periods of the Resonance Hamiltonian

Table 5.1: Classical ionisation times for ionising orbits for the $O(F^5)$ Averaged Hamiltonian with $F_s = 0.03459$, $\Omega_0 = 0.0528$, $F_\mu = 0.13$, $I_m = 0.2$, $I_e(0) = -0.4$ and field envelope 16-50-16. A sample of 1600 orbits is used, of which 228 ionise.

Ionisation time range, T_i/T_f	Percentage of Ionising orbits
20.44–20.45	5.3
45.43–45.45	13.2
57.44–57.46	1.8
68.38–74.85	79.7

with the majority of the orbits actually ionising in the switch-off period, $t/T_f > 66$, as can be seen in table 5.1. These contributions cause the sharp peak in ionisation time at the right hand edge of the $j = 2$ ionisation time curve, $T_i(F_s)$, seen in figure 5.4 (b) on page 152.

5.4 Quantal Ionisation Times

In the previous section we showed that classically the structure seen in ionisation times near a resonance is largely due to the effect of the separatrix on the orbits and their periods.

Quantally, ionisation is caused by coupling between substates, with the time-dependent behaviour determined from the Fourier components with periods, $2\pi/(\lambda_k - \lambda_l)$, where λ_k and λ_l are the eigenvalues of the coupled substates, k and l.

In this section, we will show that although the classical and quantum ionisation mechanisms are very different, the quantal ionisation times exhibit similar structures to those caused by the classical separatrix if sufficiently large quantum numbers are used.

Figures 5.21 and 5.22 show ionisation times, T_i/T_f, for the $j = 1$ and $j = 2$ resonances for the classical and quantum dynamics with various n. The classical ionisation time is the median ionisation time defined previously; i.e. the time taken for half the ionising orbits to ionise. The quantal ionisation time is the time taken for the ionisation probability to reach half its final value.

The quantal ionisation times fluctuate significantly for small P_i and so we impose a cut-off such that for $P_i(F_s) < 0.02$ we set $T_i = 0$ in figures 5.21 and 5.23. This arbitrary cut-off excludes ionisation times for small P_i where numerical errors arise. In figure 5.23 ionisation

times are shown for $n = 400$ at the $j = 2$ resonance with and without this cut-off.

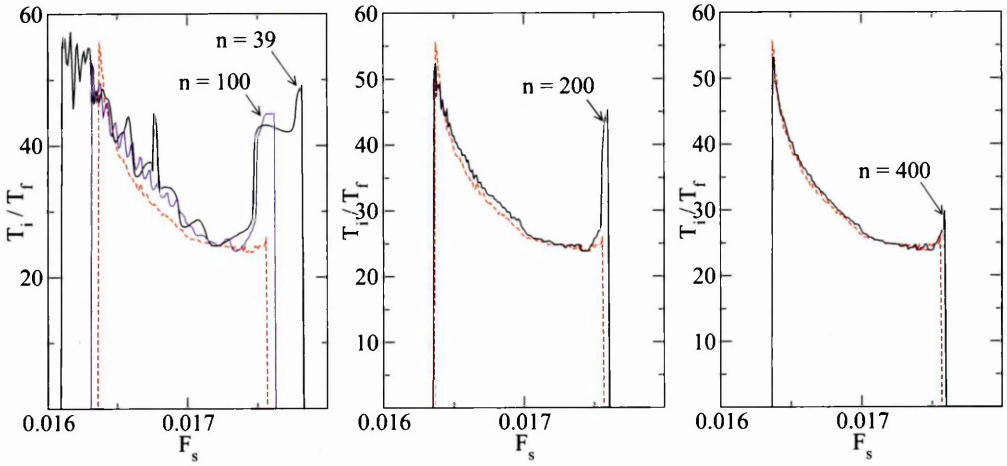

Figure 5.21 Ionisation times, T_i/T_f, for $F_\mu = 0.13$, $\Omega_0 = 0.0528$ and field envelope 16-50-16 at the $j = 1$ resonance, for various n. Corresponding m and k values are given in table 5.2 on page 171. Comparison classical curves are shown with a red dashed line for $I_m = 8/39$ and $I_e(0) = -16/39$.

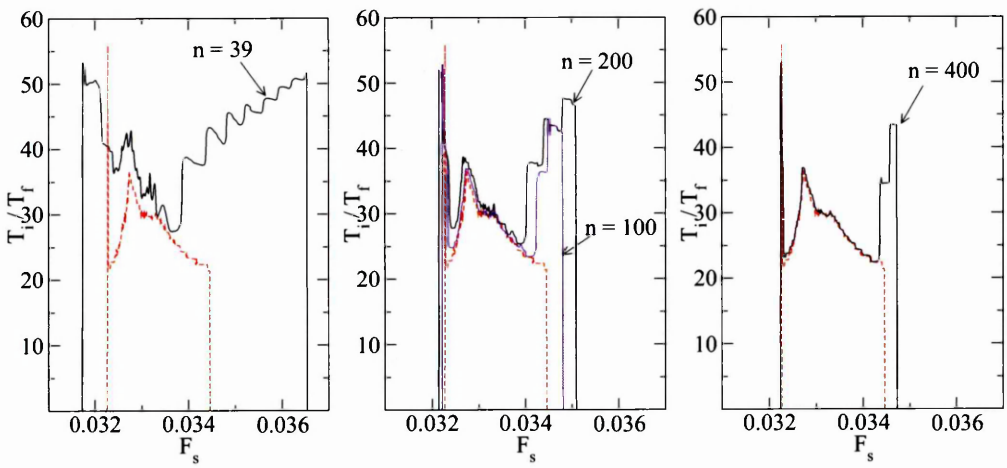

Figure 5.22 As for figure 5.21 for the $j = 2$ resonance.

Table 5.2: Initial quantum states for each n value used in figures 5.21 and 5.22.

n	m	k_i
39	8	-16
100	20	-41
200	40	-81
400	80	-161

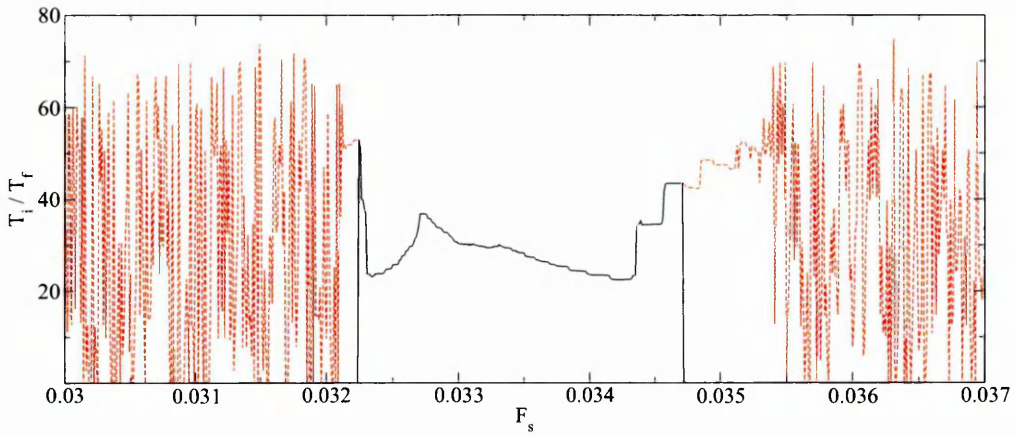

Figure 5.23 Parameters as for figure 5.21. The solid black line shows $T_i(F_s)$ for $n = 400$ with the artificial cut-off, $T_i(F_s) = 0$ for $P_i(F_s) < 0.02$ in the vicinity of the $j = 2$ resonance. The red dashed line shows $T_i(F_s)$ without the cut-off.

From figure 5.21 for the $j = 1$ resonance, we see that as n increases, the quantal ionisation time becomes progressively closer to the corresponding classical time and for $n = 400$ there is a very close match. Calculations were also carried out for $n = 800$, which showed that the difference between classical and quantal ionisation times continues to reduce as n increases.

A similar behaviour is seen for the $j = 2$ resonance in figure 5.22, with the quantal ionisation times becoming increasingly close to the classical ionisation times as n increases, although the peak at the right edge is not present classically. For $n = 800$ the peak is still present but is smaller.

Classically, ionisation at the $j = 1$ resonance is from librational orbits only, whilst for $j = 2$ both librational and rotational orbits contribute, leading to the more complex structure, including the peak at $F_s \approx 0.0327$. With the exception of the right edge peak for $j = 2$, figures 5.21 and 5.22 show that for sufficiently large n, these separatrix effects are also echoed in the

quantal dynamics.

For both resonances, as the quantum number is reduced, larger fluctuations in the quantal ionisation times are seen. For the $n = 39$ curves shown, these fluctuations obscure most of the underlying resemblance to the classical behaviour, although an increase in ionisation time is still seen at the edges of the ionisation peak for $j = 1$.

5.5 Ionisation Times for Microcanonical Distributions

In the previous sections we have shown that the presence of the separatrix leads to distinct structural features in the ionisation times for both the classical and quantal dynamics. The calculations were for fixed initial conditions, $(I_e(0), I_m)$. In this section we examine ionisation times for microcanonical distributions of initial states near resonance, allowing comparison with other calculations [52].

Classically, away from resonance, the majority of ionisation takes place during the field switch-on time, as after the initial field switch-on, changes in $I_e(t)$ are small, so that few of the remaining orbits proceed to ionisation. At resonance, $I_e(t)$ can change significantly after field switch-on, with phase speeds determined by the proximity of the orbit to the separatrix. This leads to longer ionisation times for some orbits at resonance. However, the resonance island width reduces as I_m increases whilst for fixed I_e, the critical ionisation limit, I_c, increases as I_m reduces. These changes affect the field values at which the edges of ionisation peaks occur and hence the field locations of the peaks in ionisation time. For a microcanonical distribution of initial conditions, we therefore expect averaging to remove most of the more distinct features seen for fixed initial conditions, $(I_e(0), I_m)$.

In figure 5.24, classical and quantal ionisation times are compared for a microcanonical distribution of initial conditions chosen to match those given in 2.2.2 and 3.2.2 for figures 2.15 (page 59) and 3.9 (page 112) in the vicinity of the $j = 1$ resonance for $\Omega_0 = 0.0730$ and $F_\mu = 0.14372$ using a grid size of $\delta F_s = 0.0002$. For the classical dynamics, the median ionisation time, $T_i(F_s)$, is defined as the time taken for half of the ionising orbits for a particular F_s value to have ionised. For the quantal dynamics, the median ionisation time is defined as the time taken for the ionisation probability averaged over all initial conditions at a particular

F_s value to reach half its final value. For comparison, the ionisation probabilities are shown in figure 5.25.

These figures show that the median ionisation times for both the classical and quantal dynamics have peaks at similar locations to the ionisation probability peaks and that, after averaging, the sharp peaks seen in the previous sections are missing.

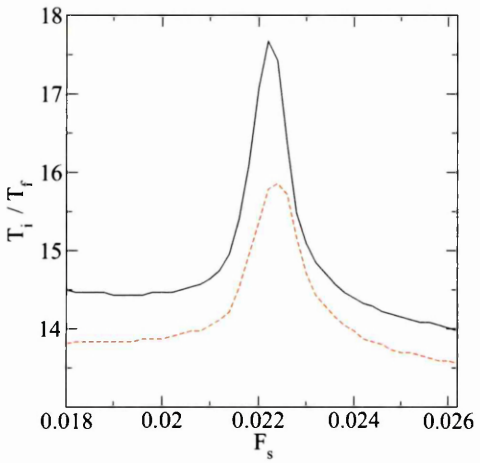

Figure 5.24 Median ionisation times, $T_i(F_s)$, for the $j = 1$ resonance, calculated for a microcanonical distribution of initial substates, $F_\mu = 0.14372$, $\Omega_0 = 0.0730$ and field envelope 16-113-16 for the Averaged Hamiltonian. Quantal ionisation times are shown with a solid black line and classical times with a red dashed line. The ionisation times are scaled by the field period, $T_f = 2\pi/\Omega_0$.

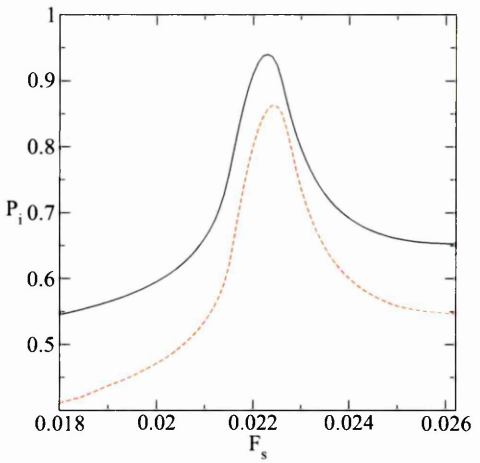

Figure 5.25 Quantal and classical ionisation probabilities, $P_i(F_s)$, with other parameters as given for figure 5.24.

The parameters for the above figures are chosen to allow comparison with the calculations of Robicheaux *et al* [52], in particular their figure 2, where quantal ionisation probabilities as a function of time, $P_i(t)$, are compared for three static field values: lying below resonance ($Fs = 0.0185$), at resonance ($F_s = 0.0221$) and above resonance ($F_s = 0.0234$). Robicheaux *et al* use units of Vcm^{-1}; in these units, the field values are $41\,\mathrm{Vcm}^{-1}$, $49\,\mathrm{Vcm}^{-1}$ and $52\,\mathrm{Vcm}^{-1}$. The ionisation probabilities are approximately the same for the choice of field values above and below resonance.

Robicheaux *et al* make the following observations based on their calculations:

1. The rate of ionisation for $t/T_f \lesssim 17$ is the same for each static field value, from which they conclude that ionisation is independent of static field strength during this period.
2. The ionisation curves, $P_i(t)$, are similar for the two off-resonance field values.
3. For $t/T_f \gtrsim 17$, ionisation mostly stops for the off-resonance field values.
4. For $17 \lesssim t/T_f \lesssim 35$, ionisation continues for the resonance field value, mostly ceasing for $t/T_f \gtrsim 35$.

In figure 5.26 we compare quantal ionisation probabilities, $P_i(t)$, for three field values, similarly chosen to lie below resonance at $F_s = 0.0212$, on resonance at $F_s = 0.0224$ and above resonance at $F_s = 0.0240$ for the Averaged Hamiltonian. The off-resonance field values are chosen as they have similar ionisation probabilities.

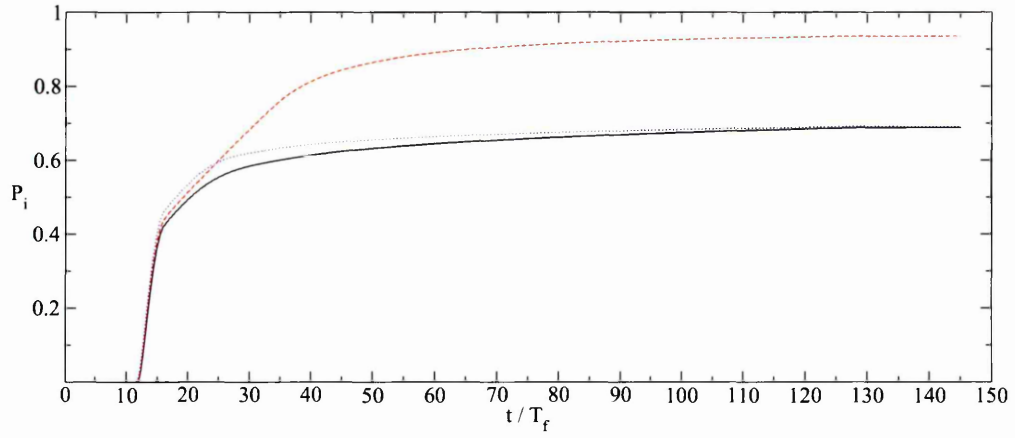

Figure 5.26 Ionisation probabilities, $P_i(t)$, for the off resonance fields, $F_s = 0.0212$ (black solid line) and $F_s = 0.0240$ (blue dotted line) and on resonance field, $F_s = 0.0224$ (red dashed line). Other parameters as for figure 5.24.

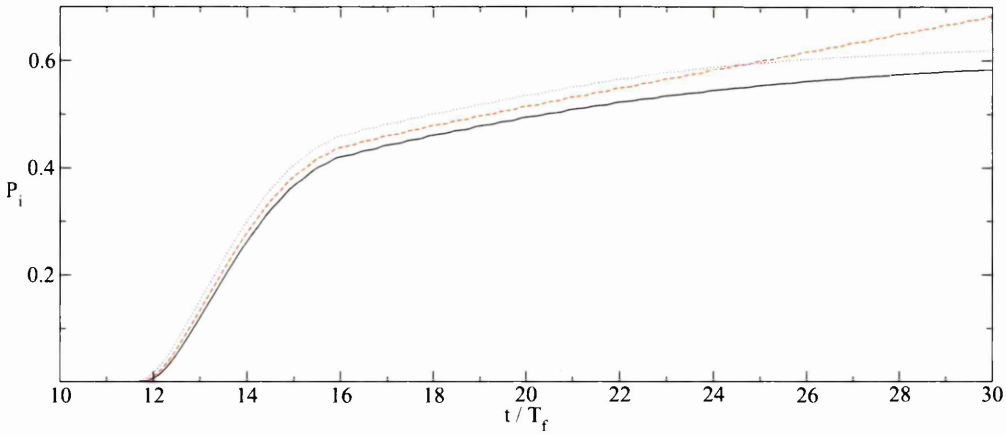

Figure 5.27 As for figure 5.26, with the region around the initial ionisation enlarged.

The ionisation behaviour for the Averaged Hamiltonian is broadly similar to that described by Robicheaux *et al.* Comparing figure 5.26 with [52] figure 2 and the observations quoted above, we note the following similarities and differences:

1. The initial ionisation rates for the Averaged Hamiltonian are similar for each of the field values for $12 \lesssim t/T_f \lesssim 15$. However, contrary to observation 1 on page 174, a closer inspection confirms that the gradients vary slightly with the static field value as can be seen in figure 5.27.

2. Ionisation starts at $t/T_f \approx 5$ for the Robicheaux calculations. For the Averaged Hamiltonian ionisation starts at $t/T_f \approx 12$, which is close to the end of the field switch-on at $t/T_f = 13$. The cause of this difference could be the different field envelopes used, as discussed in §2.2.2 on page 56. For the Robicheaux field envelope, the field would be approaching its maximum amplitude after $5T_f$ if integration is started from $t = 0$. This would suggest that the field amplitude has a non-zero value at $t = 0$ as stated in their paper.

3. From the Robicheaux calculations, ionisation continues for a longer time at resonance: $P_i(t)$ reaches 80% of its final value after $25T_f$ for the resonance field value and after $14T_f$ and $19T_f$ for the off resonance values. This is also seen for the Averaged Hamiltonian. The ionisation probability, $P_i(t)$, reaches 80% of its final value at $34T_f$ for the resonance field value and at $21T_f$ and $25T_f$ for the off-resonance field values.

4. When the difference in ionisation start times is taken into account, the ionisation times for the Averaged Hamiltonian are consistent with the Robicheaux calculations.

5. Although data is given by Robicheaux only for three field values, the median ionisation times for these fields are broadly consistent with the results presented here for the Averaged Hamiltonian, with longer median ionisation times at resonance.

The similarities between the calculations by Robicheaux *et al* and those presented here provide an independent check on the validity on the quantal method described in this thesis.

Chapter 6

Application to Higher Quantum Numbers

6.1 Introduction

In chapter §3, the quantum mechanical calculations were typically carried out for $n \lesssim 50$. However, because the basis set of eigenstates involved in the quantum mechanical approximation is relatively small, the numerical evaluation of these equations can be applied to higher quantum numbers with relatively modest computational resources. Calculations presented here have been carried out up to $n = 800$.

We have seen in earlier chapters that in the vicinity of resonances, the separatrix has significant effects on the classical dynamics and have shown that this leads to much of the structure seen in ionisation probabilities and ionisation times. These effects are also seen to manifest themselves in the quantum mechanics, becoming increasingly similar to the classical mechanics as the quantum number is increased. In this chapter we compare the quantal and classical dynamics over a broader range of fields to show on and off resonance behaviour and examine the convergence with classical behaviour for increasing quantum number.

At low quantum numbers tunnelling has a significant effect on ionisation, as shown in §3.3.1 on page 113. For increasing quantum number, the range over which tunnelling is signif-

icant, ΔI_e, becomes smaller and tunnelling generally becomes a less significant contributor to ionisation, although even for $n = 100$, tunnelling can be significant over a wide range of field values. For small resonance islands, tunnelling is an important factor even for high quantum numbers. This is explored in §6.3.

For slowly switched fields, the slow movement of the resonance island through phase space allows many of the orbits to be tangled by the separatrix. For the exact classical dynamics this has been shown [51] to lead to more complex ionisation behaviour. We show in §6.4 that similar effects are seen in the classical mechanics for the Averaged Hamiltonian and that for high quantum numbers, these effects are also mimicked in the quantum mechanics.

To understand how the computational time scales with increasing quantum number for the quantum approximation, the times were measured for quantal calculations of the ionisation probability, $P_i(F_s)$, for the principal quantum numbers, $n = 200, 300, \ldots, 1000$. For each calculation, $F_\mu = 0.13$, $\Omega_0 = 0.011414$, the field envelope is 16-50-16 and the ionisation probability is calculated for 12 equally spaced values of F_s in $[0.035, 0.03608]$. The quantum numbers, m and k_i are chosen to best fit $m/n = 0.2$ and $k_i/n = -0.4$. The results are shown in figure 6.1, from which the computational time using a linear least squares fit is estimated to scale as n^x, where $x \approx 1.7$.

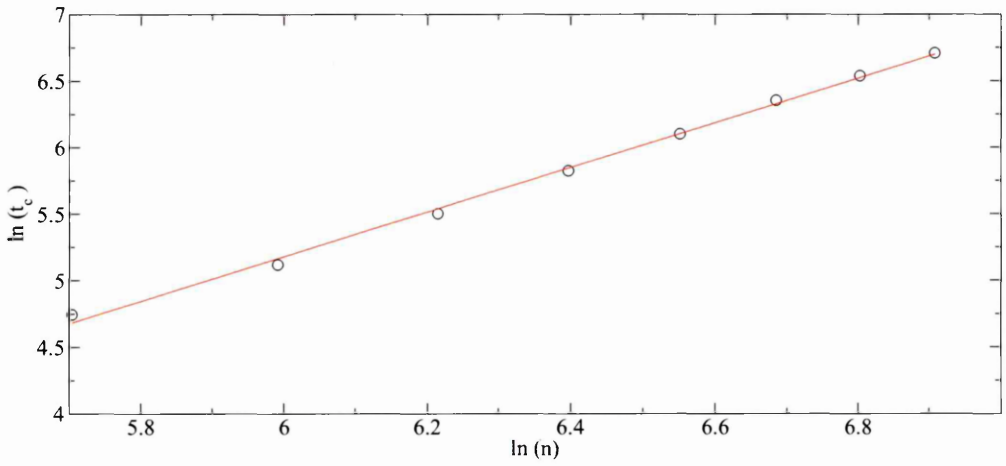

Figure 6.1 Plot of the logarithms of computational time, t_c, in seconds, against the principal quantum number, n, for the calculation described in the text. The circles mark the measured values and the red line is a linear least squares fit.

6.2 Ionisation Probability for Increasing Quantum Number

By the correspondence principle, as the principal quantum number is increased it is expected that the behaviour of the quantum mechanical system should become increasingly similar to the corresponding classical system. Here we compare ionisation probabilities for a wide range of static field values, encompassing both on and off resonance behaviour. The classical ionisation behaviour at resonance is a consequence of the separatrix effect on the orbits. As the quantum number increases, we see that these effects are manifest in the quantum mechanics as well.

In this section we also examine the effective range, ΔI_e, over which tunnelling is significant for varying quantum number and confirm that this range reduces as the quantum number increases and consequently tunnelling is less significant for higher quantum numbers.

In figures 6.2 and 6.3 the ionisation probability, $P_i(F_s)$, is shown for the $O(F^5)$ Averaged Hamiltonian for increasing principal quantum number, with parameters chosen to provide the best match to the classical parameters, $I_m = 0.2$, $I_e(0) = -0.4$, $F_\mu = 0.13$, $\Omega_0 = 0.011414$ and field envelope 16-50-16; chosen for comparison with figure 3.7 in §3.2.1. The principal quantum numbers shown are $n = 100, 200, 400$ and 800, with other quantum values given in table 3.7 on page 115. For comparison the classical ionisation curve is also shown. The F_s range is restricted to allow the differences between the ionisation curves to be more clearly seen. In figure 6.4 the classical and $n = 800$ ionisation probabilities are compared over the ranges $F_s = 0.02$–0.08. Each of the quantum calculations in figures 6.2–6.4 use the semi-classical decay function described in §3.1.3 (page 97) to include the effects of tunnelling.

The figures clearly show that as n is increased the quantum ionisation probability becomes increasingly close to the corresponding classical case. For $n = 800$ there is very little difference between the quantum and classical ionisation probabilities throughout the region considered.

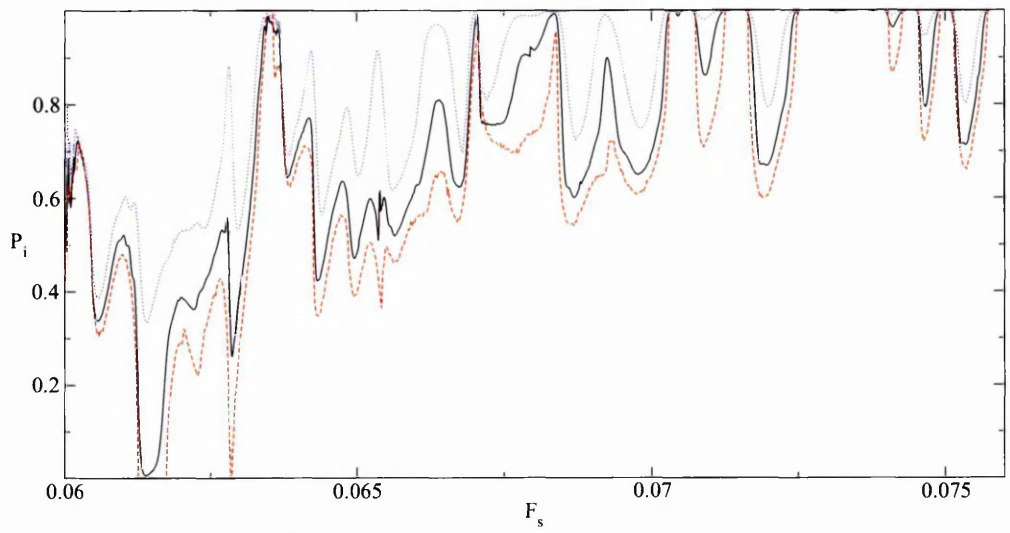

Figure 6.2 Ionisation probabilities, $P_i(F_s)$, for the $O(F^5)$ Averaged Hamiltonian, $F_\mu = 0.13$, $\Omega_0 = 0.011414$ and envelope 16-50-16 for $n = 100$ (blue dotted line) and $n = 200$ (solid black line) and classical (red dashed line) approximations.

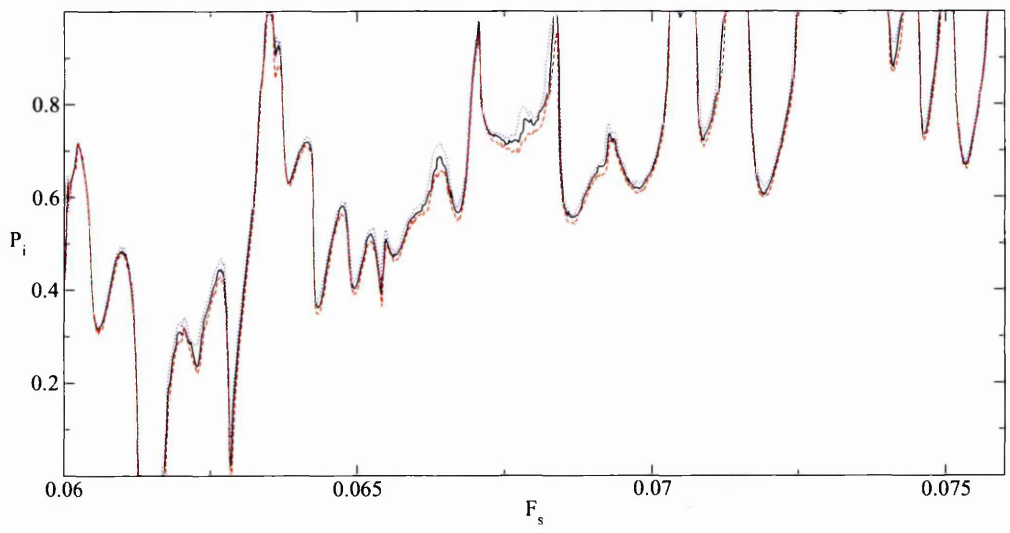

Figure 6.3 Parameters as for figure 6.2. Ionisation probabilities, $P_i(F_s)$, for $n = 400$ are shown with a blue dotted line and for $n = 800$ with a solid black line. The classical approximation is shown with a red dashed line.

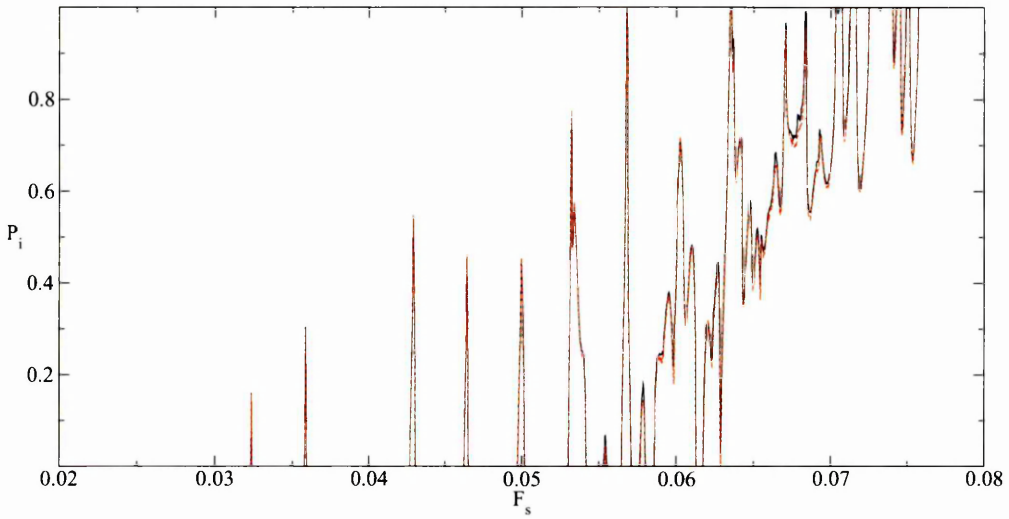

Figure 6.4 Ionisation probabilities, $P_i(F_s)$, for the $O(F^5)$ Averaged Hamiltonian, $F_\mu = 0.13$, $\Omega_0 = 0.011414$ and envelope 16-50-16 for the $n = 800$, $m = 160$ and $k_i = -321$ quantum (solid line) and classical (dashed line) approximations.

As n is increased, the effect of tunnelling on ionisation becomes less significant and for sufficiently large n tunnelling can be ignored. The calculations for figures 6.2–6.4 were also carried out using the step decay function which excludes the effect of tunnelling. The difference between the semi-classical decay and the step decay calculated probabilities reduces with increasing n. In figure 6.5 for $n = 100$ and $n = 400$ ionisation probabilities are shown with and without tunnelling. For $n = 400$, the contribution due to tunnelling is seen to be small. In general, for $n \geq 400$ the contribution due to tunnelling is small, although this is not necessarily true for the case of small resonance islands: this is discussed in §6.3. For $n = 100$, we see that tunnelling makes an appreciable contribution to ionisation, although this is not the only cause of the difference between the classical and quantal ionisation curves. For the quantum mechanics, ionisation increases for longer interaction times. For $n = 100$ we have confirmed this by comparing ionisation for various field envelopes of the form $16 - N_b - 16$ for F_s in the interval $(0.06, 0.07)$. In contrast, classically there is little ionisation for $N_b \geq 30$. The quantal dependence of ionisation on field duration was explored earlier for small quantum numbers, in §3.4 on page 126.

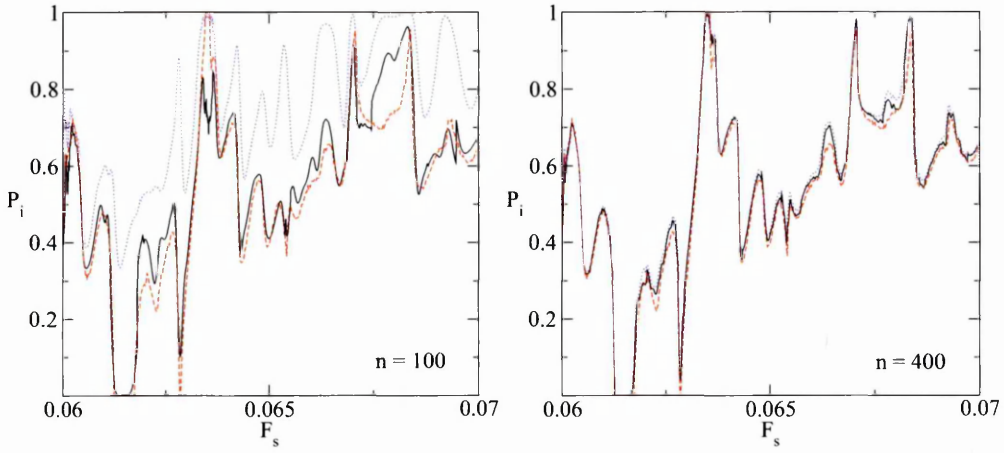

Figure 6.5 Ionisation probabilities, $P_i(F_s)$, using a semi-classical decay function (dotted blue line) and a step decay function (solid black line) for $n = 100$ and $n = 400$. The classical ionisation probability is shown with a red dashed line. All other field parameters are as for figure 6.2 with quantum initial values given in table 3.7 on page 115.

On physical grounds the effect of tunnelling is expected to reduce as n increases and the classical limit is approached. To show the effect of tunnelling on ionisation, the $O(F^5)$ Averaged Hamiltonian quantum approximation was used to calculate ionisation probabilities for various n in the absence of inter-state coupling — obtained by setting $\langle l|\hat{H}_1|k\rangle = 0$ in equation (3.4) — for each of the initial conditions, $k_i = -n+m+1, -n+m+3, \ldots, n-m-1$. The parameters used were: $\Omega_0 = 0.011414$, $F_\mu = 0.13$, $F_s = 0.05$ and the field envelope, 10-10-10. The short duration field envelope was selected to extend the k_i range over which the significant change in ionisation probability occurs. The azimuthal quantum number, m, is chosen such that $m/n = 0.2$.

Table 6.1 shows the number of initial states, Δk, over which the ionisation probability rises from 5% to 95% of its maximum value. From this we see that the number of quantum states over which tunnelling is effective is seen to remain broadly similar as n increases; hence, as n increases there is a reduction in the corresponding classical range, ΔI_e, over which tunnelling is significant, $\Delta I_e \approx 2\Delta k/n$. This can be seen in figure 6.6 which plots the ionisation probability, P_i, against k_i/n for $n = 50, 100, 200, 400$ and 800 for the semi-classical decay function (solid lines) and step decay function (dashed lines). All inter-state coupling is switched off for these calculations. The semi-classically calculated ionisation probabilities are seen to rise more

Table 6.1: The number of initial states, Δk, over which the ionisation probability rises from 0.05 to 0.95 for various values of n in the absence of inter-state coupling. The dynamical parameters are $\Omega_0 = 0.011414$, $F_\mu = 0.13$, $F_s = 0.05$, $m/n = 0.2$ and the field envelope is 10-10-10. The effective tunnelling range is $\Delta I_e = 2\Delta k/n$.

n	Δk	ΔI_e
50	4	0.160
100	5	0.100
200	5	0.050
400	5	0.025
800	4	0.010

sharply as n is increased, getting closer to the ionisation probabilities calculated for the step decay function and hence reducing the contribution from tunnelling.

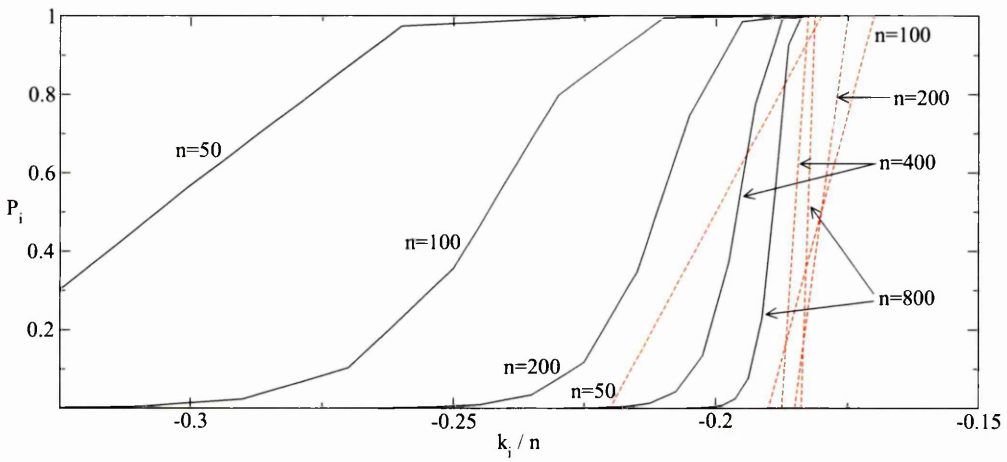

Figure 6.6 Ionisation probabilities, $P_i(k_i/n)$, for the $O(F^5)$ Averaged Hamiltonian with no inter-state interactions, $F_\mu = 0.13$, $F_s = 0.05$, $\Omega_0 = 0.011414$ and envelope 10-10-10 for the semi-classical (solid black lines) and step (red dashed lines) decay functions for $n = 50, 100, 200, 400$ and 800.

The calculations shown in this section demonstrate that as the quantum number is increased, the quantal and classical ionisation probabilities become increasingly similar, both on and off resonance: for $n = 800$, the ionisation curves are practically indistinguishable to the resolution shown in figure 6.4. The observed classical ionisation behaviour at resonance is a consequence of the separatrix effect on the orbits. These effects are also manifest in the quantum mechanics for sufficiently high quantum numbers. We have shown that the contribution to ionisation from tunnelling decreases as the quantum number increases but that even for

$n = 100$, tunnelling is still important.

6.3 The Effects of Small Resonance Islands

In this section we examine the effects of small resonance islands on the classical and quantum dynamics. This exploration requires the use of high quantum numbers: as the island size is reduced, higher quantum numbers are required for the resonance island effect on ionisation not to be obscured by the contribution from tunnelling.

An approximation for the island width was derived in §2.1.5 on page 45. From equation (2.40), page 48, the approximate resonance island width for the j-th resonance is,

$$w_R = 2\sqrt{\frac{2F_\mu\Omega_0|\widetilde{\mathcal{J}}_j|\,(1-I_m^2)}{4\beta + F_\mu\Omega_0|\widetilde{\mathcal{J}}_j|\gamma}},$$

where, from equation (2.36), page 46,

$$\beta = \frac{3}{16}\left(F_s^2 + \frac{F_\mu^2}{2}\right) - \frac{3}{512}\left(301 - 189I_m^2\right)\left(F_s^4 + 3F_s^2F_\mu^2 + \frac{3F_\mu^4}{8}\right), \quad \gamma = \left(\frac{1+I_m^2}{1-I_m^2}\right).$$

For given F_μ and Ω_0, the main factor determining the island width is the parameter, $\widetilde{\mathcal{J}}_j$, given by equation (2.31) (page 43) and depending on F_μ, F_s and Ω_0. To more clearly identify the effects of the island width without changing other dynamical parameters we carry out all calculations using the Resonance Hamiltonian, $\overline{K}_R$, and vary the island width by artificially setting $\widetilde{\mathcal{J}}_j = J_F$, where J_F is a tuning parameter. To exclude the effects of the field switch, all calculations are made using envelopes of the form $0 - N_b - 0$.

In figures 6.7 and 6.8 classical ionisation probabilities are shown for different J_F for $\Omega = 0.0528$, $F_\mu = 0.13$, $I_m = 0.2$ in the vicinity of the $j = 1$ resonance. Initial values, $I_e(0)$, are chosen so that $(I_c - I_e(0))/w_R$ is nearly constant, with slight adjustments made so that the ionisation peaks are approximately the same height for each island width. The initial values are chosen so that only librational orbits contribute to ionisation. The parameters, $J_F^{(k)}$, are given in table 6.2 and are selected so that the island size approximately halves with each successive k value. The figures show different field envelopes, 0-50-0 and 0-400-0.

Comparing the two figures, the ionisation peaks are very similar for $J_F = J_F^{(1)}$ or $J_F = J_F^{(2)}$,

but for $N_b = 50$ the $J_F = J_F^{(3)}$ ionisation peak is much smaller and no ionisation is observed for $J_F = J_F^{(4)}$ or $J_F = J_F^{(5)}$.

The differences are caused by the increase in librational period as the island size decreases. For the first two islands, the field duration is sufficient for the majority of ionising orbits to move round the resonance island sufficiently for ionisation to occur. For the $J_F = J_F^{(3)}$, 40 field cycles is insufficient for all potentially ionising orbits to reach the ionisation threshold. For the smallest two islands, the motion is so slow that no ionisation occurs in 40 field cycles.

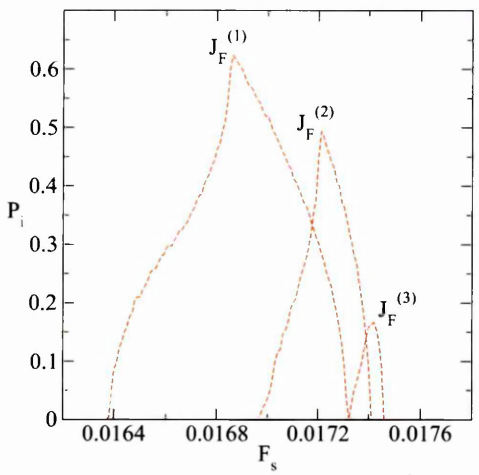

Figure 6.7 Classical ionisation probabilities, $P_i(F_s)$ for $\overline{K}_R$, $F_\mu = 0.13$, $\Omega_0 = 0.0528$ and $I_m = 0.2$ for various $J_F^{(k)}$ and the field envelope, 0-50-0.

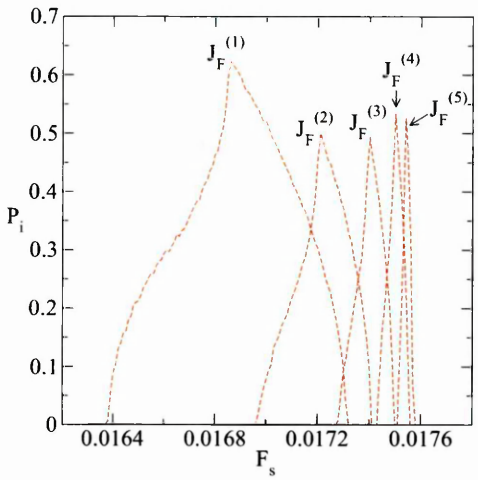

Figure 6.8 Classical ionisation probabilities, $P_i(F_s)$ for field envelope 0-400-0; other parameters as for figure 6.7.

An analysis of ionisation times was made previously, in chapter 5. Here, we make use of two results from that analysis. For librational orbits the shortest period occurs at the centre of the resonance island, and a first approximation is given by equation (5.1), page 153, as,

$$T_l \approx \frac{8\pi}{\sqrt{3F_\mu\Omega_0|\tilde{\mathcal{J}}_j|(1-I_m^2)(2F_s^2+F_\mu^2)}}.$$

In table 6.2 this expression is compared with more accurate calculations for T_l using equation (5.7) from chapter 5 for each of the island widths and, for present purposes, confirmed to provide a reasonable estimate in each case. From the approximation, for small island sizes, $w_R \propto \sqrt{|\tilde{\mathcal{J}}_j|}$ whilst $T_l \propto 1/\sqrt{|\tilde{\mathcal{J}}_j|}$. This longer period can be seen by comparing the expec-

Table 6.2: Island data calculated for $\Omega_0 = 0.0528$, $F_\mu = 0.13$ and $F_s = 0.01677$ for each forcing parameter, $J_F^{(k)}$. Island sizes, w_R, are calculated from equation (2.40). Librational time periods, T_l, are expressed as multiples of $T_f = 2\pi/\Omega_0$, and calculated from equations (5.7) and (5.1) on pages 155 and 153. The initial values, $I_e(0)$, are selected to give approximately the same height ionisation probability peaks for each $J_F^{(k)}$ value.

k	$J_F^{(k)}$	w_R	T_l/T_f	T_l/T_f (approximate)	$I_e(0)$
1	-0.25000000	1.31	21	23	-0.4000
2	-0.06250000	0.73	47	45	-0.0185
3	-0.01562500	0.38	96	91	0.2147
4	-0.00390625	0.19	194	182	0.3374
5	-0.00097656	0.09	390	364	0.3900

tation values, $\langle I_e(t)\rangle$, for two $J_F^{(k)}$ values in figures 6.9 and 6.10, with F_s values selected to lie close to the maximum value of $P_i(F_s)$ in each case. A sample set of 300 orbits are used with the initial phase angle equally distributed in the range $[0, \pi)$. Expectation curves are shown with and without ionisation enabled to show the onset of ionisation where they initially diverge. For the larger island, ionisation is seen to start at $T/T_f \approx 10$ and for the small island at $T/T_f \approx 85$; in both cases this is approximately half the librational period.

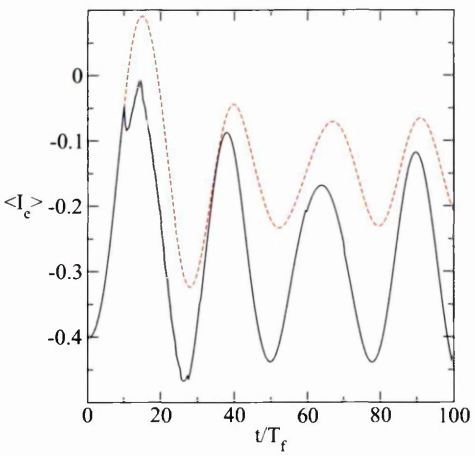

Figure 6.9 Classical $\langle I_e(t)\rangle$, calculated for $F_\mu = 0.13$, $\Omega_0 = 0.0528$, $I_m = 0.2$ and $F_s = 0.0168$ for $J_F = J_F^{(1)}$. The solid black line is shown with ionisation switched on and the dashed red line with ionisation switched off.

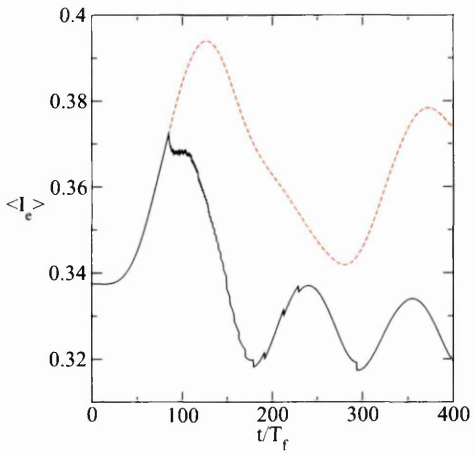

Figure 6.10 As for figure 6.9, but for $J_F = J_F^{(4)}$.

The quantum system's response to smaller island sizes is shown in figures 6.11 to 6.14 for

$n = 50, 100, 200$ and 400. For each island size the initial state, k_i, is selected to best match the $I_e(0)$ values in table 6.2. Comparison classical ionisation probabilities are also calculated, with initial conditions chosen to match the quantum initial state, $I_e(0) = k_i/n$.

Only the first three island sizes are shown in figure 6.11 for $n = 50$, as quantally, $P_i(F_s) \approx 1$ for the two smallest islands. As the island size decreases, the differences between the classical and quantum ionisation curves become more marked; this is due primarily to tunnelling.

Tunnelling contributes to ionisation for a range of substates; the extent of this range when compared to the resonance island size is important and has an effect on the observed ionisation. We define the *tunnelling region* as the size of the region in k/n with the following bounds. The lower bound is found from the smallest k value for which the ionisation probability, $P_i^{(adia)}(k) > 0.1$ and $P_i^{(adia)}(k)$ is the ionisation probability calculated for a system in an initial state, k, with off-diagonal elements set to zero and an integration time of 400 field cycles. The upper bound is found from the smallest k value for which $P_i^{(adia)}(k) > 0.9$.

At $F_s = 0.0172$ for $n = 50$, $P_i^{(adia)}(k_i) > 0.1$ for $k_i > 9$ whereas classically, ionisation starts at $k_c = 23$. The tunnelling region is $\Delta I_e \approx 0.3$; this is comparable to the island width for the third largest island and larger than the widths of the two smallest resonance islands given in table 6.2.

As n is increased the tunnelling region reduces and peaks in $P_i(F_s)$ becomes visible for smaller islands. Progressively, as n is doubled, the number of distinct peaks in $P_i(F_s)$ increases by one, until at $n = 400$ there are clear peaks for each of the five $J_F^{(k)}$ values. This is consistent with the reduction in the size of the tunnelling region as n increases: for $n = 50, 100, 200$ and 400 the tunnelling regions are 0.27, 0.16, 0.09 and 0.05. Comparing these sizes with the resonant island sizes given in table 6.2 and the quantal ionisation peaks seen in figures 6.11–6.13, we see that the ionisation peaks become less distinct for island sizes similar to or smaller than the tunnelling region size.

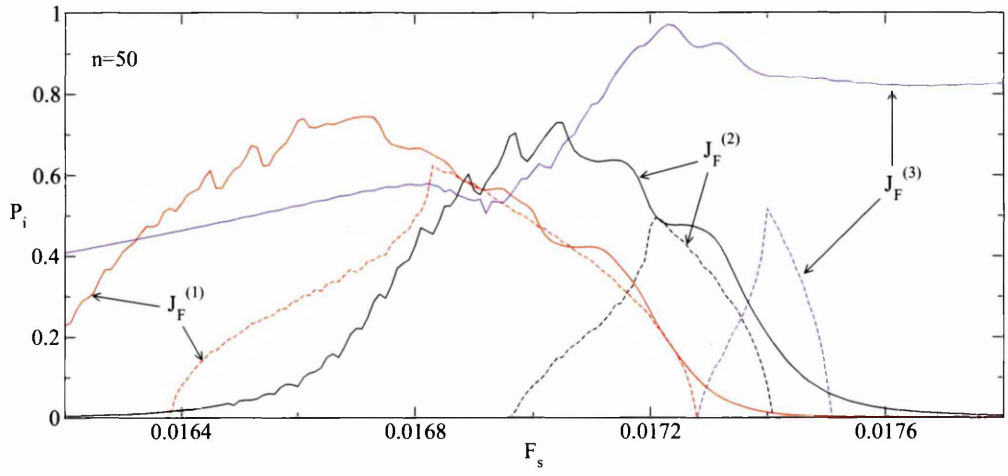

Figure 6.11 Ionisation probabilities, $P_i(F_s)$, for $F_\mu = 0.13$, $n = 50$, $I_m = m/n = 0.2$ and field envelope 0-400-0 for the first three $J_F^{(k)}$ values, with k_i values chosen to best match the $I_e(0)$ values given in table 6.2. Quantum curves are shown with solid lines. Classical results for matching $I_e(0)$ and I_m are shown with dashed lines. Different colours are used for each J_F value.

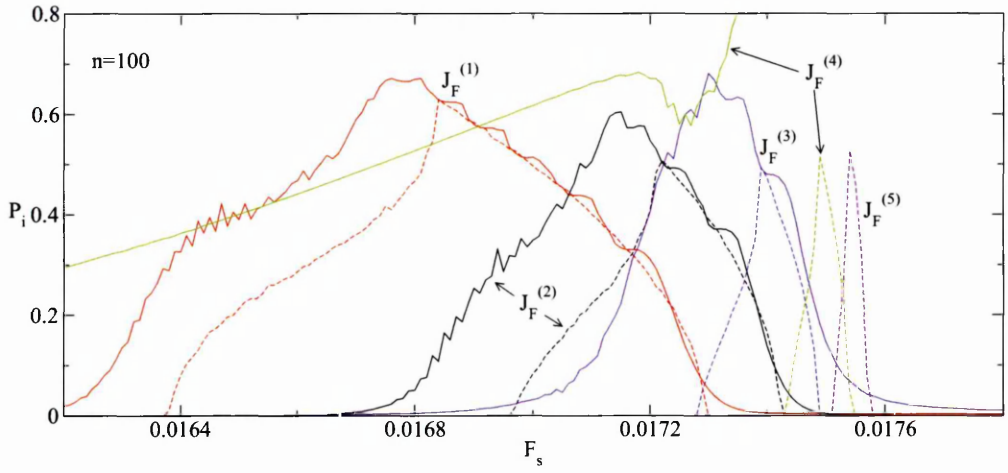

Figure 6.12 As for figure 6.11 but with $n = 100$ and with curves shown for the five J_F values given in table 6.2.

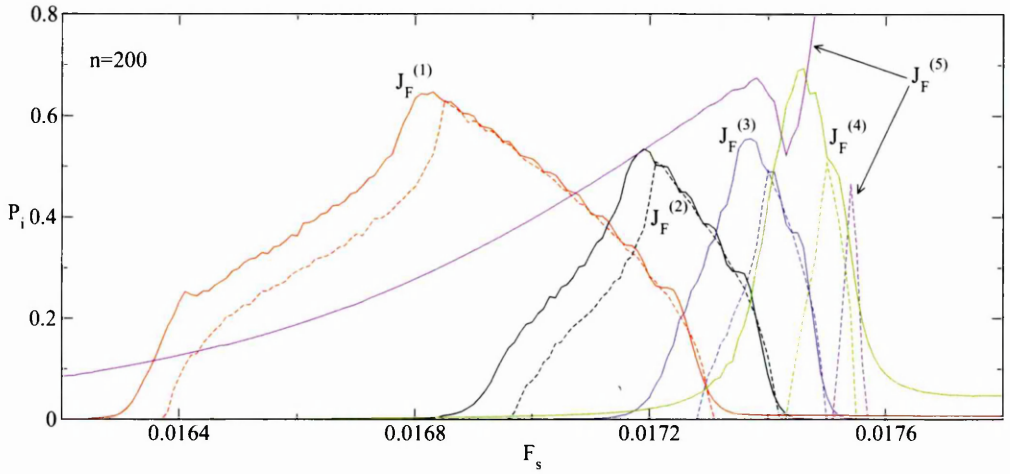

Figure 6.13 As for figure 6.11 but with $n = 200$ and with curves shown for the five J_F values given in table 6.2.

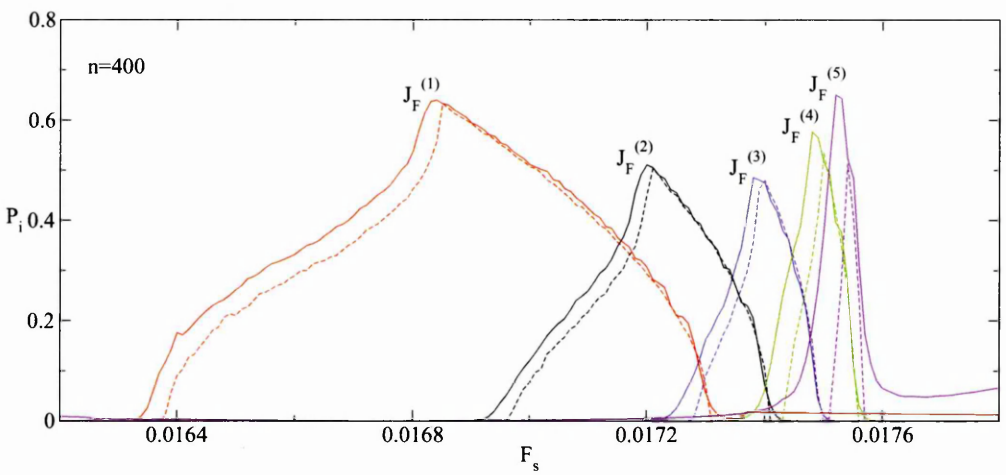

Figure 6.14 As for figure 6.11 but with $n = 400$ and with curves shown for the five J_F values given in table 6.2.

The slower librational motion observed classically is also seen in the quantum mechanics, with $\langle n_e(t) \rangle$ evolving more slowly as the island size reduces. This is shown in figure 6.15, where $\langle n_e(t)/n \rangle$ for $n = 400$ is compared with corresponding classical curves, $\langle I_e(t) \rangle$, for the $J_F = J_F^{(k)}$ values given in table 6.2. The periods of oscillation are seen to become longer with reducing island size.

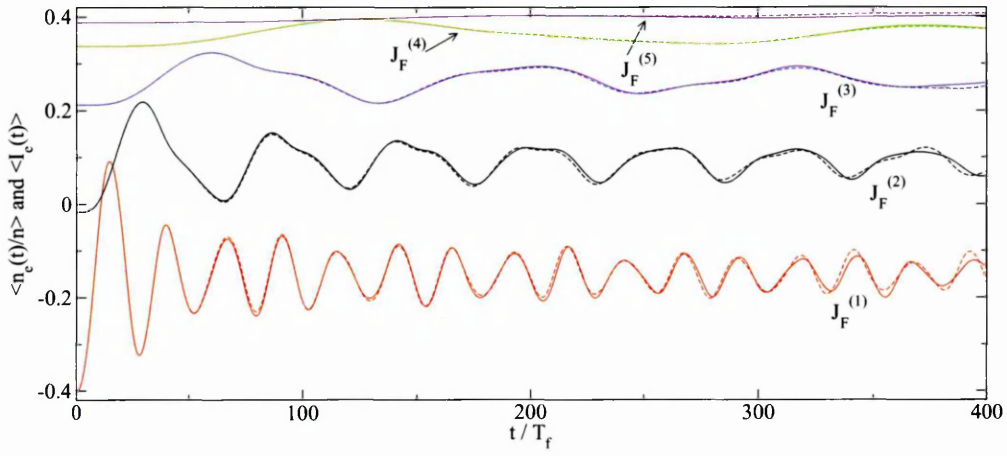

Figure 6.15 Quantum expectation curves (solid lines), $\langle n_e(t)/n \rangle$ for $n = 400$ and classical expectation curves (dashed lines), $\langle I_e(t) \rangle$, for $J_F = J_F^{(k)}$ and $k = 1, 2, \ldots, 5$. Ionisation channels are switched off. The F_s values are chosen to lie near the ionisation probability peaks, at $F_s = 0.0168, 0.0172, 0.0174, 0.0175$ and 0.01756. The m and k_i values are given in table 6.2. Field parameters are $F_\mu = 0.13$, $\Omega_0 = 0.0528$ and field envelope 0-400-0.

The slower changing expectation value, $\langle n_e(t)/n \rangle$ as the island size is reduced corresponds to a slower rate of transition between quantum states. This is confirmed in figure 6.16 for $n = 400$, which plots $|a_k(t)|^2$ for the $k = 183$ substate, calculated in the absence of ionisation. This substate is chosen as the largest k value below the classical critical ionisation limit. For clarity, the more rapidly varying curve for $J_F = J_F^{(1)}$ curve is omitted. It can be seen that as the island size is reduced $|a_k(t)|^2$ changes more slowly.

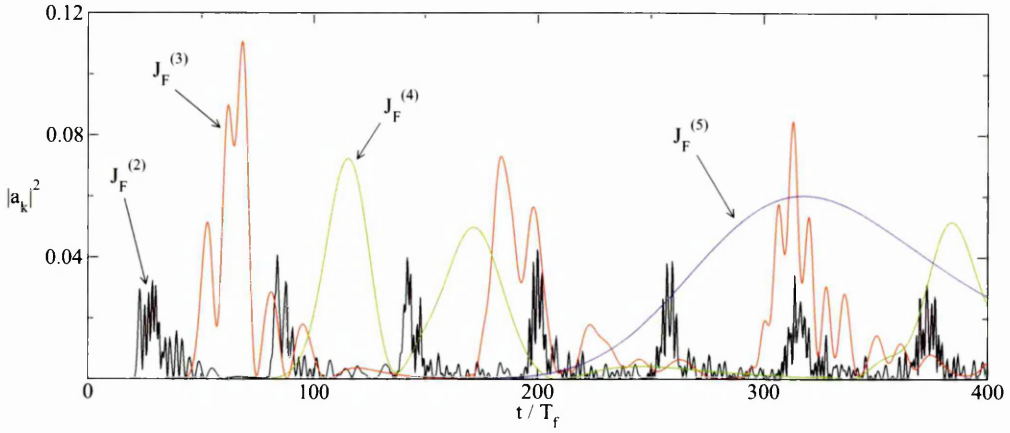

Figure 6.16 State probability densities, $|a_k(t)|^2$, calculated for $n = 400$ in the absence of ionisation for $k = 183$ for various J_F values. The field parameters and F_s values are those given for figure 6.15.

The slower rate of transition between quantum states in the region of the resonance island as the island size is reduced makes the ionisation probability more sensitive to the ionisation mechanism. At high quantum numbers for larger islands and for F_s values away from resonance, there is little difference in ionisation probabilities calculating using a step decay function rather than tunnelling. However, for the island sizes considered here, the step decay approximation increasingly underestimates the ionisation probability as the island size is reduced.

The reasons for this are presumed to be similar to those described in appendix A: because the states in the region of the first ionising state, $k = k_c$, are populated slowly, the state densities, $|a_k|$ of states $k \geq k_c$ remain very small and this effectively decouples the non-ionising states from the ionising states. This is equivalent to reducing the magnitude of $\mathcal{F}$ in equation (A.9), page 220, limiting the ionisation rate.

6.4 Field Envelopes

6.4.1 Classical Features

In earlier chapters it was observed that the field switch-on can have significant effects on the dynamics and observed behaviour such as the presence of ionisation and the shape of the ionisation curves. In this section we are concerned primarily with the effect of the field

switch-on on the quantum mechanics. Whilst the separatrix plays a significant role in classical mechanics, it occupies a relatively small area in phase space so we do not expect the separatrix to have the same effect on the quantum mechanics unless the quantum numbers — and hence the density of states in phase space — is sufficiently large. In §6.4.2 we will consider a range of quantum numbers to demonstrate this.

Before considering the quantum mechanics we examine the classical mechanics and identify some of the key observed features. These features are also seen for the exact Hamiltonian [51].

During the field switch-on, resonance islands will appear at the lower edge of phase space and pass through the evolving phase points, $\{(\psi_e(t), I_e(t))\}$. The speed of the resonance island motion depends on $\mathrm{d}\lambda/\mathrm{d}t$. In the vicinity of dynamical resonances, $F_s \approx F_s^{(j)}$, the j-th resonance island moves more slowly as $t \to T_a$ and $\mathrm{d}\lambda/\mathrm{d}t \to 0$. As the separatrix slowly crosses a phase curve comprising the phase points, $\{(\psi_e(T_a), I_e(T_a))\}$, the phase curve becomes tangled. The slower the separatrix crosses the phase curve the more tangled the curve becomes and so for slowly switched fields, the separatrix has an increased effect on the subsequent evolution of the phase curve.

Note that for $F_s > F_s^{(q)}$ where $q > 1$, each of the resonance islands, $j = 1, \ldots, q$, pass through the phase space during the field switch-on. Their effects on the phase curve are assumed to be small, as they pass quickly through the phase space allowing little time for their separatrix to affect the phase curve evolution.

To simplify the notation, the evolved curve of points $\{(\psi_e(T_a), I_e(T_a))\}$ will be labelled by $\mathcal{C}_a$ and the initial line of phase points, $\{(\psi_e(0), I_e(0))\}$, by $\mathcal{C}_0$. The subsequent motion of each phase point lying on $\mathcal{C}_a$ for times when $\lambda(t) = 1$ is determined primarily by whether the point lies inside or outside the separatrix curve boundaries of the resonance island, as demonstrated in previous chapters (for example, see chapter 4).

Figures 6.17-6.20 show the effects of different duration switch-on fields of envelope $N_a - 50 - N_a$ on ionisation for the $O(F^5)$ classical Averaged Hamiltonian for $\Omega_0 = 0.011414$, $F_\mu = 0.13$, $I_m = 0.2$ and $I_e(0) = -0.4$ near the $j = 10$ resonance. The probabilities are calculated using a grid size of $\delta F_s = 2 \times 10^{-6}$ and 300 orbits.

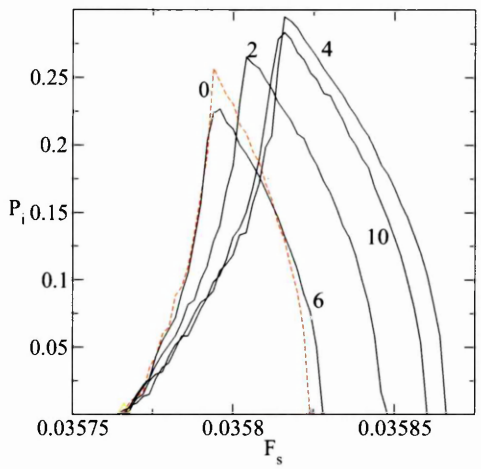

Figure 6.17 Ionisation probabilities, $P_i(F_s)$, for the classical $O(F^5)$ Averaged Hamiltonian for $F_\mu = 0.13$, $\Omega_0 = 0.011414$, $I_m = 0.2$ and various envelopes, $N_a - 50 - N_a$. Each curve is labelled by its N_a value.

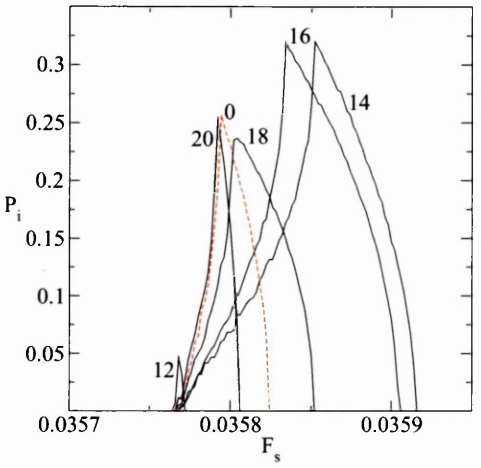

Figure 6.18 As for figure 6.17.

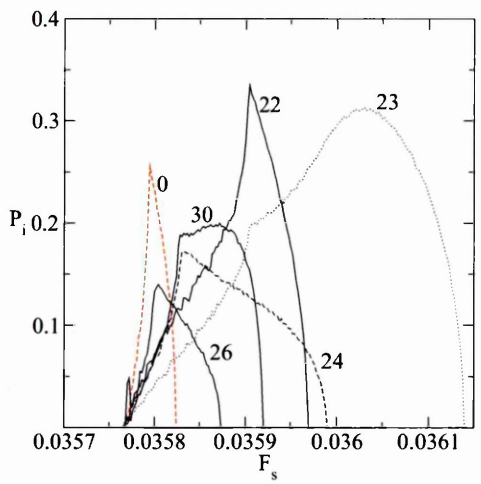

Figure 6.19 As for figure 6.17.

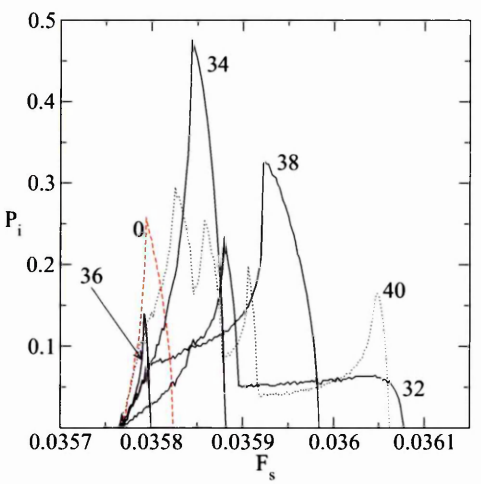

Figure 6.20 As for figure 6.17.

From the figures and from examination of the data, the following features are observed:

1. For $N_a \leq 22$ the ionisation curves are of similar shape to the $N_a = 0$ instantaneously applied field ionisation curve.

2. For $N_a \geq 23$, excluding $N_a = 28$ and $N_a = 36$, the ionisation curves become increasingly complex, sometimes with multiple local maxima. For example, for $N_a = 32$, there is a sharp peak at $F_s = 0.03588$ and a broader smaller peak at $F_s = 0.03604$.

3. There is no obvious correlation between N_a and the F_s width of the ionisation peak, or the maximum ionisation probability.

4. For $N_a = 12$ and $N_a = 36$, the ionisation peaks are very small. For $N_a = 8, 11, 13$ and 28 no ionisation is observed at all.

The observed behaviour shows the same general features as the exact classical dynamics, described in [51] §6 for the $j = 7$ resonance, although the details are different, due, at least in part, to the differences in resonance island width between the exact Hamiltonian and the approximate Hamiltonians considered here.

The observed effects on ionisation are a consequence of the changes in $I_e(t)$ occurring during the field switch-on. In figures 6.21 and 6.22 the evolved lines, $\mathcal{C}_a$, are shown for two different F_s values and for a number of different N_a values. The angle variables are transformed using equation (2.44) so that the evolved phase points can be compared with the separatrix for the Resonance Hamiltonian. For each phase point, integration is carried out for the full field duration, $N_a - 50 - N_a$, to determine whether ionisation occurs; if it does, the point is marked with a thick line.

In figure 6.21 it can be seen that for $N_a = 6, 8$ and 10, relatively small changes have occurred in $I_e(t)$ by $t = T_a$. For $F_s = 0.0358$ only librational orbits lying close to the separatrix can change sufficiently to ionise, as can be seen for $N_a = 4$ where the ionising segments lie inside the island, but the segments closest to the stable equilibrium point at the resonance island centre do not ionise. For $N_a = 6$, $\mathcal{C}_a$ lies close to the initial line, $\mathcal{C}_0$ and hence the ionisation probability is close to that observed for the instantaneously applied field, as can be seen in figure 6.17 by comparing $P_i(F_s)$ for $N_a = 0$ and $N_a = 6$. For $N_a = 8$ the evolved line, $\mathcal{C}_a$ lies wholly outside the resonance island and hence no ionisation occurs — this is true for all F_s values in the vicinity of the $j = 10$ resonance and hence no ionisation occurs for $N_a = 8$.

For the higher N_a values shown in figure 6.22, the evolved lines, $\mathcal{C}_a$, have become much more complex. In figure 6.18 it can be seen that at $F_s = 0.036$, there is ionisation for $N_a = 23$

but not for $N_a = 22$ or $N_a = 24$. From figure 6.22 it can be seen that only for $N_a = 23$ is there a segment of the $\mathcal{C}_a$ curve lying within the resonance island. For the dynamical parameters chosen, only librational orbits can be ionised, hence excluding ionisation for $Na = 22$ and $N_a = 24$.

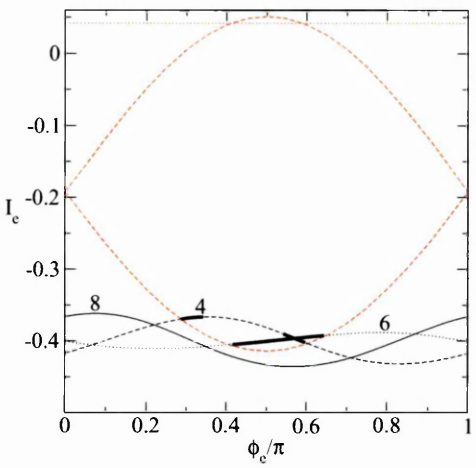

Figure 6.21 Phase space curves, $\mathcal{C}_a$, for $N_a = 4, 6$ and 8 at $t = T_a$ for the classical $O(F^5)$ Averaged Hamiltonian with $F_s = 0.0358$, $F_\mu = 0.13$, $\Omega_0 = 0.011414$, $I_m = 0.2$ and $I_e(0) = -0.4$. Thick lines show portions of phase curves which ionise later. The separatrix curves for the Resonance Hamiltonian are shown by dashed lines. The horizontal dotted line marks the critical ionisation value, $I_e = I_c$.

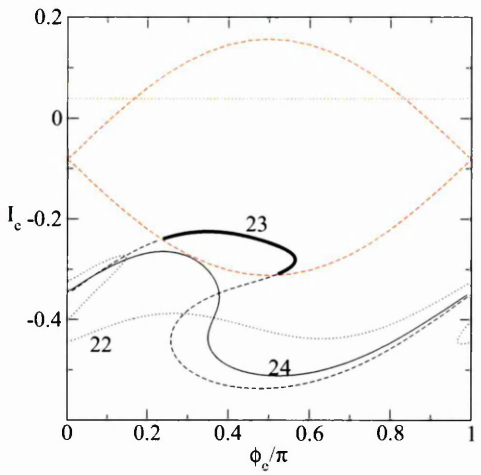

Figure 6.22 Phase space curves, $\mathcal{C}_a$, for $N_a = 22, 23$ and 24 at $t = T_a$ for $F_s = 0.036$. Other details as for figure 6.21.

6.4.2 Quantum Ionisation Probabilities for Different Envelopes

In this section we examine the ionisation probabilities for different field envelopes starting with higher quantum numbers using $n = 800$ and $n = 200$ and conclude with an examination of envelope effects at the lower quantum numbers of $n = 100$ and $n = 39$. In figures 6.23–6.26 quantum $P_i(F_s)$ curves are compared to their classical counterparts for a number of different N_a values. In each figure curves are shown for $n = 200$ and $n = 800$ with m and k_i chosen to best match the classical parameters, $I_m = 0.2$ and $I_e(0) = -0.4$.

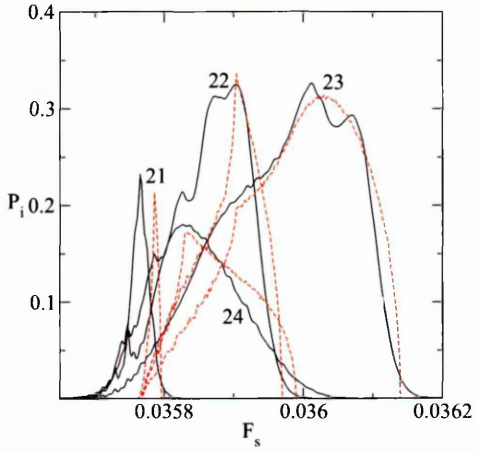

Figure 6.23 Ionisation probabilities, $P_i(F_s)$, for the quantum $O(F^5)$ Averaged Hamiltonian (solid lines) for $F_\mu = 0.13$, $\Omega_0 = 0.011414$, $n = 200$, $m = 40$, $k_i = -81$, envelope $N_a - 50 - N_a$ and N_a as marked. Comparison classical curves for $I_m = 0.2$ and $I_e(0) = -0.4$ are shown with dashed lines.

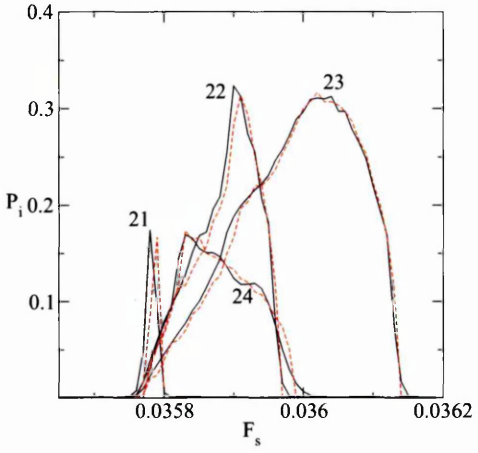

Figure 6.24 Ionisation probabilities, $P_i(F_s)$, for the quantum $O(F^5)$ Averaged Hamiltonian (solid lines) for $F_\mu = 0.13$, $\Omega_0 = 0.011414$, $n = 800$, $m = 160$, $k_i = -321$, envelope $N_a - 50 - N_a$ and N_a as marked. Comparison classical curves for $I_m = 0.2$ and $I_e(0) = -0.4$ are shown with dashed lines.

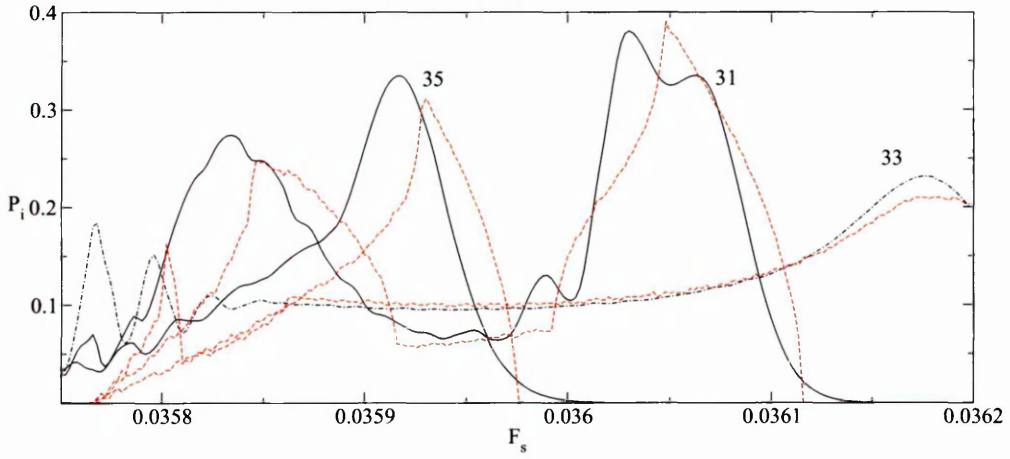

Figure 6.25 Ionisation probabilities, $P_i(F_s)$, for the quantum $O(F^5)$ Averaged Hamiltonian (solid and solid/dotted lines) for $F_\mu = 0.13$, $\Omega_0 = 0.011414$, $n = 200$, $m = 40$, $k_i = -81$, envelope $N_a - 50 - N_a$ and N_a as marked. Comparison classical curves for $I_m = 0.2$ and $I_e(0) = -0.4$ are shown with dashed lines.

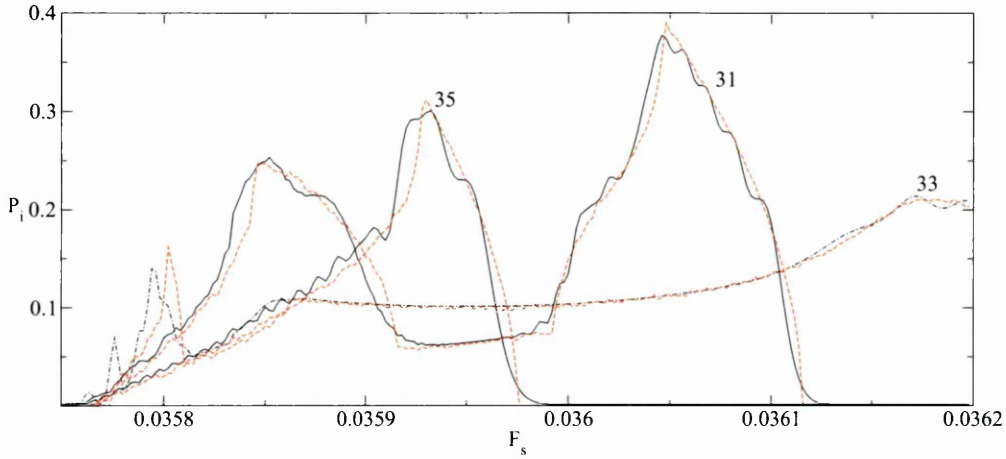

Figure 6.26 Ionisation probabilities, $P_i(F_s)$, for the quantum $O(F^5)$ Averaged Hamiltonian (solid lines) for $F_\mu = 0.13$, $\Omega_0 = 0.011414$, $n = 800$, $m = 160$, $k_i = -321$, envelope $N_a - 50 - N_a$ and N_a as marked. Comparison classical curves for $I_m = 0.2$ and $I_e(0) = -0.4$ are shown with dashed lines.

There is a very close match between the quantum and classical $P_i(F_s)$ curves. The $n = 800$ quantum curves lie closer to the classical curves, but the $n = 200$ quantum mechanics clearly also echo the classical behaviour including the complex effects that the separatrix has on the classical evolution of the initial action curve during field switch-on. For $N_a = 31$ the quantum and classical ionisation curves show two distinct ionisation peaks at $F_s \approx 0.03585$ and $F_s \approx 0.03605$, separated by a region of lower but non-zero ionisation probability. Classically, the differences can be seen to be a consequence of the complex folding of the initial action by the time $t = T_a$. This is shown in figures 6.27 to 6.29 for F_s values near the two peaks and at a point in between. They are calculated using 600 equally distributed initial orbits comprising the initial line, $\mathcal{C}_0$. The $\mathcal{C}_a$ curves are seen to undergo significant folding during the field switch-on and the shapes change considerably as F_s is varied. Although not clear from the diagrams because the phase points are no longer equally distributed, the fraction of orbits lying within the island also changes significantly, which has a direct effect on the observed ionisation probability.

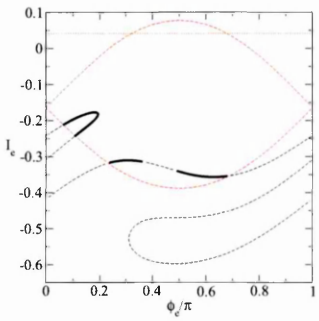

Figure 6.27 $F_s = 0.03585$

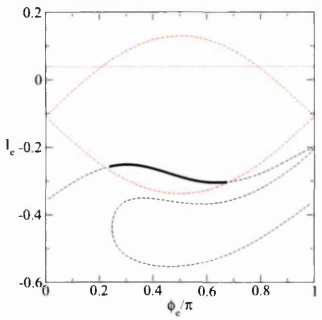

Figure 6.28 $F_s = 0.03595$

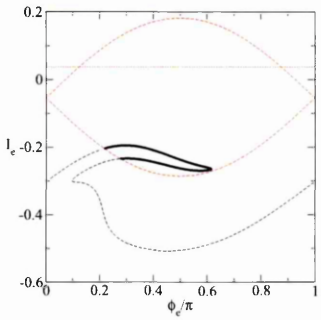

Figure 6.29 $F_s = 0.03605$

Phase space curves, $\mathcal{C}_a$, for $N_a = 31$ at $t = T_a$ for the classical $O(F^5)$ Averaged Hamiltonian with $F_\mu = 0.13$, $\Omega_0 = 0.011414$, $I_m = 0.2$ and $I_e(0) = -0.4$. Thick lines show portions of phase curves which ionise later. The separatrix curves for the Resonance Hamiltonian are shown by dashed lines. The horizontal dotted lines mark the critical ionisation values, $I_e = I_c$.

The effect of the switch-on on the quantum mechanics can be shown by plotting the probabilities, $|a_k(T_a)|$. In figures 6.30–6.32 the $n = 800$ distributions are plotted against the equivalent classical orbit density functions at each of the F_s values in figures 6.27–6.29. The classical orbit density function is calculated using 4000 equally distributed initial orbits comprising $\mathcal{C}_0$ and calculating the density of orbits in each of 800 equal intervals in the I_e range $(I_m - 1, 1 - I_m)$. In the figures shown here, the classical orbit density is then scaled to match the principal quantum number for the quantal probabilities to be compared with. The small fluctuations in the classical orbit densities are due to statistical errors. The classical folding of the line $\mathcal{C}_a$ is seen in the appearance of peaks in the classical orbit density function corresponding to the horizontal sections of the $\mathcal{C}_a$. As the field switch time, T_a, is increased, the number of folds generally increases leading to more peaks in the classical orbit density. For comparison, figure 6.33 compares the classical orbit density and $n = 800$ probability for the relatively short switch-on time of $N_a = 8$ at $F_s = 0.03567$. The simpler structure reflects the less deformed line, $\mathcal{C}_a$, seen in figure 6.21.

The quantum probabilities, $|a_k(n_e/n)|$, are seen to fluctuate but have similar underlying features to the classical orbit densities. In figure 6.32 an additional curve is depicted with a broken dashed line that removes the fluctuations by calculating an averaged $|a_k|$ value using a moving window of 9 adjacent k points.

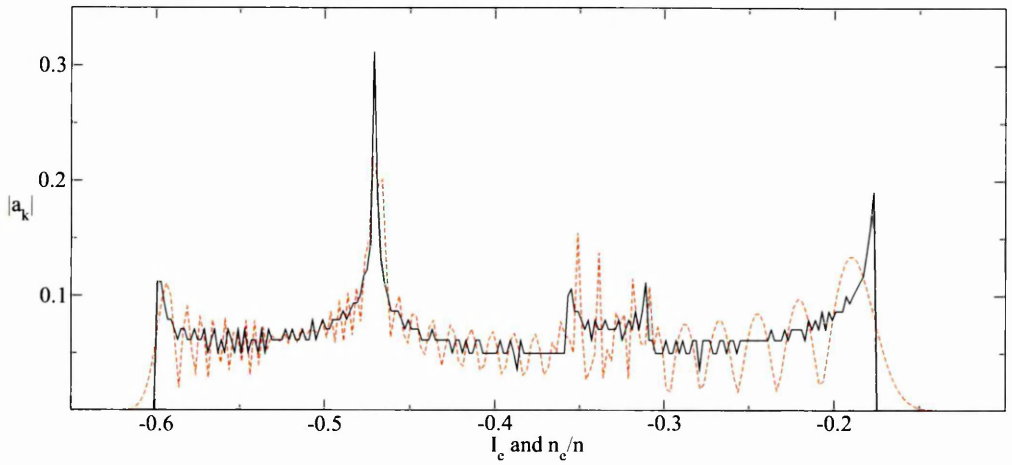

Figure 6.30 State probabilities, $|a_k(n_e/n)|$, evaluated at $t = T_a$ for $n = 800$, $m = 160$ and $k_i = -321$ for the quantum $O(F^5)$ Averaged Hamiltonian with $F_s = 0.03585$, $F_\mu = 0.13$, $\Omega_0 = 0.011414$, envelope $31 - 50 - 31$ (dashed line). A comparison classical orbit density is shown for $I_m = 0.2$ and $I_e(0) = -0.4$ (solid line). For comparison, the evolved line $\mathcal{C}_a$ is shown in figure 6.27.

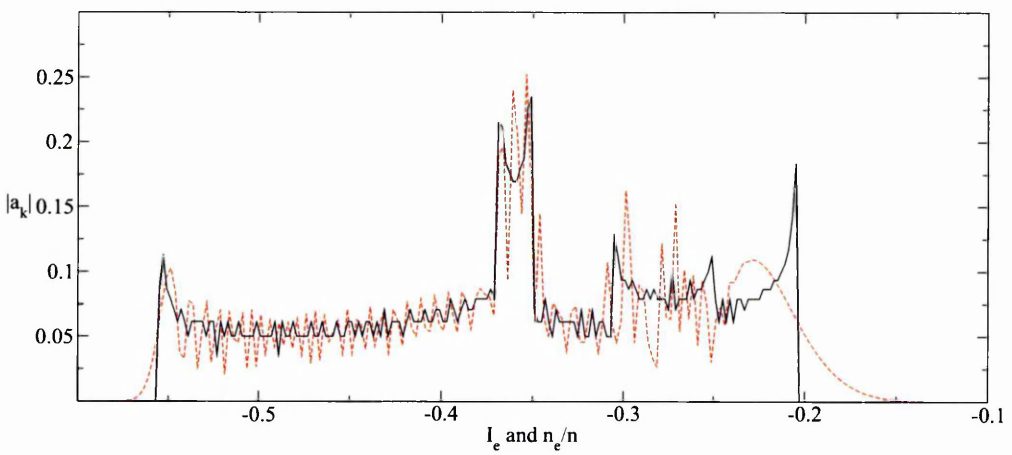

Figure 6.31 State probabilities, $|a_k(n_e/n)|$, evaluated at $t = T_a$ for $n = 800$, $m = 160$ and $k_i = -321$ for the quantum $O(F^5)$ Averaged Hamiltonian with $F_s = 0.03595$, $F_\mu = 0.13$, $\Omega_0 = 0.011414$, envelope $31 - 50 - 31$ (dashed line). A comparison classical orbit density is shown for $I_m = 0.2$ and $I_e(0) = -0.4$ (solid line). The evolved line $\mathcal{C}_a$ is shown in figure 6.28.

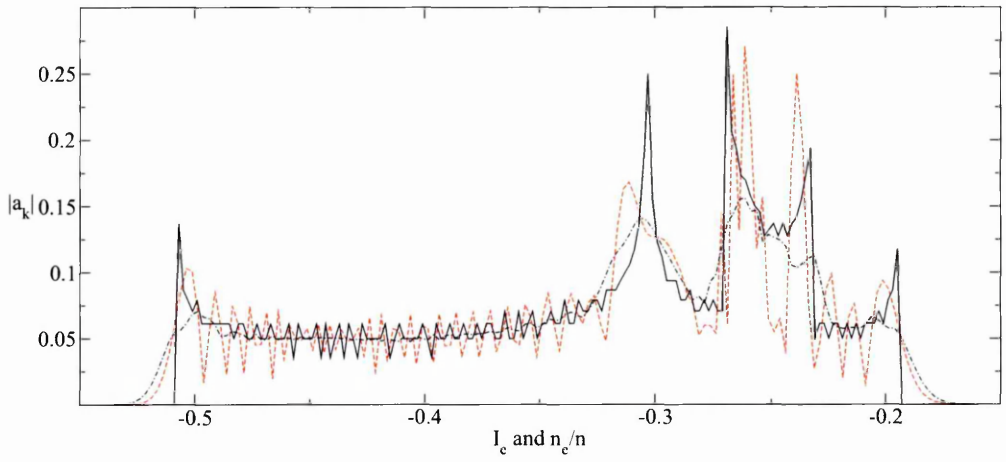

Figure 6.32 State distribution, $|a_k(n_e/n)|$, evaluated at $t = T_a$ for $n = 800$, $m = 160$ and $k_i = -321$ for the quantum $O(F^5)$ Averaged Hamiltonian with $F_s = 0.03605$, $F_\mu = 0.13$, $\Omega_0 = 0.011414$, envelope $31 - 50 - 31$ (dashed line). A comparison classical orbit density is shown for $I_m = 0.2$ and $I_e(0) = -0.4$ (solid line). The evolved line $\mathcal{C}_a$ is shown in figure 6.29.

For the classical system, some ionisation peaks are missing or very small for particular N_a values. The effect is also seen for higher quantum numbers, although in some cases the probabilities are small rather than zero. As the quantum number is reduced, ionisation by tunnelling from states below the classical limit, I_c, becomes increasingly important, contributing to increased ionisation and lowering the F_s value at which ionisation starts. In figure 6.34 the $N_a = 8$ ionisation probabilities are plotted for increasing n. It can be seen that for $n = 800$, $P_i(F_s) < 0.013$, but as n is reduced the ionisation peaks increase in magnitude. There is also a shift in the location of the ionisation probability maximum towards lower F_s as n decreases; this is discussed later.

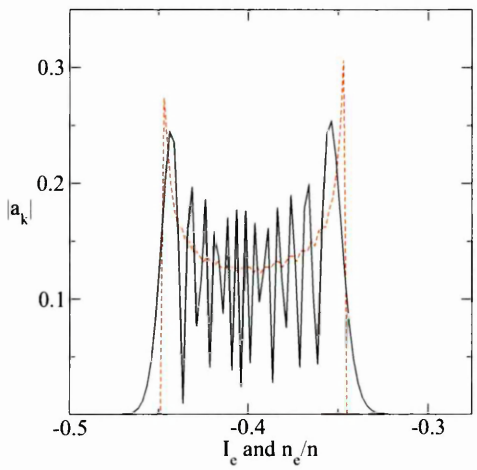

Figure 6.33 State probability, $|a_k(n_e/n)|$, evaluated at $t = T_a$ for $n = 800$, $m = 160$ and $k_i = -321$ for the quantum $O(F^5)$ Averaged Hamiltonian with $F_s = 0.03567$, $F_\mu = 0.13$, $\Omega_0 = 0.011414$, envelope $8-50-8$ (dashed line). A comparison classical orbit density is shown for $I_m = 0.2$ and $I_e(0) = -0.4$ (solid line).

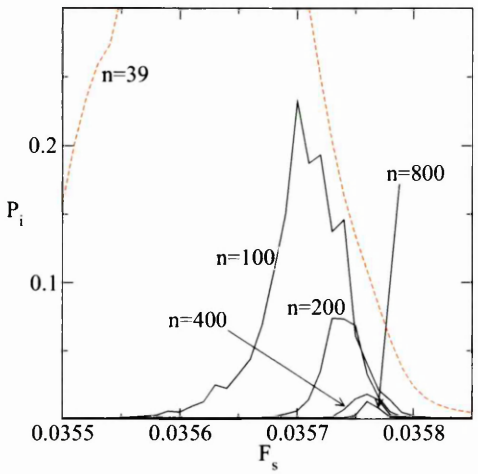

Figure 6.34 Ionisation probabilities, $P_i(F_s)$, for the quantum $O(F^5)$ Averaged Hamiltonian for $F_\mu = 0.13$, $\Omega_0 = 0.011414$, envelope $8-50-8$ and various n with m and k_i values chosen to best match $I_m = 0.2$ and $I_e = -0.4$

The envelope effects can also be seen for lower quantum numbers, although the correspondence between classical and quantum behaviour becomes less clear as the quantum number decreases. Figures 6.35 and 6.36 show ionisation probabilities for $n = 100$. The field envelopes are chosen for comparison with figures 6.23–6.26 for $n = 200$ and $n = 800$.

Although the match between quantal and classical curves is not as good for $n = 100$ as it is for higher quantum numbers, the quantal curves still echo the classical behaviour. For example, in figure 6.36 for $N_b = 31$ both the classical and quantal curves have two distinct maxima. For $N_b = 33$, there is a gradual increase in ionisation probability for $F_s > 0.0359$ for both the quantal and classical curves.

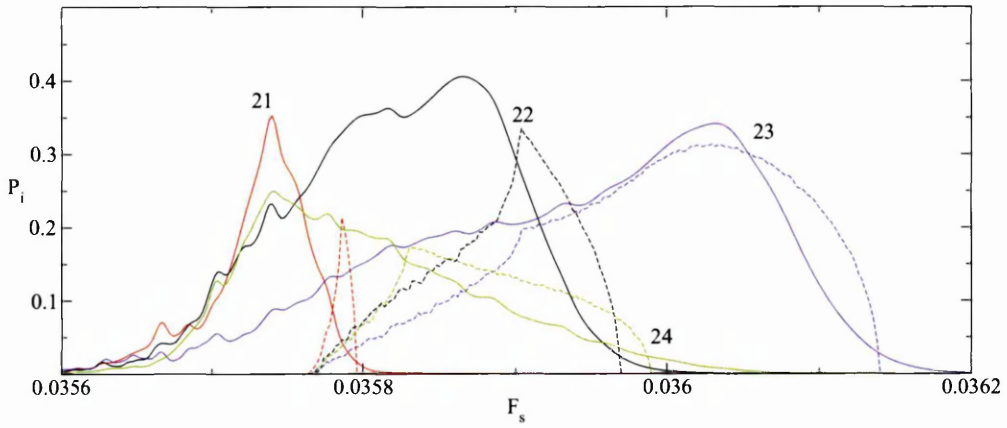

Figure 6.35 Ionisation probabilities, $P_i(F_s)$, for the quantum $O(F^5)$ Averaged Hamiltonian (solid lines) for $F_\mu = 0.13$, $\Omega_0 = 0.011414$, $n = 100$, $m = 20$, $k_i = -41$, envelope $N_a - 50 - N_a$ and N_a as marked. Comparison classical curves for $I_m = 0.2$ and $I_e(0) = -0.4$ are shown with dashed lines. A different colour is used for each N_b value.

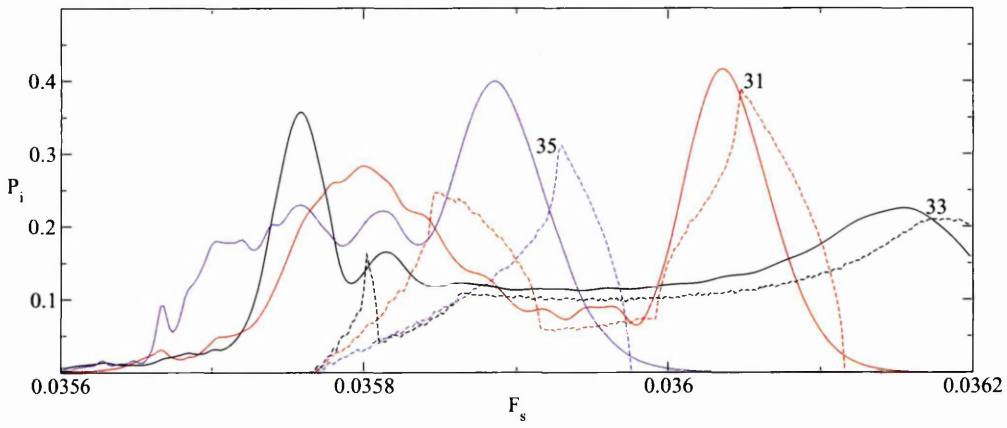

Figure 6.36 As for figure 6.35.

In figures 6.37 to 6.40 ionisation probabilities are shown for the quantum $O(F^5)$ Averaged Hamiltonian for $F_\mu = 0.13$, $\Omega_0 = 0.011414$, $n = 39$, $m = 8$, $k_i = -16$, field envelope $N_a - 50 - N_a$ and a selection of N_a values in the range $(0, 40)$.

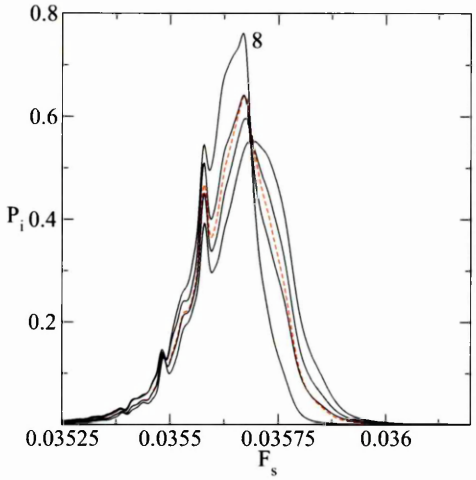

Figure 6.37 Ionisation probabilities, $P_i(F_s)$, for the quantum $O(F^5)$ Averaged Hamiltonian for $F_\mu = 0.13$, $\Omega_0 = 0.011414$, $n = 39$, $m = 8$, $k_i = -16$, envelope $N_a - 50 - N_a$ and $N_a = 0, 2, \ldots, 10$. The $N_a = 0$ curve is shown by a dashed line.

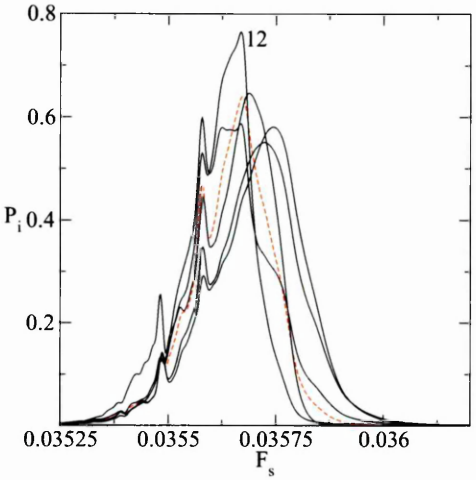

Figure 6.38 Ionisation probabilities, $P_i(F_s)$, for the quantum $O(F^5)$ Averaged Hamiltonian for $F_\mu = 0.13$, $\Omega_0 = 0.011414$, $n = 39$, $m = 8$, $k_i = -16$, envelope $N_a - 50 - N_a$ and $N_a = 0, 12, 14, \ldots, 20$. The $N_a = 0$ curve is shown by a dashed line.

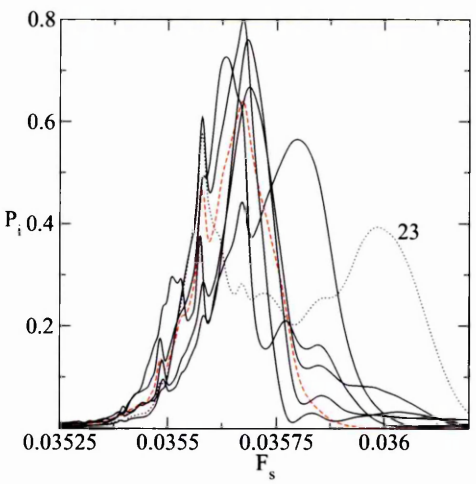

Figure 6.39 Ionisation probabilities, $P_i(F_s)$, for the quantum $O(F^5)$ Averaged Hamiltonian for $F_\mu = 0.13$, $\Omega_0 = 0.011414$, $n = 39$, $m = 8$, $k_i = -16$, envelope $N_a - 50 - N_a$ and $N_a = 0, 22, 23, 24, 26, 28$ and 30. The $N_a = 0$ curve is shown by a dashed line.

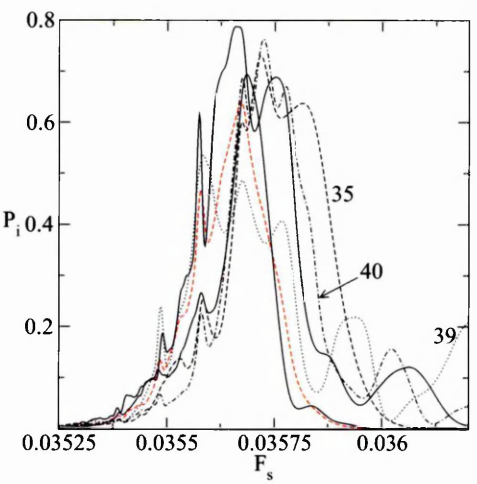

Figure 6.40 Ionisation probabilities, $P_i(F_s)$, for the quantum $O(F^5)$ Averaged Hamiltonian for $F_\mu = 0.13$, $\Omega_0 = 0.011414$, $n = 39$, $m = 8$, $k_i = -16$, envelope $N_a - 50 - N_a$ and $N_a = 0, 32, 35, 36, 39$ and 40. The $N_a = 0$ curve is shown by a dashed line.

Whilst there is no straightforward correlation between the $n = 39$ quantum and the classical ionisation probabilities there are some broad similarities. For $N_a \leq 10$, excluding $N_a = 8$, the ionisation curves are generally of similar shape with one main peak and a number of smaller peaks superimposed on the curves. The main peaks lie at lower F_s values than for the corresponding classical ionisation probabilities. As N_a is increased, the curve shapes become more complex. For $N_a = 23$, as for the classical and high quantum number ionisation curves, the maximum P_i value is at a noticeably higher F_s value than for $N_a = 22$ or $N_a = 24$. In contrast to the classical mechanics, there are no N_a values for which $P_i(F_s) = 0$ across the resonance region.

As observed for the $n = 39$ curves and in figure 6.34, the ionisation probability maxima generally lie at lower F_s values than for the classical dynamics, which is partly a consequence of ionisation tunnelling from states below the classical ionisation limit, I_c. This also explains why classically missing ionisation peaks are present, such as for $N_a = 8$: the state excitations required for ionisation are smaller than the corresponding required changes in I_e for ionisation to occur classically. This can be demonstrated by comparing the quantum ionisation probabilities with those generated using the step decay function described in §3.1.3. This excludes ionisation tunnelling from states below the classical critical limit, I_c. The curves are compared for $N_a = 5$ and $N_a = 8$ in figures 6.41 and 6.42. The step decay ionisation probabilities are considerably lower when tunnelling is excluded and have peaks at higher F_s values. The start of ionisation is also higher for the step decay function. Higher F_s values are required to cause excitation to states where ionisation can occur. This parallels classical behaviour for the start of ionisation, where ionisation starts when the top of the resonance island meets the critical ionisation value, I_c. If I_c is increased, then F_s must be increased for this condition to be met.

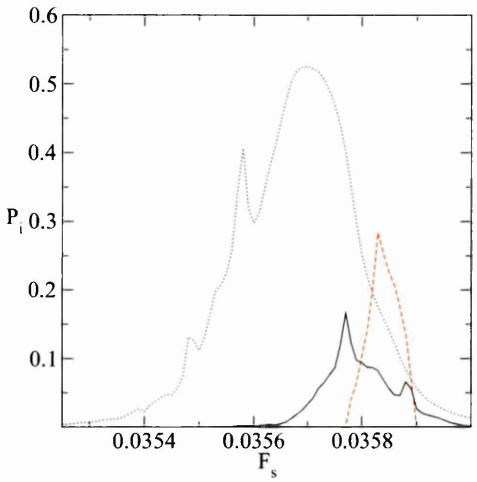

Figure 6.41 Ionisation probabilities, $P_i(F_s)$, for the $O(F^5)$ Averaged Hamiltonian for $F_\mu = 0.13$, $\Omega_0 = 0.011414$, $n = 39$, $m = 8$, $k_i = -16$ and envelope $5 - 50 - 5$. Quantum curves are shown with a black dotted line, classical curves for $I_m = 0.2$ and $I_e(0) = -0.4$ are shown with a red dashed line and quantum ionisation probabilities with a step decay function are shown with a black solid line.

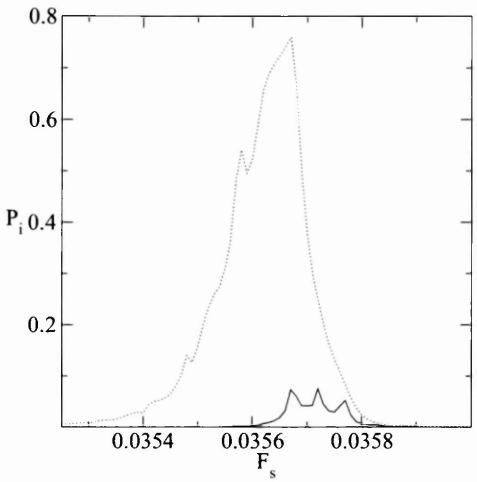

Figure 6.42 Ionisation probabilities, $P_i(F_s)$, for the $O(F^5)$ Averaged Hamiltonian for $F_\mu = 0.13$, $\Omega_0 = 0.011414$, $n = 39$, $m = 8$, $k_i = -16$ and envelope $8 - 50 - 8$. Quantum $P_i(F_s)$ with a semi-classical decay function is shown with a dotted line and quantum $P_i(F_s)$ with a step decay function is shown with a solid line. For this field envelope, classically $P_i(F_s) = 0$ for the field values shown.

6.4.3 Conclusions

For slowly switched fields, the classical dynamics for the Averaged Hamiltonian, $\overline{K}_m$, equation (2.24) (page 38), show the same general features seen for the exact Hamiltonian. As the field switch duration, T_a, is extended, the structure of the ionisation probability, $P_i(F_s)$, becomes more complex and for some switch durations, T_a, ionisation is absent altogether. We have shown that the ionisation structure is due to the tangling of the phase curve by the separatrix and that as T_a increases, the slower motion of the separatrix through phase space during the field switch-on causes the phase curve to become more tangled.

It was noted at the beginning of §6.4 that the separatrix occupies a relatively small region in phase space and consequently the quantal dynamics for a slowly switched field may not reflect the classical mechanics unless a sufficiently high quantum number is used. We have shown that for the field parameters considered here, when $n \geq 200$, the quantum mechanics closely

follows the separatrix-induced classical behaviour. As the quantum number is reduced, the correspondence becomes less clear, although for $n = 100$ the quantum ionisation probability still echoes some of the classical structure. When the quantum number is reduced to $n = 39$, the relationship between the ionisation probabilities for the classical and quantal dynamics is no longer clear; however, the ionisation probability still shows increasing complexity as the switch time is increased.

Chapter 7

Conclusions

In this thesis we made a detailed examination of the classical and quantal dynamics of an excited hydrogen atom subjected to parallel static and microwave field of frequency, Ω, which is low compared to the Kepler period of the unperturbed excited hydrogen atom, ω_K.

The system has three important frequencies: the frequency of the applied field, Ω, the Kepler frequency of the excited electron, ω_K, and the frequency of precession of the electron orbital ellipse. The behaviour of this system is mainly determined by two time scales: the ratio, Ω/ω_K, and the ratio of the frequency of precession of the electron orbital ellipse to Ω. Interaction between the microwave field and the Kepler motion of the electron can cause resonances for $p\omega_K = q\Omega$, where p and q are integers. The frequency of precession of the electron orbital ellipse depends on the static field strength. This can cause resonances with the microwave field for particular values of the static field. The two time scales mean that the motion is two-dimensional, and cannot be accurately approximated by a one-dimensional system as is the case when the static field is zero.

These resonances are manifest in experiments and calculations, with changes in ionisation seen for field values in their vicinity. For low scaled frequencies, $\Omega_0 = \Omega/\omega_K \ll 1$, peaks are observed in plots of ionisation against static field strength near the resonances.

For low scaled frequencies, Ω_0, the system changes adiabatically in response to the slowly changing field. Classically, for the system described in adiabatic action-angle variables, increasing field strength reduces the height of the potential barrier separating bound states from

the continuum. For a slowly switched on field, some states therefore ionise 'over the barrier' as the barrier height reduces with increasing field strength. Quantally, there is also a significant contribution to ionisation due to tunnelling from adiabatic states lying close to the top of the barrier.

When a static field is present, the motion remains adiabatic. Near resonances the electric action, I_e, can vary significantly, but for low scaled frequencies, the principal action, I_n, remains approximately constant for all field strengths. This fact was exploited in the development of a classical description of the present problem by Richards [51], allowing, by appropriate transformations of the Hamiltonian and averaging methods, an approximate time-dependent classical Hamiltonian with one degree of freedom to be derived. This Hamiltonian forms the basis for the work we have presented here, which is broadly in two areas. First, we have determined some characteristic properties of the classical Hamiltonian and used these to explain some of the classical behaviour of the system. Secondly, we have developed a one-dimensional quantal approximation and used this to explore the quantal behaviour of the system.

We have found that the classical approximation is a good approximation for the field strengths we are concerned with, capturing most of the features seen in calculations using the exact classical dynamics for ionisation probabilities and ionisation times. There is a reasonable match for the locations of resonances and shapes of the ionisation peaks are also reflected. For some fields (e.g. $\Omega_0 = 0.0528$) there is a very good match over most of the static field range considered; see for example, figure 2.10 on page 52.

For fields near resonance, the behaviour of the system is dominated by the presence of resonance islands in phase space and their effect on the classical orbits. We derived expressions for the locations and sizes of these resonance islands and used these to explain some of the structure seen in plots of ionisation probability against static field strength. A summary of the key features and analysis is given here:

1. Calculated resonance locations, $F_s = F_s^{(j)}$, do not always coincide with the locations of associated peaks in ionisation probability. For example, for $\Omega_0 = 0.011414$, the ionisation peaks are very narrow and many are displaced from the resonance location so that the ionisation probability is zero at $F_s = F_s^{(j)}$ (see table 2.5, page 81, and figures 2.35–2.37 on pages 82–83). From properties of the resonance island, we have found expressions for the

start and end field values, $F_s^{(start)}$ and $F_s^{(end)}$, marking the boundaries of the ionisation peak, such that the ionisation probability is non-zero for $F_s^{(start)} \leq F_s \leq F_s^{(end)}$, and shown that they have a reasonable match with numerical calculations.

2. For field strengths and initial action, $I_e(0)$, such that only librational orbits ionise, the start of ionisation, $F_s^{(start)}$, is predicted to be independent of the initial action. This was confirmed for the approximate Hamiltonian and is also seen for a number of resonances of the exact classical dynamics.

3. The predicted start of ionisation for librational orbits is independent of the field envelope. This is consistent with the numerical calculations.

4. Not all resonances produce ionisation peaks. Whether they arise depends on the resonance island width, the initial action and the critical action for ionisation. A reasonable prediction of the occurrence of ionisation peaks was obtained for instantaneously applied fields. For slowly-switched fields the predictions are less accurate, due to the evolution of the initial phase curve during field switch-on.

For fields away from resonance, the electric action, I_e, is approximately constant after the field has reached a constant amplitude. Using classical perturbation theory we have confirmed this, showing that $I_e(t)$ makes small fluctuations about a constant value and that the fluctuations are of order $O(F_\mu \Omega_0)$.

Any quantum mechanical treatment of this problem is challenged by the high quantum numbers involved and the need to include interactions between bound states and the continuum. A three-dimensional approach using a basis of unperturbed states would probably be computationally intractable for the high quantum numbers considered here.

In this thesis we develop a quantal approximation by quantising the Hamiltonian for the one-dimensional classical approximation. The choice of basis states makes the quantum approximation computationally efficient and suitable for application to problems involving large quantum numbers. The system is tri-diagonal and the computational effort for calculating the ionisation probability for a system in a single initial state increases approximately as $n^{1.7}$, where n is the principal quantum number. In contrast, the computational effort required for

calculations using the unperturbed states, even for a fixed principal quantum number and excluding the continuum interaction, increases as n^3.

The description obtained by quantising the classical approximation includes bound states only: ionisation must be included as an additional approximation. For the system described in action-angle variables, there is a potential barrier separating the bound states from the continuum; the height of this barrier reduces with increasing field strength. There are two principal mechanisms for ionisation. Electrons can be excited sufficiently to reach energies 'over the barrier', or they can ionise by tunnelling through the potential barrier to the continuum.

Both types of ionisation are incorporated by the addition of complex energies. Tunnelling ionisation rates were obtained using semi-classical decay rates obtained for low scaled frequency microwave fields in the absence of a static field. The complex energy expressions are suitable for application over a range of field strengths. The semi-classical decay rates were calculated by assuming that the field is slowly changing and treating the barrier as fixed at that point in time. This assumption must become invalid at some point as the frequency is increased, but the dynamics of tunnelling through time-varying barriers is not currently well understood. For the scaled frequencies we are concerned with Dando *et al* [21] has shown that, in the absence of static fields, the semi-classical decay rates provide a reasonable match to experiment.

There is limited published data available for the quantum numbers and scaled frequencies of interest to validate the quantal approximation. However, our calculations are consistent with the calculations of ionisation probabilities and ionisation times produced by Robicheaux *et al* [52], calculated using a split operator method with an absorbing barrier for $n = 39$, $\Omega_0 = 0.0730$ and $F_\mu = 0.14372$.

We have made ionisation probability calculations for a wide range of quantum numbers and examined the ionisation contributions due to tunnelling. We have confirmed that as the principal quantum number is reduced, tunnelling becomes increasingly significant but that even for $n = 100$, tunnelling still is important for some field strengths.

By examining the ionisation for small resonance islands, we have shown that as the island size becomes smaller, tunnelling becomes important for increasingly high quantum numbers. For the island sizes tested, tunnelling has a significant effect on ionisation for up to $n = 200$ (see for example, figures 6.13 and 6.14 on page 189).

For the classical dynamics, after the initial field switch-on, there is a distinct separation between orbits that will ionise and those that remain bound. This means that after a certain time, classically ionisation effectively ceases. In contrast, we have shown numerically that this is not always the case for the quantal dynamics. For the low quantum number, $n = 10$, for a field value off-resonance, we demonstrated in §3.4 (page 126) that the long-term ionisation rate is approximately exponentially decaying, suggesting that the rate is proportional to the population of remaining non-ionised states: effectively there is a continuous ionisation from these states to the continuum.

The difference between the classical and quantal ionisation mechanisms leads to additional structure in plots of quantal ionisation probability against time, not seen in the classical dynamics. Whereas the classical ionisation rises gradually and then ceases, the quantal ionisation shows a rise followed by additional successive steps in the ionisation probability, separated by times of lower ionisation rates — this is seen in figure 4.4 on page 136. The quantal system takes longer to reach its final ionisation probability than the corresponding classical system. The reasons for this are complicated, reflecting both the quantum nature of the ionisation mechanism and the effect of the classical separatrix on the quantal dynamics. For the classical approximation presented here, all classical orbits reaching sufficient energies ionise, so that all classical ionising orbits can undergo at most one librational or rotational period (depending on their proximity to the separatrix) before ionising. In contrast, the quantal ionisation mechanism causes only the partial depopulation of states near the ionisation limit. The remaining populated states affect the ongoing evolution of the system and lead to further rises in the ionisation rate at later times. The time scales for these subsequent occurrences are consistent with the classical evolution of the system due to the resonance island.

Near resonance at low quantum numbers, additional small peaks and troughs are seen in ionisation probability plots against field strength near resonance; these are not present in the classical dynamics. We have shown that they are associated with avoided crossings in the quasi-energies for the system, caused by the resonance. These avoided crossings increase in number as the quantum number is increased and for high quantum numbers their combined effect on transitions between states becomes increasingly similar to the classical dynamics.

The classical and quantal methods developed are used to explain the detailed resonance

behaviour seen for two neighbouring resonances, $j = 1$ and $j = 2$, for the scaled variables $\Omega_0 = 0.0528$ and $F_\mu = 0.13$. Classically, for the $j = 1$ resonance, only librational orbits can ionise, whilst for $j = 2$, both librational and rotational orbits contribute to the ionisation, leading to different ionisation behaviour. Classically, for short duration fields, two separated ionisation peaks are seen near the $j = 2$ resonance. The cause of this is shown to be (a) the different time scales associated with the librational and rotational orbits and (b) the effect of the field switch on the initial evolution of the orbits. We have demonstrated, by comparison between classical and quantal ionisation probability plots, that the complex influence of the separatrix on the classical dynamics is echoed in the quantal dynamics, even for relatively low quantum numbers, such as $n = 39$.

The effects of the separatrix also arise in the variation of ionisation times with static field strength. Away from resonance, ionisation times are determined primarily by the time taken during the field switch-on, for the field to reach a critical ionisation limit determined by the initial substate, $(I_m, I_e(0))$. At resonance, the librational and rotational periods of ionising orbits affected by the resonance island determine the ionisation times and lead to sharp peaks at the edges of the resonances for systems prepared in an initial substate, $(I_m, I_e(0))$. This is seen in figures 5.2 and 5.3 on page 149 for the exact and approximate classical dynamics. We have calculated classical expressions for the ionisation times and confirmed that these accurately capture the classical ionisation times numerically obtained for the Averaged Hamiltonian and that these also reflect the behaviour of the exact classical dynamics.

Richards [51] noted that in addition to the peaks at the edges of the resonance, an additional peak is present near the centre of the $j = 2$ resonance for $\Omega_0 = 0.0528$ and $F_\mu = 0.13$. This is also seen for the classical approximation and we have shown that in this case it is caused by the varying ionisation contributions from librational and rotational orbits at this resonance.

We have calculated resonance ionisation times using the quantum approximation. For $n \geq 100$ the ionisation times show all of the essential features seen for the classical dynamics. Even for $n = 39$, the ionisation time near the centre of a resonance shows similar features to the classical ionisation times, with longer ionisation times at the edge of the resonance. Hence the separatrix manifests itself even at the relatively low quantum numbers accessible to experiment.

In this thesis we have calculated the ionisation times for microcanonical distributions of initial states at resonance. These calculations allow comparison to be made with the calculations of Robicheaux *et al* [52] as a test of our quantal approximation. These are also of interest as they should be measurable experimentally, although this would require significant modification to the current experiments. For microcanonical distributions of initial states, the averaging over multiple states removes the sharp peaks for single state ionisation times, but a clear peak in ionisation time is seen in the region of the resonance. Individual profiles of ionisation probability against time were also calculated for particular field values. These field values were chosen for comparison with similar calculations by Robicheaux *et al* [52] (in particular, their figure 2), who considered three field values, one at resonance and one on each side of the resonance. There is a good match in the general behaviour, with slower ionisation at resonance, consistent with the explanations presented here.

For very slowly-switched fields, calculations using exact classical dynamics show that the slow motion of the separatrix tangles the phase curves and leads to complex structures in plots of ionisation probability against static field strength. We have confirmed that the same effects are seen for the classical approximation, including the suppression of ionisation for some switch durations.

The effect of the separatrix on the quantum dynamics is expected to be more limited for smaller quantum numbers as the number of states near the separatrix will be small. However, for increasing quantum number the separatrix is expected to influence the quantal behaviour. We have shown that for the high quantum numbers, $n = 200$ and $n = 800$, the quantal behaviour is very similar to the classical behaviour and that even for $n = 100$, the separatrix effects are clearly manifest in the quantal dynamics. For the smaller quantum number, $n = 39$, the ionisation behaviour is also shown to become increasingly complex with increasing switch time, although there is no obvious connection with the corresponding classical ionisation structures.

The results discussed in this thesis are theoretical predictions based upon a variety of approximations. Some of the early classical results of Richards [51], involving averages over substates, have been compared with unpublished experimental results; in general there is quite good agreement for the resonance positions and widths. However, there are currently

no equivalent experimental results for atoms in specific substates or for principal quantum numbers, $n < 30$ or $n > 50$. One of the significant findings of the current calculations is that the envelope shape can have a measurable effect on the ionisation probability. Thus, one important future goal must be to obtain detailed experimental results for atoms in particular substates over a wide range of principal quantum numbers and for various field envelopes, all other parameters being the same; the latter is a major challenge.

The theory relies on a number of approximations. Averaging methods reduce the effective number of degrees of freedom, but generally these are quite robust and usually only introduce quantitative errors. Similarly, the derivation of the quantal equations of motion should be robust for sufficiently large quantum numbers since the errors are $O(n^{-2})$: only quantitative errors are expected to be introduced by this approximation.

In both classical and quantal theories ionisation is introduced via crude approximations. For the classical approximation this ionisation mechanism can be checked by comparison with accurate numerical solutions of the equations of motion derived from the original Hamiltonian: it is found to be accurate for the low scaled frequencies examined here, where $\Omega_0 < 0.1$. In the quantum approximation it is necessary to introduce the additional, and sometimes dominant, mechanism of tunnelling through a moving barrier using time-dependent decay factors. This approximation needs a thorough theoretical investigation to determine how its accuracy depends upon the scaled frequency and the principal quantum number.

The field configuration considered here conserves the electron angular momentum in the field direction; in other words, the quantum number, m, is constant. For large $|m|$ the electron does not orbit close to the nucleus, which suggests that effects similar to those described here might be seen for other Rydberg atoms.

For hydrogen it would be interesting to investigate the effects of making the periodic component of the electric field elliptically polarised, which would increase the number of degrees of freedom of the system and hence the complexity of the dynamics.

In summary, I have derived an efficient quantal method for computing the ionisation probability of an excited hydrogen atom in parallel static and microwave fields, which is valid at low scaled frequencies. The method can be applied to fields with slowly varying field envelopes. I have tested the approximation where possible and shown it to accurately describe the general

behaviour of the system. I have used it to explore the differences in behaviour of classical and quantal ionisation probabilities. I have shown that there are significant qualitative differences at low principal quantum number, $n \approx 10$, but that as n increases these differences decrease, although there are still significant quantitative, but not qualitative, differences for n as large as 100. Even in the cases where the classical separatrix dominates the classical structure, we see convergence between the classical and quantal probabilities as n increases and even for $n = 39$, which is accessible to experiment, the effect of the separatrix is seen in the quantal ionisation probabilities.

Appendix A

Ionisation Dependence upon Step Decay Size

For the step decay function, equation (3.17), the magnitude D determines the rate of decay for ionising states. It is clear that if D is too small, ionisation will be suppressed because the decay rate will be too small. However, perhaps less intuitively, large values of D also suppress ionisation. To understand this behaviour, we start by writing the quantum mechanical equations of motion, (3.9)–(3.11), in the vector form

$$\dot{\mathbf{a}} = -iE(t)\mathbf{a} - iG(t)\mathbf{a} \tag{A.1}$$

where $E(t)$ is a diagonal matrix with elements $E(t)_{kk} = nE_R(k,t) - i\Gamma_s(k,t)/2$ and $G(t)$ is an Hermitian matrix containing the off-diagonal coupling terms given by equation (3.19), page 92.

If we restrict our attention to times for which $\lambda(t) = 1$, then the energy matrix elements are time-independent. To simplify the analysis, it is assumed that the microwave field strength, F_μ, is sufficiently weak that only ionisation from upper k states need to be considered. From equation (3.17) ionisation occurs for states $k \geq k_c$. The rate of change of the ionisation

probability can be seen to depend only on the population of the states $k \geq k_c$, as

$$\frac{\mathrm{d}|\mathbf{a}|^2}{\mathrm{d}t} = \frac{\mathrm{d}}{\mathrm{d}t}(\mathbf{a}^\dagger \mathbf{a}) = \dot{\mathbf{a}}^\dagger \mathbf{a} + \mathbf{a}^\dagger \dot{\mathbf{a}}$$

and from equations (A.1) and (3.16)

$$\begin{aligned} \frac{\mathrm{d}|\mathbf{a}|^2}{\mathrm{d}t} &= i\mathbf{a}^\dagger(E^\dagger - E)\mathbf{a} + i\mathbf{a}^\dagger(G(t)^\dagger - G(t))\mathbf{a} \\ &= -D \sum_{m=0}^{(N-k_c)/2} |a_{k_c+2m}|^2, \end{aligned} \tag{A.2}$$

as $G(t)$ is Hermitian and E_{kk} is real for $k < k_c$.

Hence, if the values $D|a_k|^2$ are small for the ionising states $k \geq k_c$, then the overall ionisation rate will also be small, with the ionisation rate limited by

$$\left|\frac{\mathrm{d}|\mathbf{a}|^2}{\mathrm{d}t}\right| \leq D. \tag{A.3}$$

Returning to the equations of motion (A.1), we have

$$\dot{a}_k + iE_{kk}a_k = -i(G(t)_{k,k-2}a_{k-2} + G(t)_{k,k+2}a_{k+2}). \tag{A.4}$$

Limits can be derived for $|a_k|$ by treating the right hand side of this equation as a driving function, suggesting a solution of the form

$$a_k(t) = \beta_k(t) \exp(-iE_{kk}t).$$

Substituting this into equation (A.4) gives the formal solution

$$\beta_k(t) = -i \int_{c_k}^{t} [G(s)_{k,k-2}a_{k-2}(s) + G(s)_{k,k+2}a_{k+2}(s)]\, e^{iE_{kk}s}\, \mathrm{d}s.$$

If we assume that the initial conditions are always of the form $a_k(0) = 1$ for some k satisfying

$k < k_c$ then $\beta_k(0) = 0$ for all $k \geq k_c$ and it follows that

$$\beta_k(t) = -i \int_0^t \left[G(s)_{k,k-2} a_{k-2}(s) + G(s)_{k,k+2} a_{k+2}(s) \right] e^{iE_{kk}s} \, \mathrm{d}s \quad \forall \quad k \geq k_c.$$

Hence

$$|\beta_k(t)| \leq \int_0^t \left[|G(s)_{k,k-2}||a_{k-2}(s)| + |G(s)_{k,k+2}||a_{k+2}(s)| \right] e^{Ds/2} \, \mathrm{d}s \quad \text{for} \quad k \geq k_c.$$

From the original Hamiltonian it can be seen that the off-diagonal matrix elements $G_{ij}(t)$ are bound such that $|G_{ij}(t)| \leq G_{ij}$ for some time-independent values, G_{ij}. If the terms $a_{k\pm2}(t)$ are also bound such that $|a_{k\pm2}(t)| < C$, then

$$|\beta_k(t)| \leq C F_k \int_0^t e^{Ds/2} \, \mathrm{d}s \quad \text{where} \quad F_k = G_{k,k-2} + G_{k,k+2},$$

which can be integrated to give

$$|\beta_k(t)| \leq \frac{2CF_k}{D} \left[e^{Dt/2} - 1 \right] \quad \text{and hence} \quad |a_k(t)| \leq \frac{2CF_k}{D} \left[1 - e^{-Dt/2} \right].$$

We therefore have the limit

$$|a_k(t)| \leq \frac{2CF_k}{D} \quad \text{for all} \quad k \geq k_c. \tag{A.5}$$

The constraint $|a_k| \leq 1$ gives the limit $C = 1$; applying this to equation (A.5) and defining $\mathcal{F}$ as the largest F_k for $k \geq k_c - 2$ provides the limit

$$|a_k(t)| \leq \frac{2\mathcal{F}}{D} \quad \text{for all} \quad k \geq k_c. \tag{A.6}$$

Condition (A.5) can be applied repeatedly to obtain limits for each of the terms, $a_{k_c}, a_{k_c+2}, \ldots, a_N$. Applying condition (A.5) to the states $k \geq k_c + 2$ with the limit C taken from equation (A.6) obtains the next inequality,

$$|a_k(t)| \leq \frac{4\mathcal{F}^2}{D^2} \quad \text{for all} \quad k \geq k_c + 2.$$

Repeating this process, we obtain the conditions

$$|a_k(t)| \leq \left(\frac{2\mathcal{F}}{D}\right)^{m+1} \quad \text{for all} \quad k = k_c + 2m, \tag{A.7}$$

where m is zero or a positive integer. Substituting these limits into equation (A.2), provides the ionisation rate limit,

$$\left|\frac{\mathrm{d}|\mathbf{a}|^2}{\mathrm{d}t}\right| \leq D \sum_{m=0}^{(N-k_c)/2} \left(\frac{2\mathcal{F}}{D}\right)^{2m+2} \tag{A.8}$$

and if $D > 2\mathcal{F}$,

$$\left|\frac{\mathrm{d}|\mathbf{a}|^2}{\mathrm{d}t}\right| < \left(\frac{4\mathcal{F}^2}{D}\right)\left(1 - \left(\frac{2\mathcal{F}}{D}\right)^2\right)^{-1}. \tag{A.9}$$

It follows that

$$\left|\frac{\mathrm{d}|\mathbf{a}|^2}{\mathrm{d}t}\right| \to 0 \quad \text{for} \quad D \to \infty.$$

The effect that extreme values of the decay constant has on the quantal dynamics is in contrast to the classical dynamics where the ionisation mechanism has no influence on the dynamical evolution of the system. For the quantal system we have shown that for $D \to \infty$, $a_k(t) \to 0$ for $k \geq k_c$. This changes the equations of motion (3.10)–(3.16) by removing the transition terms to any of the ionising states, effectively changing the upper limit from $k = N$ to $k = k_c$ and the system is equivalent to a bound system with fewer states.

Appendix B

Calculation of Time above Ionisation Limit

In §5, the theory is developed for the calculation of theoretical ionisation times using the approximate Hamiltonian given by equation (5.5). In this section further detail is provided in the calculation of T_c, the time within each period for which $I_e(t) \geq I_c$, where I_c is the critical ionisation limit.

From equations (5.6–5.8) the time, T_c, can be calculated. There are four cases to consider, depending on whether the phase curve is librational or rotational and whether the critical ionisation limit is above or below the I_e value for the separatrix nodes at $\theta = 0$ and $\theta = \pi$. In figures B.1–B.4 the four different cases are identified. In each figure a resonance island is shown with a number of phase curves shown and the ionising phase curve highlighted in bold, with a line connecting the separatrix nodes at $\theta = 0$ and $\theta = \pi$ and the intersection of the critical ionisation line with the phase curve marked as θ_c. The figures were created for the $O(F^5)$ Dynamic Averaged Hamiltonian with $\Omega_0 = 0.0528$, $F_\mu = 0.13$, $F_s = 0.03393$ and a field envelope of 0-50-0; the value for the ionisation limit, I_c, is chosen artificially to exhibit the different cases.

From equation (5.6), the time, t, shown in each figure is,

$$t = 2\int_{\pi/2}^{\theta_c} \frac{\mathrm{d}\theta_R}{\sqrt{a\cos^2 2\theta_R + b\cos 2\theta_R + c}}.$$

From the figures it can be seen that

$$T_c = \begin{cases} t, & \text{for case 1,} \\ T_l - t, & \text{for case 2,} \\ t, & \text{for case 3,} \\ T_r - t, & \text{for case 4,} \end{cases} \tag{B.1}$$

where T_l and T_r are the librational and rotational time periods and are given by equations (5.7) and (5.8) respectively.

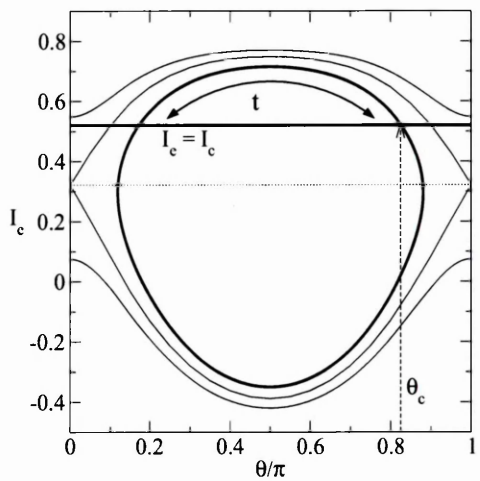

Figure B.1 Case 1: Librational ionising motion with critical ionisation limit lying above the separatrix nodes.

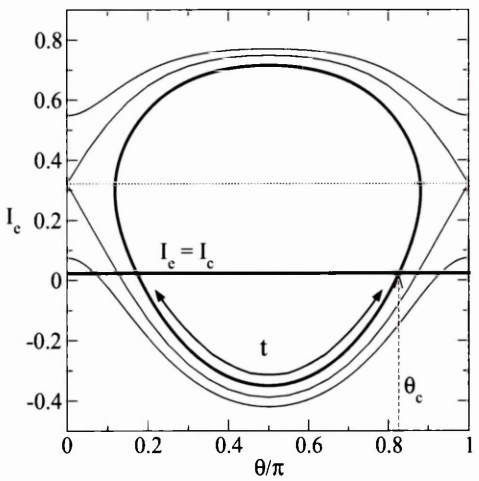

Figure B.2 Case 2: Librational ionising motion with critical ionisation limit lying below separatrix nodes.

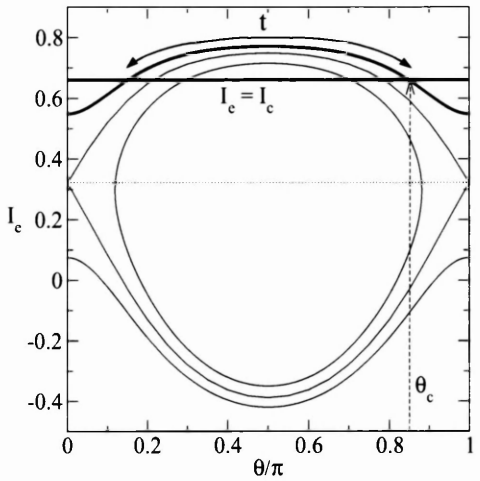

Figure B.3 Case 3: Rotational ionising motion with critical ionisation limit lying above separatrix nodes.

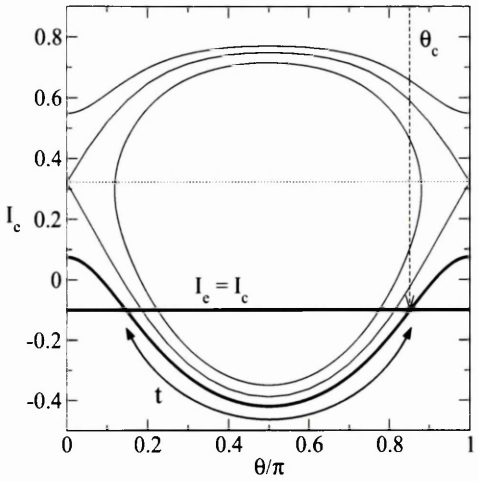

Figure B.4 Case 4: Rotational ionising motion with critical ionisation limit lying below separatrix nodes.

Bibliography

[1] Abromowitz, M., Stegun, I.A., 1972, "Handbook of mathematical functions", Dover Publications

[2] Banks, D., Leopold, J.G., 1978, J. Phys. B11 L5-L9

[3] Banks, D., Leopold, J.G., 1978, J. Phys. B11 37-46

[4] Banks, D., Leopold, J.G., 1978, J. Phys. B11 2833-43

[5] Bayfield, J.E., Koch, 1974, P.M., Phys. Rev. Lett. 33 258-261

[6] Bayfield, J.E., Gardner, L.D., J.E., Koch, P.M.,1977, Phys. Rev. Lett. 39 76-79

[7] Bayfield, J.E., Pinnaduwage, L.A., 1985, Phys. Rev. Lett. 54 313-316

[8] Blümel, R., Smilansky, U., 1987, Z. Phys. D6 83-105

[9] Blümel, R., Smilansky, U., 1990, J. Opt. Soc. Am. B7 664-679

[10] Born, M., 1927, "The mechanics of the atom", G. Bell and Sons, Ltd.

[11] Breuer, H.P., Dietz, K., Molthaus, M., 1989, J. Phys. B22 3187-3196

[12] Buchleitner, A., Delande, 1993, Phys. Rev. Lett. 70 33-36

[13] Buchleitner, A., Delande, D., Gay, J-C, 1995, J. Opt. Soc. Am. B12 505-519

[14] Buchleitner, A., Delande, 1997, Phys. Rev. A55 1585-1588

[15] Casati, G., Chirikov, B.V., Shepelyansky, D.L., 1984, Phys. Rev. Lett. 53 2525-2528

[16] Casati, G., Guarneri, I., B.V., Shepelyansky, D.L., 1988, IEEE J. Quantum Electron. 24 1420-1444

[17] Damburg, R.J., Kolosov, V.V., 1976, J. Phys. B9 3149-3157

[18] Damburg, R.J., Kolosov, V.V., 1979, J. Phys. B12 2637-2643

[19] Damburg, R.J., Kolosov, V.V., 1983, "Theoretical studies of hydrogen Rydberg atoms in electric fields", in "Rydberg states of Atoms and Molecules", ed. R.F. Stebbings and F.B. Dunning, Cambridge University Press.

[20] Dando, P., Richards, D., 1990, J. Phys. B23 3179-3204

[21] Dando, P., 1993, "The dynamics of periodically forced systems", Ph.D. thesis, The Open University.

[22] Dando, P., Richards, D., 1993, J. Phys. B26 3001-3006

[23] Hammersley, J.M., Handscomb, D.C., 1964, "Monte Carlo Methods", Metheun (Monograph on Applied Probability and Statistics)

[24] Galvez, E.J., Sauer, B.E., Moorman, L., Koch, P.M., Richards, D., 1988, Phys. Rev. Lett. 61 2011-2014

[25] Galvez, E.J., Koch, P.M., Richards, D., Zelazny, S.A., 2000, Phys. Rev. A61 060101-1

[26] Jensen, R.V., Phys. Rev. Lett., 1982, 49 1365-1368

[27] Jensen, R.V., Phys. Rev. A, 1984, 30 386-397

[28] Jensen, R.V., Phys. Rev. Lett., 1985, 54 2057-2057

[29] Jensen, R.V., Sanders, M.M., 1989, Phys. Rev. Lett. 63 2771-2775

[30] Koch, P.M., Mariani, D.R., 1981, Phys. Rev. Lett. 46 1275-1278

[31] Koch, P.M., Leeuwen, K.A.H. van, 1995, Phys. Rep. 255 289-403

[32] Koch, P.M., Galvez, E.J., Zelazny, S.A., 1999, Physica D131 90

[33] Experiments were carried out by Koch, P.M. and associates, but the results remain unpublished.

[34] Kulander, K.C., 1987, Phys. Rev. A35 445-447

[35] Kulander, K.C., 1988, Phys. Rev. A38 778-787

[36] Leopold, J.G., Percival, I.C., 1978, Phys. Rev. Lett. 41 944-947

[37] Leopold, J.G., Percival, I.C., 1979, J. Phys. B12 709-721

[38] Leopold, J.G., Richards, D., 1985, J. Phys. B18 3369-3394

[39] Leopold, J.G., Richards, D., 1986, J. Phys. B19 1125-1142

[40] Leopold, J.G., Richards, D., 1989, J. Phys. B22 1931-1961

[41] Leopold, J.G., Richards, D., 1991, J. Phys. B24 1209-1240

[42] Leopold, J.G., Richards, D., 1994, J. Phys. B27 2169-2189

[43] Leeuwen, K.A.H. van, Oppen, G. v., Renwick, S. , Bowlin, J.B., Koch, P.M., Jensen, R.V., Rath, O., Richards, D., Leopold, J.G., 1985, Phys. Rev. Lett. 55 2231-2234

[44] Landau, L.D., Lifschitz, E.M., 1976, Course of Theoretical Physics: Mechanics (Third Edition), Butterworth Heinemann

[45] Lichtenberg, A.J., Lieberman, M.A., 1992, Regular and Chaotic Dynamics (Second Edition), Springer-Verlag

[46] Meerson, B.I., Oks, E.A., Sasorov, P.V., 1979, Pis'ma Zh. Eksp. Teor. Fiz. 29 79-82

[47] Rath, O., Richards, D., 1988, J. Phys. B21 555-571

[48] Richards, D., 1987, J. Phys. B20 2171-2192

[49] Richards, D., Leopold, J.G., Koch, P.M., Galvez, E.J., Leeuwen, K.A.H. van, Moorman, L., Sauer, B.E., Jensen, R.V., 1989, J. Phys. B22 1307-1333

[50] Richards, D., 1996, J. Phys. B29 5237-5271

[51] Richards, D., 2005, New J. Phys. 7 138

[52] Robicheaux, F., Oks, E., Parker, A.L., Uzer, T., 2002, J. Phys. B35 4613-4618

[53] Sauer, B.E., Yoakum, S., Moorman, L., Koch, P.M., Richards, D., Dando, P.A., 1992, Phys. Rev. Lett. 68 468-471

[54] Shirley, J.H., 1965, Phys. Rev. 138 B979-987

[55] Susskind, S.M., Jensen, R.V., 1988, Phys. Rev. A38 711-728

[56] Zakrzewski, J., Delande, D., Gay, J-C, 1993, Phys. Rev. A47 2468-2471